PH.D. THESIS

Assessment of the possibility of improving the momentum transfer in the flow between rotating discs

Mohammadsadegh Pahlavanzadeh

Supervisor: Prof. Włodzimierz Wróblewski, DSc (Eng), PhD

Co-supervisor: Dr Krzysztof Rusin, PhD (Eng)

Scientific discipline: Environmental Engineering, Mining and Energy

Gliwice, Poland, 2025

Acknowledgment

I would like to extend my heartfelt thanks to all those whose support and contributions made this thesis possible. I am especially grateful to my supervisor, Prof. Włodzimierz Wróblewski, for his invaluable guidance, mentorship, and encouragement throughout the course of my research. I also sincerely thank my co-supervisor, Dr. Krzysztof Rusin, for his support, insightful feedback, and valuable discussions that greatly enriched this work.

My sincere appreciation goes to the Polish National Science Center for partially funding this research through the project UMO-2019/35/B/ST8/01871, titled “The enhancement of momentum transfer efficiency in the flow between rotating disks.”

Above all, I wish to express my deepest gratitude to my family members for their unwavering love, continuous support, and steady encouragement throughout this journey. Their faith in me has been a constant source of strength, and I wholeheartedly dedicate this thesis to them.

Contents

Note on thesis format

This doctoral dissertation is presented in a paper-based format consisting of five published papers. The structure of the thesis follows the order in which the studies were conducted and thematically developed, building a comprehensive understanding of the assessment of the possibility of improving the momentum transfer in the flow between rotating disks.

During the implementation of the doctoral thesis, additional roughness modeling using the Porous Medium Layer Model was conducted. This work is included in Chapter 5 ‘Roughness modeling by Porous Medium Layer Model in a Tesla turbine working on ORC fluids’, which is an addition to the monothematic series of publications presented in the previous chapters. A shortened scope of the chapters is summarized below:

- Chapter 1: Introduction
- Chapter 2: Investigation of flow characteristics in minichannel with stationary and rotating walls. (Papers I and II)
- Chapter 3: Investigation of flow characteristics between co-rotating disks of Tesla turbine considering different nozzle and supply configurations. (Papers III and IV)
- Chapter 4: Simulation of roughness using porous medium layer (PML). (Paper V)
- Chapter 5: Roughness modeling by Porous Medium Layer Model in Tesla turbine working on ORC fluids.

List of publications

The thesis consists of 5 papers listed below, categorized into three chapters. The full texts of these papers can be found in the appendices. The papers are referred to by Roman numerals throughout the thesis.

Paper I: **Pahlavanzadeh, M**., Rusin, K., Wróblewski, W., (2023). Evaluation of dynamic correction of turbulence wall boundary conditions to simulate roughness effect in minichannel with rotating walls. International Journal of Numerical Methods for Heat & Fluid Flow. https://doi.org/10.1108/HFF-03-2023-0160.

Paper II: **Pahlavanzadeh, M**., Rulik, K., Wróblewski, W., Rusin, K., (2024). Application of roughness models to stationary and rotating minichannel flows. International Journal of Numerical Methods for Heat & Fluid Flow. https://doi.org/10.1108/HFF-05-2024-0379.

Paper III: **Pahlavanzadeh, M**., Wróblewski, W., Rusin, K., (2024). On the Flow in the Gap between Co-rotating Disks of Tesla Turbine with Different Supply Configurations: A Numerical Study. Energies. https://doi.org/10.3390/EN17174472.

Paper IV: **Pahlavanzadeh, M**., Wróblewski, W., Rusin, K., (2025). Evaluation of nozzle configuration impact on flow structures and performance in Tesla turbine. International Journal of Heat and Mass Transfer. https://doi.org/10.1016/J.IJHEATMASSTRANSFER.2025.126900.

Paper V: **Pahlavanzadeh, M**., Rusin, K., Wróblewski, W., Rulik, S., (2025). Roughness effects on flow in Tesla turbine with parametric adjustment of porous layer model. Physics of Fluids. https://doi.org/10.1063/5.0247548/3329214.

CRediT authorship contribution statement

The author's contribution to each paper in the appendices are as follows:

Paper I: Mohammadsadegh Pahlavanzadeh: Conceptualization, Methodology, Software, Investigation, Validation, Formal analysis, Writing – original draft, Writing – review & editing (Mohammadsadegh Pahlavanzadeh's contribution was equal to 60%.).

Paper II: Mohammadsadegh Pahlavanzadeh: Conceptualization, Methodology, Software, Investigation, Validation, Formal analysis, Writing – original draft, Writing – review & editing (Mohammadsadegh Pahlavanzadeh's contribution was equal to 60%.).

Paper III: Mohammadsadegh Pahlavanzadeh: Conceptualization, Methodology, Software, Investigation, Validation, Formal analysis, Writing – original draft, Writing – review & editing (Mohammadsadegh Pahlavanzadeh's contribution was equal to 55%.).

Paper IV: Mohammadsadegh Pahlavanzadeh: Conceptualization, Methodology, Software, Investigation, Validation, Formal analysis, Writing – original draft, Writing – review & editing (Mohammadsadegh Pahlavanzadeh's contribution was equal to 60%.).

Paper V: Mohammadsadegh Pahlavanzadeh: Conceptualization, Methodology, Software, Investigation, Validation, Formal analysis, Writing – original draft, Writing – review & editing (Mohammadsadegh Pahlavanzadeh's contribution was equal to 55%.).

Abstract

Momentum diffusion and kinetic energy transfer remain fundamental challenges in turbomachinery, particularly for bladeless configurations such as the Tesla turbine. This radial-flow machine exhibits significant potential for applications in Organic Rankine Cycles (ORC) and Combined Heat and Power (CHP) systems, as well as micro-power generation, waste heat recovery, geothermal energy conversion, and small-scale propulsion systems. However, analyzing the flow inside the narrow gap between the co-rotating disks of the turbine is complex due to the sub-millimeter length scales, the variable cross-sectional geometry, the interaction of rotational body forces with turbulence, the influence of the configurations of the inlet nozzles, and the moving wall boundaries. Surface roughness further complicates the flow field, and the turbine's global design parameters, such as the supply and nozzle configurations, the number and dimensions of co-rotating disks, must be carefully optimized to achieve maximum efficiency.

This research begins with a systematic assessment of turbulence and roughness modeling approaches to simulate flow within narrow gaps formed by rough co-rotating disks. Two roughness models are examined: one that applies a downward shift to the dimensionless velocity profile (modification of the wall function) and another that modifies the parameters of near-wall turbulence according to the Aupoix method. These models are validated across progressively complex geometries—starting with flow over rough flat plates, followed by flow through stationary and rotating minichannels. The $k-\omega$ Shear Stress Transport (SST) turbulence model combined with Aupoix's wall correction is identified as the most reliable and accurate approach, particularly for domains requiring fine near-wall resolution (low y^+). Parametric studies demonstrate how variations in minichannel height, mass flow rate, working fluid, and roughness height influence the velocity profile and wall shear stresses.

Subsequent investigations focus on the flow phenomena in the Tesla turbine. Two supply nozzle configurations, one with six nozzles (N6) and another with forty nozzles (N40), were studied to assess the influence on flow characteristics and turbine performance. To reduce computational cost, each configuration is simulated using a domain with a representative periodic nozzle sector and a periodic diskgap sector. Large Eddy Simulation (LES) with the Smagorinsky subgrid-scale (SGS) model is employed for the N6 case and compared to results from the $k-\omega\ SST$ model. The $k-\omega\ SST$ model demonstrates adequate accuracy for engineering analysis, despite slight overprediction of flow parameters. The N40 configuration reveals increased mass flow and power generation, but a notable reduction in efficiency due to intensified inlet jet interactions and high turbulence level near the disk tips.

Inlet jet configurations are further evaluated by comparing one-to-many and one-to-one nozzle configurations. LES simulations indicate that the one-to-many configuration causes higher flow fluctuations and decreased efficiency as a result of inlet jet/disk tip interactions. The one-to-one setup, while still affected by turbulence induced by rotating walls, yields a more uniform energy transfer. These findings emphasize the critical role of supply nozzle design in reducing losses and improving turbine performance.

Since direct modeling of real surface roughness through equivalent sand-grain proves insufficient due to the lack of general correlation, a Porous Medium Layer (PML) approach is introduced. The PML method uses a porous zone on the disk surface with tunable porosity and permeability to mimic roughness-induced resistance. The investigation began with the validation of the PML model against in-house experimental tests performed for water flow in a minichannel. The parameters of the PML model are adjusted to achieve the same pressure drop as observed in the experiments. Once validated, it is applied to rotating disk systems. The performance of the PML model is compared with the Aupoix roughness model, considering different heights of roughness.

In the final stage of the study, a comprehensive analysis is conducted to simulate the effects of surface roughness on the flow within the gap between the co-rotating disks of a Tesla turbine, using two low-boiling-point working fluids: R1234yf and n-hexane. The previously validated PML model is employed to replicate the impact of realistic surface roughness on the flow characteristics of the Tesla turbine operating with real gases.

The turbulence closure used in this study was the $k-\omega\,SST$ model. The results demonstrated that the PML roughness model effectively captures the influence of surface roughness on flow characteristics, resulting in an accurate simulation of the Tesla turbine's performance in the tested cases. Furthermore, the analysis of two real working fluids—R1234yf and n-hexane—indicates that the PML model is applicable for simulating Tesla turbines operating with real gases and that fluid properties significantly influence flow throughout the expansion process.

Streszczenie

Dyfuzja pędu oraz transfer energii kinetycznej stanowią kluczowe wyzwania w maszynach przepływowych, zwłaszcza w układach bezłopatkowych, takich jak turbina Tesli. Urządzenie to, charakteryzujące się przepływem promieniowym, wykazuje duży potencjał zastosowań w organicznych obiegach Rankine'a (ORC), układach skojarzonych wytwarzania ciepła i energii elektrycznej (CHP), mikrogeneracji, odzysku ciepła odpadowego, konwersji energii geotermalnej oraz w małoskalowych systemach napędowych. Analiza przepływu w szczelinie pomiędzy wirującymi dyskami turbiny jest jednak wyjątkowo złożona ze względu na submilimetrowe skale geometryczne, zmienną geometrię przekroju poprzecznego, oddziaływanie sił bezwładnościowych związanych z ruchem obrotowym na turbulencję, wpływ konfiguracji dysz wlotowych oraz poruszające się ściany. Chropowatość powierzchni dodatkowo komplikuje strukturę pola przepływu. Główne parametry konstrukcyjne turbiny — takie jak układ zasilania i dysz, liczba oraz wymiary współwirujących dysków — wymagają optymalizacji w celu uzyskania maksymalnej sprawności.

Badania rozpoczęto od systematycznej analizy metod modelowania turbulencji i chropowatości w symulacjach przepływu przez wąskie szczeliny między wspólnie obracającymi się dyskami. Rozpatrzono dwa modele chropowatości: pierwszy, wprowadzający przesunięcie w dół bezwymiarowego profilu prędkości (modyfikacja funkcji ścianki), oraz drugi, modyfikujący parametry turbulencji przy ścianie zgodnie z metodą Aupoix. Modele te zweryfikowano na coraz bardziej złożonych geometriach — począwszy od przepływu nad chropowatą płytą płaską, poprzez przepływ w nieruchomych i obrotowych minikanałach. Model turbulencji $k-\omega$ Shear Stress Transport (SST) w połączeniu z korektą przyścienną Aupoix okazał się najbardziej wiarygodnym i dokładnym podejściem, szczególnie w domenach wymagających wysokiej rozdzielczości w obszarze przyściennym (niska wartość y^+). Badania parametryczne wykazały, że wysokość minikanału, strumień masowy, rodzaj czynnika roboczego oraz wysokość chropowatości istotnie wpływają na profil prędkości i naprężenia styczne przy ściance.

Kolejne etapy prac dotyczyły zjawisk przepływowych w turbinie Tesli. Analizie poddano dwie konfiguracje dysz zasilających: z sześcioma dyszami (N6) oraz z czterdziestoma dyszami (N40), w celu oceny ich wpływu na charakterystyki przepływu i sprawność turbiny. W celu ograniczenia kosztów obliczeń każdą konfigurację symulowano w domenie obejmującej reprezentatywny periodyczny sektor dyszy oraz periodyczny sektor szczeliny międzydyskowej. Dla przypadku N6 zastosowano symulacje typu Large Eddy Simulation (LES) z modelem podsiatkowym Smagorinsky'ego (SGS) i porównano wyniki z modelem $k-\omega\,SST$. Model $k-\omega\,SST$ wykazał wystarczającą dokładność w analizach inżynierskich, mimo nieznacznej tendencji do przeszacowywania parametrów przepływu. Konfiguracja N40 charakteryzowała się zwiększonym strumieniem masowym i wyższą mocą generowaną, lecz także spadkiem sprawności wynikającym z nasilonych interakcji strumieni wlotowych oraz wzrostu poziomu turbulencji w rejonie krawędzi dysków.

Dalsze analizy objęły porównanie konfiguracji strumieni wlotowych typu „one-to-one” oraz „one-to-many”. Symulacje LES wykazały, że układ „one-to-one” powoduje większe fluktuacje przepływu i obniża sprawność w wyniku interakcji strumieni wlotowych z krawędziami dysków. Konfiguracja „one-to-one”, mimo oddziaływania turbulencji indukowanej przez ściany wirujące, zapewniała bardziej jednorodny transfer energii. Wyniki te podkreślają kluczową rolę geometrii dysz zasilających w ograniczaniu strat i poprawie sprawności turbiny.

Ponieważ bezpośrednie modelowanie rzeczywistej chropowatości powierzchni za pomocą równoważnego ziarna piasku okazało się niewystarczające z powodu braku uniwersalnej korelacji, wprowadzono podejście oparte na warstwie ośrodka porowatego (Porous Medium Layer, PML). Metoda PML wykorzystuje strefę porowatą na powierzchni dysku, o regulowanej porowatości i przepuszczalności, w celu odwzorowania oporu wywołanego chropowatością. Walidację modelu przeprowadzono na podstawie eksperymentów własnych dla przepływu wody w minikanale, dostosowując parametry PML w taki sposób, aby odtworzyć obserwowane spadki ciśnienia. Po zwalidowaniu modelu zastosowano go w układach z wirującymi dyskami i porównano jego skuteczność z modelem Aupoix, uwzględniając różne wysokości chropowatości.

W końcowym etapie badań przeprowadzono kompleksową analizę wpływu chropowatości powierzchni na przepływ w szczelinie pomiędzy współwirującymi dyskami turbiny Tesli z wykorzystaniem dwóch czynników roboczych o niskiej temperaturze wrzenia: R1234yf oraz n-heksanu. W tym celu zastosowano uprzednio zwalidowany model PML. Do zamknięcia układu równań przepływu wykorzystano model turbulencji $k-\omega\,SST$. Wyniki wykazały, że model PML poprawnie symuluje wpływ chropowatości powierzchni na strukturę przepływu, umożliwiając wierne odwzorowanie pracy turbiny Tesli w analizowanych przypadkach. Analiza porównawcza dwóch czynników roboczych — R1234yf i n-heksanu — potwierdziła, że model PML jest przydatny w symulacjach turbiny Tesli pracującej na gazach rzeczywistych oraz, że właściwości termofizyczne czynnika mają istotny wpływ na zjawiska przepływowe w procesie rozprężania.

Nomenclature

Abbreviations

RANS	Reynolds-Averaged Navier-Stokes	_
uRANS	unsteady Reynolds-Averaged Navier-Stokes	_
LES	Larg Eddy Simulation	_
CFD	Computational Fluid Dynamics	_
ORC	Organic Rankine Cycle	_
CHP	Combined Heat and Power	_
SST	Shear Stress Transport	_
PML	Porous Medium Layer	_
DEnS	Distributed Energy Systems	_
DNS	Direct Numerical Simulation	_
SWF	Standard Wall Function	_
EWT	Enhanced Wall Treatment	_
LWMR	Law-of-the-Wall Modified for Roughness	_
SGS	Subgrid-Scale	_
WMLES	Wall-Modeled Large Eddy Simulation	_

Symbols

C	smooth-wall interception	_
C_s	roughness constant	_
C_p	specific heat at constant pressure	$J.kg^{-1}K^{-1}$
D_h	hydraulic diameter	m
d_w	wall distance	m
e	Specific internal energy	J
h_{max}	maximum height of the cell	m

h_{wn}	wall-normal grid spacing	m
f_i	specific body force	$m.s^{-2}$
k	turbulent kinetic energy per mass unit	$m^2.s^{-2}$
k_s	equivalent sand-grain roughness	–
k_P	turbulence kinetic energy at the near-wall node *P*	$m^2.s^{-2}$
k_s^+	roughness Reynolds number	–
k_w^+	dimensionless turbulent kinetic energy close to the wall	–
$\dot{m}$	mass flow rate	$kg.s^{-1}$
N	power	W
n	rotational speed	rpm
p	static pressure	Pa
q	specific heat flux per mass unit	$W.kg^{-1}$
Re	Reynolds number	–
Re_τ	friction Reynolds number	–
S	strain rate tensor	s^{-1}
T	static temperature	K
t	time step	s
U	velocity vector	$m.s^{-1}$
U^+	dimensionless mean velocity (related to wall shear stress)	–
u_τ	skin friction velocity	$m.s^{-1}$
ΔU^+	roughness function	–
y^+	dimensionless normal-wall distance (related to wall shear stress)	–
y^*	dimensionless normal-wall distance (related to turbulent kinetic energy)	–
y_P	distance from point *P* to the wall	m
κ	von Karman constant	–
ν	kinematic viscosity	$m^2.s^{-1}$

τ_w	total wall shear stress	Pa
ρ	density	$Kg.m^{-3}$
τ	tangential stress	Pa
μ	dynamic viscosity	$Pa.s$
μ_t	turbulent viscosity	$Pa.s$
α^*, β^*	closure coefficients in specific dissipation rate equation	_
σ_k	diffusion of turbulent kinetic energy	_
σ_ω	diffusion of specific dissipation rate	_
P_k	production of turbulent kinetic energy	_
Ω	angular velocity	$rad.s^{-1}$

Subscriptions

lam	laminar regime	_
t	turbulent regime	_
E	Euler equation for turbine	_
$smooth$	smooth wall surface	_
$rough$	rough wall surface	_
in	inlet	_
out	outlet	_
r	radial direction	_
θ	circumferential direction	_

Chapter 1

Introduction

1.1 Motivation

Ensuring a reliable and environmentally sustainable energy supply remains a major global challenge. While conventional sources such as coal and gas offer consistent output, they are major contributors to carbon emissions and environmental degradation. On the contrary, renewable energy sources, such as wind, solar, and hydro, provide cleaner alternatives but are limited by intermittency and geographic constraints.

To address these challenges, distributed energy systems (DEnS) are gaining traction. By decentralizing power generation and placing small-scale units near consumption points, DEnS reduce transmission losses, enhances reliability, and enables better integration of renewables. Technologies such as microturbines, CHP systems, and rooftop solar are central to these systems, especially when combined with energy storage and smart grids.

In advanced configurations, DEnS can enable individual buildings or even entire communities to achieve partial or complete energy self-sufficiency. These buildings can generate their electricity, as well as provide heating and cooling through integrated energy systems that are tailored to local needs and resource availability. Additionally, when combined with energy storage and smart grid technologies, DEnS can significantly improve load management, reduce peak demand, and support greater integration of renewables into national grids.

Ultimately, a futureproof energy system will likely depend on a diversified mix of large-scale renewable generation, supported by flexible, local distributed energy solutions that together ensure both reliability and environmental sustainability.

Waste heat plays a crucial role in enhancing energy efficiency. Currently, more than 50% of the energy consumed worldwide is lost as low-temperature waste heat [1]. For example, internal combustion engines lose approximately 60% of fuel energy as waste heat [2]. Recovering even a fraction of this wasted heat can significantly improve process efficiency and reduce fuel consumption.

Waste heat can be considered a low-temperature heat source. Several thermodynamic cycles can harness low-temperature energy sources, including the Organic Rankine Cycles (ORC), the Kalina Cycle, and the Goswami Cycle. ORC utilizes organic fluid with a low boiling point to extract energy from low-temperature sources [3]. The Kalina Cycle, which employs a variable mixture of two fluids (typically ammonia and water), allows the boiling temperature to adjust to the energy source. The Goswami cycle, which also uses a fluid mixture, has the added capability of producing both cooling energy and electricity.

Waste heat recovery systems frequently employ volumetric expanders, such as scroll, screw, vane, or piston expanders. These devices are well-suited for low mass flow rates and higher-pressure ratios and can handle two-phase working mediums [4]. Radial turbines, which share similar characteristics, are another viable option for such systems. Their ability to manage significant enthalpy drops while maintaining low peripheral speeds makes them ideal for compact, single-stage designs. In addition, radial turbines have a low degree of reaction, which improves sealing efficiency [5]. For low-power applications (i.e., up to $100 - 150\ kW$), radial expanders are often the preferred choice [5]. Tesla turbomachinery, which is a radial expander [6], finds application in various industries, including CHP and ORC systems.

ORC technology is well-suited for converting low- to medium-temperature waste heat from industrial processes, etc. [7]. The review by Daniarta et al. [8] highlights the compatibility of various thermal energy storage technologies with ORC, especially in renewable and waste heat recovery applications. ORC-based Tesla turbines [9,10] present an interesting and innovative alternative to traditional expanders in waste heat recovery systems, offering potential efficiency gains.

The Tesla turbine combines the features of volumetric expanders with a radial design. Its simplicity, high reliability, and low manufacturing costs make it a strong candidate in the micro-expander market. With fewer moving parts, the Tesla turbine provides greater durability and reduced maintenance, making it an attractive solution for small-scale applications, particularly in waste heat recovery and other distributed energy systems.

Enhancing the efficiency of the Tesla turbine is, a critical step in expanding its industrial viability. Improving its performance could substantially increase the feasibility of energy recovery systems and contribute to more effective waste heat utilization. In this context, the present research aims to assess the potential for enhancement of the Tesla turbine operation so that it becomes a competitive alternative to conventional expanders used in low-temperature applications.

1.2 Literature review

The Tesla turbine is a unique type of turbomachinery that operates based on viscous shear forces rather than the conventional blade-driven momentum transfer seen in traditional turbines. Its performance is influenced by its design, operating conditions, and the interaction between its components. This turbine consists of three main parts: the supply apparatus, the rotor, and the outlet system. The supply apparatus functions similarly to a stator in conventional turbines, converting the enthalpy of the working fluid into kinetic energy by using vanes or nozzles. As the fluid expands in the nozzles, its velocity increases, while its pressure decreases. Depending on the thermodynamic parameters and the shape of the inlet nozzles, the flow may be subsonic or supersonic. The geometric angle of the nozzle is critical, as it affects the velocity components of the working fluid [11].

The rotor is the most distinctive component of the Tesla turbine, consisting of multiple thin disks mounted on a common shaft. The fluid flowing between the disks adheres to the disk

surfaces due to intermolecular forces. This creates a no-slip condition where the fluid layer closest to the disk surface remains stationary relative to it, while the outer layers move faster, leading to momentum diffusion. Faster-moving fluid particles collide with slower ones, transferring momentum and causing the disks and rotor to rotate.

As Rice [12] pointed out, machines operating on shear forces require minimal velocity differences between the fluid and the disks and narrow spacing between the disks to maintain laminar flow. However, these conditions result in low mass flow rates and small velocity gradients, which limit power output. Using multiple disks can mitigate this issue, but it increases the turbine's size and complexity. Surface modifications, such as micro-grooving or directional roughness, can enhance momentum diffusion by disrupting the boundary layer; however, this contradicts the need for laminar flow [13].

The Tesla turbine's main drawback is its low efficiency, largely due to the supply apparatus. Laminar flow necessitates small nozzles, where the boundary layers can occupy a significant portion, increasing viscous losses [13]. Additionally, interactions between the disk edges and fluid can disrupt flow in the rotor's upper section. While the stresses on the disk walls drive the turbine, the stresses in other areas, such as the casing, are undesirable and contribute to losses [11].

To comprehensively evaluate the performance and optimization of the Tesla turbine, researchers have adopted both experimental and numerical approaches. Experimental investigations have focused on validating theoretical models, assessing performance under real operating conditions, and testing the effects of design parameters such as disk geometry, nozzle configuration, and working fluid selection. In parallel, numerical simulations, particularly those using Computational Fluid Dynamics (CFD), have provided detailed insights into the flow behavior, turbulence characteristics, and thermodynamic efficiency within the turbine. The following sections present a categorized review of key experimental and numerical studies in the field.

1.2.1 Experimental research on Tesla turbine

Experimental studies on the Tesla turbine have been essential in evaluating its practical performance, validating analytical models, and understanding the influence of design and operating parameters.

The initial experimental works primarily focused on assessing the turbine’s overall efficiency and mechanical behavior under various operating conditions. These studies investigated the influence of critical parameters such as inter-disk spacing, number of disks, p_{in}, nozzle geometry, and working fluid type on the power output and efficiency. Due to the relatively simple construction of the Tesla turbine, many researchers have also explored its applicability in micro-scale energy systems, waste heat recovery, and low-temperature energy conversion.

Warner [14] conducted one of the first experimental investigations into Tesla turbines [14] in his master's thesis. He tested a turbine consisting of two disks with an outer diameter of

$125\ mm$ and a single inlet nozzle, achieving a maximum power output of $27.5\ W$ and an efficiency of 2.9%. This work was later expanded by Leaman [14], who improved the design by incorporating multiple disks, additional nozzles, and more efficient bearings. These modifications resulted in a significantly higher output of $87\ W$ and an efficiency of 8.6%. Young [16] later conducted similar experimental efforts [15]. In a more modern study, Patel and Schmidt [16] used biomass combustion gases as a working fluid and achieved a power output of $3.2\ kW$ with an efficiency of 11%. More recently, Talluri et al. [17] carried out experiments using organic working fluid. Their turbine featured a rotor diameter of $108\ mm$, a narrow $0.1\ mm$ gap between disks, and 60 rotor channels, yielding a peak shaft efficiency of 9.62%.

More recent experimental investigations have aimed to improve turbine performance by incorporating novel design features, optimizing flow distribution, and introducing modifications such as surface roughness, flow control devices, and improved nozzle arrangements. Instrumentation advancements have allowed for more detailed measurements of pressure, velocity, temperature, and torque, enabling more accurate assessments of losses and flow characteristics inside the turbine.

Rusin et al. [18] conducted an experimental analysis of a Tesla turbine consisting of five disks, each 160 mm in diameter, with an inter-disc gap of 0.75 mm. The nozzle apparatus comprised four diverging nozzles with a minimum cross-sectional height of 2.85 mm. Air was used as the working fluid, and tests were performed at three pressure ratios: 1.4, 1.6, and 1.88. The maximum generated power was 126 W, and all power characteristics showed good agreement with numerical calculations. Pressure distribution in the plenum chamber, tip clearance, and the temperature drop between the turbine inlet and outlet were also measured. The study further indicated that the turbine efficiency could exceed 20% if the adverse effects of lateral gaps between the disks and the casing were eliminated.

A recent experimental study by Teng et al. [19] investigated the integration of a Tesla turbine as a bladeless expander in an ORC system for low-grade heat recovery (90–130°C). A prototype system was developed to evaluate the isentropic efficiency, mechanical losses, and response of the turbine to varying heat source temperatures, pump speeds ($750 - 1170\ rpm$), and electrical loads ($0.4 - 1.9\ A$). The turbine achieved a peak isentropic efficiency of 62.28% and a maximum power output of $31.76\ W$.

1.2.2 Numerical research on Tesla turbine

Numerical works provide a theoretical and computational framework for analyzing the complex flow behavior inside Tesla turbines, which is governed primarily by boundary layer and viscous effects rather than traditional blade aerodynamics. Early models were largely analytical, but advances in CFD have enabled detailed simulations of turbulent flow between rotating disks. These studies aim to predict performance metrics, identify loss mechanisms, and optimize geometry, often guiding experimental designs and reducing the need for costly trial-and-error testing.

Sandilya et al. [20] conducted a numerical study on the flow between co-rotating disks using a gas mixture of air and SO_2. Later, Lampart and Jedrzejewski [21] used CFD tools to evaluate the performance of two Tesla turbine designs with varying rotor diameters, both operating with a low-boiling-point working fluid. Sengupta and Guha [22] proposed a three-dimensional analytical model derived from the Navier-Stokes equations, simplified by order-of-magnitude analysis. Their model assumed steady, laminar, incompressible, and Newtonian flow with constant fluid properties, axial symmetry, and negligible body forces.

Qi et al. [23] used numerical simulations to investigate how disk thickness, inter-disk gap, and inlet nozzle configuration influence turbine performance. They compared two setups: a "one-to-one" configuration where each nozzle feeds a single disk gap, and a "one-to-many" setup where one nozzle distributes flow across all gaps. Their findings showed that the efficiency of the one-to-many design was highly dependent on the thickness of the disk, while the one-to-one configuration was more sensitive to changes in rotational speed.

In a subsequent study, Qi et al. [24] further analyzed turbine performance with a focus on the outlet geometry. They reported peak isentropic efficiencies of 23.91% for the one-to-one layout and 14.91% for the one-to-many, with radial outflow outperforming axial discharge.

Fiaschi and Talluri [25] conducted a two-dimensional numerical analysis of a Tesla turbine operating with supercritical CO_2. The model assumed steady, viscous, and compressible flow with real gas behavior, neglecting body forces. Their results, based on a turbine with a $0.5\ m$ rotor diameter and inlet conditions of $220\ bar$ and 150°C, showed an output of $23.4\ W$ per channel and an efficiency of 62.9%.

In aiming for a more realistic depiction of the Tesla turbine's functionality, which involves the delivery of fluid via nozzles at specific points, significant challenges emerge in understanding the flow dynamics, especially in the proximity of the jets. In this critical zone, the interaction between the incoming jet and the developing boundary layers originating from the co-rotating disks leads to complex transient behavior, necessitating a comprehensive analysis. In their study, Rusin et al. [26]. conducted a detailed examination and evaluation of a Tesla turbine model, focusing on the influence of turbulence models on the prediction of operational parameters. They systematically investigated various turbulence models, employing different temporal and spatial discretization techniques. Additionally, they analyzed the distribution of power units across the disks and compared the turbine's power predictions obtained from numerical simulations with initial experimental data. Their analysis revealed a consistent trend of overestimation across all turbulence models compared to experimental observations. This discrepancy underscores the need for further refinement and validation of turbulence models to accurately predict the operational performance of Tesla turbines.

In an earlier study, Rusin et al. [27] conducted a Tesla-style turbine comprising five co-rotating disks. They focused on efficiency optimization by fine-tuning both geometrical and operational parameters. Central to their investigations was minimizing radial tip clearance, a critical factor in preventing rotor displacement and subsequent rubbing of disks against the casing, particularly under the influence of different rotational speed and manufacturing

tolerances. Their approach primarily involved efficiency-driven numerical optimization of the Tesla turbine. This optimization process focused on refining parameters such as inlet nozzle height, inter-disk gap, nozzle angle, pressure, and rotational speed. By systematically adjusting these key variables, they aimed to enhance turbine performance and mitigate potential operational challenges associated with clearance issues and mechanical constraints. A recent investigation [28] also involves the design, fabrication, and testing of a Tesla turbine with $100\,mm$ diameter disks, central exhaust, and interchangeable nozzles. CFD simulations were used to optimize geometry and analyze viscous losses and turbulence, supporting the experimental setup. The prototype achieved up to 8% efficiency at 3–5 bar, demonstrating its suitability for small-scale, low-pressure renewable energy applications.

1.2.3 Roughness modeling

Surface roughness plays a significant role in the performance of Tesla turbines due to the dominance of viscous forces in the boundary layer flow between the rotating disks. Unlike traditional bladed turbines, the efficiency of Tesla turbines is highly sensitive to wall shear stress and momentum transfer near disk surfaces, making an accurate simulation of surface roughness essential for reliable performance prediction.

The formation of boundary layers near solid walls is a fundamental concern in CFD simulations. For example, in the case of flow over a flat plate, velocity and turbulence quantities exhibit sharp, nonlinear gradients rising from zero at the wall surface (as dictated by the no-slip condition) to their respective equilibrium freestream values further away from the wall. The performance of some systems depends on the velocity profile close to the wall and, consequently, wall shear stress due to viscosity and turbulence, which play a very important role in this regard [29–31]. Concerning the near-wall region, two ways are usually recommended in the Reynolds-averaged Navier-Stokes (RANS) approach. The first method is to calculate the turbulent viscosity in this region. Turbulence models are modified to resolve the turbulent parameters in the whole region, including the inner part of the boundary layer and the area with intense changes in the turbulent viscosity. However, this approach requires a fine mesh in these regions, which incurs high computational costs. The second approach is to employ wall functions that can model the near-wall region. Wall functions are meant to avoid excessive grid requirements. They come from analytical solutions used to satisfy the physics of flow in the near-wall region [32], and to ensure the most accurate results; usually, the first cell center must be in the log-law region [33]. Wall functions bridge the inner region between the wall and the fully turbulent part of the flow regime to calculate momentum and turbulence transport equations close to the wall rather than specifying them on the wall [34].

Rough-wall turbulent boundary layer flow is a complex physical phenomenon that increases the skin friction drag as compared to the smooth-wall case [35–37]. It can significantly affect fluid dynamics and heat transfer in flows by introducing perturbations in the flow, which lead to changes in the mean velocity profile in the boundary layer [38]. The viscous sublayer is replaced by the roughness sublayer, which enhances surface drag, pressure drop, turbulent mixing, momentum transfer, and heat transfer [39]. Roughness occurs as a result of the regular exploitation of products, as an effect of erosion, icing, deposition, or during

manufacturing. Roughness is characterized by a set of parameters that can be determined during the manufacturing process [40].

According to Nikuradse's measurements of the pressure drop in the pipe [41], the mean velocity profile in the log-law region for both smooth and rough cases is expressed as follows:

$$U^+ = \frac{1}{\kappa}\ln(y^+) + C - \Delta U^+ \tag{1}$$

$$U^+ = \frac{U}{u_\tau} \tag{2}$$

$$y^+ = \frac{u_\tau y}{\nu} \tag{3}$$

where U represents the mean velocity, u_τ is the friction velocity (defined as $u_\tau = \frac{\tau_w}{\rho}$, where τ_w and ρ are the total wall stress and fluid density, respectively), y is the normal distance to the wall, and ν is the kinematic viscosity. C and κ are the smooth-wall interception and the von Karman constant, respectively. There is still a debate about their values. However, all the proposed values differ by less than 3%. The most common values for these variables were assumed to be 5.1, and 0.41, respectively. ΔU^+represents the roughness function.

The ΔU^+term is the downward shift function on the velocity profile related to dimensionless equivalent sand-grain height. The velocity shift is adopted in the standard Law-of-the-Wall Modified for Roughness (LWMR) model). In Grigson's study [42], the roughness function based on the experimental Colebrook's data [43], is defined as:

$$\Delta U^+ = \frac{1}{\kappa}\ln\left(1 + \frac{k_s^+}{\exp(3.25\kappa)}\right) \tag{4}$$

$$k_s^+ = \frac{k_s u_\tau}{\nu} \tag{5}$$

where k_s represents the height of the sand-grain roughness.

Also, in Nikuradse's study, the velocity profile U^+ is directly linked to dimensionless roughness k_s^+ through formula:

$$U^+ = \frac{1}{\kappa} ln \frac{y^+}{k_s^+} + B \tag{6}$$

where B is calculated depending on the range of sand grain roughness:

$$\begin{array}{ll} 1 < k_s^+ < 3.5 & B = 5.5 + \frac{1}{\kappa} lnk_s^+ \\ 3.5 < k_s^+ < 7 & B = 6.59 + 1.52 lnk_s^+ \\ 7 < k_s^+ < 14 & B = 9.58 \\ 14 < k_s^+ < 68 & B = 11.5 - 0.7 lnk_s^+ \\ 68 < k_s^+ & B = 8.48 \end{array} \tag{7}$$

Cebeci and Bradshaw [44] presented a correlation to estimate the downward shift of the velocity profile due to roughness in the form:

$$\Delta U^+ = \begin{cases} 0, & k_s^+ \le k_{s\,smooth}^+ \\ \frac{1}{\kappa} ln\left[A\left(\frac{k_s^+ / k_{s\,smooth}^+}{k_{s\,rough}^+ - k_{s\,smooth}^+} \right) + C_s k_s^+ \right]^a, & k_{s\,smooth}^+ < k_s^+ \le k_{s\,rough}^+ \\ \frac{1}{\kappa} ln(A + C_s k_s^+), & k_s^+ > k_{s\,rough}^+ \end{cases} \quad (8)$$

in which the power a is given as:

$$a = sin\left[\frac{\pi}{2} \frac{log\left(k_s^+ / k_{s\,smooth}^+ \right)}{log\left(k_{s\,rough}^+ / k_{s\,smooth}^+ \right)} \right] \quad (9)$$

with A=0, $k_{s\,smooth}^+ = 2.25$, $k_{s\,rough}^+ = 90.00$ and $C_s = 0.253$.

To implement roughness, the presented wall functions require the y^+parameter to be in the logarithmic region, which can be a severe constraint and will mainly be violated by the grid. When the first element is not located in a log-law area of the flow regime, the downward shift of the velocity profile due to the roughness causes a negative value of U^+. Considering the smooth surface, wall functions that do not restrict the location of the first grid point between the wall and the logarithmic layer are called adaptive wall functions which are unable to calculate the roughness effect on the flow profile. Knopp et al. [45] presented a grid and flow adaptive wall-function method for RANS turbulence modeling with emphasis on aerodynamic flows and Kalitzin et al. [46] addressed some of the existing adaptive wall functions' shortcomings and aimed to develop an efficient and robust approach that can be applied to various turbulence models.

The determination of wall-shear stress for different geometries and generated meshes has always been an important issue, especially in turbomachinery. Additionally, the selection of the method, which includes surface roughness, has always been challenging. One of the most famous resources for calculating the friction factor is the Moody [47] diagram. It relates three factors: Darcy friction factors, Reynolds number, and relative roughness to determine the friction factor. It correlates with extensive experimental data obtained by Nikuradse for pipe flow with surfaces roughened by coating the internal surfaces with sand grains. Several researchers have recognized the shortcomings of using measured surface roughness parameters in conjunction with the Moody diagram [48]. Kandlikar et al.[49] worked on the relative roughness (up to 14%) encountered in microchannels. They re-plotted the Moody chart, considering the idea of a constricted flow diameter. Chedevergne and Aupoix [50] developed a wall function to complement $k-\omega$ turbulence model involving roughness correction. In another investigation, Chedevergne and Forooghi [51] proposed a new model

to calculate the roughness effects on flow behavior in the channel, accounting for the mixing length model.

Recently, Forooghi et al. [52] and Thakkar et al. [53] conducted Direct Numerical Simulation (DNS) investigations on various irregular rough surfaces to identify key surface parameters affecting flow properties such as ΔU^+ or k_s. These studies concur that, among these parameters, the skewness Sk of the surface height probability distribution function exhibits the greatest sensitivity in determining flow properties, particularly at constant roughness density. The literature [54,55] also discussed the implementation of roughness in simulations of simple computational domains by modifying momentum exchange. Kleinstreuer and Koo [56] related a relative surface roughness to the PML model for laminar flow. Their approach allowed the evaluation of microfluidic variables as a function of PML characteristics, i.e., layer thickness and porosity, uncertainties in measuring hydraulic diameters, and the inlet Reynolds number. Considering very narrow sections for fluid flow, like flow through micro channels or the mini gap between co-rotating disks, makes flow analysis challenging; moreover, the prediction of power generation in a Tesla turbine is highly affected by boundary layer discretization [57].

The aforementioned methods of accounting for roughness effects have rarely been applied to flows like those in the Tesla turbine and, therefore, are not calibrated properly to their complexity. The small gap size (in the range of 1µm-1mm) and the interaction of the boundary layers formed on the opposite disk surfaces prevent the boundary layer profile from full development. Moreover, high body forces arising from rotational movement and large curvature of the streamlines are issues that impact the estimation of eddy viscosity, even in the case of smooth surfaces, and are another problem to deal with in roughness methods.

In the context of computational domains at the discussed scale, flow fluctuations, lead to a transient behavior that is challenging to predict [58–60]. Much of the numerical research addressing this issue diverges from experimental data due to the limited accuracy of the applied models. Considering the computational time and expenses, simulation of such a small domain poses a challenge. Taking into account the mesh requirements and accuracy of various turbulence models, the $k-\omega\ SST$ model emerges as the most suitable option for simulating flow in such a small domain [61]. The investigation of flow between co-rotating disks, with a uniform inlet flow at the outer diameter, resembling a simplified version of the co-rotating disks in the Tesla turbine, has revealed the crucial importance of understanding flow behavior in such domains in greater detail. Rusin et al. [62] conducted a numerical and experimental investigation of the Tesla turbine under various inlet pressures and loads, identifying rotor disc roughness as a key factor in achieving high turbine efficiency and power. In newer research, a numerical study conducted by Niknam et al. [63] investigated the two-phase flow behavior of a Tesla turbine operating with R404a, aiming to enhance the efficiency of inverse cycle systems such as heat pumps and chillers. Two modeling approaches, Eulerian-Eulerian CFD and a finite-difference model, were applied to evaluate the effects of rotational speed, disk gap, and surface roughness. The results showed good

agreement with the experimental data and highlighted the influence of liquid–vapor interactions on turbine performance.

1.3 Scope of thesis

This Ph.D. research aims to assess the possibility of improving the momentum transfer in the flow between rotating disks, with particular emphasis on Tesla turbines. Several parameters influence the efficiency of Tesla turbines, including design characteristics and the surface roughness of the disks. In the present investigation, the effects of disk roughness, nozzle, and supply configuration on the turbine's efficiency are evaluated.

This thesis aims to answer the following research questions through a three-step approach, presented in Chapters 2 to 4:

- What numerical approach provides the most accurate simulation of flow between co-rotating disks, with a gap size similar to that used in a Tesla turbine, considering turbulence models, mesh quality, and roughness implementation?
- What is the effect of reducing the gap size between co-rotating disks on the flow characteristics and formation?
- How does surface roughness influence wall shear stress and flow characteristics in channel flow and in the gap between co-rotating disks?
- Which roughness modeling method best matches experimental and DNS results from the literature in benchmark cases?
- How does a nozzle jet affect the flow characteristics between co-rotating disks compared to a uniform inlet flow?
- How do the number of nozzles and their configurations affect the flow aerodynamics, efficiency, and output power of a Tesla turbine?
- What are the effects of inlet nozzle interactions with the disk edges and boundary layers on flow development and stability within the rotor gap?
- How do the $k-\omega\ SST$ turbulent model and LES approaches compare in predicting the internal flow behaviour and performance of Tesla turbines?
- How can the effect of real surface roughness be more accurately represented in CFD simulations, particularly in the context of Tesla turbine modeling?

Additionally, Chapter 5 presents a supplementary study on the effect of surface roughness in a Tesla turbine operating with real gas. In this section, the following question is answered:

- How does the surface roughness affect the performance of the Tesla turbine operating on selected ORC fluids?

In pursuit of these objectives and hypotheses, this thesis is structured around a series of five published papers and one additional study that collectively form the foundation of the research. Each publication addresses a specific aspect of the overarching research problem,

with insights from earlier studies informing the design and scope of subsequent investigations.

Chapter 2

Investigation of flow characteristics in minichannel with stationary and rotating walls – Papers I and II

2.1 The scope of the investigation

This chapter summarizes a sequence of studies (Papers I and II), which focused on investigating and improving the modeling of surface roughness effects in narrow flow domains, particularly within the scale of the gap between co-rotating disks of bladeless Tesla turbines. The flow behavior in such configurations is highly influenced by the unique geometry—submillimeter gaps, rotating disks, variable cross-sections—and the interaction of the boundary layer developing from parallel disks with effect on turbulence and momentum transfer mechanisms.

To accurately simulate the complex fluid dynamics in these conditions, the study explores various turbulence models and roughness treatment approaches. Two primary roughness modeling strategies are evaluated: wall function modifications using velocity profile shifts, and Aupoix [64] method, which adjusts turbulence quantities near the wall to reflect roughness effects. The performance and limitations of these methods are assessed across a series of test cases, beginning with flow over rough flat plates, then extending to stationary and rotating minichannels, a critical configuration for Tesla turbine operation.

The scope includes both numerical modeling and experimental validation, with comparisons made against DNS data, published experimental results, and an in-house test setup.

Key investigated parameters include:

- Gap size and domain constriction,
- Roughness height and shape,
- Flow regime transitions (laminar to turbulent),
- Wall shear stress and eddy viscosity behavior,
- Influence of disks rotation on interaction of boundary layers,
- Momentum diffusion and turbulent kinetic energy distribution.

2.2 Mathematical modeling

The numerical simulations are done using Ansys Fluent software, which makes use of the finite volume method to solve discretized Reynolds-averaged Navier Stokes equations. The governing equations involve continuity, momentum and energy conservation, in the form of:

$$\frac{\partial \rho}{\partial t} + \frac{\partial}{\partial x_i}(\rho U_i) = 0 \tag{10}$$

$$\frac{\partial (\rho U_i)}{\partial t} + \frac{\partial}{\partial x_j}\left(\rho U_j U_i\right) = -\frac{\partial p}{\partial x_i} + \frac{\partial \tau_{ji}}{\partial x_j} + \rho f_i \tag{11}$$

$$\frac{\partial \left(\rho \left(e + \frac{1}{2} U_j U_j\right)\right)}{\partial t} + \frac{\partial}{\partial x_i}\left(\rho U_i \left(e + \frac{1}{2} U_j U_j\right)\right) = -\frac{\partial}{\partial x_i}(p U_i) + \frac{\partial}{\partial x_i}\left(\tau_{ij} U_j\right) - \frac{\partial}{\partial x_i}(q_i) + \rho f_i U_i \tag{12}$$

where t is time, τ is the wall shear stress, e, p, q, U, x, and f are the internal energy, pressure, heat flux, velocity, Spatial coordinate, and body force. The fluid follows the ideal gas behavior.

Turbulent stresses τ_{ij} are modeled using the Boussinesq hypothesis, assuming a stochastic turbulence model for turbulent viscosity determination. Three two-equation turbulence models are adopted in the analyses to calculate the turbulent viscosity $k-\omega$ Shear Stress Transport ($k-\omega\ SST$), $k-\varepsilon$ with Standard Wall Function ($k-\varepsilon\ SWF$) and $k-\varepsilon$ with Enhanced Wall Treatment ($k-\varepsilon\ EWT$). The $k-\omega\ SST$ turbulence model calculates the turbulent kinetic energy (k) and specific dissipation rate (ω) as follows:

$$\frac{\partial (\rho k)}{\partial t} + \frac{\partial}{\partial x_j}\left(\rho U_j k\right) = \frac{\partial}{\partial x_j}\left[\left(\mu + \frac{\mu_t}{\sigma_k}\right)\frac{\partial k}{\partial x_j}\right] + P_k - \rho k \omega \tag{13}$$

$$\frac{\partial (\rho \omega)}{\partial t} + \frac{\partial}{\partial x_j}\left(\rho U_j \omega\right) = \frac{\partial}{\partial x_j}\left[\left(\mu + \frac{\mu_t}{\sigma_\omega}\right)\frac{\partial \omega}{\partial x_j}\right] + \alpha^* \frac{\omega}{k} P_k - \beta^* \rho \omega^2 \tag{14}$$

which makes this model able to resolve the inner parts of the boundary layer down to the wall and blend with the $k-\varepsilon$ model in the free stream. The possibility of employment of the $k-\omega\ SST$, $k-\varepsilon\ SWF$, and $k-\varepsilon\ EWT$ models in different cases is studied.

The standard wall function is based on Launder and Spalding's work [65], where the velocity profile close to the wall is calculated employing the following formula:

$$U^* = \frac{1}{\kappa}\ln\left(E y^*\right) \tag{15}$$

$$U^* = \frac{U_p c_\mu^{0.25} k_P^{0.5}}{{u_\tau}^2} \tag{16}$$

$$y^* = \frac{\rho c_\mu^{0.25} k_P^{0.5} y_P}{\mu} \tag{17}$$

where E represents the empirical constant equal to 9.793, U_p and k_P are the mean velocity of the fluid and turbulence kinetic energy at the near-wall node P, respectively, y_P is the distance from point P to the wall and μ represents the dynamic viscosity of the fluid.

The enhanced wall treatment in the $k-\varepsilon$ EWT model formulates the law-of-the wall as a single wall law for the entire wall region suggested by Kader [66]:

$$U^+ = e^{\Gamma} U_{lam}^+ + e^{\frac{1}{\Gamma}} U_t^+ \tag{18}$$

where the blending function is given by:

$$\Gamma = -\frac{a(y^+)^4}{1+by^+} \tag{19}$$

where $a = 0.01$ and $b = 5$.

The effect of roughness shape highlighted the need for investigation of different roughness methods. In this regard, the LWMR model described in the Introduction and Aupoix approach [64] are investigated. Although the LWMR model can be applied on meshes with a high enough value of y^+, Aupoix approach needs a fine mesh with y^+ smaller than one. Therefore, the computational cost is higher compared to other methods [67–69].

Aupoix approach is based on k and ω modification on the wall. This method of considering the roughness modifies the k and ω on the wall, so the turbulent properties will be calculated based on the correction on the wall. The modified turbulent parameters on the wall are calculated from the relations:

$$k_w^+ = \max(0; k_0^+) \tag{20}$$

$$k_0^+ = \frac{1}{\sqrt{\beta^*}} tanh\left[\left(\frac{ln\frac{k_s^+}{30}}{ln10} + 1 - tanh\frac{k_s^+}{125}\right) tanh\frac{k_s^+}{125}\right] \tag{21}$$

$$\omega_w^+ = \frac{300}{{k_s^+}^2}\left(tanh\frac{15}{4k_s^+}\right)^{-1} + \frac{191}{k_s^+}\left(1 - exp\left(-\frac{k_s^+}{250}\right)\right) \tag{22}$$

in which k_w^+ and ω_w^+ are values on the wall, respectively, and the constant β^* is equal to 0.09.

2.3 Zero-pressure-gradient flow over a rough plate

Hosni et al. [70] studied the flow over a rough plate with hemispheric roughness elements which have been mounted in staggered rows. The distance L between the elements is $L = 2D$ with $D = 1.27mm$ the diameter of hemispheres. The free stream velocity retained for computations is $U = 58.2m/s$. The size of the computational domain remains the same as in the case described in the previous section and the same types of boundary conditions are applied. $k-\varepsilon\,EWT$ is unable to simulate roughness then the $k-\omega\,SST$, and $k-\varepsilon\,SWF$ models are applied in this part. Roughness is simulated utilizing both Aupoix and velocity profile downward shift methods. Fig.1 b presents the velocity profile at $1.68m$ distance from the starting point of the surface which corresponds to $Re_x = 0.666 \times 10^7$. Additionally, experimental data are presented with the y^+ and $y^+ - \Delta y^+$values, in which the Δy^+ is the artificial origin of the wall distances for roughness elements placed over the flat plate. The shift indicates that within the roughness layer, there is no fluid flow.

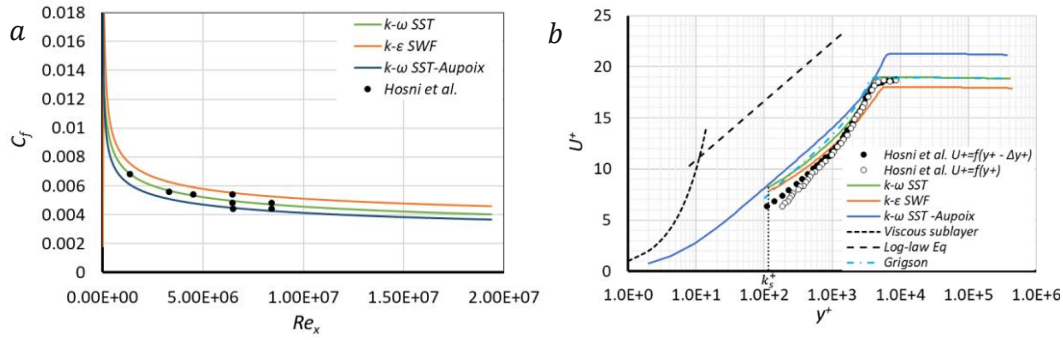

Figure 1. Comparison of simulation results of flow over a rough flat plate utilizing fine mesh with $y^+ < 1$ and experimental data [71], (a) The distribution of friction coefficient vs Re_x, (b) Velocity profile for $Re_x = 0.666 \times 10^7$.

The friction coefficient distributions presented in Fig. 1 a demonstrates a good agreement with the experimental data. The lowest friction coefficient values were observed in the case of Aupoix method, and the highest values were obtained for $k-\varepsilon\,SWF$ model with the velocity profile shift. The differences, however, vary by the distance from the wall and reach a maximum of 10% in the fully turbulent part of the flow regime. In Aupoix method, the lowest wall shear stresses are determined, and therefore the friction coefficient is the lowest, and the downward shift of the dimensionless velocity profile is the smallest. The agreement between the results proves the appropriate accuracy of both $k-\varepsilon\,SWF$ and $k-\omega\,SST$ turbulence models with implemented roughness approach in this elementary benchmark. Aupoix approach needs a fine grid to perform well, and from Fig. 1, it can be seen for lower values of y^+ in the viscous sublayer down to the wall, the velocity approaches zero, which satisfies the no-slip wall condition.

2.4 Flow between co-rotating disks

Preliminary research on simpler geometries presented in papers I, and II indicates that when the domain scale and flow cross-section are reduced, generating a compatible mesh for the $k-\varepsilon$ turbulence model with the first layer located in the log-law region of the flow regime

results in only a few cells in the normal direction to the wall, which is inappropriate. Moreover, the $k-\omega\,SST$ model, with a denser mesh in regions experiencing intense changes in eddy viscosity and a coarser mesh in farther areas, performs well. Due to its ability to switch to the $k-\varepsilon$ model, it also optimizes computational costs. The study further demonstrates that the Aupoix method of roughness artificially modifies eddy viscosity on the wall surface based on roughness parameters, eliminating the need to capture roughness in the first layer of the generated mesh. Implementing this method with the $k-\omega\,SST$ model yields good results in both stationery and rotating minichannels. The flow within the gap between two co-rotating disks is a fundamental configuration that has been extensively analyzed to understand flow structures and disk-flow interactions, both of which are essential phenomena for Tesla turbine optimum efficiency. Gap size, rotational speed (n), and roughness play crucial roles in shaping the flow structure, and boundary layer between the disks, as extensively studied in Papers I and II. Considering the case with the inner and outer diameters of the corotating disks equal to 0.04m and 0.1 m and gap size of $0.75\,mm$, n significantly affects power generation, with maximum values observed between 15000 and $17500\,rpm$. It also influences efficiency, which ranges between 2% and 40% for smooth cases. Furthermore, increasing roughness height improves efficiency by up to 44% at $10000\,rpm$. In the case of the flow through the mini gap between co-rotating disks, the velocity profile is influenced by the interaction between developing boundary layers from the parallel co-rotating disks. Fig. 2 illustrates the downward shift in the velocity profile and the increase in system efficiency resulting from the rise in roughness height, considering a $0.75\,mm$ gap size and $n=17500\,rpm$ for four different roughness levels. The tangential and radial velocities are set to $5\,m/s$ and $100\,m/s$, respectively. Higher shear stresses in the tangential direction contribute to a greater power output and thus, higher efficiency. Roughness height, as a key parameter in boundary layer development, leads to a downward shift in the velocity profile. Flow through the co-rotating disks is influenced by boundary layer formation on both parallel surfaces, and the interaction of these layers prevents the velocity profile from fully developing. This explains the observed deviation between the results of the smooth-wall case and predictions based on laminar theory and the log-law velocity distribution. Effective parameters influencing power generation and flow characteristics between simple co-rotating disks with uniform inlet flow were discussed in Papers I and II.

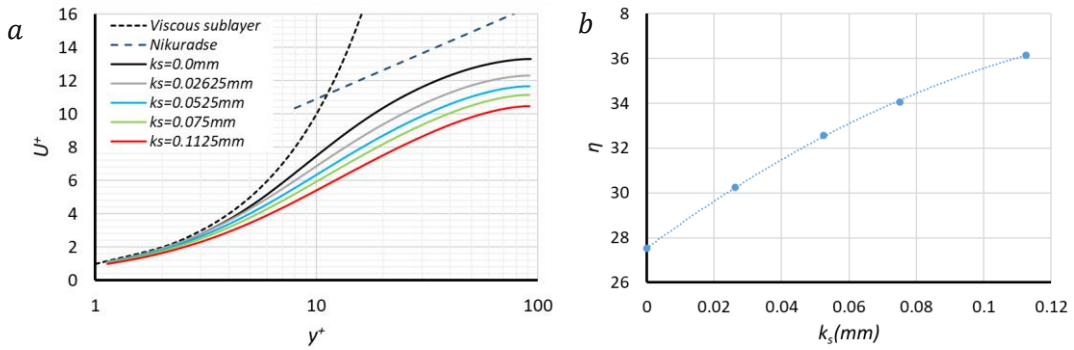

Figure 2. Velocity profile (a) and efficiency of the system for four different roughness's (b), considering tangential and radial velocity equal to $5\,m/s$ and $100\,m/s$, respectively.

2.5 Achievements

A major achievement was validating the effectiveness of the $k-\omega\ SST$ turbulence model combined with the Aupoix roughness method, which proved well-suited for simulating flow in both stationary and rotating minichannels. This combination optimized computational cost while maintaining accuracy, even in challenging near-wall regions without requiring ultra-fine meshes.

The study also demonstrated that:

- Generating a compatible mesh for the $k-\varepsilon$ turbulence model with the first layer located in the log law part of the flow regime will cause a few cells in the normal direction to the wall.

- The $k-\omega\ SST$ turbulence model performs well when applied with a refined mesh in regions of steep eddy-viscosity gradients (such as boundary layers) and a coarser mesh in the far-field. Its blending of the $k-\omega$ formulation near walls with the $k-\varepsilon$ formulation in the free stream makes it particularly suitable for simulating flow between co-rotating disks.

- Aupoix method of roughness artificially changes the eddy viscosity on the wall surface according to the roughness parameters without the need to cover the roughness with the first layer of generated mesh, and implementation of this method with the $k-\omega\ SST$ model performs well in stationary and rotating minichannels.

- Research on minichannels demonstrates that roughness elements constrict the flow cross section, leading to discrepancies between experimental results and theoretical predictions.

- A reduction in gap size from $15\ mm$ to $0.75\ mm$ demonstrated an increased interaction between the developing boundary layers from the co-rotating disks, as well as a greater discrepancy between the observed velocity profile and theoretical estimations.

- A change in n affects power generation, with a maximum value of $7\ W$ observed for a gap size of $0.75\ mm$ and a roughness height equal to 3.5% of the gap size.

- An increase in roughness height in the studied case (with a $0.75\ mm$ gap) led to an efficiency improvement from 30% to 36%, considering four roughness heights equal to 3.5%, 7%, 10%, and 15% of the gap size.

- Roughness height plays a critical role in boundary layer behavior, enhancing momentum diffusion and accelerating the transition to turbulence near the walls.

- CFD results were thoroughly validated against DNS data, experimental measurements, and an in-house test setup, confirming the robustness of the chosen methods.

Chapter 3

Investigation of flow characteristics between co-rotating disks of Tesla turbine – Papers III, and IV

3.1 The scope of the investigation

Analyzing the flow inside the gap between the co-rotating disks of the Tesla turbine presents challenges due to several factors, including submillimeter length scales, variations in flow cross-section, interactions of body forces arising from rotation with turbulence, interactions between the turbine's inlet nozzles and rotor, and moving walls. General design parameters, e.g., number of nozzles, and nozzle configuration also pose a challenge in order to achieve the full potential of this turbine. In this chapter of thesis, the following concepts are investigated.

- Nozzle Configuration and Supply System Design: The study investigates momentum diffusion and kinetic energy transfer within the narrow, submillimeter-scale gap between co-rotating disks, with particular attention to the complex flow behavior resulting from rotational effects and turbulence. It examines nozzle configurations, comparing one-to-one setups, where each nozzle feeds a single gap, to one-to-many setups, where each nozzle supplies multiple gaps. Additionally, it analyzes two supply arrangements: N6, a six-nozzle system, and N40, a forty-nozzle system, focusing on their effects on turbine efficiency, fluctuation behavior, and wall shear stress distribution.

- Turbulence modeling approaches: This section compares two turbulence modeling approaches: the $k-\omega\ SST$ model, valued for its computational efficiency and suitability for engineering applications, and LES employing the Smagorinsky SGS model, which offers high-fidelity flow characterization by explicitly resolving larger turbulent structures. The evaluation assesses how each model captures essential flow features such as flow structures, transient fluctuations, shear stress behavior, and overall turbine efficiency, highlighting their respective strengths and limitations in simulating complex turbulent flows.

3.2 Mathematical modeling

The inquiry detailed in this chapter involves conducting numerical simulations using both the $k-\omega\ SST$ turbulence model and LES. The governing equations — continuity, momentum, and energy conservation — as presented in Eq (10, 11, 12), are based on the Reynolds-averaged formulation. When LES is used, these equations are instead spatially filtered and include additional SGS terms to account for the effect of unresolved turbulence, notably the SGS stress tensor, SGS heat flux, and related energy transfer terms.

In the LES, a closure of the Navier-Stokes equations is accomplished through the implementation of the wall-modeled LES (WMLES) model, which calculates the SGS eddy

viscosity. The foundational Algebraic WMLES formulation was initially introduced in the research of Shur et al. [72]. This model integrates a mixing length model with a modified Smagorinsky model [73] and incorporates the wall-damping function proposed by Piomelli et al. [74] in the following form:

$$\nu = min\left[(\kappa d_w)^2, \left(C_{Smag}\Delta\right)^2\right].S.\left\{1 - exp\left[-\left(\frac{y^+}{25}\right)^3\right]\right\} \tag{23}$$

$$\Delta = min(max(C_w.d_w; C_w.h_{max}, h_{wn}); h_{max}) \tag{24}$$

where $\kappa = 0.4187$, $C_{Smag} = 0.2$, and $C_w = 0.15$ are constants.

3.3 Tesla turbine with different supply configurations

Two different variants of the supply system are considered with six (N6) and forty (N40) nozzles having one-to-one nozzle arrangement with the individual nozzle for each gap. To minimize computational effort, a reduced calculation domain is considered. The flow in each domain, consisting of one inlet nozzle and a periodic segment of one gap between the disks, is examined to reveal the complexity of flow structures and their impact on the Tesla turbine performance.

LES with the Smagorinsky SGS model is used to verify the results of the $k-\omega\ SST$ turbulence model in the N6-case study. Analyzing the results indicates that the $k-\omega\ SST$ model provides valuable insights with appropriate accuracy. The second case study, with forty nozzles, is simulated using the $k-\omega\ SST$ turbulence model. The research compares flow structure, flow parameters, and their impact on the system's efficiency. From the comparison between the $k-\omega\ SST$ turbulence model and LES simulation, it was observed that although the $k-\omega\ SST$ model slightly overestimates the general parameters and damps fluctuations, it still provides valuable insights for assessing flow structures.

Fig. 3 demonstrates the vorticity contours on two surfaces indicated at the outer edge of the disks and mid-radii. The surfaces are generated from the revolution of lines along the gap, between 20^0 and 30^0 located at the outer edge of the disks and in mid-radii. On each surface, two lines are defined on the edges at the 20^o and 30^o. The lines are chosen in the described locations to better demonstrate the effect of the jet and the development of boundary layers on fluctuations of parameters. Line 1 is chosen as a location with the maximum influence of the inlet jet and line 2 is 10^o away from line 1 to show how the development of boundary layers will damp the fluctuations. The two other lines are also chosen in the mid-radii location to determine the vorticity level in a region with less transient effects.

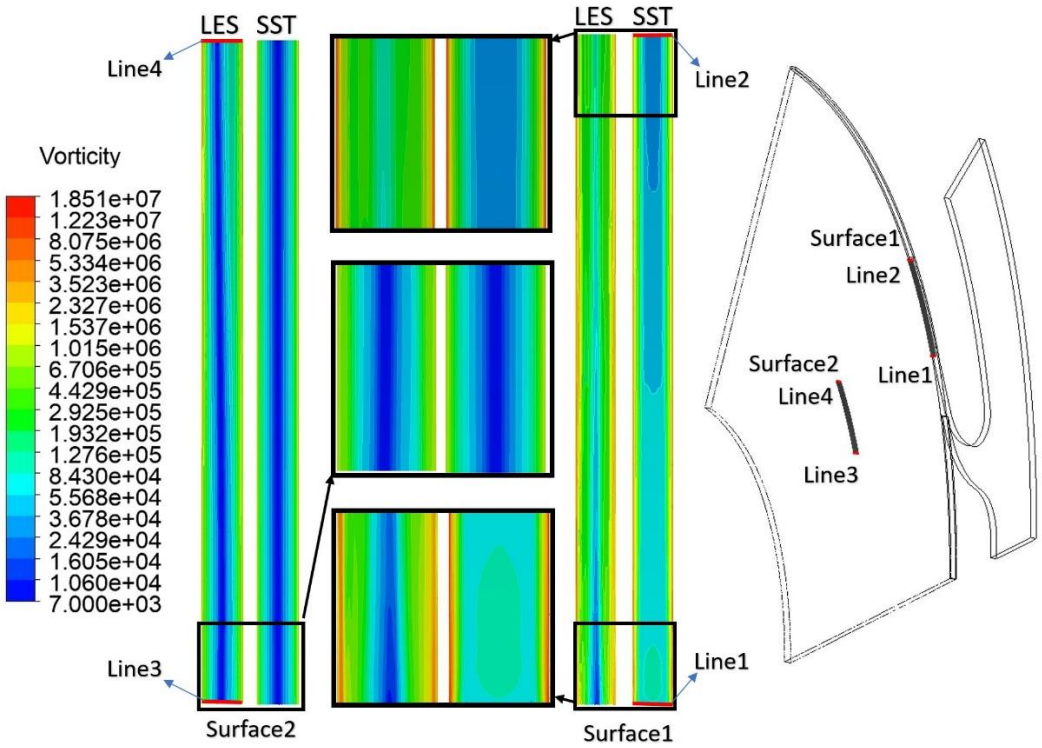

Figure 3. Vorticity contours on two surfaces at the outer edge close to the nozzle jet and in the middle of the disks. (N6 case)

Fig. 3 highlights the effect of the inlet jet on the rising level of vorticities observed in both LES and $k-\omega\,SST$ simulations. As depicted in the mid-radii contour, the fluctuation of parameters, even in LES simulation, diminishes, and the maximum magnitude of vorticities, which occurs near the walls, is in a lower range in this area.

Additionally, the mesh strategy is described in paper III as the LES requirements make this simulation computationally expensive and time-consuming. The overall benefits of this method are discussed in paper III. The conducted research on N6 revealed that the $k-\omega\,SST$ simulation overestimates the torque of 4.25%, and wall shear stress with the representation of the steady-state behavior of the system, though the LES represents a more accurate estimation of all parameters with a demonstration of the transient behavior of the system, revealing the need for high fidelity simulation to observe the fluctuation of such a phenomenon. Although the $k-\omega\,SST$ model dampens parameter fluctuations, it still provides a valuable solution for the flow. Considering the computational costs of LES simulations, this highlights the $k-\omega\,SST$ model as a fast approach with appropriate accuracy. In the LES simulation of N6, the parameters exhibit the maximum range of fluctuation in the vicinity of the outer edge of the disks. In the rest of the domain, the transient behavior appears to be smoother. Assessment of the results reveals that interactions between the inlet jet and developing boundary layers from parallel co-rotating disks establish vorticities approaching the disk's surface. Due to the extremely transient behavior of the flow in that region, it does not follow a specific trend. The outer edge of the co-rotating disks plays the most important role in power generation, as this area has the maximum distance

from the rotational axis. Consequently, in an optimized design of a Tesla turbine, the level of kinetic energy of operating flow should drop in this area. In N6, considering both components of wall shear stress, the maximum total wall shear stress occurs in the outer 20% of the disk surface, and in the rest of the domain represents an almost constant value. Considering the high number of nozzles studied in N40, this parameter depicted an increase in the vicinity of the outlet. Using a high number of nozzle jets results in a noticeable interaction of the nozzle jet, manifesting as fluctuations in parameters near the outer edge of the disks. Moreover, employing a high number of nozzles significantly increases the mass flow rate, resulting in nearly four times more power generation. However, this also causes the efficiency of the system to drop by almost 16 percent point. Table 1 represents a comparison between studied cases.

Table 1. Comparison between computed parameters from the simulations of N6 and N40 cases.

Parameter	N6 (LES)	N6 ($k-\omega\ SST$)	N40 ($k-\omega\ SST$)
The angle of fraction [deg]	60	60	9
Mass flow rate [kg/s]	0.0023	0.0022	0.0147
Mass-averaged radial velocity (gap inlet) [m/s]	-33.0	-28.2	-25.0
Mass-averaged circumferential velocity (gap inlet) [m/s]	284.8	302.4	273.7
Mass-averaged static temperature (gap inlet) [K]	257	250	261
Area-averaged gauge pressure (gap inlet) [Pa]	24775	22637	71287
Torque [Nm]	0.0400	0.0416	0.1750
Specific Power [m^2/s^2]	31882.6	34570.1	21836.7
Efficiency [%]	39.2	43.0	26.8

3.4 Tesla turbine with different nozzle configurations

This section of the study focused on two Tesla turbine configurations with six nozzles: one featuring a one-to-one nozzle arrangement with the individual nozzle for each gap (referred to as N6O-O) and the other adopting a one-to-many nozzle design where the nozzle provides fluid to all gaps (referred to as N6O-M). In N6O-O, the simulation accounted for the plenum chamber's thickness being equivalent to the gap size. In N6O-M, aside from the gap size, half of the disk's size was factored into the thickness of the supply chamber. The one-to-one configuration allowed for direct passage of the nozzle jet through the gap, while the one-to-many setup incurred losses from the interaction between the inlet jet and the disk tips. Each case exhibited symmetrical behavior every 60 degrees in the investigated geometry. To enhance computational efficiency, the simulation domain represented only a segment of the entire turbine. To minimize computational costs, only a portion of the entire domain is examined, and flow structures and their effects on Tesla turbine performance are analyzed. LES employing the Smagorinsky SGS model is used for flow simulation, enabling a comparison of flow structures, fluctuations, parameters, and their impact on system efficiency. The assessment of the mesh quality for LES simulation is presented in Paper IV.

The comparison of general parameters obtained from the LES simulation of the Tesla turbine with N6O-O and N6O-M nozzle configurations shows that the N6O-O design is 17.8 percent points more efficient, with lower mass flow rate and power generation.

Parametric analysis of the observed results demonstrates that the higher mass flow rate and the formation of a convergent-divergent nozzle structure in the area close to the inlet nozzle cause higher velocity and lower p in this region in the N6O-M case. This phenomenon shifts the area with the maximum circumferential wall shear stress slightly toward the inner diameter of the disk.

Analyzing the Reynolds stress magnitude and its distribution along the gap at different locations reveals quite different trends in the studied cases. In the N6O-M case, these values increase as they approach the mid-gap. In contrast, in the N6O-O case, where wall shear stress is the only source of fluctuations, the maximum values are observable near the disk surfaces and decrease as they approach the mid-gap.

A three-dimensional demonstration of a vortex core can well represent the source of fluctuations. For this aim, the vortex core of flow, colored by velocity magnitude utilizing the Q-Criterion method, is presented in Fig. 4. To better represent the vortexes in the area close to the nozzle jet, the Q-Criterion was set to be equal to $2.5 \times 10^9 s^{-2}$. Different Q-criterion threshold values were tested to determine the most representative level for identifying small vortices generated on the surfaces of the disks in the N6O-O configuration, and to compare them with the stronger vortices observed in the N6O-M case.

Fig. 4 demonstrates the interaction of the inlet jet flow with the disk tips in the N6O-M case. This interaction causes a convergent-divergent shape of the flow structure at the entrance to the gap. Additionally, there is a visible growing vortex from the disk surfaces. The

developing boundary layers produce vorticities in the near-wall area. Therefore, in the N6O-M case, the level of fluctuation is influenced by both phenomena.

Fig. 4 also presents the vortex generation from the disk surfaces in the N6O-O case, which is the only source of fluctuations in this configuration. The interaction of the inlet jet with the developing boundary layers, which is maximal at the outer diameter of the disks, generates vortices and fluctuations that dissipate as they approach the outlet.

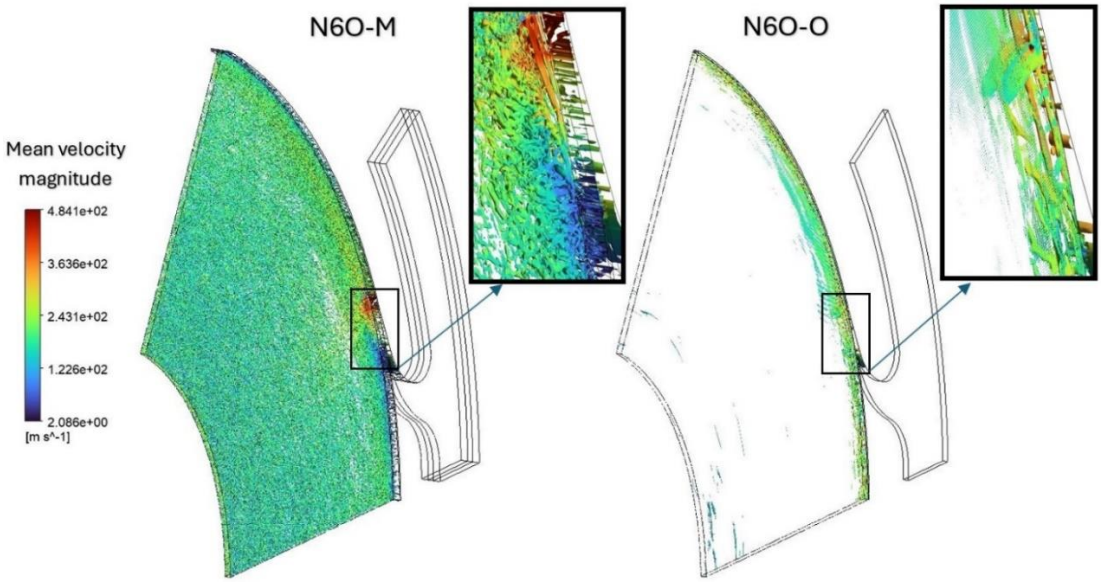

Figure 4. The vortex core of flow, colored by velocity magnitude utilizing the Q-Criterion method for Q-Criterion equal to $2.5 \times 10^9 S^{-2}$.

The main source of fluctuations in the N6O-M case is the interaction of the inlet jet with the disk tips, which results in significantly higher levels of fluctuations compared to the N6O-O case, where the only source of fluctuation is the interaction between the inlet jet and the developing boundary layers from the parallel disk surfaces.

In the N6O-O case, the viscous effect damps and lowers the level of fluctuations, whereas the turbulence generated in the N6O-M case is too strong to be damped by this effect.

In addition to the effects of nozzle design and supply configuration on the flow characteristics and performance of the Tesla turbine, surface roughness plays a significant role in momentum distribution and transfer. Accurately capturing the influence of realistic roughness profiles in CFD simulations is therefore of critical importance for reliable performance prediction.

In Paper V, a novel approach is introduced to simulate the impact of surface roughness on the Tesla turbine's performance, offering a more physically representative model and improving the accuracy of computational assessments.

3.5 Achievements

Key findings highlight that:

- The $k-\omega\, SST$ model, while slightly overestimating torque and wall shear stress (~4.25%), provides a fast and sufficiently accurate prediction for general flow behavior at a much lower computational cost.

- The LES model, though more computationally intensive, captures transient fluctuations with greater fidelity, particularly in regions near the outer edge of the disks, where vortices are generated and momentum transfer is most significant.

- The number and configuration of nozzles significantly influence flow behavior. A higher nozzle count (40 nozzles in a one-to-one configuration) increases the mass flow rate and power output (by up to a factor of four) but also leads to complex jet interactions and a reduction in system efficiency of approximately 16 percentage points compared to the case with six nozzles under the same configuration.

- Comparison of N6O-M and N6O-O nozzle designs shows that N6O-O is 17.8 percent point more efficient with lower mass flow rate and power generation, and it demonstrates slower flow, lower turbulence, and a more stable wall shear stress distribution.

- In N6O-M, convergent-divergent nozzle structure forms near the inlet, increasing velocity and lowering p, and shifting maximum wall shear stress toward the inner disk diameter. It produces stronger jet-disk interactions, higher Reynolds stresses and turbulence, especially near mid-gap, unlike the N6O-O case, where fluctuations are damped by viscous effects and remain concentrated near the walls.

- Inlet jet–disk tip interactions in N6O-M generate significantly higher fluctuations than in N6O–O, where fluctuations originate mainly from inlet jet–boundary layer interaction.

- The outer 20% of the disk is identified as the most critical zone for momentum transfer, with peak wall shear stress and maximum influence on power generation.

Chapter 4

Simulation of roughness using Porous Medium Layer (PML) – Paper V

4.1 The scope of the investigation

The most common method for incorporating surface roughness in CFD simulations is through equivalent sand grain roughness. While several estimation techniques exist, no universal formula is available. This part of the PhD research aimed to replace this traditional approach by introducing a porous layer to simulate roughness effects. The scope of this chapter is categorized as follows:

- Model development: The research introduces a Porous Medium Layer (PML) model as an alternative technique, where porous medium parameters are tuned to realistically replicate roughness impacts on flow without relying on traditional sand-grain assumptions

- Model validation: The model is validated against experimental pressure drop measurements in a minichannel. Its application to the Tesla turbine is additionally compared with predictions from the Aupoix roughness model.

- Application to Tesla turbine flow: CFD simulations incorporating the PML model utilize the $k-\omega\ SST$ turbulence model, which has been cross-checked with LES results for smooth-wall conditions. A parametric study investigates the effects of three different porous layer thicknesses on turbine efficiency, flow characteristics, and momentum transfer, highlighting the potential of the PML approach for improved roughness representation in turbine flow analyses.

4.2 Mathematical modeling

In the PML method, a porous layer modifies the resistance to fluid flow, and the momentum term should be amended on porous parameters.

The governing equations involve continuity, momentum, and energy conservation in the following form:

$$\frac{\partial \alpha\rho}{\partial t}+\frac{\partial}{\partial x_j}\left(\alpha\rho U_j\right)=0 \tag{25}$$

$$\frac{\partial\left(\alpha\rho U_j\right)}{\partial t}+\frac{\partial}{\partial x_j}\left(\alpha\rho U_i U_j\right)=-\alpha\frac{\partial p}{\partial x_i}+\frac{\partial \alpha\tau_{ij}}{\partial x_j}+\alpha\rho f_i-R \tag{26}$$

$$\frac{\partial\left(\alpha\rho\left(e+\frac{1}{2}U_iU_i\right)\right)}{\partial t}+\frac{\partial}{\partial x_j}\left(\alpha\rho U_j\left(e+\frac{1}{2}U_iU_i\right)\right) = -\frac{\partial}{\partial x_j}(\alpha pU_j)+\frac{\partial}{\partial x_j}(\alpha\tau_{ij}U_i)-\frac{\partial}{\partial x_j}(q_j)+\rho f_iU_i \quad (27)$$

where α is porosity, and R is the resistance term to flow in the porous medium.

Inside the porous layer, the porosity may vary, $0 \leq \alpha < 1$, and the resistance term can be presented as:

$$R = \left(R_C + R_F U_i^{\beta}\right)U_i \quad (28)$$

where R_C is a resistance constant, R_F is the resistance speed factor, and β is a resistance speed power (for $\alpha = 1$, $R = 0$).

Assuming steady fully developed 2-D flow in an isotropic porous medium, the resistance part of Eq. 26, according to the Brinkman-Forchheimer-extended Darcy equation, can be written as:

$$R = \frac{\mu}{K}u + \frac{\rho C_f}{K^{1/2}}u^2 \quad (29)$$

In which the C_f is equal to 0.55, K is the permeability, $R_C = \frac{\mu}{K}$, and $R_F = \frac{\rho C_f}{K^{1/2}}$.
In the present approach, the resistance constant (R_C) and the resistance speed factor (R_F) are defined as a function of porosity (α). The porosity changes from 0 at the base of the porous zone to 1 at the interface with fluid. This variable is counted as the representative of roughness obstacles, and then the deviation of this parameter from the basement up to the interface will change. In this investigation, porosity is assumed to be a second-order function of the thickness of the porous zone with the derivation of zero at the interface between the porous and flow zones. Moreover, R_C is defined to be a function of porosity ($R_C = \frac{\mu}{K(\frac{\alpha^3}{(1-\alpha)^2})}$) and R_F is a function of R_C ($R_F = \frac{\rho C_f}{(\frac{\mu}{R_C})^{1/2}}$).

Moreover, the viscosity of the fluid is corrected according to the Einstein equation. An effective viscosity, μ_e, is introduced to account for the effect of the porous medium on the diffusion term in the momentum equation:

$$\mu_e = \mu_r\mu \quad (30)$$

$$\mu_r = 1 + 2.5(1-\alpha) \quad (31)$$

The $k-\omega$ SST model constituted the turbulence closure, in which the transport equations of turbulence kinetic energy k and specific dissipation rate ω are solved:

$$\frac{\partial(\alpha\rho k)}{\partial t}+\frac{\partial}{\partial x_j}\left(\alpha\rho U_j k\right)=\frac{\partial}{\partial x_j}\left[\left(\mu+\frac{\mu_t}{\sigma_k}\right)\frac{\partial k}{\partial x_j}\right]+P_k-\alpha\rho k\omega \tag{32}$$

$$\frac{\partial(\alpha\rho\omega)}{\partial t}+\frac{\partial}{\partial x_j}\left(\alpha\rho U_j \omega\right)=\frac{\partial}{\partial x_j}\left[\left(\mu+\frac{\mu_t}{\sigma_\omega}\right)\frac{\partial \omega}{\partial x_j}\right]+\alpha^*\frac{\omega}{k}P_k-\beta^*\alpha\rho\omega^2 \tag{33}$$

4.3 Tesla turbine simulation with roughness model

The performance of the PML roughness model was initially tested on a minichannel. In this part of the study, CFD simulation of water flow through the channel was carried out characterized by a width (z) of $50\,mm$, a length (x) of $150\,mm$, and a height (y) of $0.75\,mm$, at varying flow velocities. A developed inlet flow and ambient pressure at the outlet were considered. The side walls were non-slip and smooth, and the top and bottom walls were rough.

The simulation incorporated roughness using the Aupoix method and applied drag correction via a PML model for a roughness height of $60\,\mu m$. The thickness of the porous layer was set equal to the highest roughness peak, while permeability was adjusted to modify drag generation within the minichannel. To ensure that the drag in the minichannel matched the theoretical predictions for a roughness height of $60\,\mu m$, the permeability was set to $K = 23\,nm^2$. The CFD simulation results were validated against experimental investigations conducted on a minichannel of the same dimensions and equipped with identical roughness height. In the next phase, the PML model was implemented in the simulation of the Tesla turbine.

The analysis focuses on a Tesla turbine design featuring six nozzles. Given the turbine's symmetrical geometry, which repeats every 60 degrees, then only 1/6 of the gap is considered in the computational domain as simulating the entire structure would demand an excessive number of computational cells, significantly increasing the calculation time. The nozzle configuration used in this study is referred to as a "one-to-many" design, where a single nozzle supplies fluid to all the gaps between the co-rotating disks.

In this section, the performance of the adjusted parameters of the PML roughness method is tested in Tesla turbine simulations. The global parameters obtained from these simulations are then compared with those obtained from Aupoix method. A porous medium layer with the same modifications as those tested in the minichannel was applied to the disk surfaces of the Tesla turbine. Fig. 5 shows the porosity distribution along the gap, with values ranging from zero at the wall to one where the flow encounters no resistance. The other porous parameters were defined as functions of porosity.

Three heights of roughness were considered in this study: $30\,\mu m$ (N6-S-R30), $60\,\mu m$ (N6-S-R60), and $120\,\mu m$ (N6-S-R120). A comparison of the turbine general parameters for the rough and smooth cases is presented in Table 2.

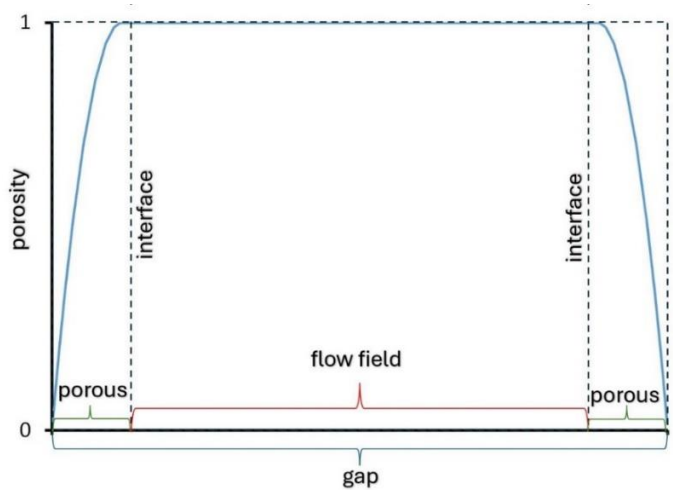

Figure 5. Schematic of the porosity distribution along the gap between co-rotating disks

In the model, the porous medium layer is added on both sides of the disk surfaces. With an increase in porous layer thickness, the flow cross-section also increases. As demonstrated in Table 2, there is no change in the mass flow rate with the increase in the thickness of the porous layer. The addition of the PML enhances momentum transfer, leading to increased torque generation. This effect becomes more pronounced with greater porous layer thickness. A constant mass flow rate combined with a substantial increase in torque generation, enhances the turbine's efficiency. Additionally, the increase in momentum transfer between the operating fluid and the rotating disks influences the distribution of the velocity components.

The generated power is evaluated using two approaches: by integrating the torque over the rotor surface (Eq. 34) and by applying the Euler turbine equation (Eq. 35), as expressed below:

$$N = \Omega \int T dA \tag{34}$$

$$N_E = \left(v_{\theta,in} r_{in} - v_{\theta,out} r_{out}\right) \dot{m} \Omega \tag{35}$$

where Ω [rad/s] is the angular velocity, T is the torque, A is the disk surface area, v_θ is the circumferential (tangential) velocity, and r is the radius of the disk.

Table 2. Comparison of general parameters obtained for the smooth and rough cases.

Parameter	N6-S-S	N6-S-R30 (PML)	N6-S-R30 (Aupoix)	N6-S-R60 (PML)	N6-S-R60 (Aupoix)	N6-S-R120 (PML)	N6-S-R120 (Aupoix)
Mass flow rate $[kg/s]$	8.00e-3	8.05e-3	8.08e-3	8.05e-3	8.00e-3	8.06e-3	8.04e-3
p $[Pa]$ **(at gap inlet)**	47722	40353	39140	37016	35902	28604	32962
Torque $[Nm]$	0.103	0.112	0.119	0.123	0.125	0.141	0.132
Power (Eq. 34) $[W]$	189	204	217	225	229	258	241
Power (Eq. 35) $[W]$	190	208	218	221	227	257	240
Efficiency [%]	29.2	31.4	33.1	34.7	35.2	39.7	37.0
Specific power (Eq. 34/mass flow rate) $[m^2/s^2]$	23592	25851	268556	28517	28625	32637	29975

The enhancement of momentum transfers due to the addition of the porous layer leads to increased torque generation. This effect increases with the thickness of the porous layer and alters the distribution of the velocity components.

Fig. 6 compares the distribution of the radial and tangential components of the velocity in a mid-gap plane by the increase in the porous layer.

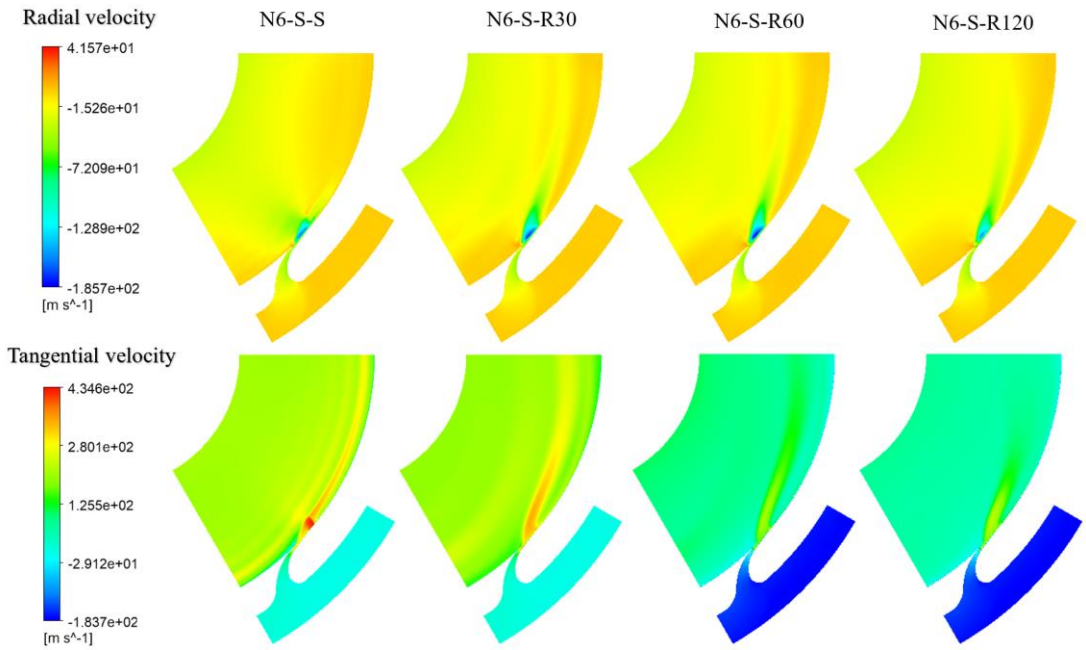

Figure 6. Radial and Tangential velocity profiles of all smooth and rough cases on a plane, defined in mid-gap.

The velocity distribution in the radial direction is influenced by three factors: centripetal force, pressure force, and viscous force. The magnitude of their effects may vary with n. An increase in shear stress, a component of viscous forces, affects the formation of both velocity components. As the level of roughness on the surface of the co-rotating disks increases, it leads to greater momentum transfer between the operating fluid and the disks resulting in a faster drop in the energy level of the flow. The tangential component of velocity, responsible for torque generation, also decreases faster with increased wall shear stress due to higher roughness height, thus improving momentum transfer. This occurs because the rough surfaces reduce the boundary layer thickness, causing enhanced interaction between the fluid and the rotating surfaces leading to more effective drag force generation, which increases torque and power output.

The increased roughness also tends to intensify turbulence within the flow. In a smooth case, the flow may remain more laminar, but when surface roughness is introduced, small-scale eddies and vortices form, amplifying the level of turbulence. This turbulence can promote more intense mixing of the fluid and create higher energy dissipation, affecting the overall efficiency of the turbine. The tangential component of velocity, responsible for torque generation, also decreases faster with increased wall shear stress due to higher roughness height, thus improving momentum transfer.

In this chapter, the performance of the PML model is evaluated. As discussed in Chapter 1, the Tesla turbine has potential applications in ORC, CHP, and CCHP systems. ORC working fluids are compatible with low-temperature heat sources, which makes them particularly attractive for further investigation.

Chapter 5 focuses on analyzing the performance of the Tesla turbine when operating with various ORC gases.

4.4 Achievements

Key achievements include:

- The development and validation of a PML model, based on experimental data from a minichannel matching the Tesla turbine's gap height, shows that this method can accurately capture real roughness geometries in simulations without fine near-wall meshing, thereby lowering computational costs while preserving accuracy.

- Comparison with the Aupoix roughness method illustrates that PML yields compatible trends with only minor discrepancies in the general parameters.

- The flow separation because of inlet jet to the gap creates a converging–diverging pattern of inlet flow at this area. As the height of the roughness increases, this phenomenon is dampened by viscous forces, leading to a smoother transfer of operating flow from the inlet to the outlet.

- Increasing the roughness height in the PML model accelerated the decay of kinetic energy in the flow, improving the system's efficiency compared to the Aupoix model.

- For the range of roughness heights studied, the Aupoix and PML models exhibited a maximum efficiency difference of 2.7 percentage points, corresponding to a roughness height of $120\ \mu m$.

- Analyzing the results from the smooth and two rough cases ($30\ \mu m$, and $60\ \mu m$) at different n reveals that roughness has the greatest impact on improving turbine efficiency when the n is in the range of 17 000–26 000. The efficiency improvement observed with the implementation of a 60 μm porous layer compared to the smooth case was 4.61 percent point at 22000 (rev/min)

This method represents a versatile and validated strategy for simulating surface roughness effects in rotating machinery.

Chapter 5

Roughness modeling by Porous Medium Layer model in Tesla turbine working on ORC fluids

5.1 The scope of the investigation

Tesla turbine shows significant potential for ORC systems. In this chapter, a comprehensive analysis is performed to simulate surface roughness effects on the flow within the gap between the co-rotating disks of a Tesla turbine, using two low-boiling media, R1234yf and n-hexane as the working fluids. The scope of investigation is as follows:

– Turbulence modeling approaches: Flow simulations are conducted with the $k-\omega\ SST$ turbulence model to assess how surface roughness influences momentum transfer, key flow parameters, and overall turbine efficiency.

– Roughness modeling: The investigation compares flow characteristics for the two fluids within the Tesla turbine, demonstrating that the PML model effectively captures roughness effects and contributes to improved turbine efficiency. Comparative analysis between smooth and rough surface cases is conducted to quantify efficiency improvements and understand fluid-specific behavior.

5.2 Background

Among the various technologies explored to improve energy conversion efficiency in small- to medium-scale systems, the Tesla turbine [75] has garnered renewed attention due to its suitability for low-grade heat sources, such as those used in ORC systems [76–78]. Talluri et al. [79] developed a design procedure for a Tesla turbine for ORC applications. A throughout optimization method was performed by evaluating the losses of each component and introducing a detailed rotor model.

A previous study by Rusin et al. [27] investigated a Tesla-type turbine equipped with five co-rotating disks, aiming to enhance efficiency by refining both geometrical and operational parameters. The study primarily utilized a numerical optimization approach driven by efficiency considerations. The optimized parameters identified in their research serve as a reference for the present section of the study.

The most popular method of defining and accounting for the roughness in CFD simulations is by applying the representative parameter: the equivalent sand grain roughness. It can be determined by estimations based on various roughness parameters, documented in Kadivar et al. [80] where they conducted a review on turbulent flow over rough surfaces.

Recent DNS studies by Forooghi et al.[52] and Thakkar et al.[53] have explored the impact of various irregular rough surfaces on flow characteristics, focusing on key parameters such as ΔU^+ and k_s. Their findings suggest that among these factors, the skewness (S_k) of the surface height probability distribution function is the most influential in determining flow behavior, particularly when roughness density remains constant.

Kleinstreuer and Koo [56] established a methodology facilitating the analysis of microfluidic parameters based on PML properties, including layer thickness and porosity, as well as measurement uncertainties related to hydraulic diameter and the inlet Reynolds number. It incorporates realistic estimates of the PML Darcy number, surface roughness, and effective flow area to align with experimentally observed friction factors in micro-scale channels.

Pahlavanzadeh et al. [81] investigated the possibility of parametric modification of the PML model to implement roughness in the simulation of a Tesla turbine. The method was systematically examined in minichannel flow before being applied to the Tesla turbine. Initially, the PML model was compared against the Aupoix roughness model and experimental data from the minichannel.

The difference in gap size between Tesla turbines operating with air and those designed for ORC fluids is primarily due to the differences in fluid properties and operating conditions. The optimal size of the gap in a Tesla turbine is largely determined by the viscosity, density, and heat transfer properties of the fluid. Air-driven turbines usually require larger gaps to maintain efficient energy conversion and avoid excessive pressure losses, while ORC-based turbines benefit from smaller gaps which cause the flow tends to stay laminar, maintaining strong boundary layer adhesion to the disk surfaces where the Tesla turbine extracts energy through viscous shear [82].

In the present part of investigation, a Tesla turbine with six nozzles and optimized geometry based on Rusin et al. [27] is considered. As the operating flow is considered to be an ORC fluid, the gap size between co-rotating disks is in a smaller range. The method of implementation of roughness in Tesla turbine is addition of a porous medium layer on the surface examined by Pahlavanzadeh et al. in [81].

5.3 Mathematical model

The numerical simulations in this part of the study were carried out using ANSYS CFX due to its robust handling of rotating machinery and energy transport equations, which ensures thermodynamic consistency and enables reliable evaluation of flow and performance parameters in the Tesla turbine.

A finite-volume method is used to resolve discretized Reynolds-averaged Navier-Stokes equations. The investigation detailed in the paper involved conducting numerical simulations using the $k-\omega\ SST$ turbulence model.

In the PML approach, a porous layer alters the fluid flow resistance, requiring adjustments to the momentum term and turbulence closure on porous material parameters as described in

Chapter 4. Also, the distribution of porous parameters along the porous layer is the same as previous chapter.

5.4 Validation of numerical model on minichannel flow

The performance of the PML method in minichannel water flow is studied in Pahlavanzadeh et al. [81]. The paper presented the simulation of flow in a minichannel and validation of the results with an in-house experimental test setup. Roughness was implemented in the simulation using both the PML method and the Aupoix method. Fig. 7 represents a schematic of real roughness, the equivalent sand grain roughness used in the Aupoix method, and the porous layer in the PML method. There are various methods to estimate equivalent sand-grain roughness (k_s) based on different roughness parameters, but no universal formula exists for this calculation. In the current study, given the uniform distribution of the targeted roughness, the k_s in the Aupoix method was set equal to the roughness height.

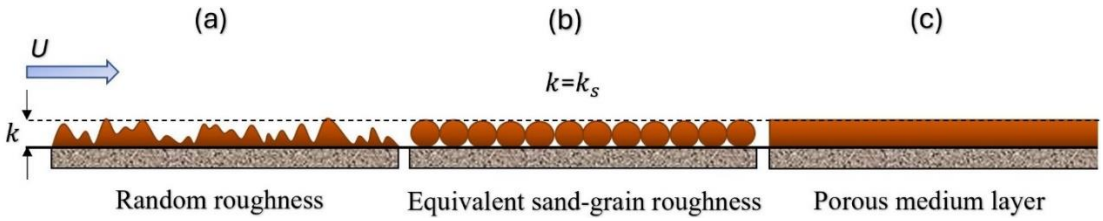

Figure 7. Schematics of (a) real random roughness, (b) equivalent sand-grain roughness, and (c) porous layer with the same thickness as the highest roughness peak.

The CFD simulation of water flow through the channel was carried out characterized by a width (z) of $50\ mm$, a length (x) of $150\ mm$, and a height (y) of $0.75\ mm$, at varying flow velocities. A fully developed flow at the inlet and ambient pressure at the outlet were considered. The side walls were non-slip and smooth and the top and bottom walls were rough.

The simulation incorporated roughness using two methods: the aforementioned Aupoix method and PML model, for a roughness height of $60\ \mu m$. The thickness of the porous layer was equal to the highest roughness peak, and the permeability is used to modify the drag generation in the minichannel. To generate the same drag in the minichannel as it results from the theoretical lines for the roughness height equal to $60\ \mu m$, the permeability was adjusted to be $K = 23\ nm^2$. The theoretical Fanning friction factor for laminar flow was obtained from:

$$f = \frac{C}{Re} \tag{36}$$

where the constant C depends on the aspect ratio of the channel $\alpha^* = \frac{h}{w}$, with h and w being the dimensions of a rectangular channel:

$$C = 24(1 - 1.3553\alpha^* + 1.9467\alpha^{*2} - 1.7012\alpha^{*3} + 0.9564\alpha^{*4} - 0.2537\alpha^{*5}) \tag{37}$$

The Swamee and Jain [83] approximation is used to solve the Fanning friction factor in the turbulent regime:

$$f = 0.0625\left[ln\left(\frac{\frac{k}{D_h}}{3.7} + \frac{5.74}{Re^{0.9}}\right)\right]^{-2} \quad (38)$$

From the in-house test rig the necessary flow parameters were collected to determine the friction factor for different Reynolds numbers:

$$Re = \frac{\rho U D_h}{\mu} \quad (39)$$

where D_h is the hydraulic diameter and can be calculated based on real or constricted dimensions of the channel.

Experiments were performed on minichannels that spanned a range of Re to capture the transition from laminar to fully turbulent flow regimes. This empirical study included channels with rough surfaces where aluminium oxide sheets with rough structures were attached to the top and bottom walls of the channel, having arithmetic mean deviation (R_a) of 11.3 μm, root mean square (R_q) of 13.16 μm, maximum peak to valley height of the profile (R_z) of 49.8 μm, and a total aluminum oxide sheet thickness, considered as the total roughness height (h_r) of 60 μm. The test rig is presented in Fig. 8.

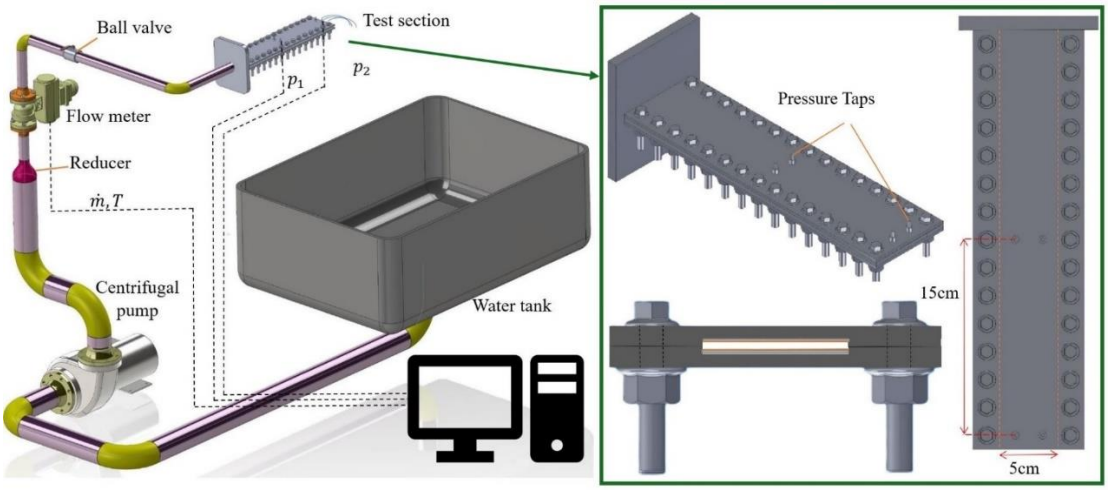

Figure 8. Schematic of the in-house water test rig

The literature [84,85] discusses that there is no fluid flow below a specific height of the roughness elements. As a result, the effective flow cross-sectional area can be reduced due to the height of the roughness. Consequently, demonstrating the friction factor considering the actual dimensions of the channel might represent a deviation from theoretical estimations of friction factors in laminar and turbulent regimes. The comparison of the friction factors obtained from the CFD simulations and theoretical predictions shows that the drag correction achieved using the PML method in the minichannel is appropriate and closely aligns with the theoretical estimations.

In this study, the performance of the roughness model for simulating expansion in the Tesla turbine was evaluated for real fluids R1234yf and n-hexane.

5.5 Tesla turbine simulation

This section outlines the integration of a Tesla turbine within an ORC system, which serves as the foundation of this study. The ORC is a thermodynamic process designed to efficiently transform low-temperature heat sources into mechanical energy, making it highly applicable for the utilization of renewable energy. In the following, the schematic of ORC system, the computational domain and the selected boundary conditions are presented. Additionally, a mesh independence study is conducted to assess the required mesh quality and density for consistent simulation results. Finally, the outcomes of the Tesla turbine simulations using the PML roughness model for two selected real gases are presented.

5.5.1 Computational domain and boundary conditions

The aimed ORC system consists of several essential components: a condenser, a pump, an evaporator, and a Tesla turbine. The cycle begins with the pump pressurizing the fluid before it enters the evaporator, where it absorbs heat from an external source. As a result, the fluid transitions to a superheated state, depending on the steam quality, before being directed into the Tesla turbine.

The thermodynamic behavior of the working fluid throughout the cycle is depicted in the temperature-entropy (T-s) diagram in Fig. 9, providing a visual representation of the process.

This T-s diagram represents a thermodynamic cycle of an ORC. The cycle includes key state points such as the pump inlet (1), evaporator inlet (2), nozzle inlet (3), rotor inlet (4) and rotor outlet (5).

The simulated part of the cycle corresponds to the Tesla turbine expansion process (between points 3, 4, and 5). The working fluid enters the turbine in a superheated state to enhance efficiency and avoid condensation, which could impact the turbine performance.

The diagram also highlights pinch-point temperature differences ($\Delta T_{pp,evap}$, and $\Delta T_{pp,cond}$) to indicate heat exchange constraints. The hot source (red line) and cold source (blue line) show the T variations in the evaporator and condenser.

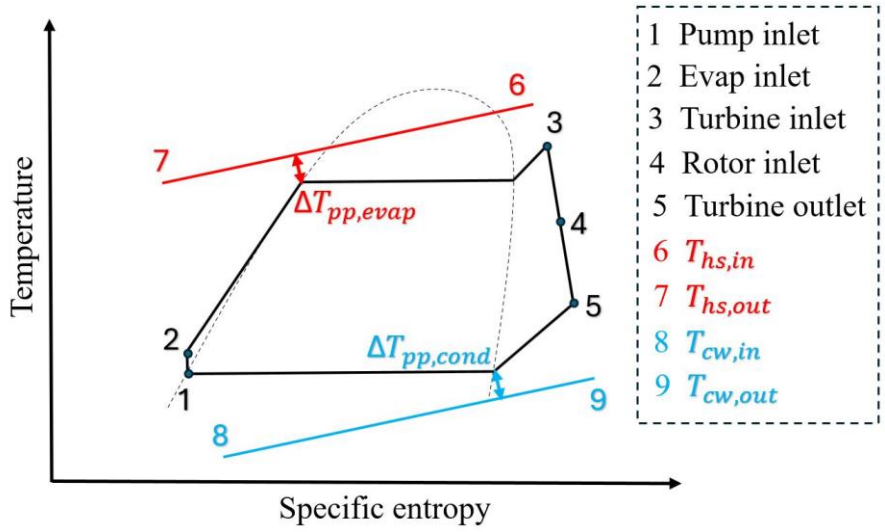

Figure 9. Schematic of the subcritical ORC cycle. The diagram highlights pinch-point temperature differences ($\Delta T_{pp,evap}$, $and\ \Delta T_{pp,cond}$) to indicate heat exchange constraints. The hot source (red line) and cold source (blue line) show the T variations in the evaporator and condenser.

The thermodynamic parameters of both studied real gases were chosen assuming that expansion is in the superheated region to avoid the two-phase flow, which is not the aim of the present study.

The analysis focuses on a Tesla turbine design featuring six nozzles. Given the turbine's symmetrical geometry, which repeats every 60 degrees, simulating the entire structure would demand an excessive number of computational cells, significantly increasing the calculation time. The nozzle configuration used in this study is referred to as a "one-to-many" design, where a single nozzle supplies fluid to all the gaps between the co-rotating disks.

The absolute coordinate system is applied to model the plenum chamber, nozzle, and tip clearance regions, while the rotating frame is used for the gap between the co-rotating disks, incorporating porous zones to simulate surface roughness. The computational domain is divided into three distinct sections.

1. Plenum chamber: This section is a part of the turbine's supply system.
2. Nozzle: A converging nozzle with a throat size of 0.7 mm, oriented at an 8-degree angle relative to the tangential direction.
3. Gap between co-rotating disks: Represent 1/6th of the disk perimeter (equivalent to 60 degrees), with outer and inner diameters of 160 mm and 80 mm, respectively. This part includes the porous zones that simulate the roughness of the turbine's disk surfaces.

A schematic of the computational domain and employed boundary conditions is demonstrated in Fig. 10. Co-rotating disks have outer and inner diameters of 160 mm and 80 mm, respectively, and the gap size between them is 0.12 mm. The roughness is implemented by erosion of material from the disks surface, the main flow field is maintained to be constant, and two porous layers are added on both sides of the gap in rough cases. The

radial tip clearance between the casing and the disks is set at $0.25\,mm$, based on the constraints of the real Tesla turbine design and manufacturing limitations. Periodic boundary conditions were applied on both sides of the disk sector with an angle of 60 degrees. The thickness of the plenum chamber is equal to the thickness of the size of the gap plus the disk ($2.12\,mm$). Symmetry boundary conditions were applied on both sides of the chamber.

Table 3 presents the boundary conditions selected for each case. These conditions were applied in the CFD simulations to ensure that the working fluids remained in the superheated vapor region, thereby enabling accurate modeling of single-phase flow within the Tesla turbine. The outlet p assigned for R1234yf was $1.05\,MPa$, and for n-hexane, $36930\,Pa$, which corresponds to saturation temperatures of 40°C and 42°C, respectively. Under these conditions, the entire expansion process occurs within the superheated region.

Table 3. Boundary conditions for the simulation of R1234yf and n-hexane expansion

Boundary condition	R1234yf	n-hexane
Total pressure ($p_{t,in}$) [MPa]	1.26	0.126
Total temperature ($T_{t,in}$) [K]	358.5	358.5
Turbulence intensity (inlet) [%]	5	5
Static pressure (p_{out}) [Mpa]	1.05	0.036930
Rotational speed [rpm]	1000-7000	5000-22000

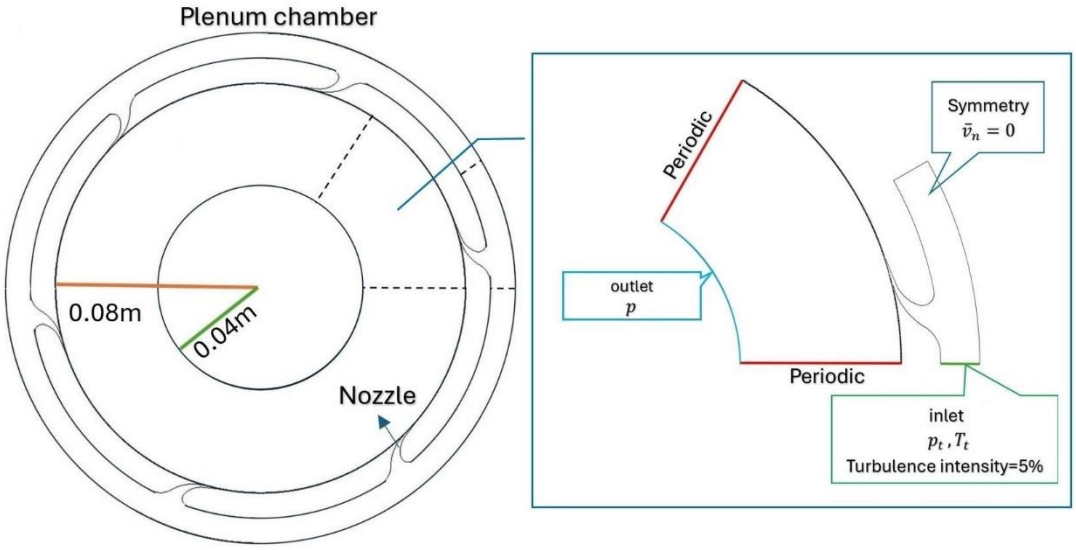

Figure 10. Schematic of the computational domain and location of boundary conditions

5.5.2 Numerical approach

The Tesla turbine was simulated in steady state using the RANS method and $k-\omega\,SST$ turbulence model. To ensure numerical stability and accuracy, the high-resolution scheme

was employed for both advection and turbulence equations. The mesh independence study was carried out by varying the number of nodes along the radii, circumferential, and gap of the computational domain. In all cases, the hexahedral mesh was generated with the thickness of the first layer next to the disks surface and interface between porous zone and the main flow field to be $< 1\mu m$ to ensure that y^+<1 on the wall. In simulations involving flow over porous media, particularly in cases with small flow cross-sections, sharp parameter gradients often arise at the interface between the flow field and the porous layer. To address this issue, the thickness of the mesh layer on both sides of the interface must be sufficiently fine. Accordingly, various mesh layer thicknesses in this region were tested, and the layer thickness was progressively reduced to be $< 1\mu m$ which demonstrated minimum parameter gradients. In each case, the efficiency of the turbine is determined as follows:

$$\eta = \frac{h_{t,in} - h_{t,out}}{h_{t,in} - h_{ts,out}} \tag{40}$$

Fig. 11 represents the mesh independence study with the efficiency of the system obtained in each case. As demonstrated, the minimum change in system efficiency is observed when the total number of nodes reaches 2.8 million. Therefore, the mesh grid used in all cases studied in this investigation includes the same number of nodes.

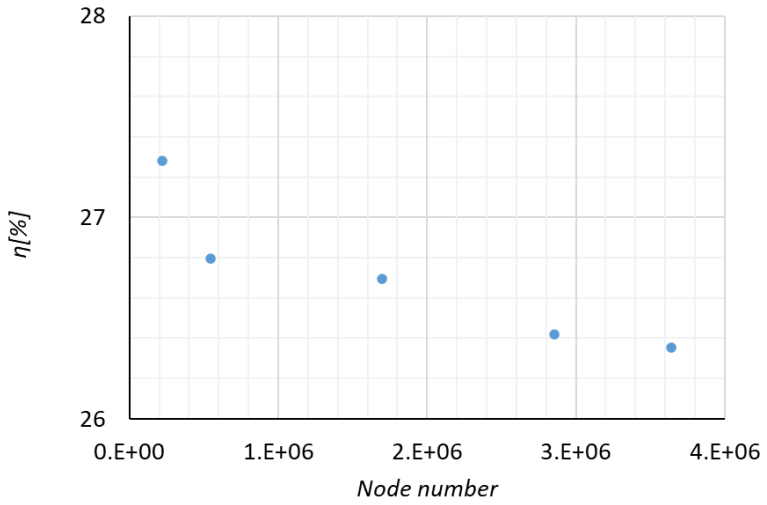

Figure 11. Turbine efficiency obtained from different meshes

5.5.3 Tesla turbine simulation with roughness

In this section, the performance of the adjusted parameters of the PML roughness method is tested in Tesla turbine simulations. A porous medium layer with the same modifications as those tested in Pahlavanzadeh et al. [81] was applied to the disk surfaces of the Tesla turbine. The porosity distribution along the gap has values ranging from zero at the wall to one where the flow encounters no resistance. The other porous parameters were defined as functions of porosity.

The simulation of the Tesla turbine was carried out considering a thickness of the porous medium layer of 28.8 μm, as caused by changing the working fluid, compared to 60 μm in Pahlavanzadeh et al. [81] and reduction of the gap size. Since the operating fluid considered in the current study is a real gas, the gap size is six times smaller than in their study. However, considering six times smaller PML thickness cannot demonstrate the impact of surface roughness on flow characteristics and turbine efficiency, then a thicker PML layer is used in both cases.

Fig. 12 presents the characteristic efficiency of the system operating with R1234yf and n-hexane as working fluids at different n for both smooth and rough cases.

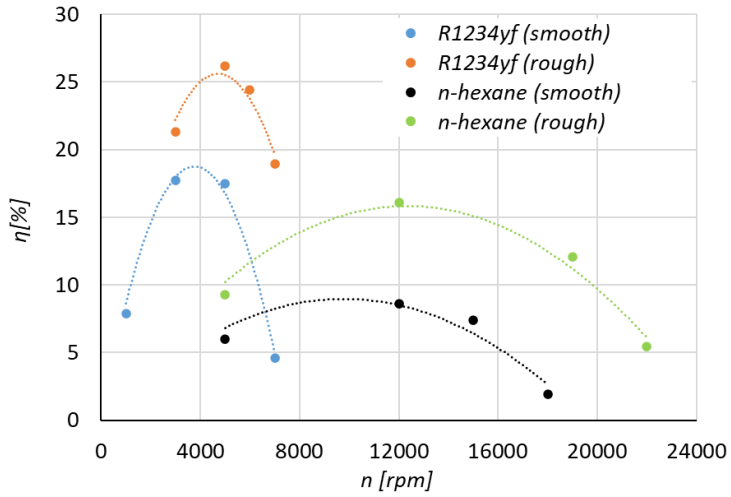

Figure 12. Efficiency characteristic of the Tesla turbine working with R1234yf and n-hexane in different n.

R1234yf shows peak efficiency at lower speeds (~5000 rpm), with rough surfaces yielding a maximum of ~27%, compared to ~18% for smooth, representing a 50% improvement. On the other hand, n-hexane performs best at higher speeds (~12000 rpm), where roughness increases peak efficiency from ~8% to ~15%, an 87.5% gain. The efficiency curves for all cases follow a parabolic trend, peaking before declining. These results demonstrate that surface roughness enhances efficiency for both fluids. R1234yf is more suitable for low to moderate speeds, while n-hexane excels at higher speeds. The analysis highlights the critical role of both the selection of working fluids and surface condition in maximizing Tesla turbine efficiency.

The distribution of mass-weighted radial and circumferential velocity components along the gap—from the outer to the inner radius are shown in Fig. 13. For n-hexane, the cases at n of $5000, 12000, and\ 19000\ rpm$ are presented, whereas for R1324yf, the speeds of $3000, 5000, and\ 7000\ rpm$.

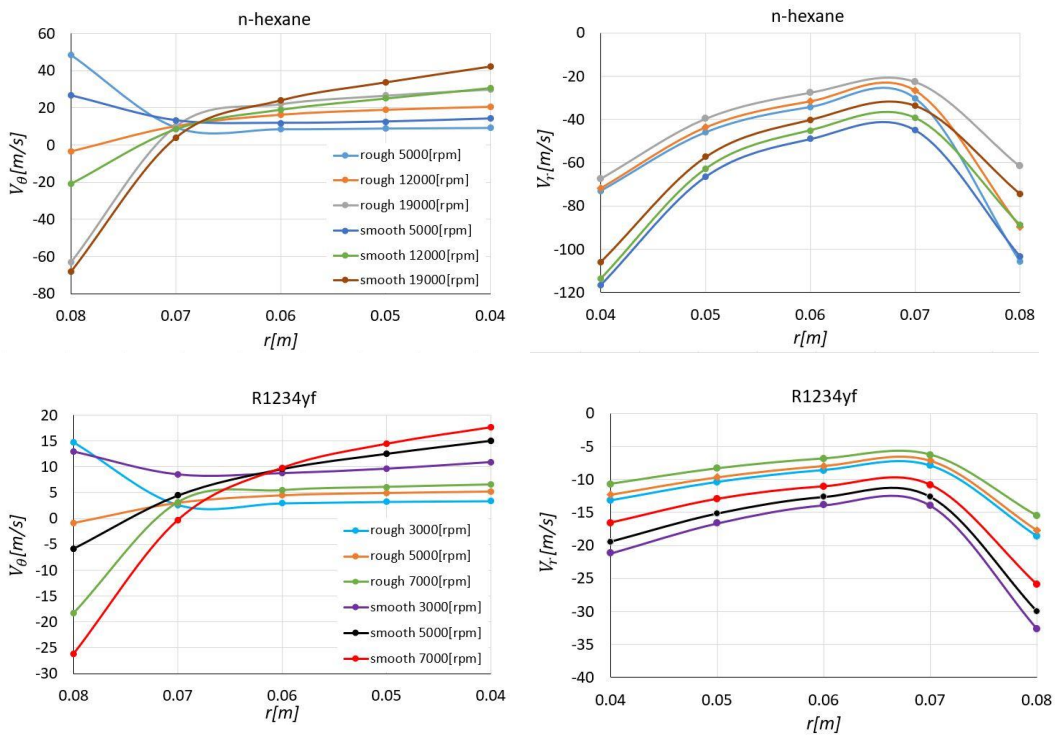

Figure 13. Radial distribution of mass-weighted tangential and radial velocity components in the gap for r1324yf and n-hexane.

The upper row corresponds to n-hexane, while the lower row represents R1234yf. The x-axis across all subplots denotes the radial position in meters, showing how the flow evolves from the gap entrance toward the outlet. The legend indicates n, distinguishing between rough and smooth surface conditions.

In both studied real gases, the results demonstrate that the tangential velocity becomes negative near the outer region of the gap at most investigated n, indicating a reversal in flow direction due to strong viscous effects and secondary flow development. At the entrance to the gap, the absolute value of the tangential velocity increases with increasing n and is consistently higher in the smooth surface cases compared to the rough ones. This suggests that rough surfaces enable more efficient angular momentum transfer from the working fluid to rotating disks in the initial region. The appearance of negative tangential velocity at the outer radii—where the distance to the rotational axis is greatest—implies an adverse effect on turbine performance, as it reflects low momentum transfer and reduced efficiency. Additionally, higher tangential velocities are observed near the outlet at higher n and in smooth surface cases, indicating more effective momentum transfer. However, the presence of surface roughness appears to reduce the tangential velocity near the outer edge, highlighting its influence in altering boundary layer behavior and possibly enhancing energy dissipation in the flow.

The radial velocity is consistently negative, reflecting the inward radial flow from the outer to inner diameter of the turbine gap. Lower n (e.g. $3000\ rpm$) show a stronger gradient of radial velocity and more abrupt decay in this velocity component, especially on smooth

surfaces, suggesting enhanced energy transfer and flow development under reduced surface resistance.

R1234yf exhibits generally lower velocity magnitudes across all cases. The curves are flatter, indicating a more uniform angular momentum distribution. The radial velocity also shows a more gradual gradient and lower peak values. This suggests a more stable and controlled flow, albeit less dynamic in behavior. Surface roughness effects are more prominent at higher n. n-hexane generally shows higher values of radial velocity, indicating a faster approach of operating flow from the gap entrance to the outlet.

To further evaluate the performance of the selected real gases, the relative Mach number on a mid-gap plane is presented in Fig. 14. For assessing the system at maximum efficiency, R1234yf is evaluated at $5000\ rpm$, while n-hexane is analyzed at $12000\ rpm$.

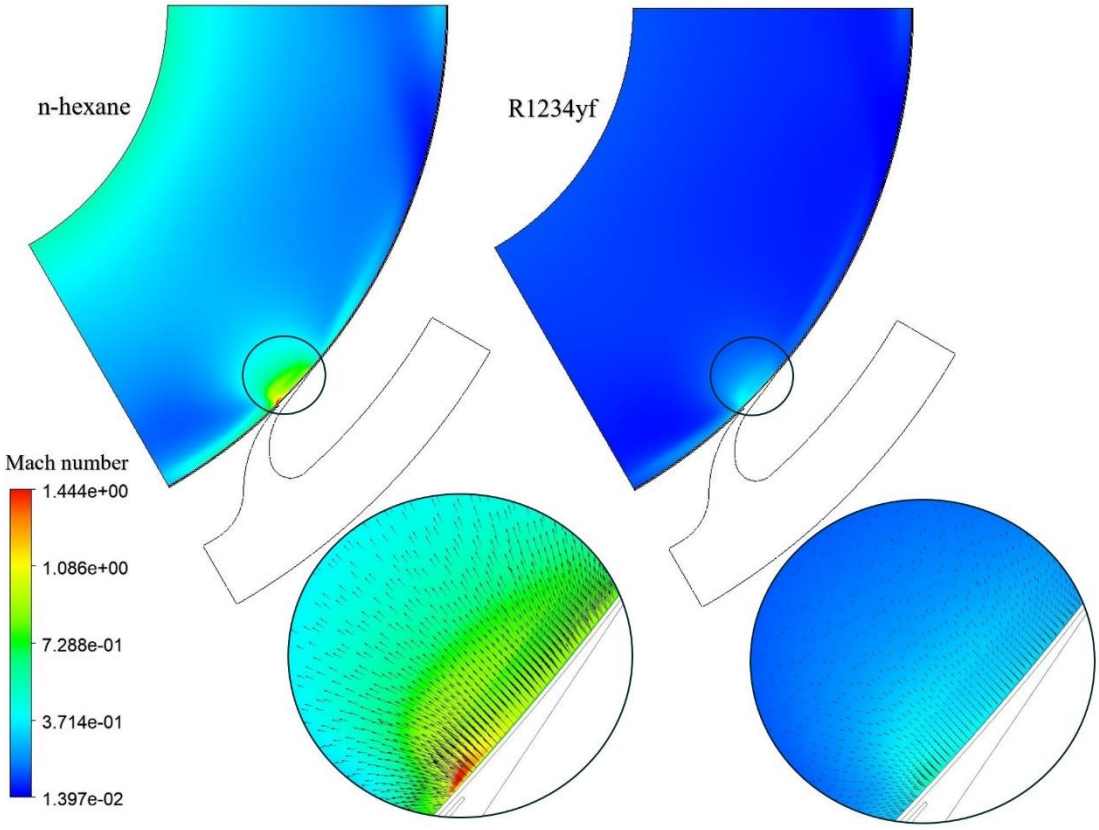

Figure14. Distribution of the Mach number and vector of velocity magnitude on a plane located at the mid-gap for both studied operating fluids

Fig. 14 shows a considerably higher Mach number in the vicinity of the nozzle jet for n-hexane, which leads to flow blockage in this region. The Mach number in this area is nearly three times higher for n-hexane compared to R1234yf. The dominant velocity component in the gap is tangential velocity. In the case of n-hexane, the flow blockage causes a reduction in the tangential component and an increase in the radial component of the velocity. In the zoomed-in region, the velocity vectors are scaled according to magnitude, clearly illustrating

the significantly higher fluid velocity in this area for n-hexane. It also represents higher inlet flow to the gap and stronger reverse flow in the circumferential direction.

To investigate the velocity distribution along the gap, three radial locations are selected. Fig. 15 illustrates the locations within the schematic of the computational domain, corresponding to radii of $0.05\ m$, $0.06\ m$, and $0.07\ m$. The tangential and radial components of the velocity along the gap are illustrated in this figure. On the x-axis of both plots, $Z_0 = h/2$, where h is the gap size between the disk surfaces, including both the porous zone and the main flow region.

In Fig. 15, the tangential and radial velocity profiles are shown at three radial positions for R1234yf and n-hexane, operating at $5000\ rpm$ and $12000\ rpm$, respectively. Despite the higher n for n-hexane, its overall efficiency is lower compared to R1234yf, and the velocity profiles help explain this discrepancy.

For n-hexane, the tangential velocity exhibits a parabolic distribution across the gap, with peak values ranging from approximately 22.5 to $27.5\ m/s$ as the radius decreases. This pattern reflects strong viscous entrainment and significant angular momentum concentrated in the center of the gap. However, the steep gradients near disk surfaces may cause increased viscous dissipation and localized losses, reducing overall efficiency. The radial velocity in n-hexane also shows intense inward flow, with values in the range $(-58, -35\ m/s)$. This rapid transport through the gap limits the residence time of the working fluid, reducing the opportunity for effective energy transfer to the rotating disks.

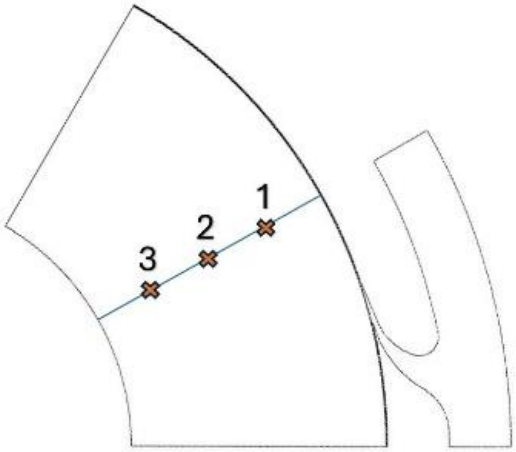

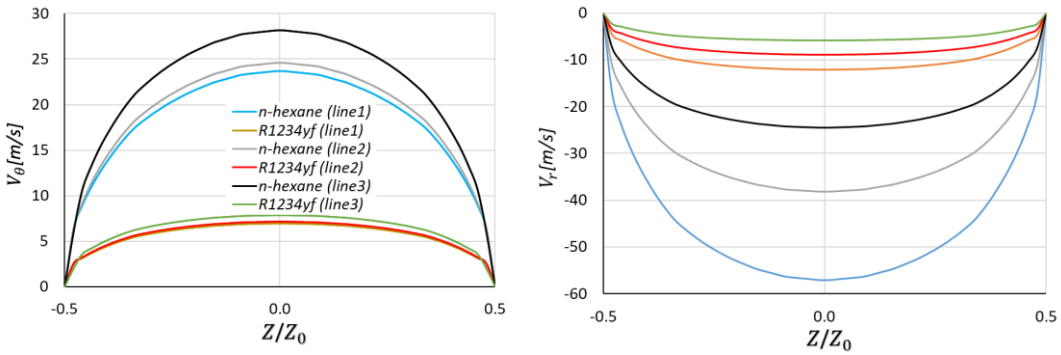

Figure 15. Distribution of tangential and radial velocity along the gap at three selected locations with a radius of 0.05, 0.06, and 0.07 m.

In contrast, R1234yf displays a much flatter and smoother tangential velocity profile, with values between ~6.5 and ~10 m/s. Although the overall flow speed is lower compared to other working fluids, the uniform tangential distribution promotes a more stable and consistent shear interaction with the rotor disks. Radial velocity is also more moderate, ranging from - 13 to $-9\ m/s$, results in a longer interaction time within the disk gap. This extended residence time allows for more effective momentum diffusion, contributing to the higher observed efficiency, even at reduced n. However, it should be noted that while longer interaction time generally improves efficiency under laminar conditions, it does not always correlate with higher power output, which depends more directly on the mass flow rate and radial velocity.

In summary, n-hexane's high flow velocity allows it to pass through the gap more quickly, but this comes with drawbacks such as increased energy dissipation and reduced interaction time. Despite its lower flow velocity, R1234yf maintains a more efficient internal flow regime, highlighting the critical role of fluid properties and flow control in Tesla turbine performance.

5.6 Achievements

Key achievements include:

- The validated model was applied to simulate an expansion of two ORC fluids—R1234yf and n-hexane— in the Tesla turbine, demonstrating the adaptability of the method for fluids with real gas properties and a wide range of operating speeds.

- The surface roughness can significantly improve turbine efficiency:

    - For R1234yf, efficiency increased from ~18% to ~27% at 5000 rpm.
    - For n-hexane, efficiency rose from ~8% to ~15% at 12000 rpm.

- Flow analysis revealed that R1234yf provided a more uniform and stable velocity field, contributing to better energy extraction at lower speeds. In contrast, n-hexane generated a stronger but less efficient flow due to high dissipation and reduced residence time.

- The roughness model helped mitigate certain factors that limited the system's performance with n-hexane, leading to improved flow uniformity and enhanced angular momentum transfer.

Summary and Conclusions

This study presented a comprehensive numerical investigation of flow characteristics and efficiency optimization methods for Tesla turbines, with a specific focus on simulating the narrow gap flow between co-rotating rough disks. All presented chapters were integrated to formulate a deep understanding of turbulence modeling, roughness simulation, and their effects on turbine efficiency and flow characteristics.

The research conducted investigated the suitability of different turbulence models and roughness methods. It was concluded that while the standard $k-\omega\,SST$ model performs efficiently in capturing the general steady-state behavior of the flow, the LES provides a superior representation of transient phenomena, especially near the outer edges of the disks where vorticity and fluctuations are dominant. Despite higher computational costs, LES revealed detailed insights into flow structures and fluctuations, making it invaluable for high-fidelity simulations. Nevertheless, the $k-\omega\,SST$ model remains a practical tool for broader parametric studies due to its lower resource demand and adequate accuracy.

Special attention was given to the implementation of wall roughness. The Aupoix method effectively adjusts eddy viscosity near rough walls, allowing the simulation of rough-wall effects without requiring mesh refinement at the micro-scale of roughness features. In addition, the PML model emerged as a powerful alternative to simulate complex roughness effects. By adjusting porous parameters to mimic specific roughness profiles, the PML approach was validated against experimental data and showed strong agreement with theoretical friction trends. It was also effective across different working fluids, including water, R1234yf, and n-hexane, demonstrating its adaptability.

Across the studies, roughness was consistently shown to enhance momentum transfer, particularly in the boundary layers developing near disk surfaces. Increased roughness height led to earlier laminar-to-turbulent transition, greater k, and more uniform velocity profiles near the walls. These changes contributed to higher power output, efficiency, and higher values of wall shear stress, especially in the outer disk region, which is critical due to its maximal distance from the rotational axis. In fact, simulations showed that roughness height and n strongly influenced efficiency: at certain operational ranges (e.g., $17000-26000\,rpm$, having air as operating fluid), increasing the roughness height by $60\,\mu m$ increases efficiency by up to 4.61 percentage points compared to smooth configurations.

Parametric analyses revealed complex interactions between flow parameters and turbine design. For instance, increased nozzle counts enhanced mass flow rate and power generation but also led to increased turbulence and reduced efficiency. The design of the inlet nozzle (one-to-one, and one-to-many nozzle configurations) significantly affected flow dynamics: convergent-divergent nozzle flow shapes inside the gap because of one-to-many nozzle configuration generated stronger fluctuations and higher wall shear stress, impacting Reynolds stress distribution and energy dissipation patterns. These effects were more pronounced when jet interaction with disk tips intensified turbulent behavior.

Finally, utilizing a unique design of Tesla for different ORC gases demonstrated the importance of the compatibility of the working fluid with design parameters. In the studied Tesla turbine, R1234yf promoted more stable flow profiles and better energy extraction at lower speeds, while n-hexane induced faster radial flows with more dissipation. The roughness-induced improvements in both cases illustrated the benefit of enhanced angular momentum transfer, a critical factor in bladeless turbine efficiency.

In conclusion, this integrated research confirms that detailed CFD modeling of roughness effects, turbulence selection, and operational parameters plays a vital role in optimizing Tesla turbine performance. Among the modeling strategies, LES is most suitable for high-accuracy needs, while the $k-\omega\,SST$ model offers efficient parametric exploration. Roughness must be carefully engineered to ensure favorable boundary layer characteristics and efficient energy conversion. Future work should expand implementation of roughness using PML model, examining more real roughness parameters in modification of PML layer parameters and finally finding a co-relation to connect them for the most precise simulation of roughness effect on flow characteristics.

Key Findings of the Thesis are listed in 6 categories as follows:

1- Turbulence modeling:
   - The $k-\omega\,SST$ model provided reliable predictions of flow behavior and shear stress in the co-rotating disk configurations and Tesla turbine simulations, particularly for benchmark validation cases and roughness modeling, while offering a good balance between accuracy and computational efficiency.
   - LES offers superior resolution of transient and complex flow phenomena, especially near the outer disk edges where vorticity and fluctuations are dominant, making it ideal for high-fidelity simulations.
2- Roughness modeling approaches:
   - There is no universally accepted method to determine the equivalent sand-grain roughness, and conventional roughness models (e.g., Aupoix) fail to accurately represent the influence of actual roughness geometries on flow behavior, especially in flows with small cross-sectional dimensions.
   - The Aupoix roughness model produced results consistent with the validation case of the minichannel; however, it still has limitations, such as its simplified representation of roughness and its limited applicability to small or confined flows.
   - The PML model emerged as a robust and flexible alternative for modeling rough surfaces. It was validated against experimental data and performed well, matching theoretical friction trends.
3- Impact of roughness on flow and efficiency:
   - Roughness enhances momentum transfer by promoting earlier transition to turbulence and increasing k near disk surfaces.
   - Higher roughness leads to more uniform velocity profiles, greater wall shear stress particularly in the outer disk region, and significantly improved power output and efficiency.

- In optimal operational ranges (e.g., $17000 - 26000\ rpm$ with air), efficiency improvements of up to 4.61 percent point were observed due to roughness height of $60\ \mu m$.

4- Effect of design parameters:
   - Increasing nozzle count raises mass flow rate and power output but can also increase turbulence and reduce overall efficiency.
   - Nozzle configuration (e.g., one-to-one vs. one-to-many) significantly affects flow behavior:
   - One-to-many configurations induce stronger velocity fluctuations and higher wall shear stress.
   - Jet interactions with disk tips intensify turbulence and affect Reynolds' stress and energy dissipation.
5- Working fluid compatibility:
   - The performance of the Tesla turbine is highly dependent on matching the working fluid with the design.
   - R1234yf supported more stable flow and efficient energy extraction at lower n.
   - n-hexane induced faster radial flow, and more energy dissipation yet still benefited from roughness-enhanced momentum transfer.
6- General contribution and optimization strategy:
   - The study confirms that accurate CFD modeling, particularly turbulence and roughness modeling, is critical to optimizing Tesla turbine design.
   - Roughness engineering plays a pivotal role in controlling boundary layer behavior and improving energy conversion efficiency.
   - The PML model holds strong potential for future refinement by incorporating real roughness geometry into its parameter definitions.

Bibliography

[1] Mahmoudi A, Fazli M, Morad MR. A recent review of waste heat recovery by Organic Rankine Cycle. Appl Therm Eng 2018;143:660–75. https://doi.org/10.1016/J.APPLTHERMALENG.2018.07.136.

[2] Sprouse C, Depcik C. Review of organic Rankine cycles for internal combustion engine exhaust waste heat recovery. Appl Therm Eng 2013;51:711–22. https://doi.org/10.1016/J.APPLTHERMALENG.2012.10.017.

[3] Imre AR, Daniarta S, Błasiak P, Kolasiński P. Design, Integration, and Control of Organic Rankine Cycles with Thermal Energy Storage and Two-Phase Expansion System Utilizing Intermittent and Fluctuating Heat Sources—A Review. Energies 2023, Vol 16, Page 5948 2023;16:5948. https://doi.org/10.3390/EN16165948.

[4] Imran M, Usman M, Park BS, Lee DH. Volumetric expanders for low grade heat and waste heat recovery applications. Renewable and Sustainable Energy Reviews 2016;57:1090–109. https://doi.org/10.1016/J.RSER.2015.12.139.

[5] Fiaschi D, Manfrida G, Maraschiello F. Design and performance prediction of radial ORC turboexpanders. Appl Energy 2015;138:517–32. https://doi.org/10.1016/J.APENERGY.2014.10.052.

[6] Tesla N. Nikola Tesla U.S. Patent 1,061,206 - Turbine, 1913.

[7] Kaczmarczyk TZ, Żywica G, Witanowski Ł, Klonowicz P, Lampart P, Ihnatowicz E. Selection and analysis of the main components of a 10 kW CHP ORC system powered by waste heat from the food drying process. Energy 2025;328:136511. https://doi.org/10.1016/J.ENERGY.2025.136511.

[8] Daniarta S, Nemś M, Kolasiński P. A review on thermal energy storage applicable for low- and medium-temperature organic Rankine cycle. Energy 2023;278:127931. https://doi.org/10.1016/J.ENERGY.2023.127931.

[9] Moradi R, Habib E, Bocci E, Cioccolanti L. Investigation on the use of a novel regenerative flow turbine in a micro-scale Organic Rankine Cycle unit. Energy 2020;210:118519. https://doi.org/10.1016/J.ENERGY.2020.118519.

[10] Usman M, Imran M, Haglind F, Pesyridis A, Park BS. Experimental analysis of a micro-scale organic Rankine cycle system retrofitted to operate in grid-connected mode. Appl Therm Eng 2020;180:115889. https://doi.org/10.1016/J.APPLTHERMALENG.2020.115889.

[11] Sengupta S, Guha A. A theory of Tesla disc turbines. Proceedings of the Institution of Mechanical Engineers, Part A: Journal of Power and Energy 2012;226:650–63. https://doi.org/10.1177/0957650912446402.

[12] Rice W. An Analytical and Experimental Investigation of Multiple-Disk Turbines. Journal of Engineering for Power 1965;87:29–36. https://doi.org/10.1115/1.3678134.

[13] Butenko VA, Rylov YP, Chikov VP. Experimental investigation of the characteristics of small-sized nozzles. Fluid Dynamics 1976;11:936–9. https://doi.org/10.1007/BF01026418/METRICS.

[14] Leaman A.B. The Design, Construction and Investigation of a Tesla Turbine : Audley B. Leaman : Free Download, Borrow, and Streaming : Internet Archive 1950. https://archive.org/details/leaman (accessed August 4, 2025).

[15] Young S.K.P. The investigation and analysis of the Tesla Turbine. University of Illinois, 1957.

[16] Patel N, Schmidt DD. Biomass Boundary Layer Turbine Power System. Proceedings of the 2002 International Joint Power Generation Conference 2009:931–4. https://doi.org/10.1115/IJPGC2002-26035.

[17] Talluri L, Dumont O, Manfrida G, Lemort V, Fiaschi D. Experimental investigation of an Organic Rankine Cycle Tesla turbine working with R1233zd(E). Appl Therm Eng 2020;174:115293. https://doi.org/10.1016/J.APPLTHERMALENG.2020.115293.

[18] Rusin K, Wróblewski W, Rulik S, Majkut M, Strozik M. Performance Study of a Bladeless Microturbine. Energies 2021;14:3794. https://doi.org/10.3390/EN14133794.

[19] Teng S, Li L, Yan C, An D, Zhao Y, Xi H. Multi-parameter experimental study of a tesla turbine applied to an organic Rankine cycle system for low-grade heat utilisation. Energy Convers Manag 2025;333:119824. https://doi.org/10.1016/J.ENCONMAN.2025.119824.

[20] Sandilya P, Biswas G, Rao DP, Sharma A. Numerical simulation of the gas flow and mass transfer between two coaxially rotating disks. Numeri Heat Transf A Appl 2001;39:285–305. https://doi.org/10.1080/104077801300006599;WGROUP:STRING:PUBLICATION.

[21] Lampart P., Jędrzejewski Ł. Investigations of aerodynamics of Tesla bladeless microturbines | Lampart | Journal of Theoretical and Applied Mechanics. Journal of Theoretical and Applied Mechanics 2011.

[22] Sengupta S., Guha A. A Theory of Tesla Disc Turbines: Sayantan Sengupta and Abhijit Guha | PDF | Turbine | Fluid Dynamics 2012. https://www.scribd.com/document/503026472/10-1-1-1010-5455 (accessed August 4, 2025).

[23] Qi W, Deng Q, Jiang Y, Yuan Q, Feng Z. Disc Thickness and Spacing Distance Impacts on Flow Characteristics of Multichannel Tesla Turbines. Energies 2019, Vol 12, Page 44 2018;12:44. https://doi.org/10.3390/EN12010044.

[24] Qi W, Deng Q, Jiang Y, Feng Z, Yuan Q. Aerodynamic performance and flow characteristics analysis of Tesla turbines with different nozzle and outlet geometries. Proceedings of the Institution of Mechanical Engineers, Part A: Journal of Power and Energy 2019;233:358–78. https://doi.org/10.1177/0957650918785312;PAGE:STRING:ARTICLE/CHAPTER.

[25] Fiaschi D, Talluri L. Design and off-design analysis of a Tesla Turbine utilizing CO2 as working fluid. E3S Web of Conferences, 2019, p. 113. https://doi.org/10.1051/e3sconf/201911303008.

[26] Rusin K, Wróblewski W, Rulik S. The evaluation of numerical methods for determining the efficiency of Tesla turbine operation. Journal of Mechanical Science and Technology 2018;32:5711–21. https://doi.org/10.1007/S12206-018-1118-4.

[27] Rusin K, Wróblewski W, Rulik S. Efficiency based optimization of a Tesla turbine. Energy 2021;236:121448. https://doi.org/10.1016/J.ENERGY.2021.121448.

[28] Sivaramakrishnaiah M, Reddy RM, Reddy AD, Ravitheja A, Paramasivam P, Yusuf M, et al. Numerical analysis of energy dynamics in a bladeless turbine nozzle. International Journal of Low-Carbon Technologies 2025;20:1383–91. https://doi.org/10.1093/IJLCT/CTAF093.

[29] Schosser C, Lecheler S, Pfitzner M. A Test Rig for the Investigation of the Performance and Flow Field of Tesla Friction Turbines. ASME Turbo ExpoAt, vol. 1B, American Society of Mechanical Engineers (ASME); 2014. https://doi.org/10.1115/GT2014-25399.

[30] Rusin K, Wróblewski W, Rulik S. The evaluation of numerical methods for determining the efficiency of Tesla turbine operation. Journal of Mechanical Science and Technology 2018 32:12 2018;32:5711–21. https://doi.org/10.1007/S12206-018-1118-4.

[31] Azimy N, Saffarian MR. Investigation of thermal characteristics and entropy generation in a solar collector including Fly Ash-Cu hybrid nanofluids: Numerical approach using mixture model. Eng Anal Bound Elem 2023;152:169–84. https://doi.org/10.1016/J.ENGANABOUND.2023.04.002.

[32] Zhang F, Zhou Z, Zhang H, Yang X. A new single formula for the law of the wall and its application to wall-modeled large-eddy simulation. European Journal of Mechanics - B/Fluids 2022;94:350–65. https://doi.org/10.1016/J.EUROMECHFLU.2022.03.013.

[33] Suga K, Craft T, Iacovides H. An analytical wall-function for turbulent flows and heat transfer over rough walls. International Journal of Heat and Fluid 2006;27:852–66.

[34] Chedevergne F. Analytical wall function including roughness corrections. Int J Heat Fluid Flow 2018;73:258–69. https://doi.org/10.1016/J.IJHEATFLUIDFLOW.2018.08.001.

[35] Suastika IK, Hakim ML, Nugroho B, Nasirudin A, Utama IKAP, Monty JP, et al. Characteristics of drag due to streamwise inhomogeneous roughness. Ocean Engineering 2021;223:108632. https://doi.org/10.1016/J.OCEANENG.2021.108632.

[36] Lalegani F, Saffarian MR, Moradi A, Tavousi E. Effects of different roughness elements on friction and pressure drop of laminar flow in microchannels. Int J Numer Methods Heat Fluid Flow 2018;28. https://doi.org/10.1108/HFF-04-2017-0140.

[37] Bezaatpour J, Ghiasirad H, Bezaatpour M, Ghaebi H. Towards optimal design of photovoltaic/thermal facades: Module-based assessment of thermo-electrical performance,

exergy efficiency and wind loads. Appl Energy 2022;325:119785. https://doi.org/10.1016/J.APENERGY.2022.119785.

[38] Sun J, He YL, Tao WQ. A molecular dynamics study on heat and mass transfer in condensation over smooth/rough surface. Int J Numer Methods Heat Fluid Flow 2011;21. https://doi.org/10.1108/09615531111105425.

[39] Kadivar M, Tormey D, McGranaghan G. A review on turbulent flow over rough surfaces: Fundamentals and theories. International Journal of Thermofluids 2021;10. https://doi.org/10.1016/J.IJFT.2021.100077.

[40] Orlandi P, Leonardi S. DNS of turbulent channel flows with two- and three-dimensional roughness. Journal of Turbulence 2009;7:1–22. https://doi.org/10.1080/14685240600827526.

[41] Nikuradse J. Laws of Flow in Rough Pipes Nikuradse. National Advisory Committee For Aeronautics; 1933.

[42] Grigson C. Drag Losses of New Ships Caused by Hull Finish. Journal of Ship Research 1992;36:182–96. https://doi.org/10.5957/JSR.1992.36.2.182.

[43] Colebrook CF. Turbulent Flow in Pipes, with particular reference t o the Transition Region between the Smooth and Rough Pipe Laws. Journal of the Institution of Civil Engineers 1939;11:133–56. https://doi.org/10.1680/ijoti.1939.13150.

[44] Cebeci T, Bradshaw P. Momentum transfer in boundary layers. vol. 4. 1977.

[45] Knopp T, Alrutz T, Schwamborn D. A grid and flow adaptive wall-function method for RANS turbulence modelling. J Comput Phys 2006;220:19–40. https://doi.org/10.1016/J.JCP.2006.05.003.

[46] Kalitzin G, Medic G, Iaccarino G, Durbin P. Near-wall behavior of RANS turbulence models and implications for wall functions. J Comput Phys 2005;204:265–91. https://doi.org/10.1016/J.JCP.2004.10.018.

[47] Moody LF. Friction factors for pipe flow | BibSonomy. Transactions of the ASME 1944. https://www.bibsonomy.org/bibtex/22539414e7f58ccbe181597970148d3b5/thorade (accessed August 1, 2022).

[48] Moody LF. Friction factors for pipe flow | BibSonomy. Transactions of the ASME 1944. https://doi.org/http://www.chem.mtu.edu/~fmorriso/cm310/MoodyLFpaper1944.pdf.

[49] Kandlikar SG, Schmitt D, Carrano AL, Taylor JB. Characterization of surface roughness effects on pressure drop in single-phase flow in minichannels. Physics of Fluids 2005;17:100606. https://doi.org/10.1063/1.1896985.

[50] Chedevergne F, Aupoix B. Accounting for wall roughness effects in turbulence models : a wall function approach. 7 Th European Conference for Aeronautics and Aerospace sciences (EUCASS), 2017. https://doi.org/10.13009/EUCASS2017-372.

[51] Chedevergne F. Analytical wall function including roughness corrections. Int J Heat Fluid Flow 2018;73:258–69. https://doi.org/10.1016/J.IJHEATFLUIDFLOW.2018.08.001.

[52] Forooghi P, Stroh A, Magagnato F, Jakirlić S, Frohnapfel B. Toward a Universal Roughness Correlation. Journal of Fluids Engineering, Transactions of the ASME 2017;139. https://doi.org/10.1115/1.4037280/371945.

[53] Thakkar M, Busse A, Sandham N. Surface correlations of hydrodynamic drag for transitionally rough engineering surfaces. Journal of Turbulence 2017;18:138–69. https://doi.org/10.1080/14685248.2016.1258119.

[54] Ozgumus T, Mobedi M, Ozkol U. Determination of Kozeny Constant Based on Porosity and Pore to Throat Size Ratio in Porous Medium with Rectangular Rods. Engineering Applications of Computational Fluid Mechanics 2014;8:308–18. https://doi.org/10.1080/19942060.2014.11015516.

[55] Forooghi P, Frohnapfel B, Magagnato F, Busse A. A modified Parametric Forcing Approach for modelling of roughness. Int J Heat Fluid Flow 2018;71:200–9. https://doi.org/10.1016/J.IJHEATFLUIDFLOW.2018.03.019.

[56] Kleinstreuer C, Koo J. Computational Analysis of Wall Roughness Effects for Liquid Flow in Micro-Conduits. J Fluids Eng 2004;126:1–9. https://doi.org/10.1115/1.1637633.

[57] Rusin K, Wróblewski W, Rulik S. Efficiency based optimization of a Tesla turbine. Energy 2021;236:121448. https://doi.org/10.1016/J.ENERGY.2021.121448.

[58] Thomazoni ALR, Ermel C, Schneider PS, Vieira LW, Hunt JD, Ferreira SB, et al. Influence of operational parameters on the performance of Tesla turbines: Experimental investigation of a small-scale turbine. Energy 2022;261:125159. https://doi.org/10.1016/J.ENERGY.2022.125159.

[59] Wang H, Luo K, Huang C, Zou A, Li D, Qin K. Numerical investigation of partial admission losses in radial inflow turbines. Energy 2022;239:121870. https://doi.org/10.1016/J.ENERGY.2021.121870.

[60] Lampart P, Jędrzejewski Ł. Investigations of aerodynamics of Tesla bladeless microturbines. Journal of Theoretical and Applied Mechanics 2011.

[61] Pahlavanzadeh M, Rusin K, Wróblewski W. Evaluation of dynamic correction of turbulence wall boundary conditions to simulate roughness effect in minichannel with rotating walls. Int J Numer Methods Heat Fluid Flow 2023;ahead-of-print. https://doi.org/10.1108/HFF-03-2023-0160/FULL/PDF.

[62] Rusin K, Wróblewski W, Strozik M. Comparison of methods for the determination of Tesla turbine performance. Journal of Theoretical and Applied Mechanics 2019;57:563–75. https://doi.org/10.15632/JTAM-PL/109602.

[63] Niknam PH, Talluri L, Ciappi L, Fiaschi D. Numerical assessment of a two-phase Tesla turbine: Parametric analysis. Appl Therm Eng 2021;197:117364. https://doi.org/10.1016/J.APPLTHERMALENG.2021.117364.

[64] Aupoix B. Roughness corrections for the k-ω shear stress transport model: Status and proposals. Journal of Fluids Engineering, Transactions of the ASME 2015;137. https://doi.org/10.1115/1.4028122/374661.

[65] Launder BE, Spalding DB. The numerical computation of turbulent flows. Comput Methods Appl Mech Eng 1974;3:269–89. https://doi.org/10.1016/0045-7825(74)90029-2.

[66] Kader BA. Temperature and concentration profiles in fully turbulent boundary layers. Int J Heat Mass Transf 1981;24:1541–4. https://doi.org/10.1016/0017-9310(81)90220-9.

[67] Villedieu P, Trontin P, Chauvin R. Glaciated and mixed phase ice accretion modeling using ONERA 2D icing suite. 6th AIAA Atmospheric and Space Environments Conference, vol. 51, Japan Soc. of Med. Electronics and Biol. Engineering; 2014. https://doi.org/10.2514/6.2014-2199.

[68] Trontin P, Kontogiannis A, Blanchard G, Villedieu P. Description and assessment of the new ONERA 2D icing suite IGLOO2D. 9th AIAA Atmospheric and Space Environments Conference, AIAA AVIATION, American Institute of Aeronautics and Astronautics Inc, AIAA; 2017. https://doi.org/10.2514/6.2017-3417.

[69] Radenac E. Validation of a 3D ice accretion tool on swept wings of the SUNSET2 program. 8th AIAA Atmospheric and Space Environments Conference, American Institute of Aeronautics and Astronautics Inc, AIAA; 2016. https://doi.org/10.2514/6.2016-3735.

[70] Hosni MH, Coleman HW, Garner JW, Taylor RP. Roughness element shape effects on heat transfer and skin friction in rough-wall turbulent boundary layers. Int J Heat Mass Transf 1993;36:147–53. https://doi.org/10.1016/0017-9310(93)80074-5.

[71] Hosni MH, Coleman HW, Garner JW, Taylor RP. Roughness element shape effects on heat transfer and skin friction in rough-wall turbulent boundary layers. Int J Heat Mass Transf 1993;36:147–53. https://doi.org/10.1016/0017-9310(93)80074-5.

[72] Shur ML, Spalart PR, Strelets MK, Travin AK. A hybrid RANS-LES approach with delayed-DES and wall-modelled LES capabilities. Int J Heat Fluid Flow 2008;29:1638–49. https://doi.org/10.1016/J.IJHEATFLUIDFLOW.2008.07.001.

[73] Smagorinsky .J. General Circulation Experiments with the Primitive Equations 1963. https://eurekamag.com/research/084/250/084250654.php (accessed December 22, 2023).

[74] Piomelli U, Moin P, Ferziger JH. Model consistency in large eddy simulation of turbulent channel flows. Physics of Fluids 1988;31:1884–91. https://doi.org/10.1063/1.866635.

[75] Tesla N. Nikola Tesla U.S. Patent 1,061,206 - Turbine, 1913.

[76] Manfrida G, Pacini L, Talluri L. An upgraded Tesla turbine concept for ORC applications. Energy 2018;158:33–40. https://doi.org/10.1016/J.ENERGY.2018.05.181.

[77] Ganguly A, Sengupta S, Pramanik S. Waste heat recovery using Tesla turbines in Rankine cycle power plants: Thermofluid dynamic characterization, performance assessment and exergy analysis. Appl Therm Eng 2022;207:118141. https://doi.org/10.1016/J.APPLTHERMALENG.2022.118141.

[78] Ji F, Bao Y, Zhou Y, Du F, Zhu H, Zhao S, et al. Investigation on performance and implementation of Tesla turbine in engine waste heat recovery. Energy Convers Manag 2019;179:326–38. https://doi.org/10.1016/J.ENCONMAN.2018.10.071.

[79] Talluri L, Fiaschi D, Neri G, Ciappi L. Design and optimization of a Tesla turbine for ORC applications. Appl Energy 2018;226:300–19. https://doi.org/10.1016/J.APENERGY.2018.05.057.

[80] Kadivar M, Tormey D, McGranaghan G. A review on turbulent flow over rough surfaces: Fundamentals and theories. International Journal of Thermofluids 2021;10. https://doi.org/10.1016/J.IJFT.2021.100077.

[81] Pahlavanzadeh M, Rusin K, Wróblewski W, Rulik S. Roughness effects on flow in Tesla turbine with parametric adjustment of porous layer model. Physics of Fluids 2025;37. https://doi.org/10.1063/5.0247548/3329214.

[82] Pacini L, Ciappi L, Talluri L, Fiaschi D, Manfrida G, Smolka J. Computational investigation of partial admission effects on the flow field of a tesla turbine for ORC applications. Energy 2020;212:118687. https://doi.org/10.1016/J.ENERGY.2020.118687.

[83] Swamee PK, Jain AK. Explicit Equations for Pipe-Flow Problems. Journal of Hydraulic Engineering 1976.

[84] Kandlikar SG, Schmitt D, Carrano AL, Taylor JB. Characterization of surface roughness effects on pressure drop in single-phase flow in minichannels. Physics of Fluids 2005;17:100606. https://doi.org/10.1063/1.1896985.

[85] Pahlavanzadeh M, Rulik S, Wróblewski W, Rusin K. Application of roughness models to stationary and rotating minichannel flows. International Journal of Numerical Methods for Heat & Fluid Flow 2024;ahead-of-print. https://doi.org/10.1108/HFF-05-2024-0379.

Appendices

In this Chapter, the full-text papers that were briefly described in Chapters 2 - 4 are presented. The papers are listed in the following order:

Paper I: **Pahlavanzadeh, M**., Rusin, K., Wróblewski, W., (2023). Evaluation of dynamic correction of turbulence wall boundary conditions to simulate roughness effect in minichannel with rotating walls. International Journal of Numerical Methods for Heat & Fluid Flow. Vol. 33, Page 3915–3939. https://doi.org/10.1108/HFF-03-2023-0160.

Paper II: **Pahlavanzadeh, M**., Rulik, K., Wróblewski, W., Rusin, K., (2024). Application of roughness models to stationary and rotating minichannel flows. International Journal of Numerical Methods for Heat & Fluid Flow. Vol. 34, Page 4085–4106. https://doi.org/10.1108/HFF-05-2024-0379.

Paper III: **Pahlavanzadeh, M**., Wróblewski, W., Rusin, K., (2024). On the Flow in the Gap between Co-rotating Disks of Tesla Turbine with Different Supply Configurations: A Numerical Study. Energies. Vol. 17, Page 4472 https://doi.org/10.3390/EN17174472.

Paper IV: **Pahlavanzadeh, M**., Wróblewski, W., Rusin, K., (2025). Evaluation of nozzle configuration impact on flow structures and performance in Tesla turbine. International Journal of Heat and Mass Transfer. Vol. 243, Page 126900. https://doi.org/10.1016/J.IJHEATMASSTRANSFER.2025.126900.

Paper V: **Pahlavanzadeh, M**., Rusin, K., Wróblewski, W., Rulik, S., (2025). Roughness effects on flow in Tesla turbine with parametric adjustment of porous layer model. Physics of Fluids. Vol. 37 https://doi.org/10.1063/5.0247548/3329214.

Paper I

Evaluation of dynamic correction of turbulence wall boundary conditions to simulate roughness effect in minichannel with rotating walls.

Evaluation of dynamic correction of turbulence wall boundary conditions to simulate roughness effect in minichannel with rotating walls

Mohammadsadegh Pahlavanzadeh, Krzysztof Rusin and Wlodzimierz Wróblewski
Department of Power Engineering and Turbomachinery, Silesian University of Technology, Gliwice, Poland

Received 30 March 2023
Revised 13 June 2023
Accepted 4 August 2023

Abstract

Purpose – The purpose of this study is an assessment of the existing roughness models to simulate the flow in the narrow gap between corotating and rough disks. A specific configuration of the flow through the gap, which forms a minichannel with variable cross sections and rotating walls, makes it a complex problem and, therefore, worth discussing in more detail.

Design/methodology/approach – Two roughness models were examined, the first one was based on the wall function modification by application of the shift in the dimensionless velocity profile, and the second one was based on the correction of turbulence parameters at the wall, proposed by Aupoix. Due to the lack of data to validate that specific case, the approach to deal with was selected after a systematic study of reported test cases. It started with a zero-pressure-gradient boundary layer in the flow over a flat plate, continued with flow through minichannels with stationary walls, and finally, focused on the flow between corotating discs, pertaining each time to smooth and rough surfaces.

Findings – The limitations of the roughness models were highlighted, which make the models not reliable in the application to minichannel flows. It concerns turbulence models, near-wall discretization and roughness approaches. Aupoix's method to account for roughness was selected, and the influence of minichannel height, mass flow rate, fluid properties and roughness height on the velocity profile between corotating discs in both smooth and rough cases was discussed.

Originality/value – The originality of this study is the evaluation and validation of different methods to account for the roughness in rotating mini channels, where the protrusions can cover a substantial part of the channel. Flow behavior and performance of different turbulence models were analyzed as well.

Keywords Corotating disks, Minichannel flows, Roughness model, Boundary layer

Paper type Research paper

Nomenclature

A = Area;
c = Smooth-wall interception;
C_s = Roughness constant;

The presented research was conducted within the UMO-2019/35/B/ST8/01871 research project financed by the Polish National Science Centre and internal project 08/050/BKM_22/0271 financed by the Silesian University of Technology.

International Journal of Numerical Methods for Heat & Fluid Flow
Vol. 33 No. 12, 2023
pp. 3915-3939

0961-5539
DOI 10.1108/HFF-03-2023-0160

C_p = Specific heat at constant pressure;
D_h = Hydraulic diameter;
E = Empirical constant;
e = Inner energy;
f = Fanning friction factor;
f_i = Gravitational force;
h = Channel height;
h_{cf} = Constricted channel height;
k = Turbulent kinetic energy;
k_s = Equivalent sand-grain roughness;
k_P = Turbulence kinetic energy at the near-wall node P;
k_s^+ = Roughness Reynolds number;
$k_{s\,smooth}^+$ = Lower band of transitionally rough regime;
$k_{s\,rough}^+$ = Upper band of transitionally rough regime;
k_w^+ = Dimensionless turbulent kinetic energy close to the wall;
$\dot{m}$ = Mass flow rate;
N = Rotational speed;
p = Pressure;
Re = Reynolds number;
Re_τ = Friction Reynolds number;
R_a = Arithmetic mean deviation;
r = Roughness height;
T = Temperature;
t = Time step;
U = Mean velocity;
U^+ = Dimensionless mean velocity (related to wall shear stress);
U^* = Dimensionless mean velocity (related to turbulent kinetic energy);
U_p = Mean velocity at the near-wall node P;
U_{lam}^+ = Dimensionless mean velocity in laminar flow;
U_{turb}^+ = Dimensionless mean velocity in turbulent flow;
U_∞ = Free stream velocity;
u_τ = Skin friction velocity;
ΔU^+ = Roughness function;
y^+ = Dimensionless normal-wall distance (related to wall shear stress);
y^* = Dimensionless normal-wall distance (related to turbulent kinetic energy); and
y_P = Distance from point P to the wall.

Greek letters

κ = Von Karman constant;
v = Kinematic viscosity;
τ_w = Total wall stress;
ρ = Density;
τ = Tangential stress;
μ = Dynamic viscosity;
Γ = Blending function;
ω = Specific dissipation rate;
ω_w^+ = Dimensionless specific dissipation rate close to the wall;
ε = Turbulent dissipation rate;
ε_r = Height of the roughness;

α^* = Aspect ratio of the channel;
ω_a = Angular velocity;
η = System efficiency; and
γ = Heat capacity ratio.

1. Introduction

The boundary layer formation near solid contours is an essential issue in computational fluid dynamic (CFD) simulation. In these regions, flow velocity and turbulence quantities vary abruptly in a nonlinear way from zero on the wall surface (as imposed by the no-slip condition) to their respective equilibrium freestream values, far away from the wall (Farzaneh-Gord *et al.*, 2018). The performance of some systems depends on the velocity profile of the flow close to the wall and wall shear stress arising from fluid viscosity and turbulence, which play a very important role in this regard (Azimy and Saffarian, 2023; Rusin *et al.*, 2018; Schosser *et al.*, 2014). Concerning the near wall region, two ways are usually recommended in Reynolds-averaged Navier–Stokes (RANS) approach. The first method is to calculate the turbulent viscosity in this region. Turbulence models are modified to resolve the turbulent parameters in the whole region, including the inner part of the boundary layer and the area with intense changes in the turbulent viscosity. This approach, however, requires fine mesh in these regions, which entails high computational costs. The second approach is to employ wall functions, which can model the near-wall region. Wall functions are meant to circumvent the excessive grid requirements. They come from analytical solutions used to satisfy the physics of the flow in the near-wall region (Zhang *et al.*, 2022) and to ensure the most accurate results; usually, the first cell center needs to be in the log-law region (Suga *et al.*, 2006). Wall functions bridge the inner region between the wall and the fully turbulent part of the flow regime to calculate momentum and turbulence transport equations close to the wall rather than specifying them on the wall (Chedevergne, 2018).

Rough-wall turbulent boundary layer flow is a complex physical phenomenon that increases the skin friction drag as compared to the smooth wall case (Bezaatpour *et al.*, 2022; Lalegani *et al.*, 2018; Suastika *et al.*, 2021). It can significantly affect the fluid dynamics and heat transfer in flows by introducing perturbations in the flow, which lead to changes in the mean velocity profile in the boundary layer (Sun *et al.*, 2011). The viscous sublayer is replaced by the roughness sublayer, which enhances surface drag, pressure drop, turbulent mixing, momentum transfer and heat transfer (Kadivar *et al.*, 2021). Roughness occurs as a result of the normal exploitation of products, as an effect of erosion, icing or deposition or during manufacturing. Roughness is characterized by a set of parameters that can be determined during the manufacturing process (Orlandi and Leonardi, 2009).

According to Nikuradse's (1933) measurements of the pressure drop in the pipe, the mean velocity profile in the log-law region for both smooth and rough cases is expressed as follows:

$$U^+ = \frac{1}{\kappa}\ln\left(y^+\right) + C - \Delta U^+ \tag{1}$$

$$U^+ = \frac{U}{u_\tau} \tag{2}$$

$$y^+ = \frac{u_\tau y}{\nu} \tag{3}$$

where U represents the mean velocity, u_τ is the skin friction velocity (defined as $u_\tau = \frac{\tau_w}{\rho}$, where τ_w and ρ are the total wall stress and fluid density, respectively), y is the normal distance to the wall and ν is the kinematic viscosity. C and κ are the smooth-wall interception and the von Karman constant, respectively. There is still a debate about their values. However, all the proposed values differ by less than 3%. In our study, these values were assumed to be 5.1 and 0.41, respectively. ΔU^+ represents the roughness function.

The ΔU^+ term is the roughness effect on the velocity profile related to dimensionless equivalent sand-grain height. The velocity shift is adopted in the standard Law-of-the-Wall Modified for Roughness model (LWMR model). In Grigson's (1992) study, the roughness function based on the experimental investigation of Colebrook's (1939) data, is defined as:

$$\Delta U^+ = \frac{1}{\kappa}\ln\left(1 + \frac{k_s^+}{\exp(3.25\kappa)}\right) \tag{4}$$

$$k_s^+ = \frac{k_s u_\tau}{\nu} \tag{5}$$

where k_s represents the sand-grain roughness height.

Also, in Nikuradse's study, the velocity profile U^+ is directly linked to dimensionless roughness k_s^+ through formula:

$$U^+ = \frac{1}{\kappa} ln \frac{y^+}{k_s^+} + B \tag{6}$$

where B is calculated depending on the range of sand grain roughness:

$$\begin{array}{ll} 1 < k_s^+ < 3.5 & B = 5.5 + \frac{1}{\kappa} lnk_s^+ \\ 3.5 < k_s^+ < 7 & B = 6.59 + 1.52 lnk_s^+ \\ 7 < k_s^+ < 14 & B = 9.58 \\ 14 < k_s^+ < 68 & B = 11.5 - 0.7 lnk_s^+ \\ 68 < k_s^+ & B = 8.48 \end{array} \tag{7}$$

Also, Cebeci and Bradshaw (1977) presented a correlation to estimate the downward shift of the velocity profile due to roughness in the form:

$$\Delta U^+ = \begin{cases} 0, & k_s^+ \le k_{s\,smooth}^+ \\ \frac{1}{\kappa} ln \left[A \left(\frac{k_s^+ / k_{s\,smooth}^+}{k_{s\,rough}^+ - k_{s\,smooth}^+} \right) + C_s k_s^+ \right]^a, & k_{s\,smooth}^+ < k_s^+ \le k_{s\,rough}^+ \\ \frac{1}{\kappa} ln\left(A + C_s k_s^+\right), & k_s^+ > k_{s\,rough}^+ \end{cases} \tag{8}$$

in which the power a is given as:

$$a = sin\left[\frac{\pi}{2}\frac{log\left(k_s^+ / k_{s\,smooth}^+\right)}{log\left(k_{s\,rough}^+ / k_{s\,smooth}^+\right)}\right] \tag{9}$$

with A = 0, $k_{s\,smooth}^+ = 2.25$, $k_{s\,rough}^+ = 90.00$ and $C_s = 0.253$.

To implement roughness, the presented wall functions require the y^+ to be in the logarithmic region, which can be a severe constraint and will mainly be violated by the grid. When the first element is not located in a log-law area of the flow regime, the downward shift of the velocity profile due to the roughness causes a negative value of U^+. Considering the smooth surface, wall functions that do not restrict the location of the first grid point between the wall and the logarithmic layer are called adaptive wall functions, which are unable to calculate the roughness effect on the flow profile. Knopp *et al.* (2006) presented recently a grid and flow adaptive wall-function method for RANS turbulence modeling with emphasis on aerodynamic flows, and Kalitzin *et al.* (2005) addressed some of the existing adaptive wall functions' shortcomings and aim to develop an efficient and robust approach that can be applied to various turbulence models. Considering the rough surface, when the first cell is in the inner parts of the boundary layer, like the viscose sublayer, the combination of turbulence models decreases the computational costs, in the inner parts of the boundary layer and the region close to the wall with tenser changes in turbulent viscosity, this parameter will be calculated using denser mesh, and for the region in the far field, wall-function will be used which needs a coarser mesh.

Determination of wall shear stress for different geometries and generated meshes has always been an important issue, especially in turbomachinery. Additionally, the selection of the method, which includes surface roughness, has always been challenging. One of the most famous resources for calculating the friction factor is the Moody (1944) diagram. It represents one of the most well-known used resources, relating three-factor of Darcy friction factors, Reynolds number and relative roughness. It correlates with extensive experimental data obtained by Nikuradse for the pipe flow with surfaces roughened by coating the internal surfaces with sand grains. Several researchers have recognized the shortcomings of using measured surface roughness parameters in conjunction with the Moody diagram. Kandlikar *et al.* (2005) worked on relative roughness (up to 14%) encountered in microchannels. They replotted the Moody chart, considering the idea of a constricted flow diameter. Chedevergne and Aupoix (2017) developed a wall function to complement $k - \omega$ turbulence model involving roughness correction. In another investigation, Chedevergne and Forooghi (2020) proposed a new model to calculate the roughness effects on flow behavior in the channel, considering the mixing length model. Considering very narrow sections for fluid flow, like flow through micro channels or the mini gap between corotating disks, makes the flow analysis challenging. Flow through corotating disks has applications in various industries, such as in Tesla turbomachinery (Tesla, 1913), combined heat and power or organic Rankine cycle-based (ORC) systems (Moradi *et al.*, 2020; Usman *et al.*, 2020). The prediction of power generation in the Tesla turbine is highly affected by boundary layer discretization (Rusin *et al.*, 2021a, 2021b).

The aforementioned methods of accounting for roughness effects rarely have been applied to flows like in the Tesla turbine and, therefore, are not calibrated properly to their complexity. Small gap size (in the range of 1 μm–1mm) and the interaction of the boundary

layers formed at the opposite disk surfaces prevents the boundary layer profile from full development. Moreover, high body forces arising from the rotational movement and large curvature of the streamlines are issues impacting the estimation of eddy viscosity even in the case of smooth surfaces and are another problem to deal with in the roughness methods. For these reasons, the main aim of the presented study is to assess the validity of the approaches used for accounting for roughness in a flow between corotating disks.

These studies started with the simple domain and progressed to more complex ones, considering mesh quality, turbulence model and roughness approach to finally select the most accurate way to simulate flow between corotating disks. The roughness approach, implemented in the numerical model, was validated on the experimental data and DNS results reported in the literature for standard configurations. Velocity profiles were modeled and studied in both the channel flow and the flow in the gap between corotating disks. In all cases, the effect of roughness on wall-shear stresses was included and related to the available reference data. Roughness is a primary parameter that promises to increase the torque on the disk shaft.

2. Mathematical model

The purpose of the study is to investigate the roughness effect on the flow between corotating disks. To approach this aim, various three-dimensional cases, turbulence models and roughness models are investigated.

The numerical simulation is done using Ansys Fluent software, which makes use of the finite volume method to solve discretized RANS equations. The governing equations involve continuity, momentum, energy conservation and ideal gas law in the form:

$$\frac{\partial \rho}{\partial t} + \frac{\partial}{\partial x_i}(\rho U_i) = 0 \tag{10}$$

$$\frac{\partial (\rho U_i)}{\partial t} + \frac{\partial}{\partial x_j}\left(\rho U_j U_i\right) = -\frac{\partial p}{\partial x_i} + \frac{\partial \tau_{ji}}{\partial x_j} + \rho f_i \tag{11}$$

$$\begin{aligned} &\frac{\partial \left(\rho\left(e + \frac{1}{2} U_j U_j\right)\right)}{\partial t} + \frac{\partial}{\partial x_i}\left(\rho U_i\left(e + \frac{1}{2} U_j U_j\right)\right) \\ &\quad = -\frac{\partial}{\partial x_i}(p U_i) + \frac{\partial}{\partial x_i}\left(\tau_{ij} U_j\right) - \frac{\partial}{\partial x_i}(q_i) + \rho f_i U_i \end{aligned} \tag{12}$$

where t is time, τ is the wall shear stress, e, p, q and f are the internal energy, pressure, heat flux and gravity force.

Turbulent stresses τ_{ij} are modeled using the Boussinesq hypothesis, assuming a stochastic turbulence model for turbulent viscosity determination. Three two-equation turbulence models are adopted in the analyses to calculate the turbulent viscosity $k - \omega$ with shear stress transport ($k - \omega$ *SST*), $k - \varepsilon$ with standard wall function ($k - \varepsilon$ *SWF*) and $k - \varepsilon$ with enhanced wall treatment ($k - \varepsilon$ *EWT*). The $k - \omega$ *SST* turbulence model calculates the turbulent kinetic energy (k) and specific dissipation rate (ω) in the whole region, which makes this model able to resolve the inner parts of the boundary layer down to the wall and blend with the $k - \varepsilon$ model in the free stream. The possibility of employment of the $k - \omega$ *SST*, $k - \varepsilon$ *SWF* and $k - \varepsilon$ *EWT* models in different cases is studied.

the plate edge $X = 0$. Figure 1(b) presents the velocity profile for $Re_X = 0.762 \times 10^7$. The obtained results from the $k - \omega\ SST$ and $k - \varepsilon\ EWT$ models represent compatibility with the experimental data. For the M1 mesh, the value of y^+ is not in the range recommended for the $k - \varepsilon\ SWF$ model; therefore, an unphysical downward shift in the velocity profile is observed. Wall shear stress was overestimated, resulting in higher values of both: friction velocity and friction coefficient.

Figure 2 shows the results from the $M2$ mesh. The $k - \varepsilon\ SWF$ operates acceptably for meshes with the values of y^+ located in the log-law region, while $k - \varepsilon EWF$ and $k - \omega\ SST$ perform well in the whole range of y^+.

The $k - \varepsilon\ EWT$ model uses equation (16) as a single wall law in the whole domain, so this model in the studied mesh distributions performs well on different meshes, and the calculated eddy viscosity is not affected by the grid spacing.

3.2 Zero-pressure-gradient flow over a rough plate

Hosni *et al.*(1993) studied the flow over a rough plate with hemispheric roughness elements, which have been mounted in staggered rows. The distance L between the elements is $L = 2D$ with $D = 1.27\,mm$, the diameter of hemispheres. The free stream velocity retained for computations is $U = 58.2 m/s$. The size of the computational domain remains the same as in the case described in the previous section, and the same types of boundary conditions are applied. $k - \varepsilon EWT$ is unable to simulate roughness, then the $k - \omega\ SST$ and $k - \varepsilon\ SWF$ models are applied in this part. Roughness is simulated using both Aupoix's and velocity profile downward shift methods. As Aupoix's approach needs a fine mesh close to the wall, it can be implemented on the $M1$ mesh. Figure 3(b) presents the velocity profile at a $1.68\,m$ distance from the starting point of the surface, which corresponds to $Re_X = 0.666 \times 10^7$ calculated on $M1$ mesh. Additionally, experimental data are presented with the y^+ and $y^+ - \Delta y^+$values, in which the Δy^+ is the artificial origin of the wall distances for roughness elements placed over the flat plate. The shift indicates that within the roughness layer, there is no fluid flow.

Figure 3 compares the performance of $k - \varepsilon\ SWF$, $k - \omega\ SST$ models and experimental data. Considering $k - \varepsilon\ SWF$ model with a roughness approach, when the height of the roughness is higher than the height of the first element, the model numerically relocates the first element, following equation (21) to cover the roughness:

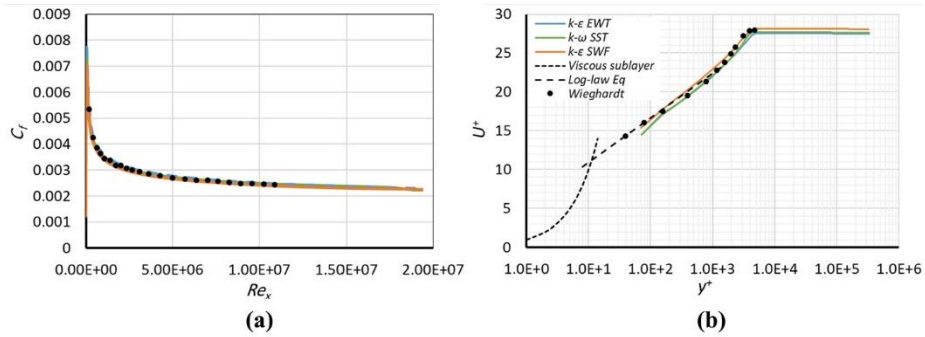

Notes: (a) The distribution of friction coefficient vs Re_X; (b) velocity profile for $Re_X = 0.76206 \times 10^7$

Source: Figure by authors

Figure 2. Comparison of simulation results of flow over a smooth flat plate (mesh $M2$) and experimental data (Wieghardt and Tillmann, 1944)

$$y^+_{new} = y^+_{old} + \frac{k^+_s}{2} \tag{21}$$

Hence, the roughness element will be immersed within the first mesh cell, and the y^+ will be in the recommended range for this model.

As can be seen in Figure 3, the relocation of the first element caused the y^+_{new} to be in the recommended range for $k-\varepsilon$ *SWF* then the results are in good agreement with experiments.

The friction coefficient distributions were similar in all investigated models and generally in good agreement with the experimental data. The lowest friction coefficient values were observed in the case of Aupoix's method, and the highest values were obtained for $k-\varepsilon$ *SWF* model with the velocity profile shift. The differences, however, vary by the distance from the wall and reach a maximum of 10% in the fully turbulent part of the flow regime. In Aupoix's method, the lowest wall shear stresses are determined, and therefore, the friction coefficient is the lowest, and the downward shift of the dimensionless velocity profile is the smallest. The agreement between the results proves the appropriate accuracy of both $k-\varepsilon$ *SWF* and $k-\omega$ *SST* turbulence models with implemented roughness approach in this elementary benchmark. Aupoix's approach needs a fine grid to perform well, and from Figure 3, it can be seen for lower values of y^+ in the viscous sublayer down to the wall, the velocity approaches zero, which satisfies the no-slip wall condition.

The development of the boundary layer is presented in Figure 4. The velocity profile is plotted at the distance of 0.186 m, 0.372 m, 0.56 m, 1.12 m and 1.68 m from the edge of the rough plate, which corresponds to Re_X equal to 0.73×10^6, 0.14×10^7, 0.221×10^7, 0.442×10^7 and 0.666×10^7.

Closer to the beginning of the rough surface, the boundary layer is not fully developed, then the thickness of the boundary layer is smaller. In this area, because of the high-velocity gradient close to the wall surface, the wall shear stress and the friction velocity are higher, which causes a downward shift of the velocity profile. Proceeding from the leading edge, changes in the maximum value of U^+ are smaller, indicating a developed boundary layer. In the furthermost chosen point of 1.68 m, studied by Hosni, the boundary layer is well developed.

3.3 Kandlikar et al. experiments for minichannel flow

The investigation of the flow through a minichannel begins with the validation of numerical results with the experimental results of Kandlikar *et al.* (2005). They studied a flow through

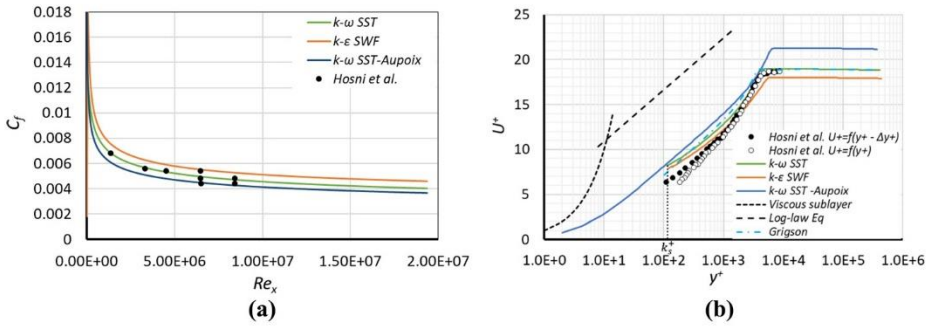

Figure 3.
Comparison of simulation results of flow over a rough flat plate (mesh *M*1) and experimental data (Hosni *et al.*, 1993)

Notes: (a) The distribution of friction coefficient vs Re_X; (b) velocity profile for $Re_X = 0.666 \times 10^7$

Source: Figure by authors

smooth and rough channels with 10.03 mm width (w), 100 mm length (l) and 0.5 mm height (h) in different velocities. The Fanning friction factor f was estimated for different Re numbers and compared with the results of the theoretical formula for both smooth and rough cases. In the study of Kandlikar *et al.* (2005), the theoretical Fanning friction factor for laminar flow was obtained from:

$$f = \frac{C}{Re} \tag{22}$$

where the constant C depends on the aspect ratio of the channel $\alpha^* = \frac{h}{w}$, with h and w being the dimensions of a rectangular channel:

$$C = 24\left(1 - 1.3553\alpha^* + 1.9467\alpha^{*2} - 1.7012\alpha^{*3} + 0.9564\alpha^{*4} - 0.2537\alpha^{*5}\right) \tag{23}$$

The Swamee and Jain (1976) approximation is used to solve the Fanning friction factor in the turbulent regime:

$$f = 0.0625\left[ln\left(\frac{\frac{k}{D_h}}{3.7} + \frac{5.74}{Re^{0.9}}\right)\right]^{-2} \tag{24}$$

The hydraulic diameter D_h is estimated for the rough case based on both actual and constricted heights. The constricted height of the channel is h_{cf} calculated following the relation:

$$hc_f = h - 2k \tag{25}$$

where the h_{cf} is the constricted channel height, h is the channel height and k represents the average roughness height which is equal to 72.9 μm.

Figure 5 demonstrates the tooth shape roughness and the distribution of them on the up and bottom surfaces of the channel studied by Kandlikar *et al.* (2005). To calculate the equivalent sand-grain roughness k_s, there are different proposals in the literature. Two

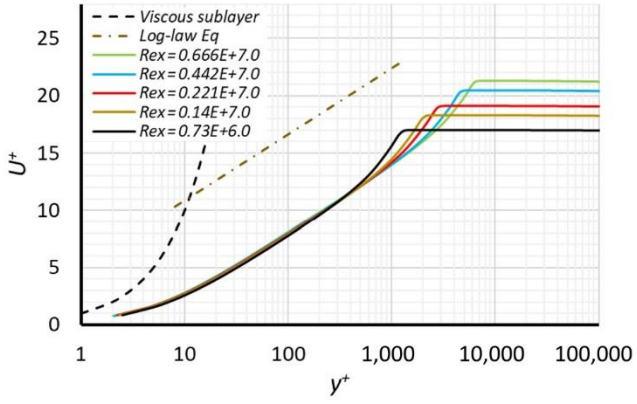

Source: Figure by authors

Figure 4.
Dimensionless velocity profile of flow over a rough flat plate (mesh $M1$) obtained from $k-\omega$ SST and Aupoix's model in five different locations

estimations are used in this regard proposed by Stimpson *et al.* (2017) [equation (26)] and Sigal and Danberg (2012) [equation (27)]:

$$\frac{k_s}{D_h} = 18\left(\frac{R_a}{D_h}\right) - 0.05 \tag{26}$$

$$\frac{k_s}{r} = \left\{0.00321\Lambda_s^{4.925}, 1.4 \le \Lambda_s \le 4.89\,8, 4.89 \le \Lambda_s \le 13.25\ 151.711\Lambda_s^{-1.1379}, 13.25 \le \Lambda_s \le 100\right\} \tag{27}$$

$$\Lambda_s = \left(\frac{S}{S_f}\right)\left(\frac{A_f}{A_s}\right)^{-1.6} \tag{28}$$

where R_a is the arithmetic mean deviation of the roughness profile, A_f is the ratio of the frontal area of a single roughness element, A_s is the windward wetted surface area of the single roughness element, S is the reference surface area before the addition of roughness and S_f is the total frontal area of the roughness. Considering the value of R_a, which was equal to 17 μm and other roughness parameters, equations (26) and (27) correspond to the equivalent sand-grain roughness of $k_s = 271\ \mu m$ and $k_s = 350\ \mu m$.

In the CFD simulation, the computational domain is divided into two parts of the same size. Each part has 10.03 mm in width (w), 200 mm in length (l) and 0.5 mm in height (h). The first part of the domain is made with no-slip walls to have a developed velocity profile at the inlet of the second part. In the second part of the domain, the top and bottom walls are rough, and the side walls with the no-slip condition are assumed. A fine mesh with 1 M nodes and a maximum value of y^+ less than one is generated. The $k - \omega\ SST$ turbulence model and Aupoix's approach are employed. Figure 6 presents a comparison of the experimental data, numerical results and results from empirical formulas for laminar and turbulent friction factors for both smooth and rough channels. In the rough channel, the results of numerical simulation for both $k_s = 271\ \mu m$ and $k_s = 350\ \mu m$ are plotted.

Considering the smooth channel, the results of the CFD simulations are in good agreement with the theory and experiment for the laminar flow and slightly overestimate the friction

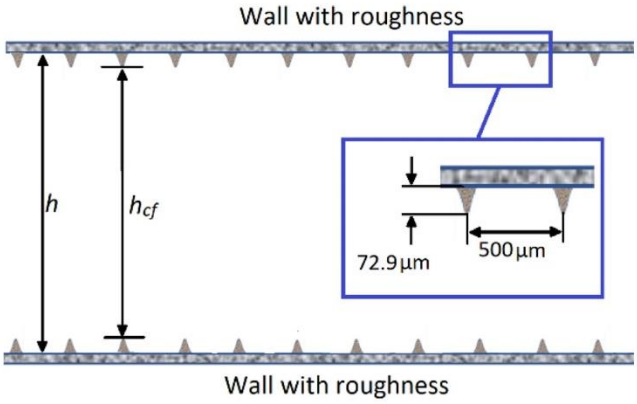

Figure 5.
Scheme of minichannel and roughness shape according to the experiment of Kandlikar *et al.* (2005)

Source: Figure by authors

factor in the turbulent part. The numerically obtained curve deviates from the straight line earlier and gives a discrepancy against experimental data for $Re = 3{,}500$ of about 0.04. The right plot is presenting the Fanning friction factor as a function of the Reynolds number for rough cases. The theoretical estimation of friction factor in a turbulent regime is based on $k = 72.9\ \mu m$ and the actual dimensions of the channel. The considerable discrepancy between the experimental friction factor obtained by Kandlikar *et al.* (2005) and theoretical estimations in laminar and turbulent flow regimes demonstrates the importance of roughness geometry on the generated friction factor. The geometry of height used tooth shape roughness affects the flow characteristic. For this reason, they also presented the friction factor based on constricted hydraulic diameter and flow parameters, which, in this case, better agreement with theory is obtained. Considering the results of numerical simulation, the effect of an increase in sand-grain roughness's height is more visible in a turbulent regime. In laminar flow, roughness does not have a considerable effect on the friction factor, as the obtained value from both 271 μm and 350 μm sand-grain roughness are almost the same, and in good agreement with the theory. The discrepancy between the theory and the experimental results in the turbulent part was explained by an inaccurate representation of the roughness parameters for the assumed roughness shape in the experiment. The geometrical configuration of roughness investigated in the experiment can be classified as the intermediate type of roughness between the d-type and k-type roughness suggested by Perry *et al.* (1969). This intermediate type of roughness may not behave as the random three-dimensional roughness assumed in both theoretical and numerical models. Comparing the constricted friction factor presented in Kandlikar *et al.* (2005) with Figure 6, a better agreement is seen with the higher sand-grain roughness value.

3.4 Yuan and Piomelli direct numerical simulations for minichannel flow

An open-channel flow was calculated, using the direct numerical simulations (DNS), by Yuan and Piomelli (2014). The domain with dimensions of $6\,h \times 1\,h \times 3\,h$ in x-, y- and z-directions, respectively, is considered (Figure 7). No-slip and symmetry boundary conditions are applied to the bottom and top walls, respectively. The symmetry at the top wall makes the flow similar to the one between two parallel plates. Periodic boundary conditions are used on side walls. To drive the flow, a constant pressure gradient was assumed between front and back surfaces, and to achieve this aim, cyclic transfer of parameters from the outlet to the inlet till convergence is used. A high-roughness with $\frac{k_s}{h} = 0.07$ is used to simulate fully rough flow, and the results are presented in a constant value of friction

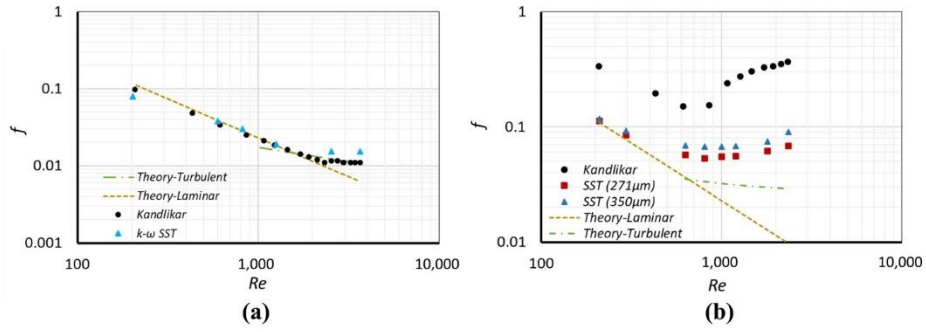

Source: Figure by authors

Figure 6.
Comparison of the results of CFD simulations with experimental data (Kandlikar *et al.*, 2005) and theoretical formulas for laminar and turbulent flows as a function of *Re* (a) for smooth minichannel and (b) for rough minichannel

Reynolds number $Re_\tau = \frac{\rho u_\tau D_h}{\mu}$ equal to 1,000, where u_τ represents friction velocity and D_h is the hydraulic diameter. The $k - \omega\ SST$ model is used to simulate the smooth minichannel flow. Moreover, for the rough case, the $k - \varepsilon\ SWF$ model and $k - \omega\ SST$ model with Aupoix's approach are used. Preserving the relative dimensions as given in by Yuan and Piomelli (2014) and assuming the height of the channel (2 h) is equal to 1 mm; the domain dimensions are $3 \times 0.5 \times 1.5$ mm with $35\,\mu m$ height of the roughness and the same boundary conditions as in the DNS simulation are used.

Using the $k - \varepsilon\ SWF$ turbulence model, the first layer of mesh is relocated according to equation (21) to secure an appropriate near-wall distance. Both smooth and rough simulations are done using a fine mesh with 1 million nodes, and the y^+ in the range of 0.293 and 0.296 using periodic boundary conditions achieves almost constant parameters in the whole domain.

Figure 8 compares the DNS simulation of both smooth and rough cases, with the log-law equation, and the downward shift of the mean velocity profile according to equation (4). Theorical downward shift of the velocity profile is calculated considering the height of the roughness and obtained friction velocity from the simulation which is in perfect agreement with DNS simulation of the rough case. The velocity profile is defined in the middle of the domain. Moreover, a comparison between different used turbulence models and DNS simulation is presented. In both utilized turbulence models, the calculated k_s^+ based on friction velocity and height of the roughness is equal to 72, which is the proposed number in literature. In both smooth and rough cases, the results of numerical simulation and DNS of Yuan and Piomelli are in good agreement. The first element of mesh in $k - \varepsilon\ SWF$ turbulence model is relocated then the obtained y^+ is appropriate for this model. The maximum value of U^+ and the friction velocity obtained from both used models are the same; still, the relocation of the mesh network makes this model unable to calculate flow characteristics in the near wall area. With the benefit of fine mesh in the laminar part of the flow regime, $k - \omega\ SST$ can resolve flow properties in inner parts of the boundary layer with the accepted accuracy.

4. Flow between corotating disks

The flow in the gap between two corotating discs is the standard basic configuration which is analyzed intensively to discover the flow structures and flow-discs interaction as essential phenomena for the Tesla turbine performance. The gap size, rotational speed and roughness

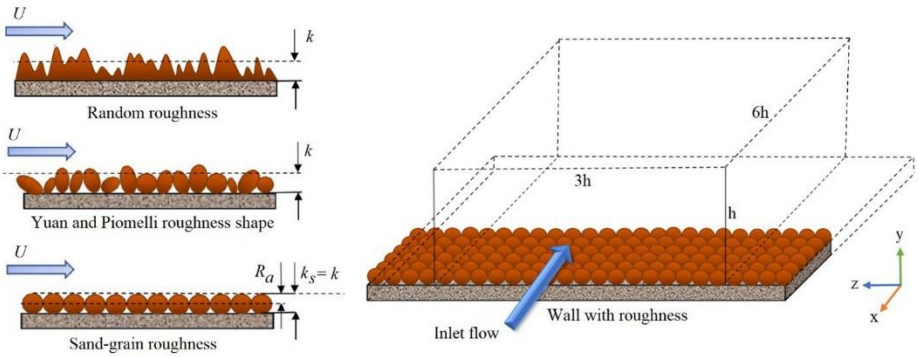

Figure 7.
Schematic of the minichannel and sand-grain roughness

Source: Figure by authors

are vital in shaping the flow structure between discs. The systematic study of Aupoix's method performance with different parameters is presented in the following sections.

4.1 Gap sizes study

The gap size between the rotational disks of the Tesla turbine has to be small enough, and therefore, the channel between discs is of minichannel type. In this study, the effect of gap size reduction on the velocity profile for both smooth and rough cases is investigated. The inner and outer diameters of the corotating disks are 0.04 m and 0.1 m, respectively, and three gap sizes equal to 15 mm, 7.5 mm and 0.75 mm are chosen for the study. Figure 9 depicts the scheme of the computational domain. Flow in half of the gap is simulated, owing to the domain being concise to a rotating disk surface on one side and a symmetry boundary on the other side. The velocity at the inlet and static pressure at the outlet is defined.

In the first step, the case was defined in such a way that the same value of $Re_\tau = 1{,}000$, as in the DNS benchmark study, could be reproduced inside the gap equal to 0.75 mm. To achieve this aim, the simulation is done considering the water as the working medium. Radial and tangential velocity at the inlet is set equal to 2 m/s and 15.25 m/s, respectively, and rotational speed is set to 500 rev/min. To make possible a comparison of roughness effects on the velocity profile, the same roughness height of 3.5% of the gap size is considered, which is relatively high. The $k - \omega$ *SST* model with Aupoix's approach of roughness was employed on the mesh with 386,630 nodes for a 0.75 mm gap which increased up to 1.7 million nodes for a 15 mm gap size. The maximum value of y^+ was less than one (Yuan and Piomelli, 2014).

In Figure 10, the simulation results are compared to theoretical estimations of smooth and rough cases. In all cases, the dimensionless velocity profile is plotted always at the location in the middle of the disk. The obtained Re_τ for the smallest gap size is equal to 1,028 and for bigger gaps, as the friction velocity and hydraulic diameter are bigger, Re_τ increases. The rise in mentioned variables causes a stronger downward shift of the velocity profile. In 0.75 mm gap size, the turbulent region is reduced strongly in this type of channel flow. The transitional region goes into the bulk region almost immediately. In Figure 10, the rough cases are depicted compared to equation (4). Generally, the tendency that the dimensional

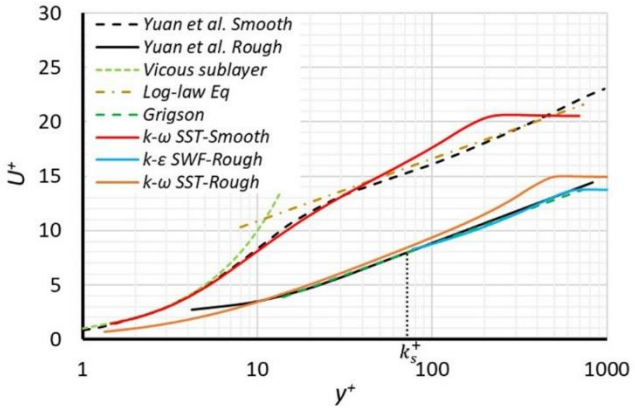

Source: Figure by authors

Figure 8.
Comparison of the dimensionless velocity profiles from DNS simulation (Yuan and Piomelli, 2014) with the log-law equation (smooth), Grigson formula (rough) and the present CFD simulations

The standard wall function is based on Launder and Spalding's (1974) work, where the velocity profile close to the wall is calculated using the following formula:

$$U^* = \frac{1}{\kappa}\ln(Ey^*) \tag{13}$$

$$U^* = \frac{U_p c_\mu^{0.25} k_P^{0.5}}{u_\tau^2} \tag{14}$$

$$y^* = \frac{\rho c_\mu^{0.25} k_P^{0.5} y_P}{\mu} \tag{15}$$

where E represents the empirical constant equal to 9.793, U_p and k_P are the mean velocity of the fluid and turbulence kinetic energy at the near-wall node P, respectively, y_P is the distance from point P to the wall and μ represents the dynamic viscosity of the fluid.

The enhanced wall treatment in the $k-\varepsilon EWT$ model formulates the law-of-the wall as a single wall law for the entire wall region suggested by Kader (1981):

$$U^+ = e^{\Gamma} U^+_{lam} + e^{\frac{1}{\Gamma}} U^+_{turb} \tag{16}$$

where the blending function is given by:

$$\Gamma = -\frac{a(y^+)^4}{1+by^+} \tag{17}$$

where $a = 0.01$ and $b = 5$.

The effect of roughness shape highlighted the need for investigation of different roughness methods. In this regard, the LWMR model described in the Introduction and Aupoix's (2015) approach are investigated. Although the LWMR model can be applied on meshes with a high enough value of y^+, Aupoix's approach needs a fine mesh with y^+ smaller than one. Therefore, the computational cost is higher compared to other methods (Radenac, 2016; Trontin *et al.*, 2017; Villedieu *et al.*, 2014).

Aupoix's approach is based on k and ω modification on the wall. This method of considering the roughness modifies the turbulent kinetic energy k and specific dissipation rate ω on the wall, so the turbulent properties will be calculated based on the correction on the wall. The modified turbulent parameters on the wall are calculated from the relations:

$$k_w^+ = \max\left(0; k_0^+\right) \tag{18}$$

$$k_0^+ = \frac{1}{\sqrt{\beta^*}} tanh\left[\left(\frac{ln\frac{k_s^+}{30}}{ln10} + 1 - tanh\frac{k_s^+}{125}\right) tanh\frac{k_s^+}{125}\right] \tag{19}$$

$$\omega_w^+ = \frac{300}{k_s^{+2}}\left(tanh\frac{15}{4k_s^+}\right)^{-1} + \frac{191}{k_s^+}\left(1 - exp\left(-\frac{k_s^+}{250}\right)\right) \tag{20}$$

in which k_w^+ and ω_w^+ are values on the wall, respectively, and the constant β^* is equal to 0.09.

3. Preliminary test cases

Due to the lack of data to validate the flow in the minichannel with rotating rough walls, the approach to deal with this problem needs to be selected after a systematic study of well-reported standard test cases. Therefore, the preliminary study covers both the case of a zero-pressure-gradient boundary layer in the flow over a flat plate and the flow through minichannels with stationary walls where the walls are smooth or rough.

3.1 Zero-pressure-gradient flow over a smooth plate

At the beginning, the standard zero-pressure-gradient flow over a smooth plate is studied. The flow data was adopted from experimental studies (Wieghardt and Tillmann, 1944). The Mach 0.2 flow under ambient conditions was examined.

The flow is simulated in the domain with 530 cm length and 200 cm height. The top and side boundaries are considered pressure far-field and symmetry. The bottom surface of the calculation domain is divided into two parts. The first part, 30 cm long, is a free-slip wall, and the second part, 5 m in length, starting at the coordinate $X = 0$, is a switch with a no-slip condition where the boundary layer begins to develop.

Two meshes with different first element sizes are generated to study the performance of various turbulence models and the impact of mesh quality on the accuracy of the results. Meshes are orthogonal and have 500 nodes along the x-axis, and 114 nodes along the y-axis, with four layers in the z-direction. The meshes are generated with different distributions in a near-wall region. Mesh $M1$ with the 250 k nodes and the value of $y^+ = 1$ was the finer mesh with the first element located in the viscous sublayer, and $M2$ has a coarser mesh in the near wall region, and the first element in a log-law part of the velocity profile ($y^+ = 35$).

Three turbulence models, $k - \omega\, SST$, $k - \varepsilon\, SWF$ and $k - \varepsilon\, EWT$, are selected to account for the turbulent stresses. It is recommended for the $k - \omega\, SST$ model to be applied on the fine mesh with the value of y^+ equal to or smaller than one to ensure that the flow in the low-Reynolds region can be resolved accurately. Also, the $k - \varepsilon\, SWF$ model should be used on meshes with the first element in the log-low region so the turbulent parameters and eddy viscosity are estimated based on a standard boundary layer profile. For the $k - \varepsilon\, EWT$ model, no such restriction exists, and the first grid node can be in a viscous sublayer or a log-law region.

Figure 1 presents the results for the $M1$ mesh. Figure 1(a) depicts the friction coefficient distributions as a function of the Reynolds number $Re_X = \frac{\rho U_\infty X}{\mu}$ defined as a distance from

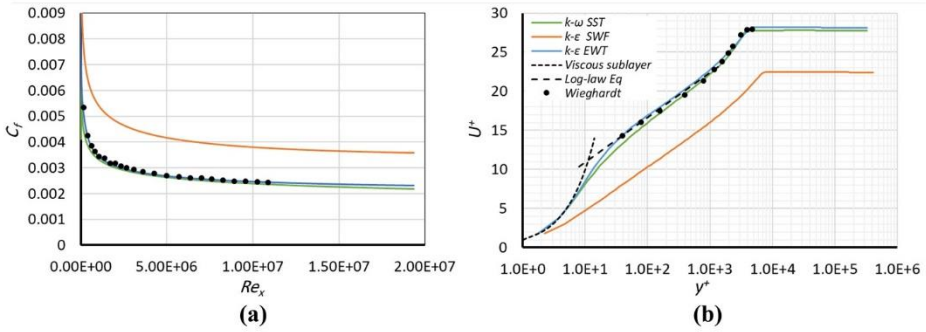

Figure 1.
Comparison of simulation results of flow over a smooth flat plate (mesh $M1$) and experimental data (Wieghardt and Tillmann, 1944)

Notes: (a) The distribution of friction coefficient vs Re_X; (b) velocity profile for $Re_X = 0.76206 \times 10^7$

Source: Figure by authors

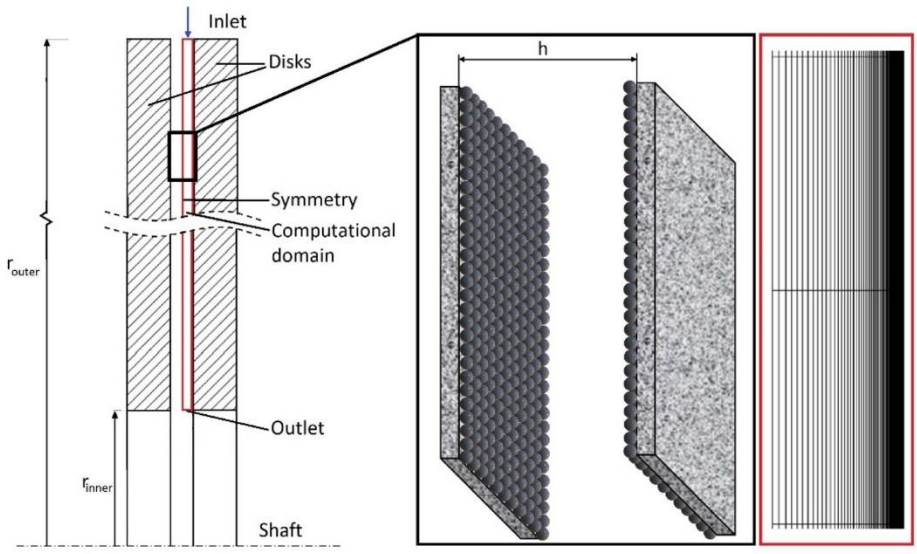

Figure 9.
Sketch of the computational domain in the gap between the discs and a schematic of the generated mesh

Source: Figure by authors

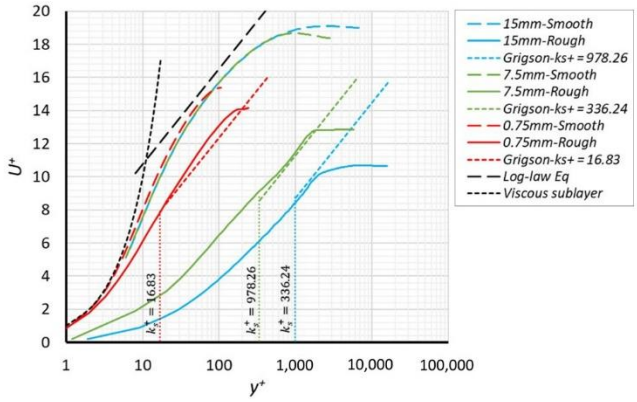

Figure 10.
Calculated dimensionless velocity profiles of flow between corotating disks with different gap sizes considering 2 m/s and 15.25 m/s as the radial and tangential velocities, respectively, and roughness equal to 3.5% of the gap size

Source: Figure by authors

velocity profile is shifted down is preserved, and the value of this shift is similar to that which results from the theoretical lines.

The effect of the reduction in gap size is visible in Figure 10. By reducing in gap size, the region of the core flow, represented by the horizontal part of the profile, becomes shorter. In the case of the 0.75 mm gap size, the standard core flow vanishes.

In the second step, the air is used as the operating fluid. Simulations are done for the same three gap sizes. The rotational speed of 17,500 rev/min was assumed, which is in the range of optimal values of the Tesla turbine studied by Rusin *et al.* (2018). Both smooth and rough surfaces are considered, and the roughness equal to 3.5% of the gap size was assumed as in the

previous cases. The tangential velocity at the inlet is equal to 100 m/s, and the investigation is done for radial velocities equal to 2 m/s, 3 m/s and 5 m/s in an inward direction.

To demonstrate the effect of reduction in gap size on velocity formation in the computational domain, the wall shear stress contours are presented in Figure 11. The assumed radial velocity was equal to 5 m/s.

Figure 11 illustrates the importance of gap size on generated wall shear stress and consequently on the Re_τ. This value varies from inlet to outlet; for a 15 mm gap $Re_\tau = 1{,}000$–38,672, for a 7.5 mm gap $Re_\tau = 950$–16,497 and for 0.75 mm $Re_\tau = 148$–507. The reduction in gap size reduces the wall shear stress intensively. The maximum value of wall shear stress in all cases is obtained in the area close to the outlet where the most developed turbulent flow is present. The minimum values are close to the inlet.

In the cases with a gap size equal to 15 mm and 7.5 mm, similar and higher values of Re_τ were obtained, compared to the values from the DNS benchmark, but in the case of 0.75 mm gap size, the Re_τ is significantly lower. Figure 12 demonstrates the velocity profile at the mid-radius for the 7.5 mm gap domain. In Figure 12, radial velocities equal to 2 m/s and 3 m/s are investigated to demonstrate the effect of mass flow rate on the downward shift of the velocity

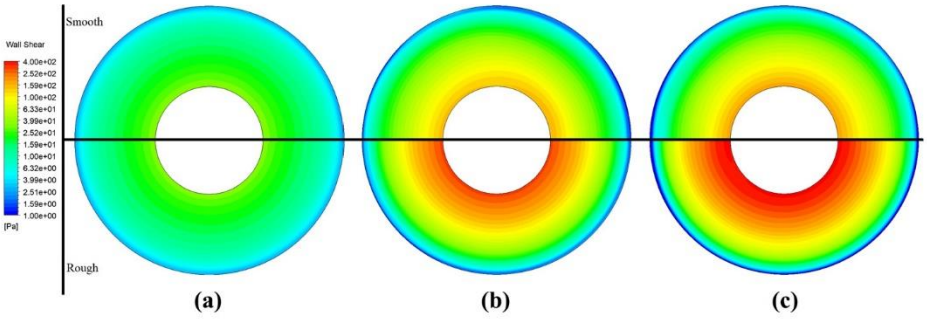

Source: Figure by authors

Figure 11.
Wall shear stress of smooth and rough case with roughness equal to 3.5% of gap size for gap sizes equal to (a) 0.75 mm, (b) 7.5 mm and (c) 15 mm, considering the tangential and radial velocity of 100 m/s and 5 m/s, respectively

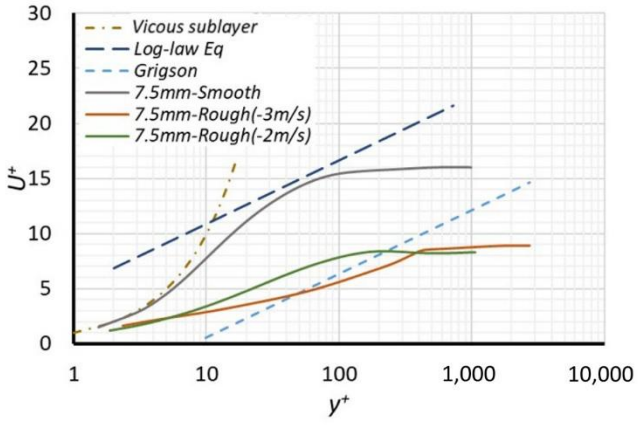

Source: Figure by authors

Figure 12.
Velocity profiles of 7.5 mm gap size at mid-disk location, considering the tangential velocity of 100 m/s and two radial velocities equal to 2 m/s and 3 m/s compared to theoretical estimations of the smooth case and rough velocity profile shifted according to Yuan and Piomelli (2014)

profile compared with the theoretical velocity profiles for the smooth and rough case of the DNS study.

A comparison between Figures 12 and 10 demonstrates the influence of fluid properties on obtained friction velocity and Re_τ. Moreover, employing air as the operating flow, the velocity profile hardly follows the log-law regime due to the lack of a fully developed boundary layer. Figure 12 also depicts the effect of mass flow rate on the value of Re_τ and downward shift of velocity profile due to the roughness. In the smallest studied gap size, the importance of mass flow rate, which is directly related to radial velocity, is even bigger. The airflow in the gap of 0.75 mm, roughness equal to 3.5% of the gap size and radial velocities equal to 2 m/s and 5 m/s are studied.

Figure 13 shows the effect of the change in mass flow rate on the velocity profile in the mid-disk radii. Implementation of roughness in the case with 2 m/s radial velocity reflects no substantial change in the velocity profile. An increase in radial velocity rises the maximum obtainable y^+ from 55 to 93, and roughness implementation presents a more downward shift in the velocity profile. Comparison of the velocity profile of flow in 7.5 mm and 0.75 mm gap size with 2 m/s radial velocity presented in Figures 13 and 12 reveals the intense effect of the gap size on the development of the boundary layer by means of maximum obtained y^+ and U^+. Considering the range of y^+ in both cases, the velocity profile of a 0.75 mm gap almost covers the transient part of the flow regime, yet a fully turbulent regime is visible in the velocity profile of a 7.5 mm gap size.

Interaction of boundary layers and boundary layer development can also be investigated by analysis of the eddy viscosity ratio; in this regard, the eddy viscosity ratio in the middle of the gap between corotating disks in three different gap sizes equal to 15 mm, 7.5 mm, 0.75 mm and considering 100 m/s and 5 m/s as the tangential and radial velocity is demonstrated in Figure 14.

The minimum obtainable value for viscosity ratio is equal to one, which stands for laminar flow, and the maximum value for a 0.75 mm gap is 7.78. For bigger gap sizes, the contours show a more developed boundary layer at the same distance from the inlet, and in all the studied cases, the maximum average viscosity ratio is obtained in the region close to the outlet. The flow analysis should be done at a distance from the disk's center where the profile is well-

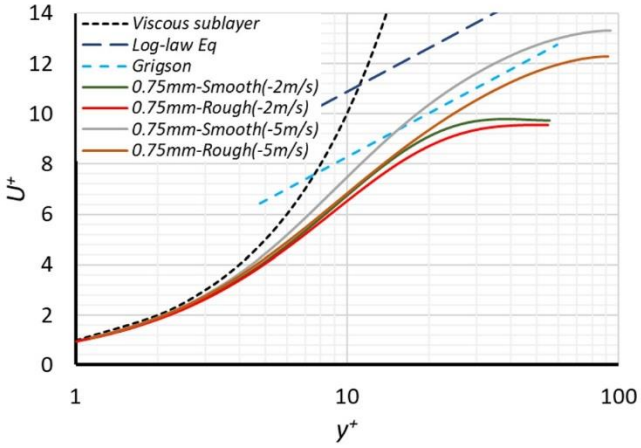

Figure 13.
Velocity profiles of 0.75 mm gap size at mid-disk location, considering tangential velocity equal to 100 m/s and two radial velocities equal to 2 m/s and 5 m/s compared to theoretical estimations

Source: Figure by authors

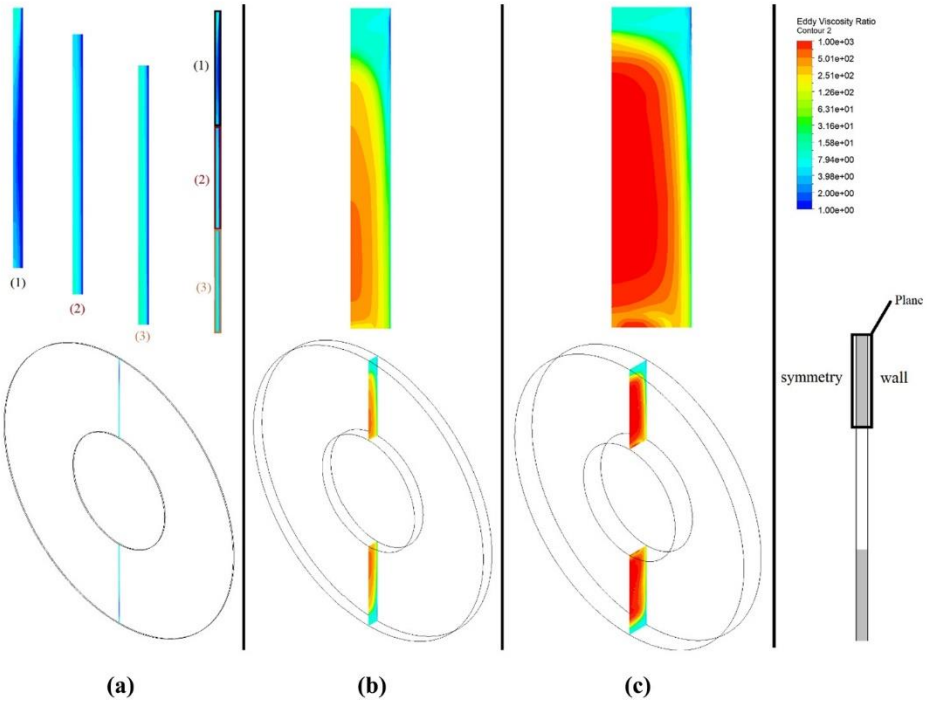

Source: Figure by authors

Figure 14. Eddy viscosity ratio of cases with roughness equal to 3.5% of gap size in the computational model for gap size equal to (a) 0.75 mm, (b) 7.5 mm and (c) 15 mm, considering radial and tangential velocity equal to 5 m/s and 100 m/s, respectively

developed and is not affected by boundary conditions. As discussed, the less developed boundary layer is in the area close to the inlet. To show the importance of this issue, Figure 15 presents the velocity profile of flow in the smooth 0.75 mm gap plotted at five radii for the same boundary conditions, with a radial velocity of 5 m/s.

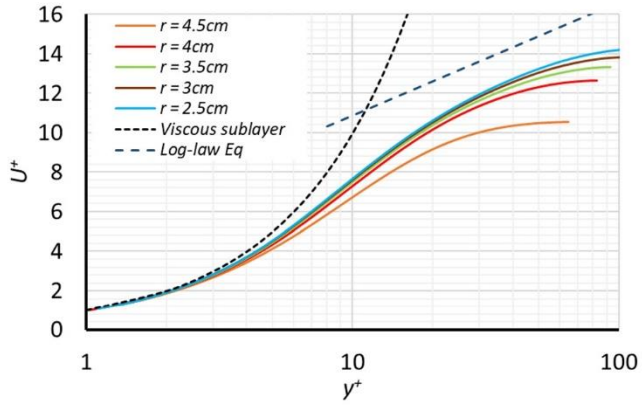

Source: Figure by authors

Figure 15. Mean velocity profiles of airflow through smooth 0.75 mm gap size at different radii considering radial and tangential velocity equal to 5 m/s and 100 m/s, respectively

The velocity profiles plotted for different radii demonstrate the influence of boundary conditions on the development of the boundary layer. The boundary layer profile develops along the wall from inlet to outlet, and its shape at the outlet is close to the theoretical line for the smooth case. For the rest of the study, velocity profiles are plotted in the middle of the disk to avoid the effect of used boundary conditions on velocity profile formation.

4.2 Influence of rotational speed

The effect of the rotational speed of parallel disks is investigated in this part; the rotational speed is increased step by step considering the smooth and rough surface of the disks. The studied domain is the same as the previous case. The roughness height is equal to 3.5% of the gap size. Radial and tangential velocities are equal to 5 m/s and 100 m/s, respectively, considering air as the working medium. The $k - \omega$ *SST* calculates the turbulent parameters using the fine mesh with 386,630 nodes with the maximum value of y^+ less than one.

The only variable here is the rotational speed. Figure 16 represented the generated power based on the integral of tangential stresses over the disk surface and the efficiency of the system (Rusin *et al.*, 2021a, 2021b) at different rotational speeds.

Power and system's efficiency are determined from the following relations:

$$N = \omega_a \int r \times \tau dA \tag{29}$$

$$\eta = \frac{N}{\dot{m} c_p T_{in} \left(1 - \left(\frac{p_{out}}{p_{in}}\right)^{\frac{\gamma-1}{\gamma}}\right)} \tag{30}$$

Simulations are done for seven different rotational speeds, and generated power and efficiency of the system are depicted in Figure 16. Implementation of roughness in simulation increases the generated power and efficiency of the system in all studied rotational speeds. As can be seen, in the studied range of rotational speed, the maximum efficiency of the system came up at approximately 17,500 rev/min. The

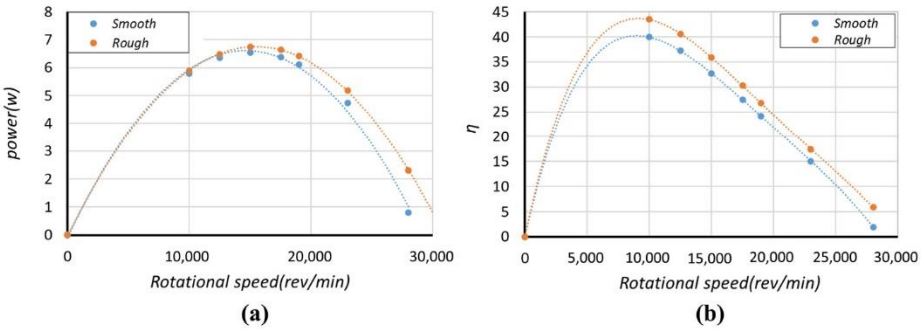

Figure 16.
(a) Generated power and (b) efficiency of the system vs rotational speed for the smooth and rough case with roughness height equal to 3.5% of gap size, considering the radial and tangential velocity at the inlet equal to 5 m/s and 100 m/s, respectively, and 0.75 mm gap size

Source: Figure by authors

change in rotation speed between 15,000 rev/min and 19,000 rev/min did not make a considerable change in the generated power, so the study with the rough surfaces was carried out for the rotational speed equal to 17,500 rev/min.

4.3 Influence of roughness height

To investigate the effect of roughness on the velocity profile and efficiency of the system, simulations carried on for five different roughness on the same domain and boundary condition as the previous case. The $k - \omega$ *SST* turbulence model on the same mesh as for the previous case was used. The results are presented in Figure 17.

Figure 17 shows the downward shift and increase in system efficiency due to the increase in roughness height. Higher shear stresses in the tangential direction contributed to a higher power, thus higher efficiency. Roughness height as an effective parameter on boundary layer formation causes a downward shift in the velocity profile. Flow through the corotating disks is affected by the boundary layer development at two parallel surfaces, and the interaction of the two boundary layers causes the velocity profile not to be fully developed,

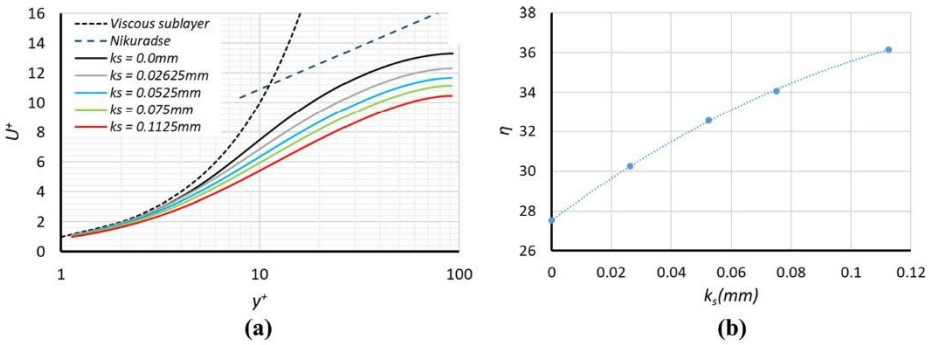

Source: Figure by authors

Figure 17. (a) Velocity profile and (b) efficiency of the system for four different roughness, considering radial and tangential velocity equal to 5 m/s and 100 m/s, respectively

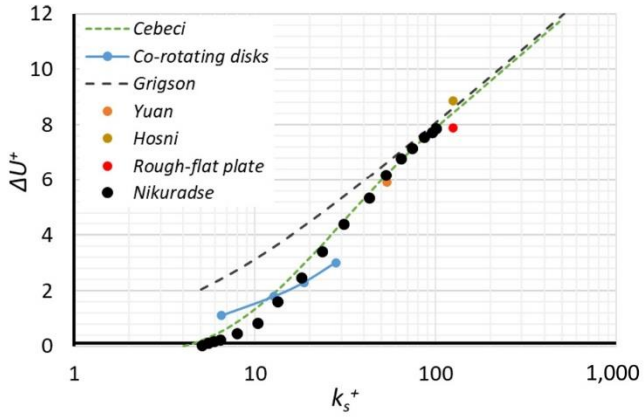

Source: Figure by authors

Figure 18. Comparison of the downward shift of the mean velocity profile vs dimensionless roughness height for airflow between corotating disks considering radial and tangential velocity equal to 5 m/s and 100 m/s, respectively, and all other studied cases

which describes the discrepancy between the results of the smooth case and the laminar theory and log-law equation.

Figure 18 demonstrates the downward shift of the velocity profile because of roughness calculated based on this study with 17,500 rev/min and other investigations.

In Figure 18, the estimated value of the downward shift of the velocity profile by the Grigson equation in lower values of k_s^+ is higher than other investigations. Good agreement of calculated downward shift of velocity profile based on the proposed study with other references demonstrates the accuracy of the simulation. Studied parameters are the most effective ones on the interaction of boundary layers developing from parallel corotating disks, and they impact the velocity profile formation in the computational domain.

5. Summary and conclusions

The study aims to investigate the best approach to simulate the flow in the narrow gap between corotating rough disks, e.g. in a Tesla turbine. To deal with this issue, standard cases of zero gradient-pressure flow over smooth and rough flat plates, flow through a minichannel with smooth and rough walls, and inward flow between the corotating discs are studied. Different mesh distributions, turbulence models and roughness methods are tested to find the most accurate way to simulate inward flow through the mini gap between corotating disks.

When the scale of the domain and flow cross section is reduced:

- Generating a compatible mesh for the $k - \varepsilon$ turbulence model with the first layer located in the log law part of the flow regime will cause a few cells in the normal direction to the wall, which is inappropriate.
- The $k - \omega$ *SST* model with denser mesh in the area with intense changes in eddy viscosity and coarser mesh in the farther area performs well and due to the capability of switching to $k - \varepsilon$, optimizes the calculation costs.
- Aupoix method of roughness artificially changes the eddy viscosity on the wall surface according to the roughness parameters without the need to cover the roughness with the first layer of generated mesh, and implementation of this method with $k - \omega$ *SST* model performs well in stationary and rotating minichannels.

Channel size, mass flow rate, fluid properties and roughness height are studied as the effective parameters on boundary layer formation in rotational minichannel. An increase in rotational speed caused substantial growth in generated power and a change in efficiency between 22% and 37%. Moreover, an increase in the height of the roughness raised the efficiency to 47%.

In the case of flow through the mini gap between the corotating disks, the velocity profile is affected by the interaction of developing boundary layers from the parallel corotating discs, and gap size, fluid properties, mass flow rate and roughness height are investigated as the effective parameters on this phenomenal.

References

Aupoix, B. (2015), "Roughness corrections for the k-ω shear stress transport model: Status and proposals", *Journal of Fluids Engineering*, Vol. 137 No. 2, doi: 10.1115/1.4028122/374661.

Azimy, N. and Saffarian, M.R. (2023), "Investigation of thermal characteristics and entropy generation in a solar collector including fly Ash-Cu hybrid nanofluids: numerical approach using mixture model", *Engineering Analysis with Boundary Elements*, Vol. 152, pp. 169-184, doi: 10.1016/J.ENGANABOUND.2023.04.002.

Bezaatpour, J., Ghiasirad, H., Bezaatpour, M. and Ghaebi, H. (2022), "Towards optimal design of photovoltaic/thermal facades: module-based assessment of thermo-electrical performance, exergy efficiency and wind loads", *Applied Energy*, Vol. 325, p. 119785, doi: 10.1016/J.APENERGY.2022.119785.

Cebeci, T. and Bradshaw, P. (1977), *Momentum Transfer in Boundary Layers*, Vol. 3 Hemisphere Publishing Corp.; McGraw-*Hill Book Co*, Washington, DC, New York, NY.

Chedevergne, F. (2018), "Analytical wall function including roughness corrections", *International Journal of Heat and Fluid Flow*, Vol. 73, pp. 258-269, doi: 10.1016/J.IJHEATFLUIDFLOW.2018.08.001.

Chedevergne, F. and Aupoix, B. (2017), "Accounting for wall roughness effects in turbulence models: a wall function approach", *7Th European Conference for Aeronautics and Aerospace Sciences (EUCASS)*, doi: 10.13009/EUCASS2017-372.

Chedevergne, F. and Forooghi, P. (2020), "On the importance of the drag coefficient modelling in the double averaged Navier-Stokes equations for prediction of the roughness effects", *Journal of Turbulence*, Vol. 21 No. 8, pp. 463-482, doi: 10.1080/14685248.2020.1817465.

Colebrook, C.F. (1939), "Turbulent flow in pipes, with particular reference to the transition region between the smooth and rough pipe laws", *Journal of the Institution of Civil Engineers*, Vol. 11 No. 4, pp. 133-156, doi: 10.1680/IJOTI.1939.13150.

Farzaneh-Gord, M., Pahlevan-Zadeh, M.S., Ebrahimi-Moghadam, A. and Rastgar, S. (2018), "Measurement of methane emission into environment during natural gas purging process", *Environmental Pollution*, Vol. 242, pp. 2014-2026, doi: 10.1016/J.ENVPOL.2018.07.027.

Grigson, C. (1992), "Drag losses of new ships caused by hull finish", *Journal of Ship Research*, Vol. 36 No. 2, pp. 182-196, doi: 10.5957/JSR.1992.36.2.182.

Hosni, M.H., Coleman, H.W., Garner, J.W. and Taylor, R.P. (1993), "Roughness element shape effects on heat transfer and skin friction in rough-wall turbulent boundary layers", *International Journal of Heat and Mass Transfer*, Vol. 36 No. 1, pp. 147-153, doi: 10.1016/0017-9310(93)80074-5.

Kader, B.A. (1981), "Temperature and concentration profiles in fully turbulent boundary layers", *International Journal of Heat and Mass Transfer, Pergamon*, Vol. 24 No. 9, pp. 1541-1544, doi: 10.1016/0017-9310(81)90220-9.

Kadivar, M., Tormey, D. and McGranaghan, G. (2021), "A review on turbulent flow over rough surfaces: fundamentals and theories", *International Journal of Thermofluids*, Vol. 10 No. 151, doi: 10.1016/J.IJFT.2021.100077.

Kalitzin, G., Medic, G., Iaccarino, G. and Durbin, P. (2005), "Near-wall behavior of RANS turbulence models and implications for wall functions", *Journal of Computational Physics*, Vol. 204 No. 1, pp. 265-291, doi: 10.1016/J.JCP.2004.10.018.

Kandlikar, S.G., Schmitt, D., Carrano, A.L. and Taylor, J.B. (2005), "Characterization of surface roughness effects on pressure drop in single-phase flow in minichannels", *Physics of Fluids*, Vol. 17 No. 10, p. 100606, doi: 10.1063/1.1896985.

Knopp, T., Alrutz, T. and Schwamborn, D. (2006), "A grid and flow adaptive wall-function method for RANS turbulence modelling", *Journal of Computational Physics*, Vol. 220 No. 1, pp. 19-40, doi: 10.1016/J.JCP.2006.05.003.

Lalegani, F., Saffarian, M.R., Moradi, A. and Tavousi, E. (2018), "Effects of different roughness elements on friction and pressure drop of laminar flow in microchannels", *International Journal of Numerical Methods for Heat and Fluid Flow*, Vol. 28 No. 7, doi: 10.1108/HFF-04-2017-0140.

Launder, B.E. and Spalding, D.B. (1974), "The numerical computation of turbulent flows", *Computer Methods in Applied Mechanics and Engineering*, Vol. 3 No. 2, pp. 269-289, doi: 10.1016/0045-7825(74)90029-2.

Moody, L.F. (1944), "Friction factors for pipe flow | BibSonomy", Transactions of the ASME, available at: www.bibsonomy.org/bibtex/22539414e7f58ccbe181597970148d3b5/thorade (accessed 1 August 2022).

Moradi, R., Habib, E., Bocci, E. and Cioccolanti, L. (2020), "Investigation on the use of a novel regenerative flow turbine in a micro-scale organic Rankine cycle unit", *Energy*, Vol. 210, p. 118519, doi: 10.1016/J.ENERGY.2020.118519.

Nikuradse, J. (1933), "Laws of flow in rough pipes, Nikuradse", National Advisory Committee For Aeronautics.

Orlandi, P. and Leonardi, S. (2009), "DNS of turbulent channel flows with two- and three-dimensional roughness", *Journal of Turbulence*, Vol. 7 No. 53, pp. 1-22, doi: 10.1080/14685240600827526.

Perry, A.E., Schofield, W.H. and Joubert, P.N. (1969), "Rough wall turbulent boundary layers", *Journal of Fluid Mechanics*, Vol. 37 No. 2, pp. 383-413, doi: 10.1017/S0022112069000619.

Radenac, E. (2016), "Validation of a 3D ice accretion tool on swept wings of the SUNSET2 program", *8th AIAA Atmospheric and Space Environments Conference*, American Institute of Aeronautics and Astronautics Inc, AIAA, doi: 10.2514/6.2016-3735.

Rusin, K., Wróblewski, W. and Rulik, S. (2018), "The evaluation of numerical methods for determining the efficiency of tesla turbine operation", *Journal of Mechanical Science and Technology*, Vol. 32 No. 12, pp. 5711-5721, doi: 10.1007/S12206-018-1118-4.

Rusin, K., Wróblewski, W. and Rulik, S. (2021a), "Efficiency based optimization of a tesla turbine", *Energy, Pergamon*, Vol. 236, p. 121448, doi: 10.1016/J.ENERGY.2021.121448.

Rusin, K., Wróblewski, W., Rulik, S., Majkut, M. and Strozik, M. (2021b), "Performance study of a bladeless microturbine", *Energies*, Vol. 14 No. 13, p. 3794, doi: 10.3390/EN14133794.

Schosser, C., Lecheler, S. and Pfitzner, M. (2014), "A test rig for the investigation of the performance and flow field of tesla friction turbines", *ASME Turbo ExpoAt*, Vol. 1B, doi: 10.1115/GT2014-25399.

Sigal, A. and Danberg, J.E. (2012), "New correlation of roughness density effect on the turbulent boundary layer", *AIAA Journal*, Vol. 28 No. 3, pp. 554-556, doi: 10.2514/3.10427.

Stimpson, C.K., Snyder, J.C., Thole, K.A. and Mongillo, D. (2017), "Scaling roughness effects on pressure loss and heat transfer of additively manufactured channels", *Journal of Turbomachinery*, Vol. 139 No. 2, doi: 10.1115/1.4034555/378795.

Suastika, I.K., Hakim, M.L., Nugroho, B., Nasirudin, A., Utama, I.K.A.P., Monty, J.P. and Ganapathisubramani, B. (2021), "Characteristics of drag due to streamwise inhomogeneous roughness", *Ocean Engineering*, Vol. 223, p. 108632, doi: 10.1016/J.OCEANENG.2021.108632.

Suga, K., Craft, T. and Iacovides, H. (2006), "An analytical wall-function for turbulent flows and heat transfer over rough walls", *International Journal of Heat and Fluid Flow*, Vol. 27 No. 5, pp. 852-866.

Sun, J., He, Y.L. and Tao, W.Q. (2011), "A molecular dynamics study on heat and mass transfer in condensation over smooth/rough surface", *International Journal of Numerical Methods for Heat and Fluid Flow*, Vol. 21 No. 2, doi: 10.1108/09615531111105425.

Swamee, P.K. and Jain, A.K. (1976), "Explicit equations for pipe-flow problems", *Journal of Hydraulic Engineering*, Vol. 1.

Tesla, N. (1913), "Nikola tesla U.S. Patent 1,061,206 – Turbine".

Trontin, P., Kontogiannis, A., Blanchard, G. and Villedieu, P. (2017), "Description and assessment of the new ONERA 2D icing suite IGLOO2D", *9th AIAA Atmospheric and Space Environments Conference, AIAA AVIATION, American Institute of Aeronautics and Astronautics Inc, AIAA*, doi: 10.2514/6.2017-3417.

Usman, M., Imran, M., Haglind, F., Pesyridis, A. and Park, B.S. (2020), "Experimental analysis of a micro-scale organic Rankine cycle system retrofitted to operate in grid-connected mode", *Applied Thermal Engineering*, Vol. 180, p. 115889, doi: 10.1016/J.APPLTHERMALENG.2020.115889.

Villedieu, P., Trontin, P. and Chauvin, R. (2014), "Glaciated and mixed phase ice accretion modeling using ONERA 2D icing suite", *6th AIAA Atmospheric and Space Environments Conference*, Vol. 51, Japan Society of Med. Electronics and Biol. Engineering, do: 10.2514/6.2014-2199.

Wieghardt, K. and Tillmann, W. (1944), "On the turbulent friction layer for rising pressure", NASA.

Yuan, J. and Piomelli, U. (2014), "Roughness effects on the Reynolds stress budgets in near-wall turbulence", *Journal of Fluid Mechanics*, Vol. 760, doi: 10.1017/JFM.2014.608.

Zhang, F., Zhou, Z., Zhang, H. and Yang, X. (2022), "A new single formula for the law of the wall and its application to wall-modeled large-eddy simulation", *European Journal of Mechanics – B/Fluids*, Vol. 94, pp. 350-365, doi: 10.1016/J.EUROMECHFLU.2022.03.013.

Further reading

Turbulent Flat Plate (2022), NASA, available at: www.grc.nasa.gov/www/wind/valid/fpturb/fpturb.html (accessed 26 July 2022).

Corresponding author

Mohammadsadegh Pahlavanzadeh can be contacted at: mohammadsadegh.pahlavanzadeh@polsl.pl or sadegh_pahlavan@yahoo.com

Paper II

Application of roughness models to stationary and rotating minichannel flows.

Application of roughness models to stationary and rotating minichannel flows

Mohammadsadegh Pahlavanzadeh, Sebastian Rulik, Włodzimierz Wróblewski and Krzysztof Rusin
Department of Power Engineering and Turbomachinery, Silesian University of Technology, Gliwice, Poland

International Journal of Numerical Methods for Heat & Fluid Flow

4085

Received 16 May 2024
Revised 8 July 2024
6 August 2024
Accepted 6 August 2024

Abstract

Purpose – The performance of a bladeless Tesla turbine is closely tied to momentum diffusion, kinetic energy transfer and wall shear stress generation on its rotating disks. The surface roughness adds complexity of flow analysis in such a domain. This paper aims to assess the effect of roughness on flow structures and the application of roughness models in flow cross sections with submillimeter height, including both stationary and rotating walls.

Design/methodology/approach – This research starts with the examination of flow over a rough flat plate, and then proceeds to study flow within minichannels, evaluating the effect of roughness on flow characteristics. An in-house test stand validates the numerical solutions of minichannel. Finally, flow through the minichannel with corotating walls was analyzed. The k-ω SST turbulent model and Aupoix's roughness method are used for numerical simulations.

Findings – The findings emphasize the necessity of considering the constricted dimensions of the flow cross section, thereby improving the alignment of derived results with theoretical estimations. Moreover, this study explores the effects of roughness on flow characteristics within the minichannel with stationary and rotating walls, offering valuable insights into this intricate phenomenon, and depicts the appropriate performance of chosen roughness model in studied cases.

Originality/value – The originality of this investigation is the assessment and validation of flow characteristics inside minichannel with stationary and corotating walls when the roughness is implemented. This phenomenon, along with the effect of roughness on the transportation of kinetic energy to the rough surface of a minichannel in an in-house test setup, is assessed.

Keywords Minichannel, Corotating disks, Roughness parameters, Turbulence parameters, Friction factor

Paper type Research paper

Nomenclature

A = area;
D_h = hydraulic diameter;
e = inner energy;
f = fanning friction factor;
f_i = gravitational force;
h = channel Height;

This presented research was conducted within the UMO-2019/35/B/ST8/01871 research project financed by the Polish National Science Centre and statutory research funds for young scientists financed by the Silesian University of Technology.

International Journal of Numerical Methods for Heat & Fluid Flow
Vol. 34 No. 11, 2024
pp. 4085-4106

0961-5539
DOI 10.1108/HFF-05-2024-0379

h_{cf} = constricted channel height;
h_r = height of the roughness;
k = turbulent kinetic energy;
k_s = equivalent sand-grain roughness;
k_s^+ = roughness Reynolds number;
k_w^+ = dimensionless Turbulent kinetic energy close to the wall;
m = mass flow rate;
p = pressure;
q = heat flux;
Re = Reynolds number;
Re_τ = friction Reynolds number;
R_a = arithmetic mean deviation;
R_q = root means square roughness;
T = temperature;
t = time step;
U = mean velocity;
U^+ = dimensionless mean velocity (related to wall shear stress);
U_∞ = free stream velocity;
u_τ = friction velocity;
ΔU^+ = roughness function; and
y^+ = dimensionless normal-wall distance (related to wall shear stress).

Greek letters

κ = von Karman constant;
ν = kinematic viscosity;
τ_w = total wall stress;
τ_{ij} = total stress ($\tau_{Turb} + \tau_{lam}$);
ρ = density;
τ = tangential stress;
μ = dynamic viscosity;
ω = specific dissipation rate;
ω_w^+ = dimensionless Specific dissipation rate close to the wall;
ε = turbulent dissipation rate; and
α^* = aspect ratio of the channel.

1. Introduction

Mini and micro-channels possess a high ratio of surface area to volume, which can augment the influence of surface roughness on fluid flow. Surface roughness can initiate flow separation and turbulence, leading to alterations in the velocity profile (Lalegani *et al.*, 2018; Maciejewska and Piasecka, 2020; Xie *et al.*, 2014).

Also, drag prediction and reduction in minichannel is an active field of research with various applications. Chang *et al.* (2019) performed direct numerical simulations (DNSs) of a turbulent channel flow with a lubricated micro-grooved surface to investigate the effects of this surface on the slip characteristics at the interface and the friction drag.

Minichannel simulation has been an active area of research for several decades, with applications in kinetic energy transport, drag prediction and heat transfer. Roughness elements, which increase turbulence and heat transfer in minichannels, have also been an active field of research. Below is a summary of a group of investigations, categorized by their year of publication.

(1) 1990s: In the early days, researchers focused on developing analytical models to study fluid flow and heat transfer in minichannels. These models were based on assumptions such as laminar flow, constant wall temperature and steady-state conditions.

(2) 2000s: With the increasing availability of computational resources, researchers began to use numerical simulations to study minichannel flow and heat transfer. These simulations used finite element or finite volume methods to solve the Navier–Stokes equations and the heat transfer equations. The simulations were able to capture more complex flow phenomena such as turbulence and multiphase flow.

(3) 2010s: In this decade, there has been a growing interest in using high-performance computing and machine learning techniques to simulate minichannel flow and heat transfer. This has enabled the simulation of larger and more complex minichannel geometries and flow regimes.

Table 1 represents an overview of selected investigations about rectangular minichannels that use water as the operating flow in different hydraulic diameters.

In recent years, research on minichannels spans various fields and applications, including micro and nanofluidic, electronics cooling, biomedical engineering and energy conversion and storage (Daadoua *et al.*, 2024; Kim *et al.*, 2023).

In fluid dynamics, energy conversion, especially between the operating flow and the rotor, which is the main application of this concept, is of great importance. Roughness is a substantial factor that affects the flow characteristics in the studied domain (Aliakbari *et al.*, 2023; Rusin *et al.*, 2021). This effect in small-scale domains is even more significant. In the minichannel flow, the presence of roughness elements can substantially alter the flow behavior. When it comes to computational domain with a very small flow cross section, mesh requirement and implementation of roughness become even more challenging. Pahlavanzadeh *et al.* (2023a) discussed the appropriate mesh, turbulence model and roughness method for such a domain.

Table 1. Selected literature for single-phase water flow through a minichannel

Author	$D_h(\mu m)$	Re	L/D_h
Riddle *et al.* (1991)	86–96	96–982	156–180
Rahman (2000)	299–491	285–3234	94–154
Pfund *et al.* (2000)	128–521	60–3450	156–240
Baviere *et al.* (2004)	14–593	0.1–7985	138–429
Kohl *et al.* (2005)	24.9–99.8	5–2068	220–534
Kandlikar *et al.* (2005)	335–1819	200–5700	55–298
Schmitt and Kandlikar (2005)	769–1820	0–3500	83
Hao *et al.* (2006)	153–191	100–2300	120–149
Brackbill and Kandlikar (2007)	125–429	30–7000	207–712
Gamrat *et al.* (2008)	191–585	30–6000	128–261
Wibel and Ehrhard (2009)	128–386	300–3,000	197–209
Tam *et al.* (2011)	1,000–2,000	700–7,000	150–300
Wagner and Kandlikar (2012)	542–1745	5–3,400	87–337
Vajravel *et al.* (2019)	2670	175–553	1.96–54

Notes: The studies addressed in Table 1 were conducted between 1990s and 2010s covering a wide range of Reynolds number (Re) and hydraulic diameter (D_h) investigating different applications of minichannel usage

Source: Table by authors

The presence of corotating walls in a minichannel introduces complexity to flow characteristics and incorporates additional effective parameters into the system's evaluation and has some industrial applications. The increase in momentum transfer between the operating flow and rotating surface connected to the rotor has lots of applications in friction turbomachines like the Tesla turbine (Tesla, 1913). Walls as the main source of turbulence and the formation of a boundary layer greatly affect the performance of such systems (Farzaneh-Gord *et al.*, 2018). Flow properties, domain size and surface roughness are the essential quantities needed to be considered in the analysis of flow behavior in the Tesla turbine, which can be simplified as a group of minichannels with corotating walls (Pahlavanzadeh *et al.*, 2023b; Rusin *et al.*, 2023).

Research into the flow behavior and formation of boundary layers near smooth and rough surfaces is a fast-developing field that has been extensively explored. Two main approaches have been proposed to account for the roughness. The first approach involves using the logarithmic law of the wall to shift the dimensionless profile downward based on roughness parameters. However, this approach requires adaptation of the wall function. The second approach involves modifying the turbulence parameters on the wall to artificially increase the wall shear stress. Both methods have their own advantages and disadvantages. The first method requires a coarse grid to adapt the wall function, which may be problematic in highly confined internal flows, but is generally useful in external flows. The second method, on the other hand, requires a fine mesh, which significantly increases the computational cost.

Chedevergne and Aupoix (2017) created a wall function to supplement the RANS turbulent model that considers roughness correction. Another study by Chedevergne and Forooghi (2020) proposed a new model that incorporates mixing length to calculate the impact of roughness on flow behavior within channels. In Grigson's (1992) study, the performance of finishes simulating hull surfaces under trial conditions is examined. The friction coefficient is measured at full scale for numerous examples. In addition, the accuracy of the methods used to obtain real data on the velocity loss functions of the surfaces is assessed, and the roughness function is detailed below:

$$\Delta U^{+} = \frac{1}{\kappa}\ln\left(1 + \frac{k_s^{+}}{\exp\left(3.25\kappa\right)}\right) \tag{1}$$

$$k_s^{+} = \frac{k_s u_\tau}{\nu} \tag{2}$$

where k_s stands for sand-grain roughness, u_τ is the friction velocity (defined as $u_\tau = \frac{\tau_w}{\rho}$, where τ_w and ρ correspond to the total wall stress and fluid density, respectively) and ν is the kinematic viscosity.

Aupoix (2015) proposed a different method to account for roughness in k-ω models used for flow simulation. This method involves modifying the turbulent parameters on the wall based on equivalent sand-grain roughness.

Surface roughness parameters are used to describe the texture or irregularity of a surface. They are commonly used in engineering, manufacturing and other industries where surface quality is important to implement the roughness in the flow simulation, equivalent sand-grain roughness (k_s) is a useful parameter.

Sand-grain roughness can be calculated on the basis of different roughness parameters. Stimpson *et al.* (2017) calculated this parameter as a function of the arithmetic mean deviation (R_a) and hydraulic diameter (D_h):

$$\frac{k_s}{D_h} = 18\left(\frac{R_a}{D_h}\right) - 0.05 \tag{3}$$

Moreover, Nikuradse (1933) [equation (4)] and Colebrook (1939) [equation (5)] estimated sand-grain roughness based on root means square roughness (R_q):

$$k_s = 2.294R_q \tag{4}$$

$$k_s = 1.306R_q + 0.078\left(R_q{}^2\right) \tag{5}$$

In this study, sand-grain roughness is calculated using different estimations and the Aupoix method is used to investigate the effect of roughness on the characteristics of flow each study case. A systematic study of reported test cases was done to approach the main aim of the present investigation which is the analysis of flow characteristics and structures between corotating disks with uniform inlet flow and proof of the chosen methodology. The investigation tested the performance of chosen methods in different flow cross sections. It started with a zero-pressure-gradient boundary layer in the flow over a flat plate, continued with flow through minichannels with stationary walls, including tests on an in-house test setup and, finally, focused on the flow between corotating disks.

2. Mathematical model

The numerical investigations were conducted using Ansys fluent, a commercially available software based on the finite volume method. To approach to the main aim of study, standard three-dimensional (3D) cases are tested using *k–ω SST* as the turbulent model and roughness method derived by Aupoix (2015). The appropriate performance of *k–ω SST* turbulence model Aupoix's roughness method in mini flow cross sections were tested by Pahlavanzadeh *et al.* (2023a) and the results were compared with other roughness methods and turbulence models. Pahlavanzadeh *et al.* (2023a) tested the performance of this combination across different scales of computational models and demonstrated its effectiveness. In this study, different methods for roughness implementation and turbulent models were investigated. The results showed that the combination of the *k–ω* SST model and the Aupoix (2015) roughness method performed well in investigated domains, considering the real dimensions of the channel without constriction. In the present study, the same methods for the computational fluid dynamics (CFD) analysis were applied.

The discretized Reynolds-averaged Navier–Stokes equations for a compressible fluid are solved using the finite volume method. The governing equations, in the form of continuity, momentum and energy conservation, are used:

$$\frac{\partial \rho}{\partial t} + \frac{\partial}{\partial x_j}(\rho U_j) = 0 \tag{6}$$

$$\frac{\partial(\rho U_i)}{\partial t} + \frac{\partial}{\partial x_j}(\rho U_j U_i) = -\frac{\partial p}{\partial x_i} + \frac{\partial \tau_{ji}}{\partial x_j} + \rho f_i \tag{7}$$

$$\frac{\partial\left(\rho\left(e + \frac{1}{2}U_jU_j\right)\right)}{\partial t} + \frac{\partial}{\partial x_i}\left(\rho U_i\left(e + \frac{1}{2}U_jU_j\right)\right) = -\frac{\partial}{\partial x_i}(pU_i) + \frac{\partial}{\partial x_i}(\tau_{ij}U_j) - \frac{\partial}{\partial x_i}(q_i) + \rho f_i U_i \tag{8}$$

The Aupoix method involves modifying the turbulent parameters on the wall, which leads to artificial changes in the eddy viscosity. The degree of change depends on the dimensionless sand-grain roughness:

$$k_w^+ = \max\left(0; k_0^+\right) \tag{9}$$

$$k_0^+ = \frac{1}{\sqrt{\beta^*}} tanh\left[\left(\frac{ln\frac{k_s^+}{30}}{ln10} + 1 - tanh\frac{k_s^+}{125}\right) tanh\frac{k_s^+}{125}\right] \tag{10}$$

$$\omega_w^+ = \frac{300}{k_s^{+2}}\left(tanh\frac{15}{4k_s^+}\right)^{-1} + \frac{191}{k_s^+}\left(1 - exp\left(-\frac{k_s^+}{250}\right)\right) \tag{11}$$

where dimensionless values of k_w^+ and ω_w^+ are representative of modified turbulent kinetic energy and specific dissipation rate. To investigate flow characteristics between corotating disks, a systematic approach is used to test the performance of the chosen methods across different scales of computational domains.

3. Flow over a rough flat plate

The research commences with an examination of a straightforward scenario involving flow over a rough flat plate. In their study, Hosni *et al.* (1993) investigated the zero-pressure gradient incompressible turbulent boundary layer air flow over a flat plate featuring hemispheric roughness elements, each with a diameter of D = 1.27 mm. The simulation encompasses a computational domain with dimensions of 5 m in length and 2 m in height, where a free stream inlet velocity of U = 58.2 m/s is imposed. The simulation employs specific boundary conditions: pressure far field and symmetry for the top and side surfaces, whereas a no-slip wall condition is applied to the bottom surface to account for roughness effects. To carry out this simulation, the k–ω model and the Aupoix method are used. The mesh requirement for both employed model and method is a fine mesh with a y^+ value less than one. Accordingly, a fine mesh configuration is adopted, consisting of 400 nodes in the streamwise direction, 140 nodes in the vertical direction and four layers in the spanwise direction. The results of the study, obtained using the k–ω model in conjunction with the Aupoix method at X = 1.68 m, are compared to theoretical estimation of downward shift of velocity profile [equation (1)] and experimental data from Hosni and presented in Figure 1.

After determining the roughness height and obtaining the friction velocity, the calculation of k_s^+ is performed using equation (2). Subsequently, an assessment of the downward shift of the velocity profile is carried out using equation (1). The figure illustrates the favorable performance of the k–ω *SST* turbulent model in simulating roughness, using the Aupoix method.

In the transient and turbulent segment of the profile, there is a notable alignment between the results of numerical simulation, theoretical prediction of a downward shift of velocity profile [equation (1)] and experimental data. The agreement proves the appropriate accuracy of the used model for the standard case in the macro scale. Furthermore, the study investigates the influence of the roughness constant, which is a function of the roughness distribution on the wall. In this part of the research, simulations are conducted with two values for the roughness constant: 0.5 and 1, corresponding to uniform and nonuniform roughness distributions, respectively. The friction coefficient at various distances from the leading edge, characterized by the dimensionless value of $Re_X = \frac{\rho U_\infty X}{\mu}$, is presented in Figure 2.

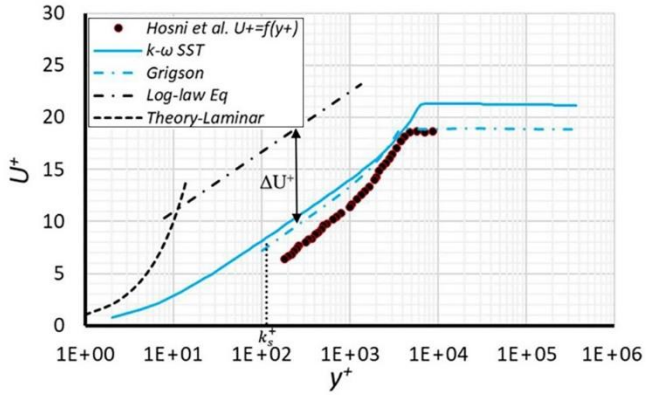

Source: Figure by authors

Figure 1. Numerical simulation of flow over a flat plate compared to the experimental study conducted by Hosni *et al*. (1993)

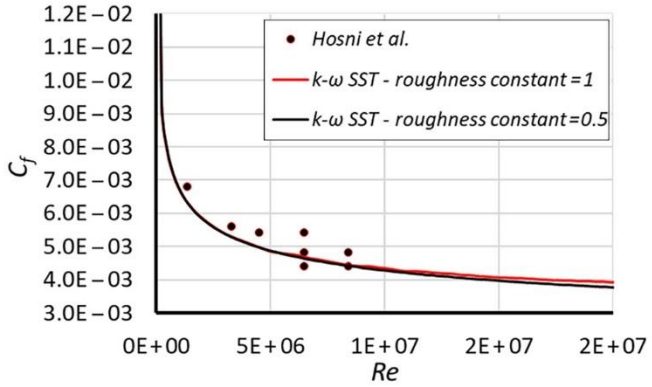

Source: Figure by authors

Figure 2. Effect of roughness constant on friction coefficient

In regions far from the plate's leading edge, where the boundary layer is fully developed, a roughness constant of 1 increases shear stress, indicating that a fully rough surface generates slightly higher drag compared to a semi-rough distribution of roughness elements. However, the increase is negligible, confirming that for higher Re the friction factor is independence of Re. This observation suggests that considering the used model and roughness method, the parameter of uniformity of the roughness distribution does not play a substantial role in the studied case.

4. Minichannel flow

To approach the main purpose of this investigation, preliminary study cases are chosen to find the best way to implement roughness in both CFD and experimental investigations. Minichannels

with heights within the range of the gaps between corotating disks of Tesla turbine, as investigated in Pahlavanzadeh *et al.* (2023a), are chosen for validation. In this section, the minichannel is investigated both numerically and experimentally. The used turbulence model and roughness method are validated with the DNS investigation of Yuan and Piomelli (2014), experiments of Kandlikar *et al.* (2005) and finally with the results of in-house tests on minichannel.

4.1 Validation against direct numerical simulation data

Yuan and Piomelli (2014) conducted DNS simulations to calculate open-channel flow. The simulation used a domain with dimensions of $6 \times 1 \times 3h$ in the streamwise, vertical and spanwise directions, respectively. The bottom and top walls were assigned no-slip and symmetry boundary conditions, respectively. This top-wall symmetry setup resembles flow between parallel plates. Periodic boundary conditions were implemented on the side walls. To drive the flow, a constant pressure gradient was established between the front and back surfaces. The convergence was achieved through cyclic parameter transfer from the outlet to the inlet. Figure 3 shows a schematic of the computational domain and the specific shape of the roughness studied by Yuan and Piomelli.

For the simulation of fully rough flow simulation, a high roughness of $\frac{k_s}{h} = 0.07$ was adopted, resulting in a constant friction Reynolds number $Re_\tau = \frac{\rho u_\tau D_h}{\mu}$ of 1,000, where u_τ denotes the friction velocity and D_h is the hydraulic diameter. Smooth minichannel flow was simulated using the *k–ω SST* model. In the case of rough flow, the *k–ω SST* model with Aupoix's approach was used.

Adhering to Yuan and Piomelli's proportions and assuming that a channel height of 2 h equates to 1 mm, the domain dimensions were adjusted to $3 \times 0.5 \times 1.5$ mm. The roughness height was set at 35 μm, and the boundary conditions matched those used in the DNS simulation. The operating fluid was compressible air at the temperature of 300 K.

For smooth and rough simulations, a refined mesh with 1 million nodes and y^+ lower than 0.4 in all the domains was used. The implementation of periodic boundary conditions helped to maintain consistent parameters throughout the entire domain.

Figure 4 presents a comparison between the DNS simulations for both smooth and rough cases, the results of the present study and the theoretical velocity profile in the viscous sublayer and logarithmic part. This calculation is in excellent agreement with the DNS simulation of the rough case. The velocity profile is defined at the midpoint of the domain.

The simulation yields a calculated k_s^+ value of 72, based on friction velocity and roughness height, which aligns with the recommendation in the literature. The results obtained show strong agreement with both DNS simulation and theoretical predictions in both smooth and rough cases. Despite being influenced by the interaction of boundary layers between parallel surfaces, the results remain consistent with both theoretical lines and DNS simulation across the laminar and turbulent regions of the boundary layer. In the rough case, where the obtained Reynolds number (Re_τ) is 1,000 and the actual downward shift of the velocity profile is nearly identical to the expected value. The equivalent downward shift in velocity profile demonstrates the similarity in friction generation. This observation underscores the effective performance of the model and method within the confined computational domains.

4.2 Comparison with the experiments of Kandlikar et al. *(2005)*

The exploration of flow dynamics within a minichannel begins with the validation of computational results via experimental data presented by Kandlikar *et al.* (2005). They examined the airflow through channels with a width (w) of 10.03 mm, length (l) of 100 mm and height (h) of 0.5 mm, at various flow velocities. The Fanning friction factor (f) was deduced across a range of Reynolds numbers (Re) and compared with the pertinent

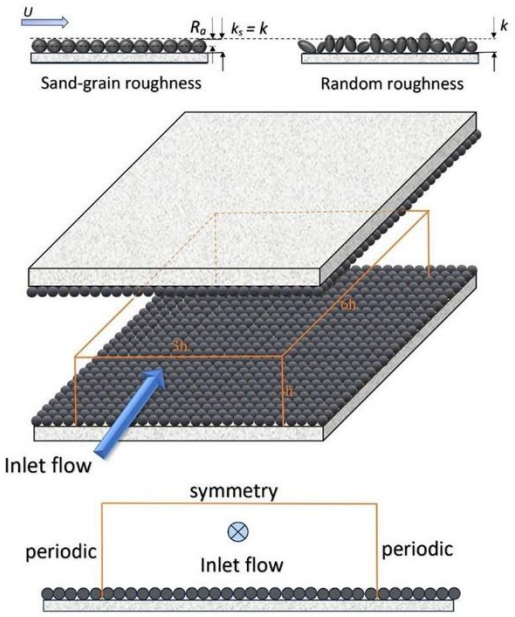

Source: Figure by authors

Figure 3. Schematic of computational domain in Yuan and Piomelli DNS simulation

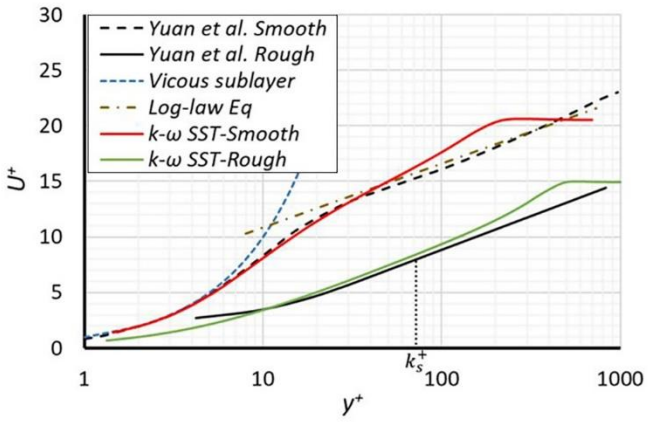

Source: Figure by authors

Figure 4. Comparison of the dimensionless velocity profiles of DNS simulation (Yuan and Piomelli, 2014) with the theoretical velocity profile of the smooth case and the present CFD simulation

theoretical equation, applied in the context of both smooth and rough-channel scenarios. In the experiments conducted by Kandlikar *et al.* (2005), the theoretical Fanning friction factor pertinent to laminar flows was ascertained through the following formulation:

$$f = \frac{C}{Re} \tag{12}$$

where the constant C is contingent upon the channel's aspect ratio denoted as $\alpha^* = \frac{h}{w}$, where h and w represent the dimensions of a rectangular conduit:

$$C = 24\left(1 - 1.3553\alpha^* + 1.9467\alpha^{*2} - 1.7012\alpha^{*3} + 0.9564\alpha^{*4} - 0.2537\alpha^{*5}\right) \tag{13}$$

The Swamee and Jain (1976) approximation is used to resolve the Fanning friction factor within the turbulent regime:

$$f = 0.0625\left[ln\left(\frac{\frac{h_r}{D_h}}{3.7} + \frac{5.74}{Re^{0.9}}\right)\right]^{-2} \tag{14}$$

The hydraulic diameter D_h for the rough scenario is approximated using measurements from both the real height and the constricted height. The constricted height of the channel is determined by using the following equation:

$$h_{cf} = h - 2h_r \tag{15}$$

Here, the constricted channel height h_{cf}, the overall channel height h and the average roughness height represented by h_r (which is 72.9 μm) are involved in the equation.

Various methods have been proposed in the existing literature to compute the equivalent sand grain roughness, denoted as k_s. In this context, two approaches are used. The first was suggested by Stimpson *et al.* (2017) as shown in equation (3), whereas the second is from Sigal and Danberg (2012) as expressed in equation (16):

$$\frac{k_s}{h_r} = \begin{cases} 0.00321\Lambda_s^{4.925}, & 1.4 \le \Lambda_s \le 4.89 \\ 8, & 4.89 \le \Lambda_s \le 13.25 \\ 151.711\Lambda_s^{-1.1379}, & 13.25 \le \Lambda_s \le 100 \end{cases} \tag{16}$$

$$\Lambda_s = \left(\frac{S}{S_f}\right)\left(\frac{A_f}{A_s}\right)^{-1.6} \tag{17}$$

In this context, A_f signifies the proportion of the frontal area of an individual roughness element, A_s denotes the windward wetted surface area of a single roughness element, S represents the baseline surface area before the inclusion of roughness and S_f accounts for the complete frontal area of the roughness. With the given value of R_a being 17 μm and accounting for other roughness characteristics, the outcomes of equations (3) and (16) yield the values of equivalent sand-grain roughness of k_s = 271 μm and k_s = 350 μm, respectively.

The computational framework in the CFD simulation involves dividing the computational domain into two equal parts. Each segment measures 10.03 mm in width (w), 200 mm in length (l) and 0.5 mm in height (h). The initial portion of the domain uses no-slip

walls to establish a fully developed velocity profile at the entrance of the second segment. In the latter section of the domain, the upper and lower walls are characterized by roughness, whereas the side walls apply the no-slip condition. A refined mesh comprising 1 million nodes is generated, ensuring a maximum value of y^+ below one. Depend on the flow Reynolds number, the simulation uses laminar or the *k–ω SST* turbulence model along with the Aupoix approach to implement roughness. Figure 5 illustrates the contrast among the experimental data, the numerical findings and the results obtained from the empirical formulas for the smooth case. Dai *et al.* (2014) presented a comparison between different literature considering the roughness in the rectangular minichannels. In their investigation, the friction factor obtained from different literature is presented, categorized by the ratio of the height of roughness (h_r) to hydraulic diameter of the channel (D_h). Figure 6 demonstrates a comparison among the experimental data of Kandlikar, presented experiments in Dai *et al.* (2014), the numerical simulation outcomes for k_s values of 271 and 350 μm, and the results obtained from the empirical formulas for the rough cases.

Examining the smooth channel scenario in Figure 5, the results of the CFD simulations align well with both theoretical predictions and experimental observations regarding laminar flow. However, there is a slight overestimation of the friction factor in the turbulent regime. The numerically derived points show a divergence from the experimental data near the *Re* = 3,500 by approximately 0.005.

The Fanning friction factor is depicted in Figure 6, as a function of the Reynolds number for rough cases. The theoretical calculations of the friction factor under turbulent conditions are based on smooth and roughness heights of h_r = 72.9, 271 and 350 μm coupled with the actual dimensions of the channel. A notable disparity emerges between the experimentally determined friction factor by Kandlikar *et al.*, other experimental investigations with the same ratio of roughness to hydraulic diameter and the theoretically estimated values in the laminar and turbulent flow regimes. This variance underscores the substantial influence of roughness geometry on the resulting friction factor. The roughness elements affect the flow structures in the channel and flow between roughness obstacles. The specific geometry that involves a tooth-shaped roughness height significantly shapes the flow behavior. The data derived from numerical simulation depicts

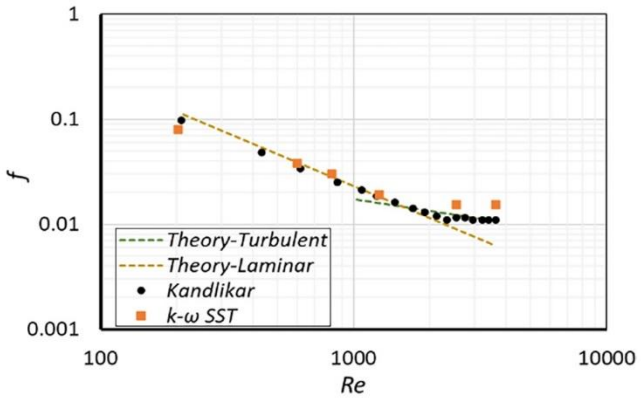

Source: Figure by authors

Figure 5. Comparison of the results of CFD simulations with experimental data (Kandlikar *et al.*, 2005) and theoretical formulas for laminar and turbulent flows as a function of Re for smooth minichannel

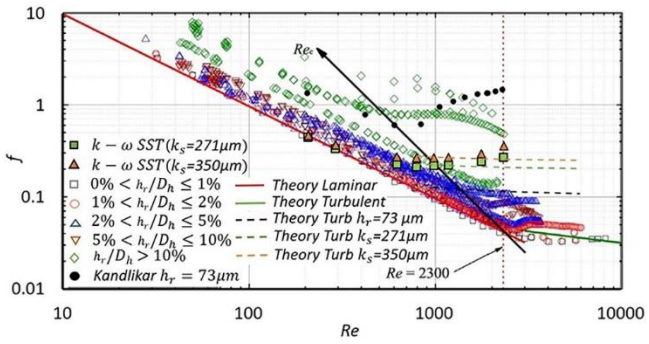

Source: Figure by authors

Figure 6. Comparison of the results from CFD simulations with experimental data of Kandlikar *et al.* (2005), Dai *et al.* (2014) results and theoretical formulas for laminar and turbulent flows as a function of Re for rough minichannel

a good alignment with theoretical lines in both laminar and turbulent regime still it should be taken into the account that the used method of roughness only modifies the turbulent regime and is not effective on laminar part. In Figure 7, an alternative depiction of the friction factor is presented based on the constricted hydraulic diameter and flow parameters, leading to better agreement with theoretical predictions. Kandlikar *et al.* presented the results of their experiment considering the constricted dimensions of the channel and claimed that there is no flow under a specific height of the roughness, which may vary based roughness geometry.

4.3 In-house stationary test setup

To approach the main aim of the present study, which is an assessment of flow characters between corotating disks with the same size as the gap between corotating disks of the Tesla turbine, a test setup was prepared.

Figure 8 demonstrates a schematic of an in-house test rig to investigate the flow in minichannels. The test rig consists of the water flow through the channel characterized by a width (w) of 50 mm, a length (l) of 150 mm and a height (h) of 0.75 *mm*, at varying flow velocities. Figure 9 represents the schematic of the test section dimensions of the minichannel and roughness shape.

The in-house test rig collects the required flow parameters to calculate friction factor in different *Re*. Experiments were conducted on minichannels that covered a range of Reynolds numbers (*Re*) to encompass the transition from laminar to fully turbulent flow regimes. This empirical investigation involved the use of both smooth channel and channel equipped with rough surfaces. In the context of the rough minichannel, a sheet with the roughness obstacles made of aluminum oxide with the R_a of 11.3 μm, R_q of 13.16 μm and average roughness height (h_r) of 60 μm was fixed to the channel walls. Pressure measurements were taken at two distinct points along the channel, 15 cm apart from each other. The total length of the channel is 30 cm. The first 15 cm is considered to let the flow become well developed and the pressure is collected from two locations, in the middle of the channel and close to the outlet. The water flow rate and temperature are collected from the flow meter and measurements were averaged every second. The data from both the smooth and rough cases were used to compute the friction factor. Pump operation increases the water temperature and every

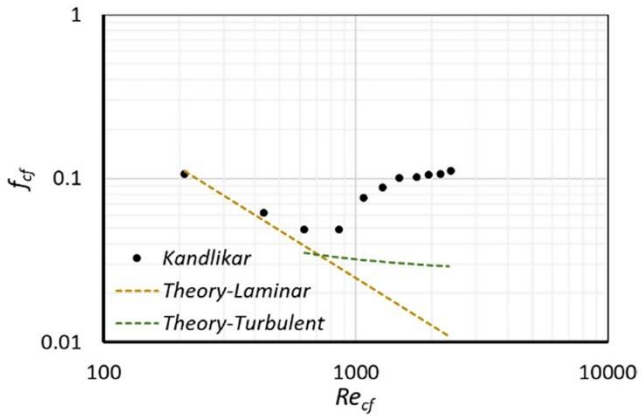

Source: Figure by authors

Figure 7. Comparison of constricted experimental data (Kandlikar *et al.*, 2005) and theoretical formulas for laminar and turbulent flows as a function of Re for a rough minichannel

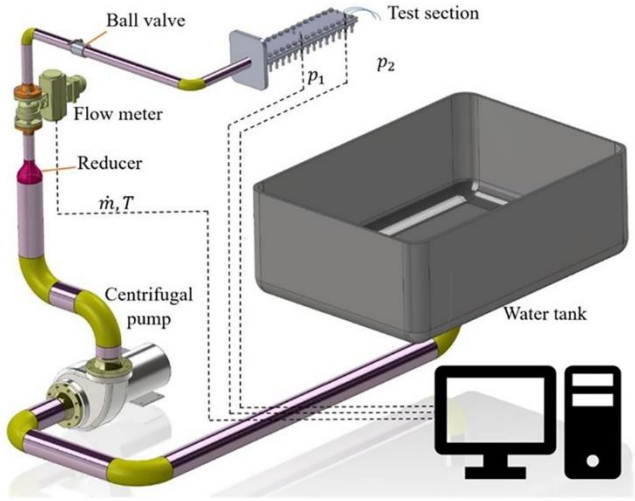

Source: Figure by authors

Figure 8. Schematic of in-house test rig

change in flow rate causes transient behavior of system which reaches to an almost steady state after a while. In an almost steady state, to minimize the transient behavior, water flow rate and temperature were averaged every second. The pressure drop is calculated with the summation of uncertainties of measurements in pressure transducer and pressure reading,

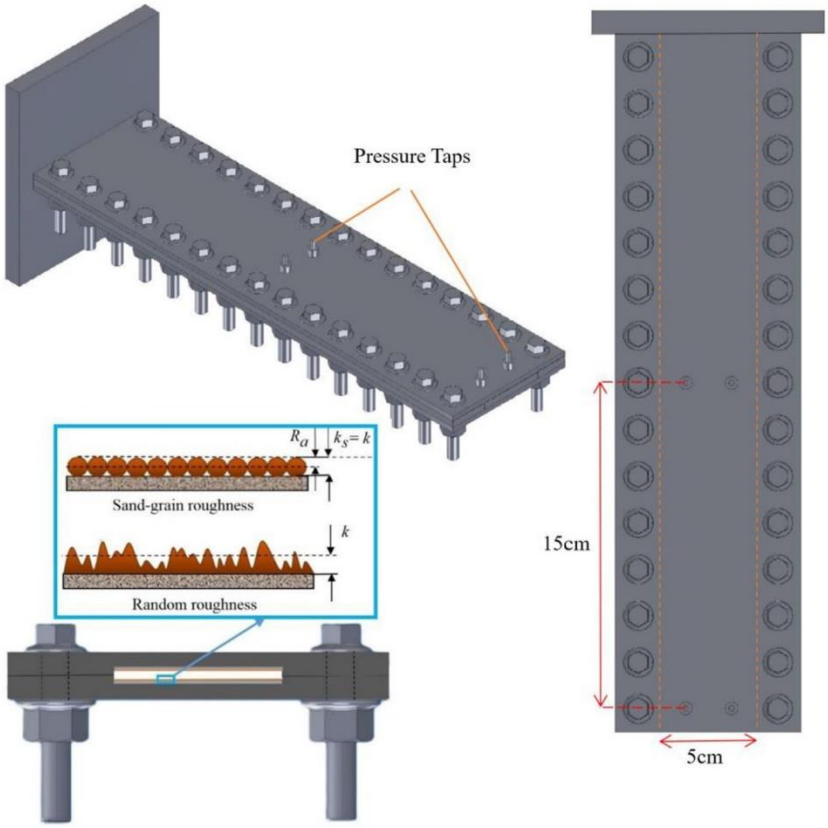

Source: Figure by authors

Figure 9. Schematic of the test section with the approximate roughness shape

which was 0.25% and 2%, respectively. The flow rate and temperature measurements were also done with the accuracy of 0.5% and ±0.1°C.

CFD simulations were conducted to model the flow within the minichannel for both scenarios involving smooth and rough surfaces. In the case of rough surfaces, the simulation incorporated the roughness using the Aupoix method, with a roughness height of 60 μm being considered.

Figure 10 illustrates a comparison between the results of experiments, CFD simulations and the theoretical predictions of the friction factor. The assessment is conducted within both the laminar regime [using equation (12)] and the turbulent regime [using equation (14)]. The experimental results of the rough case are presented with considerations for both the constricted and actual dimensions of the channel. Notably, the alignment of results with the theory when using the constricted dimensions of the channel indicates that flow is impeded below a certain roughness height, as indicated by the observations in Figure 11.

As illustrated in Figure 10, there exists good agreement between the empirical observations, CFD simulations and theoretical predictions regarding the friction coefficients.

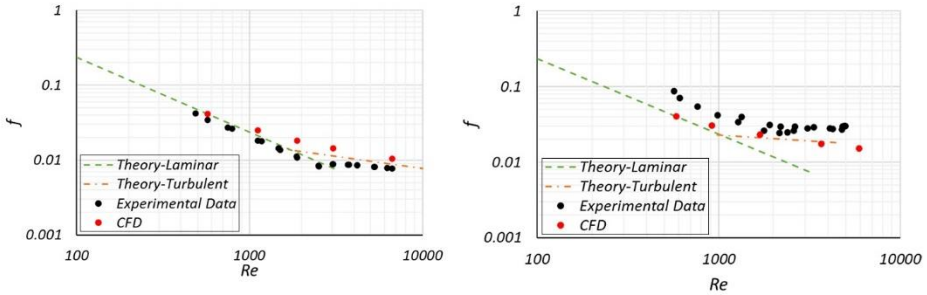

Source: Figure by authors

Figure 10. Comparison of the results of CFD simulations with experimental test results and theoretical formulas for laminar and turbulent flows as a function of Re for (a) smooth and (b) rough minichannel

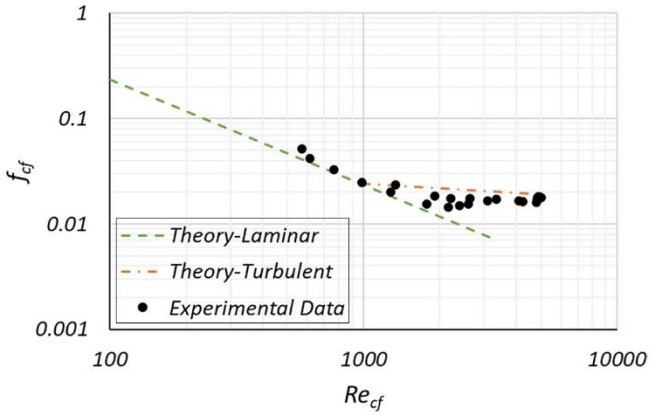

Source: Figure by authors

Figure 11. Comparison of experimental test results of rough case considering constricted dimensions of the minichannel and theoretical formulas for laminar and turbulent flows

The most notable dissimilarity emerges within the laminar flow regime at Reynolds number (*Re*) 480, which is 11.2%. As the Reynolds number increases beyond this threshold, the observed discrepancies progressively diminish.

In the context of a roughened minichannel, this study presents two distinct visual representations. Figure 10 delineates the outcomes of empirical investigations conducted on actual flow cross-sectional dimensions, whereas Figure 11 shows analogous findings derived from constricted dimensions. In Figure 10, the excellent agreement between CFD simulations and theoretical estimations depicts the efficacy of the methodology of accounting for roughness effects. However, a noticeable departure from theoretical expectations is evident within the experimental results presented in Figure 10, with the most pronounced discrepancies manifesting under laminar flow conditions. Figure 11 unveils a

compelling agreement between experimental observations under constrained dimensions and theoretical projections. This agreement shows that introducing roughness with specific height into a channel leads to a reduction in the cross-sectional area available for flow and that there will be no flow below a certain height of roughness. Considering the geometry of the roughness elements, no flow occurs below a certain height of the roughness. Matchup between theoretical estimations and experimental results considering constricted dimensions of the minichannel based on the average roughness height indicate that in the specific studied roughness, no flow occurs below average roughness height.

5. Flow through the gap between corotating disks

The research primarily investigates the inflow between corotating disks. It includes an evaluation of the effectiveness of the selected turbulent model and roughness approach. Due to the considerable complexity of the issue, which encompasses factors like the microscale dimensions of the gap, variable flow cross sections, and moving walls, performing flow analysis is a challenging endeavor.

To study the effect of roughness, simulations of compressible airflow are being carried out in a 0.75 mm gap (h) between corotating disks with outer and inner diameters of 0.1 m and 0.04 m, respectively. The outer and inner diameters of the gap operate as the inlet and outlet boundary conditions, respectively. The inlet was assumed to have a tangential velocity of 100 m/s and a radial velocity of 5 m/s, along with a turbulent intensity of 5%. For simplicity, the gap is simulated with a rotating disk on one side and symmetry as the boundary condition on the other. A refined mesh with about 387,000 nodes and a maximum y^+ value of less than one is used in the computational domain. The study examines five different roughness heights: 2%, 3.5%, 5%, 7% and 10% of the gap size (h), with all results compared to the smooth case. Figure 12 shows the viscosity ratio in the middle of the gap from the inlet to the outlet. This viscosity ratio, an indicator of turbulence levels, illustrates the impact of roughness on turbulent flow development.

An increase in roughness height results in a higher viscosity ratio. Near the inlet, the rise in viscosity ratio compared to the smooth case is minimal. The maximum difference happens in the middle of the channel where the boundary layer development and the effect of roughness on momentum diffusion become more evident. A higher viscosity ratio indicates a transition from a laminar to a turbulent boundary layer. As it is presented in the zoomed area of the Figure 12, initially, near the inlet, the turbulent flow with a turbulence intensity of 5% transitions to laminar, but as it moves from the inlet to the outlet, the roughness causes the boundary layers to become fully turbulent.

Furthermore, Figure 13 illustrates the influence of the roughness height on the downward shift of the velocity profile.

Raising the height of the roughness elements leads to a downward shift in the velocity profile and an increase in the viscosity ratio. The difference between the velocity profile and the theoretical smooth case is due to the underdevelopment and interaction of parallel boundary layers. Including roughness in the simulation results in this downward shift. In Figure 13, different roughness heights are shown as dimensionless values, with velocity profiles starting from the top of the sand-grain roughness, as there is no flow within the roughness elements. Greater roughness height increases turbulent kinetic energy near the wall. Moving away from the wall toward the symmetric boundary, boundary layer interactions are expected. Figure 14 illustrates the turbulent kinetic energy and turbulent eddy dissipation in the middle of the domain for cases with varying roughness heights compared to the smooth case.

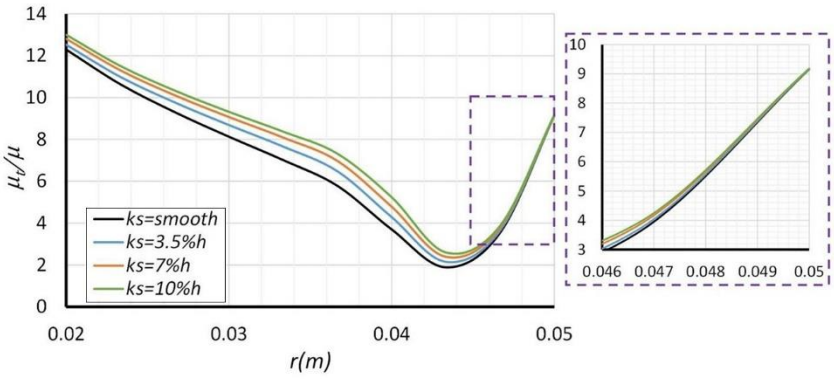

Source: Figure by authors

Figure 12. Effect of roughness on the viscosity ratio along the radius and at the mid-gap, considering roughness heights equal to 3.5%, 7% and 10% of the gap size

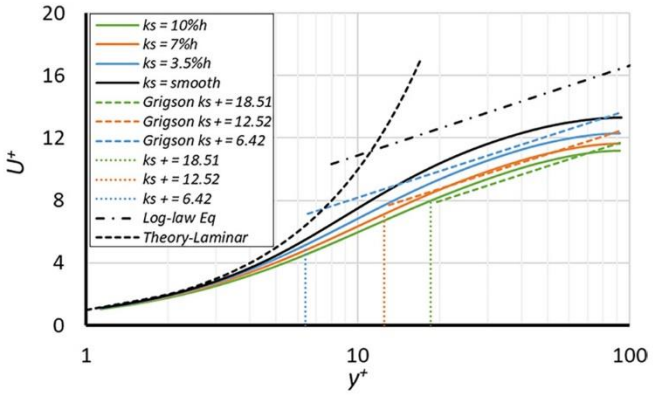

Source: Figure by authors

Figure 13. Comparison of the velocity profile of the flow in the middle of the disk for smooth case and cases with three different roughness heights against theoretical lines

Elevated roughness levels amplify velocity fluctuations near the wall, leading to an increase in momentum diffusion in the near-wall region with an increase in roughness height increase in the roughness height raises both turbulent kinetic energy and eddy dissipation specifically in the area near the wall. The growth reaches 26% for turbulent kinetic energy and 44% for turbulent eddy dissipation. The parameter's behavior in the vicinity of a symmetric boundary is less influenced by the roughness height. In Figure 15, the velocity components of smooth and five different sand-grain roughness heights (k_s) and compared. The velocity components are plotted along the gap at a radius of 0.035 m. All the simulations are done considering the same velocity inlet then because of energy lost due to roughness implementation, lower velocity magnitude in both radial and tangential components of the

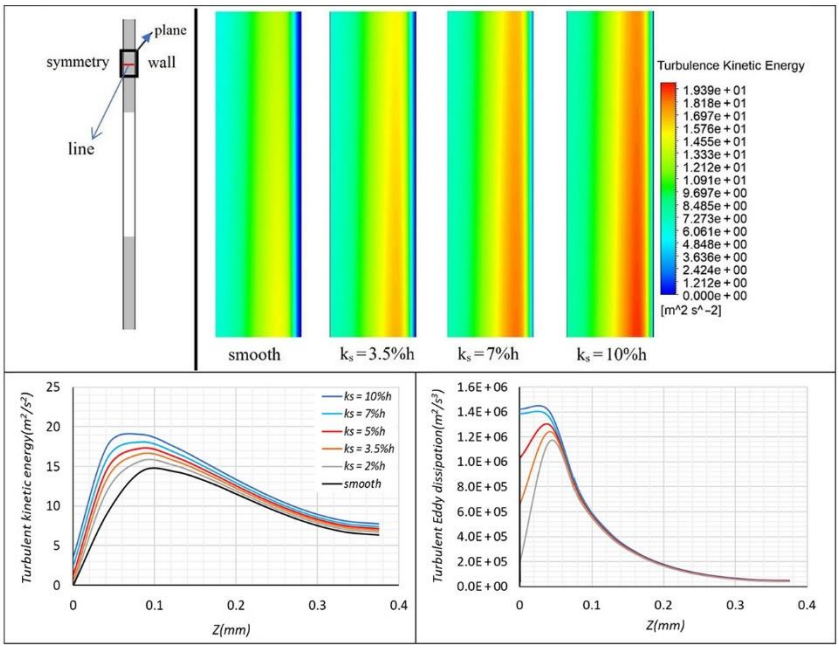

Source: Figure by authors

Figure 14. Demonstration of turbulent kinetic energy on a plane in the mid-radii for three roughness height compared to smooth case and comparison of turbulent kinetic energy and turbulent Eddy dissipation of different cases in the middle of the domain

rough case is visible. The plot reveals an increase in the magnitude of the radial velocity close to the wall, which subsequently diminishes with distance from the wall. In particular, the smooth case displays the most substantial changes at radial velocity in the examined location. The radial velocity profile attains its maximum value in the vicinity of the wall. This phenomenon is observed in both smooth and rough cases and contributes to the discrepancy between the resolved velocity profile and the theoretical predictions.

A downward shift in the velocity profile accelerates the transition to a turbulent regime. By examining factors like turbulent kinetic energy, turbulent eddy viscosity, viscosity ratio and radial velocity distribution in the near-wall region, it becomes clear that increasing roughness height enhances momentum diffusion and shear stress in this specific area.

6. Conclusions

A set of initial investigations was conducted to evaluate the effectiveness of the selected turbulence model and roughness method across varying degrees of complexity in domains, ranging from simple to more intricate configurations. In addition, the study systematically examines the impact of domain size, with thorough validation of results against DNS, experimental data and the outcomes derived from an in-house test setup in each specific case. Analyzing the data derived from literature and in-house test setup

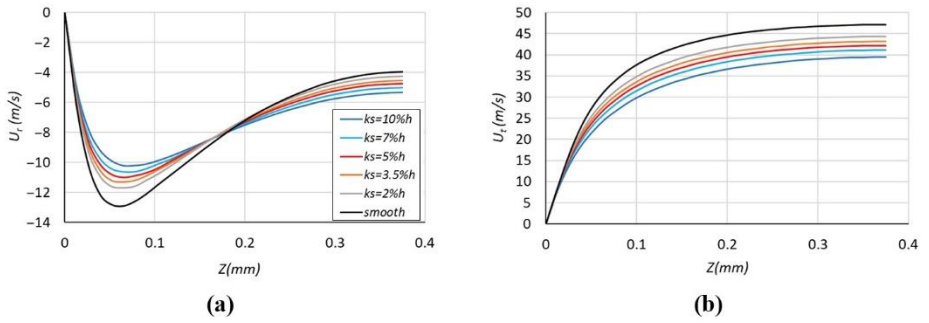

Source: Figure by authors

Figure 15. (a) Radial and (b) tangential velocity components at mid-disk for different roughness heights

depicts the effect of roughness on constriction of minichannel dimensions and flow cross section. Moreover, the agreement of the obtained CFD results with the validation cases reveals the sufficient performance of the used turbulence model and roughness method.

The distribution of velocity components in spanwise direction is intricately influenced by factors such as variable flow cross section, moving walls and the narrow gap size. These factors contribute to an increase in the radial velocity near the wall, which diminishes in the proximity of the symmetry region. This impact is also evident in the turbulent kinetic energy and viscosity ratio. It indicates increased diffusion of momentum near the wall compared to the symmetrical vicinity. Roughness plays a significant role in the formation of the velocity profile and causes the drop of the energy level moving from inlet to outlet.

Examining the flow between two disks that are rotating together, we observe that an increase in the roughness height results in an increase in the ratio of viscosity. This leads to a faster transition from laminar flow to a turbulent one closer to the wall. In addition, the level of roughness affects the turbulent kinetic energy and momentum diffusion, with a higher roughness height leading to greater values of these parameters near the wall. In the middle of the gap, close to symmetry, the flow is influenced by the interaction of boundary layers, impacting the flow parameters in this region.

References

Aliakbari, K., Ebrahimi-Moghadam, A., Pahlavanzadeh, M. and Moradi, R. (2023), "Performance characteristics and exhaust emissions of a single-cylinder diesel engine for different fuels: experimental investigation and artificial intelligence network", *Energy*, Vol. 284, p. 128760, doi: 10.1016/J.ENERGY.2023.128760.

Aupoix, B. (2015), "Roughness corrections for the k-ω shear stress transport model: status and proposals", *Journal of Fluids Engineering*, Vol. 137 No. 2, p. 21202, doi: 10.1115/1.4028122/374661.

Baviere, R., Ayela, F., Le Person, S. and Favre-Marinet, M. (2004), "An experimental study of water flow in smooth and rough rectangular micro-channels", *International Conference on Nanochannels*, 2004, *Asmedigitalcollection*, doi: 10.1115/ICMM2004-2338ï.

Brackbill, T. and Kandlikar, S. (2007), "Effects of low uniform relative roughness on single-phase friction factors in microchannels and minichannels", *Asmedigitalcollection.Asme.OrgTP*

Brackbill, SG KandlikarInternational Conference on Nanochannels, 2007, asmedigitalcollection.Asme.Org.

Chang, J., Jung, T., Choi, H. and Kim, J. (2019), "Predictions of the effective slip length and drag reduction with a lubricated micro-groove surface in a turbulent channel flow", *Journal of Fluid Mechanics*, Vol. 874, pp. 797-820, doi: 10.1017/JFM.2019.468.

Chedevergne, F. and Aupoix, B. (2017), "Accounting for wall roughness effects in turbulence models : a wall function approach", *7 Th European Conference for Aeronautics and Aerospace Sciences (EUCASS)*, doi: 10.13009/EUCASS2017-372.

Chedevergne, F. and Forooghi, P. (2020), "On the importance of the drag coefficient modelling in the double averaged Navier-Stokes equations for prediction of the roughness effects", *Journal of Turbulence*, Vol. 21 No. 8, pp. 463-482, doi: 10.1080/14685248.2020.1817465.

Colebrook, C.F. (1939), "Turbulent flow in pipes, with particular reference to the transition region between the smooth and rough pipe laws", *Journal of the Institution of Civil Engineers*, Vol. 11 No. 4, pp. 133-156, doi: 10.1680/ijoti.1939.13150.

Daadoua, M., Mathew, B. and Alnaimat, F. (2024), "Experimental investigation of pressure drop and heat transfer in minichannel with smooth and pin fin surfaces", *International Journal of Thermofluids*, Vol. 21, p. 100542, doi: 10.1016/J.IJFT.2023.100542.

Dai, B., Li, M. and Ma, Y. (2014), "Effect of surface roughness on liquid friction and transition characteristics in micro- and mini-channels", *Applied Thermal Engineering*, Vol. 67 Nos 1/2, pp. 283-293, doi: 10.1016/J.APPLTHERMALENG.2014.03.028.

Farzaneh-Gord, M., Pahlevan-Zadeh, M.S., Ebrahimi-Moghadam, A. and Rastgar, S. (2018), "Measurement of methane emission into environment during natural gas purging process", *Environmental Pollution*, Vol. 242, pp. 2014-2026, doi: 10.1016/J.ENVPOL.2018.07.027.

Gamrat, G., Favre-Marinet, M., Le Person, S., Bavière, R. and Ayela, F. (2008), "An experimental study and modelling of roughness effects on laminar flow in microchannels", *Journal of Fluid Mechanics*, Vol. 594, pp. 399-423, doi: 10.1017/S0022112007009111.

Grigson, C. (1992), "Drag losses of new ships caused by hull finish", *Journal of Ship Research*, Vol. 36 No. 2, pp. 182-196, doi: 10.5957/JSR.1992.36.2.182.

Hao, P.F., Yao, Z.H., He, F. and Zhu, K.Q. (2006), "Experimental investigation of water flow in smooth and rough silicon microchannels", *Journal of Micromechanics and Microengineering*, Vol. 16 No. 7, p. 1397, doi: 10.1088/0960-1317/16/7/037.

Hosni, M.H., Coleman, H.W., Garner, J.W. and Taylor, R.P. (1993), "Roughness element shape effects on heat transfer and skin friction in rough-wall turbulent boundary layers", *International Journal of Heat and Mass Transfer*, Vol. 36 No. 1, pp. 147-153, doi: 10.1016/0017-9310(93)80074-5.

Kandlikar, S.G., Schmitt, D., Carrano, A.L. and Taylor, J.B. (2005), "Characterization of surface roughness effects on pressure drop in single-phase flow in minichannels", *Physics of Fluids*, Vol. 17 No. 10, p. 100606, doi: 10.1063/1.1896985.

Kim, H.G., Shah, Y. and Kim, S.M. (2023), "Experimental investigation and analysis of two-phase flow instability of flow boiling in a mini-channel heat sink", *International Journal of Heat and Mass Transfer*, Vol. 213, p. 124309, doi: 10.1016/J.IJHEATMASSTRANSFER.2023.124309.

Kohl, M.J., Abdel-Khalik, S.I., Jeter, S.M. and Sadowski, D.L. (2005), "An experimental investigation of microchannel flow with internal pressure measurements", *International Journal of Heat and Mass Transfer*, Vol. 48 No. 8, pp. 1518-1533, doi: 10.1016/J.IJHEATMASSTRANSFER.2004.10.030.

Lalegani, F., Saffarian, M.R., Moradi, A. and Tavousi, E. (2018), "Effects of different roughness elements on friction and pressure drop of laminar flow in microchannels", *International Journal of Numerical Methods for Heat and Fluid Flow*, Vol. 28 No. 7, pp. 1664-1683, doi: 10.1108/HFF-04-2017-0140/FULL/PDF.

Maciejewska, B. and Piasecka, M. (2020), "Time-dependent study of boiling heat transfer coefficient in a vertical minichannel", *International Journal of Numerical Methods for Heat and Fluid Flow*, Vol. 30 No. 6, pp. 2953-2969, doi: 10.1108/HFF-12-2018-0781/FULL/PDF.

Nikuradse, J. (1933), "Laws of flow in rough pipes Nikuradse", Nikuradse, National Advisory Committee for Aeronautics.

Pahlavanzadeh, M., Rusin, K. and Wróblewski, W. (2023a), "Evaluation of dynamic correction of turbulence wall boundary conditions to simulate roughness effect in minichannel with rotating walls", *International Journal of Numerical Methods for Heat and Fluid Flow*, Vol. 33 No. 12, pp. 3915-3939, doi: 10.1108/HFF-03-2023-0160/FULL/PDF.

Pahlavanzadeh, M., Rusin, K. and Wróblewski, W. (2023b), "Assessment of turbulent parameters modification to model roughness in the flow between rotating disks of Tesla turbine", Simulation and Environmental Impact of Energy Systems, doi: 10.52202/069564-0048.

Pfund, D., Rector, D., Shekarriz, A., Popescu, A. and Welty, J. (2000), "Pressure drop measurements in a microchannel", *AIChE Journal*, Vol. 46 No. 8, pp. 1496-1507, doi: 10.1002/aic.690460803.

Rahman, M.M. (2000), "Measurements of heat transfer in microchannel heat sinks", *International Communications in Heat and Mass Transfer*, Vol. 27 No. 4, pp. 495-506, doi: 10.1016/S0735-1933(00)00132-9.

Riddle, R.A., Contolini, R.J., Bernhardt, A.F., Riddle, R.A., Contolini, R.J. and Bernhardt, A.F. (1991), "Design calculations for the microchannel heatsink", *STIN*, Vol. 91, p. 22534.

Rusin, K., Wróblewski, W. and Rulik, S. (2021), "Efficiency based optimization of a Tesla turbine", *Energy*, Vol. 236, p. 121448, doi: 10.1016/J.ENERGY.2021.121448.

Rusin, K., Wróblewski, W., Rulik, S., Pahlavanzadeh, M. and Hasani Malekshah, E. (2023), "Investigation on the influence of surface roughness of rotating microchannel on flow conditions", Volume 13D: Turbomachinery—Multidisciplinary Design Approaches, Optimization, and Uncertainty Quantification; Radial Turbomachinery Aerodynamics; Unsteady Flows in Turbomachinery, *American Society of Mechanical Engineers Digital Collection*, doi: 10.1115/GT2023-101917.

Schmitt, D. and Kandlikar, S. (2005), "Effects of repeating microstructures on pressure drop in rectangular minichannels", *Asmedigitalcollection.Asme.OrgDJ Schmitt, SG KandlikarInternational Conference on Nanochannels*, 2005, asmedigitalcollection.Asme.Org.

Sigal, A. and Danberg, J.E. (2012), "New correlation of roughness density effect on the turbulent boundary layer", *AIAA Journal*, Vol. 28 No. 3, pp. 554-556, doi: 10.2514/3.10427.

Stimpson, C.K., Snyder, J.C., Thole, K.A. and Mongillo, D. (2017), "Scaling roughness effects on pressure loss and heat transfer of additively manufactured channels", *Journal of Turbomachinery*, Vol. 139 No. 2, p. 21003, doi: 10.1115/1.4034555/378795.

Swamee, P.K. and Jain, A.K. (1976), "Explicit equations for pipe-flow problems", *Journal of Hydraulic Engineering*, Vol. 102, pp. 657-664.

Tam, L.M., Tam, H.K. and Ghajar, A.J. (2011), "Simultaneous heat transfer and pressure drop measurements for a horizontal micro-tube", ASME/JSME 2011 8th Thermal Engineering Joint Conference, AJTEC 2011, *American Society of Mechanical Engineers Digital Collection*, doi: 10.1115/AJTEC2011-44218.

Tesla, N. (1913), "Nikola Tesla U.S. Patent 1,061,206 - Turbine".

Vajravel, L.V., Kuppusamy Swaminathan, S., Baskaran, S. and Kalpoondi Sekar, R. (2019), "Experimental investigations on heat transfer in a new minichannel heat sink", *International Journal of Thermal Sciences*, Vol. 140, pp. 144-153, doi: 10.1016/J.IJTHERMALSCI.2019.02.029.

Wagner, R.N. and Kandlikar, S.G. (2012), "Effects of structured roughness on fluid flow at the microscale level", *Heat Transfer Engineering*, Vol. 33 No. 6, pp. 483-493, doi: 10.1080/01457632.2012.624850.

Wibel, W. and Ehrhard, P. (2009), "Experiments on the laminar/turbulent transition of liquid flows in rectangular microchannels", *Heat Transfer Engineering*, Vol. 30 Nos 1/2, pp. 70-77, doi: 10.1080/01457630802293449.

Xie, G., Li, S., Sunden, B. and Zhang, W. (2014), "Computational fluid dynamics for thermal performance of a water-cooled minichannel heat sink with different chip arrangements", *International Journal of Numerical Methods for Heat and Fluid Flow*, Vol. 24 No. 4, pp. 797-810, doi: 10.1108/HFF-01-2013-0013/FULL/PDF.

Yuan, J. and Piomelli, U. (2014), "Roughness effects on the Reynolds stress budgets in near-wall turbulence", *Journal of Fluid Mechanics*, Vol. 760, p. R1, doi: 10.1017/JFM.2014.608.

Corresponding author
Mohammadsadegh Pahlavanzadeh can be contacted at: mohammadsadegh.pahlavanzadeh@polsl.pl and sadegh_pahlavan@yahoo.com

Paper III

On the Flow in the Gap between Co-rotating Disks of Tesla Turbine with Different Supply Configurations: A Numerical Study

energies

MDPI

Article

On the Flow in the Gap between Corotating Disks of Tesla Turbine with Different Supply Configurations: A Numerical Study

Mohammadsadegh Pahlavanzadeh, Włodzimierz Wróblewski * and Krzysztof Rusin

Department of Power Engineering and Turbomachinery, Silesian University of Technology, 44-100 Gliwice, Poland; mohammadsadegh.pahlavanzadeh@polsl.pl (M.P.); krzysztof.rusin@polsl.pl (K.R.)
* Correspondence: wlodzimierz.wroblewski@polsl.pl

Abstract: Momentum diffusion and kinetic energy transfer in turbomachinery have always been significant issues, with a considerable impact on the performance of the bladeless Tesla turbine. This radial turbine shows high potential for various energy applications, such as Organic Rankine Cycle or combined heat and power systems. Analyzing the flow inside the gap between the corotating disks of the Tesla turbine presents challenges due to several factors, including submillimeter length scales, variations in flow cross-section, interactions of body forces arising from rotation with turbulence, interactions between the turbine's inlet nozzles and rotor, and moving walls. General design parameters, e.g., number of nozzles, also pose a challenge in order to achieve the full potential of this turbine. In this research, two different variants of the supply system are considered with six and forty nozzles. To minimize computational expenses, a portion of the entire domain is considered. The flow in each domain, consisting of one inlet nozzle and a segment of one gap between the disks, is examined to reveal the complexity of flow structures and their impact on the Tesla turbine performance. Large Eddy Simulation (LES) with the Smagorinsky subgrid-scale model is used to verify the results of the *k*-ω Shear-Stress Transport (SST) turbulence model in the first case study with six nozzles. Analyzing the results indicates that the *k*-ω SST model provides valuable insights with appropriate accuracy. The second case study, with forty nozzles, is simulated using the *k*-ω SST turbulence model. The research compares flow structure, flow parameters, and their impact on the system's performance. From the comparison between the *k*-ω SST turbulence model and LES simulation, it was observed that although the *k*-ω SST model slightly overestimates the general parameters and damps fluctuations, it still provides valuable insights for assessing flow structures. Additionally, the mesh strategy is described, as the LES requirements make this simulation computationally expensive and time-consuming. The overall benefits of this method are discussed.

Keywords: large eddy simulation; Smagorinsky subgrid; turbulence; Tesla turbine

Citation: Pahlavanzadeh, M.; Wróblewski, W.; Rusin, K. On the Flow in the Gap between Corotating Disks of Tesla Turbine with Different Supply Configurations: A Numerical Study. *Energies* **2024**, *17*, 4472. https://doi.org/10.3390/en17174472

Academic Editors: Daniela Anna Misul and Simone Salvadori

Received: 20 August 2024
Revised: 28 August 2024
Accepted: 3 September 2024
Published: 6 September 2024

1. Introduction

In recent years, there has been a rising fascination with mini expanders, which are increasingly utilized in diverse industries, such as combined heat and power, or systems based on the Organic Rankine Cycle (ORC) [1–3]. These devices are characterized by their notable attributes, including reliable operation under various conditions and cost-effective production [4]. Among these mini expanders is the Tesla turbine, classified within the realm of friction turbomachinery [5]. The efficiency of friction turbomachines hinges on the transfer of momentum occurring between the operational flow and rotating disks through momentum diffusion [6,7]. Walls play a crucial role as the primary source of turbulence and the establishment of boundary layers. In the context of friction turbomachinery, these walls function as kinetic energy exchangers, exerting a noteworthy influence on the overall performance of such systems [8,9].

To assess the flow behavior in the near-wall region, the theoretical wall functions have been formulated [10–13]. Nevertheless, in scenarios involving small flow cross-sections, it becomes imperative to consider other influential parameters and phenomena, such as the interaction of boundary layers. This consideration may result in outcomes that deviate from the theoretical predictions [14–16].

Despite being invented more than a century ago, the Tesla turbine received minimal attention until the past decade. The increasing demand for harnessing low-energy sources has sparked a renewed interest in adopting expanders with characteristics akin to the Tesla turbine, known for their simplicity, affordability, and adaptable construction.

Diverging from conventional bladed turbines, the Tesla turbine is a bladeless machine for fluid flow, converting fluid enthalpy into mechanical energy through viscous forces [17,18]. This transformation occurs within the rotor, which consists of multiple disks spaced closely together. By leveraging fluid viscosity, momentum diffusion from the fluid to the disks transpires. The working medium enters the rotor at the outer edge of the disks, and the initial fluid layer adheres to the disk surface due to adhesive forces and, in some cases, the Coanda effect. Collisions between particles from faster and slower fluid layers facilitate momentum exchange, transferring momentum to the first fluid layer in contact with the disk, thereby initiating rotor rotation.

Reducing the area of the flow cross-section has a notable impact on flow characteristics [19–21]. In the context of submillimeter dimensions, the development and interaction of boundary layers, coupled with flow fluctuations, lead to a transient behavior that is challenging to predict. Much of the numerical research addressing this issue diverges from experimental data due to the limited accuracy of the applied models [22]. Simulating such phenomena using Computational Fluid Dynamics (CFD) poses challenges, and considering the mesh requirements of various turbulence models, the k-ω SST model emerges as the most suitable option for simulating flow in such a small domain [6,23]. The investigation of flow between corotating disks, with a uniform inlet flow at the outer diameter, resembling a simplified version of the corotating disks in the Tesla turbine, has revealed the crucial importance of understanding flow behavior in such domains in greater detail [7]. For a more realistic representation of the Tesla turbine operation, where nozzles deliver fluid at given points, challenges arise in characterizing flow features, particularly in the vicinity of the jet. In this zone, the interaction of the inlet jet with developing boundary layers from the corotating disks intensifies the transient behavior, necessitating a more meticulous analysis. Rusin et al. [24] provided an analysis and evaluation of a Tesla turbine model, highlighting the influence of turbulence models on predicting the turbine's operational conditions. They examined various turbulence models using different time and space discretization approaches. Additionally, they determined the distribution of power units across the disks and compared the turbine's power predictions from numerical analysis with preliminary experimental findings. They observed an overestimation across all utilized turbulence models compared to experimental data.

In one of their earlier works, Rusin et al. [25] constructed a Tesla-type turbine featuring five corotating disks and a plenum chamber equipped with 4 nozzles. They conducted an optimization based on efficiency to identify optimal geometrical and operational parameters. Throughout their investigations, they aimed to minimize radial tip clearance to prevent rotor displacement from causing disk rubbing against the casing due to rotational speed and manufacturing inaccuracies. They focused on efficiency-based numerical optimization of the Tesla turbine, optimizing parameters such as inlet nozzle height, inter-disk gap, nozzle angle, pressure, and rotational velocity.

Building upon recent literature, the current study focuses on a turbine with optimized parameters to further investigate flow characteristics within the gap between corotating disks. A high-fidelity simulation method like LES proves beneficial in providing a more accurate estimation of the transient behavior of the system [26–28].

The lack of experimental data in flow analysis inside the gap between corotating disks of a Tesla turbine poses a challenge in accepting the results of turbulent models and

highlights the need to prove their accuracy and reliability. Moreover, the literature suggests that the turbulence models, e.g., *k*-ω SST, tend to dampen fluctuations, particularly in areas where the flow is turbulent but not fully developed, resulting in smoother flow behavior in the computational domain [29,30]. Moreover, the body forces arising from the rotation may contribute to the overestimation of eddy viscosity in the case of RANS models. This study focuses on considering only a fraction of the Tesla turbine rotor, namely 1/6 and 1/40 of its perimeter, employing a supply system with 6, and 40 nozzles. The first case with a lower number of nozzles was simulated to verify the results obtained from the *k*-ω SST model against a high-fidelity model. Another aspect investigated is the effect of the number of nozzles on flow structures. Considering the derived results from the first case, the *k*-ω SST model is employed to simulate the case with the higher number of nozzles. The objective is to precisely analyze the flow between the corotating disks of the turbine and to assess the reliability of *k*-ω SST model in this study case.

2. Governing Equations

The inquiry detailed in the paper involved conducting numerical simulations using both the *k*-ω SST turbulence model and LES.

The governing equations involve continuity, momentum, and energy conservation in their respective forms.

$$\frac{\partial \rho}{\partial t} + \frac{\partial}{\partial x_j}(\rho U_j) = 0 \tag{1}$$

$$\frac{\partial (\rho U_j)}{\partial t} + \frac{\partial}{\partial x_j}(\rho U_i U_j) = -\frac{\partial p}{\partial x_i} + \frac{\partial \tau_{ij}}{\partial x_j} + \rho f_i \tag{2}$$

$$\frac{\partial \left(\rho \left(e + \frac{1}{2} U_i U_i\right)\right)}{\partial t} + \frac{\partial}{\partial x_j}\left(\rho U_j \left(e + \frac{1}{2} U_i U_i\right)\right) = -\frac{\partial}{\partial x_j}(p U_j) + \frac{\partial}{\partial x_j}(\tau_{ij} U_i) - \frac{\partial}{\partial x_j}(q_j) + \rho f_i U_i \tag{3}$$

The $k - \omega$ *SST* model constituted the turbulence closure, in which the transport equations of turbulence kinetic energy k and specific dissipation rate ω are solved:

$$\frac{\partial (\rho k)}{\partial t} + \frac{\partial}{\partial x_j}(\rho U_j k) = \frac{\partial}{\partial x_j}\left[\left(\mu + \frac{\mu_t}{\sigma_k}\right)\frac{\partial k}{\partial x_j}\right] + P_k - \rho k \omega \tag{4}$$

$$\frac{\partial (\rho \omega)}{\partial t} + \frac{\partial}{\partial x_j}(\rho U_j \omega) = \frac{\partial}{\partial x_j}\left[\left(\mu + \frac{\mu_t}{\sigma_\omega}\right)\frac{\partial \omega}{\partial x_j}\right] + \alpha \frac{\omega}{k} P_k - \beta \rho \omega^2 \tag{5}$$

In the LES, closing the Navier–Stokes equations is accomplished through the implementation of the wall-modeled large eddy simulation (WMLES) model, which calculates the subgrid-scale (SGS) eddy viscosity. The foundational algebraic WMLES formulation was initially introduced in the research of Shur et al. [31]. This model integrates a mixing length model with a modified Smagorinsky model [32] and incorporates the wall-damping function proposed by Piomelli et al. [33].

$$\nu = min\left[(\kappa d_w)^2,\ (C_{Smag}\Delta)^2\right].S.\left\{1 - exp\left[-\left(\frac{y^+}{25}\right)^3\right]\right\} \tag{6}$$

$$\Delta = min(max(C_w.d_w; C_w.h_{max}, h_{wn}); h_{max}) \tag{7}$$

where $\kappa = 0.4187$, $C_{Smag} = 0.2$, and $C_w = 0.15$ are constants.

3. Model Definition

3.1. Calculation Domain and Boundary Conditions

The numerical investigations were conducted using Ansys Fluent (2024 R1), a commercially available software based on the finite volume method. Two Tesla turbine concepts

were the focus of the study: one with six nozzles (referred to as N6) and the other with forty nozzles (referred to as N40). Air was selected as the operating fluid, and the simulations followed ideal gas behavior. In each case, the geometry of the investigation exhibited symmetrical behavior every 60 and 9 degrees. To optimize computational efficiency, the simulation domain represented only a portion of the entire turbine. Simulating the entire apparatus would require a large number of cells, leading to a substantial increase in both simulation time and costs while not providing a significant improvement in the data quality.

In simulations, the absolute coordinate system was employed. The computational domain consisted of three separate sections. The first section is a plenum chamber and acts as the supply system. The second section is a converging nozzle with a throat size of 0.7 mm, oriented at an 8-degree angle with respect to a tangential direction. The final part represents 1/6 and 1/40 of the gap between two corotating disks (60 and 9 degrees), with outer and inner diameters of 160 mm and 80 mm, respectively. The considered interdisk gap size is 0.75 mm, and the radial tip clearance between the casing and the disks is set at 0.25 mm, which is minimized based on the constraints of real Tesla turbine design and manufacturing limitations. Periodic boundary conditions were applied on both sides of the disc sector in N6 with a central angle of 60 degrees, and in N40 with an angle of 9 degrees, as shown in Figure 1. The simulation considered the thickness of the plenum chamber to be equal to the gap size, and symmetric boundary conditions were applied on both sides of the chamber. The flow in the computational domain was simulated in an absolute frame, and the walls of corotating disks were set to rotate. To simplify the computational model, the thickness of the domain was equated to the size of the gap. This configuration establishes a one-to-one design where each gap is linked to its corresponding nozzle jet [34]. This setup facilitates the direct passage of the nozzle jet through the gap, thereby ignoring losses from the interaction between the inlet jet and the disk tips. The rotational speed, which was set at 17,500 RPM, the geometry of the turbine, and selected operating and boundary conditions were determined based on our previous study of a Tesla turbine, which resulted in maximum efficiency [16]. Additionally, the inlet conditions include a gauge total pressure of 2 bars, a total temperature of 300 K, and a turbulence intensity of 5%. Ambient pressure is applied at the outlet.

The numerical solution of the conservation equations Involves a weighted average of second-order upwind and central interpolations of variables. Time discretization is implemented using a second-order implicit transient formulation.

Figure 1 depicts a schematic of the studied cases, including different parts of the computational domains and the employed boundary condition in each case. Moreover, the utilized mesh in each case is illustrated. The meshing strategy is discussed in the next section.

3.2. Mesh for k-Omega SST Model

In this section, the mesh for N6, which was simulated using the uRANS method and *k*-ω SST turbulence model, is presented. The mesh independence study was conducted by varying the number of nodes in radial, circumferential, and axial directions within the range of 60–412, 27–156, and 15–43, respectively. In all cases, the hexahedral mesh was generated with the first layer thickness of 0.5 µm to ensure that $y^+ < 1$.

In the mesh independence check, the focus was on the gap between corotating disks. In the gap, the node distribution in the radial direction was denser in the rotor tip region, with the minimum and maximum node distances of 0.1 mm and 0.5 mm, respectively. In the circumferential direction, the higher resolution close to the nozzle jet was applied with minimum and maximum spacing of 0.1 mm and 0.3 mm, respectively. In the plenum chamber, the hexahedral mesh is generated with an edge size in the range of 0.05–0.2 mm and a total node number of 600 k. Throughout all cases, a constant number of nodes in the plenum chamber was considered to ensure the same conditions at the inlet into the gap.

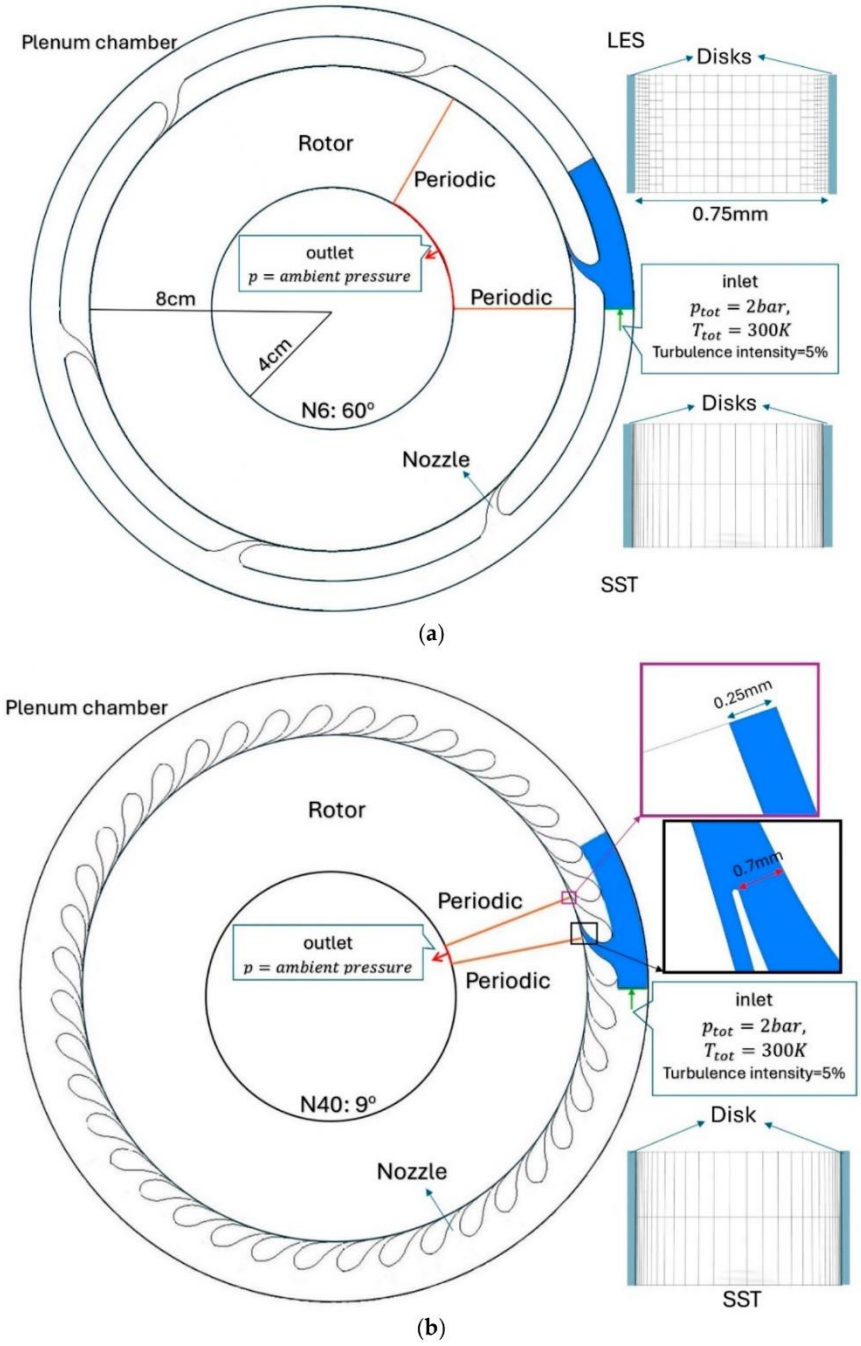

Figure 1. Schematic of the computational domains, boundary conditions, and generated mesh for (**a**) N6, and (**b**) N40.

In each case, the total torque T and power generated N considering the full gap between two corotating disks were calculated by:

$$T = \int r \times \tau dA \tag{8}$$

$$N = \omega_a \int r \times \tau dA \tag{9}$$

Torque generation, as a global parameter, is used to verify the mesh independence study. This parameter directly or indirectly accounts for many flow and thermodynamic quantities, such as velocity gradients, pressure gradients, and changes in viscosity due to temperature, all of which contribute to wall shear stresses that form the basis of torque. It is worth mentioning that torque is quite sensitive to mesh quality and refinement, making it a strong candidate for mesh assessment.

Table 1 presents the generated torque for all the studied meshes in this regard. The generated power in every mesh setup is depicted in Figure 2. As it is shown, changes in power generation for the mesh size in the gap higher than 1.3 million are lower than 0.25%. Furthermore, for mesh sizes higher than 2.4 million, the generated power is almost constant. Then, the chosen number of nodes for further steps of study is 2.4 million nodes in the gap between corotating disks, utilizing 400 nodes in the circumferential direction, 150 nodes in the radial direction, and 40 nodes along the gap with a growth ratio of 1.38. The total number of nodes in this case reached 3 million, including the plenum chamber. Since N40 was a subset of N6, the mesh generation for this case involved a distribution of 60 nodes in the circumferential direction, 150 nodes in the radial direction, and 40 nodes in the spanwise direction, with an equal number of nodes in the plenum chamber.

Table 1. Node distribution, total number of nodes, and torque generation for the mesh independence study.

Nodes Distribution				Torque (Nm)
Radial Direction	Circumferential Direction	Spanwise	Total	
156	412	43	2,763,696	0.04157
150	400	40	2,400,000	0.04157
122	362	30	1,324,920	0.0415
65	154	24	240,240	0.04145
27	60	15	24,300	0.04101

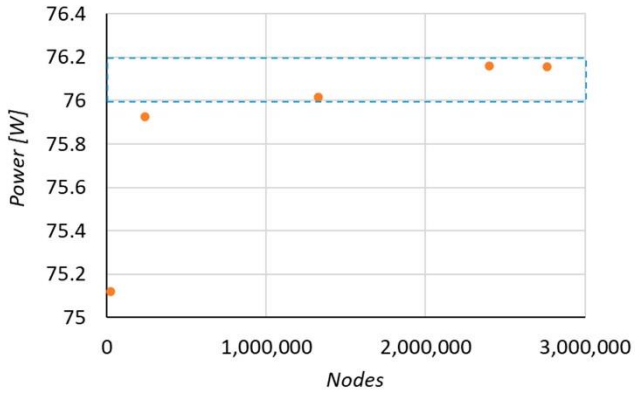

Figure 2. Power generation computed for different meshes (N6).

The selected time step of 0.001 s resulted in smooth convergence. To assess the convergence of the solution, the mass balance, torque generation, and fluctuation of static pressure and velocity magnitude at selected points with the crucial nozzle effect were measured. Additionally, after convergence, the residuals were observed to be between 10^{-4} and 10^{-5}. The study examined the relationship between parameter fluctuations and the size of time steps used in simulations. Transient flow simulations were conducted with

testing of time steps ranging from 10^{-3} s to 10^{-6} s. Starting with a time step of 10^{-6} s, which corresponds to the Courant number of 1 in the whole computational domain, we tested progressively larger time steps in each phase to evaluate the parameters' sensitivity. No parameter fluctuations were detected during this stage of the study. Therefore, a time step of 0.001 s was selected for other calculations.

3.3. Mesh for LES

The required mesh for LES simulation is only generated in the gap between the corotating disks of N6. The supply chamber is simulated by employing the same mesh as the *k*-ω SST. For the initial phase of the LES simulation, 5 million cubic cells were employed, initialized with the converged *k*-ω SST solution obtained after 10,000 iterations. The success of an LES simulation requires the resolution of at least 80% of the turbulent kinetic energy. To achieve this, it is necessary to resolve eddies whose sizes are larger than approximately half the size of the integral length scale (l_0). The integral length scale is a local quantity that can be evaluated using k and ω values obtained from the Reynolds–Averaged Navier–Stokes (uRANS) simulation:

$$l_0 = \frac{k^{0.5}}{(C_\mu \omega)} \tag{10}$$

where $C_\mu = 0.09$.

Based on Kolmogorov's energy spectrum to resolve 80% of the eddies we have:

$$\frac{l_0}{\Delta} \geq 4.8 \tag{11}$$

where $\Delta = \sqrt[3]{cell\ volume}$.

To adhere to the mesh requirements stipulated by the LES, adjustments were made to the cubic mesh. The presence of rotating walls induced the generation of small eddies in the adjacent wall area. To meet the LES criteria in at least 90% of the domain, the mesh underwent two rounds of modification, achieving a total number of cells of 50 million. The mesh modification process was conducted to ensure that the ratio of the integral length scale to cell size (l_0/Δ) remained higher than 4.8. This entailed two rounds of modification to the first two layers of the source mesh near the walls, accompanied by a switch from the *k*-ω SST model to LES. The thickness of the first mesh layer adjacent to the wall, after two modifications, was adjusted to 13 µm, corresponding to a y^+ value of approximately 1.6.

The simulation achieved convergence after 72,000 iterations, with the initial time step set at 10^{-8} and gradually increased to 10^{-6}. The Courant number was checked at each step. The maximum Courant number in the case of the time step equal to 10^{-7} was equal to one. A schematic representation of the computation domain, boundary conditions, and the modified mesh is depicted in Figure 1.

4. Results and Discussion

4.1. Comparison k-ω SST and LES Simulations for N6

The findings from both *k*-ω SST and LES simulations indicate that the mass flow rate considering the full gap between corotating disks was measured at 0.00221 kg/s and 0.0023 kg/s, respectively. At the nozzle's inlet and outlet, the average gauge pressures were determined to be 2 bar and 0.3 bar, respectively. Additionally, the average total temperature at the nozzle's inlet was 300 K, and the average static temperature at the nozzle's outlet was 238 K. This difference implies a nozzle efficiency of 96%.

The primary goal of this investigation is to thoroughly assess the flow characteristics within the gap between corotating disks. Consequently, the average parameters at the inlet of the gap are of considerable significance. The mass average radial velocity for *k*-ω SST and LES were −28.19 m/s, and −33 m/s, respectively. Moreover, the circumferential velocity of *k*-ω SST was 302.44 m/s, and this value for LES simulation was equal to 284.18 m/s.

The primary component of velocity in this context is the circumferential one. In the case of LES, the high-fidelity simulation resolves the generated vorticities at the outer diameter of the disks, which introduces additional resistance to the flow in this region. At the same time, the literature suggests that the *k*-ω SST model tends to dampen fluctuations (due to overestimation of eddy viscosity), particularly in areas where the flow is turbulent but not fully developed [29,30]. Due to the undeveloped boundary layer at the outer diameter of the disks, this damping effect is most pronounced in this area. Moreover, the angle of attack can slightly change due to the aforementioned phenomena, which impacts the velocity components. Consequently, a higher level of vorticities presented by LES and damping of fluctuations by *k*-ω SST causes the LES to present lower circumferential velocity compared to the *k*-ω SST at the entrance to the gap. Furthermore, the average temperature of mass flow was calculated to be 250 K and 257 K for *k*-ω SST and LES simulation, respectively, while the area-averaged gauge pressure was recorded as 22,637 Pa and 24,775 Pa.

The crucial factor In assessing the turbine's performance involves analyzing the torque generated on the walls. In the initial stage, this parameter is scrutinized using both the *k*-ω SST turbulence model and the LES simulation. The torque values obtained from the *k*-ω SST and LES simulations were 0.0417 Nm and 0.0400 Nm, respectively.

The system's efficiency is determined based on the total-to-static enthalpy drop by the following formula:

$$\eta = \frac{N}{\dot{m} c_p T_{in} \left(1 - \left(\frac{p_{out}}{p_{in}} \right)^{\frac{\gamma - 1}{\gamma}} \right)} \tag{12}$$

Considering Equation (9), the power derived from *k*-ω SST and LES simulations were 76.4 W and 73.3 W, respectively. Furthermore, from Equation (12), the system efficiency in the *k*-ω SST and LES simulations was determined to be 43.0% and 39.21%, respectively.

The 4.2% overestimation of torque by the *k*-ω SST model prompts further consideration, particularly considering the distribution of wall shear stress on the rotating walls. To explore this further, it is possible to visualize the circumferential and radial wall shear stress, represented as a contour on a rotating wall and as distribution along the radial lines. These lines are presented in Figure 3, where they are labeled, as A, B, C, and D. Lines A and D are located at 15 and 45 degrees in mid-gap. Additionally, lines B and C are positioned at a 30-degree angle on the surfaces of both rotating disks.

The wall shear stress represents the energy transfer between the operating flow and the rotating disks, with only the circumferential component generating torque around the rotational axis. Figure 3 illustrates the distribution of both components of wall shear stress on the rotating disk.

As depicted in Figure 3, the maximum values of both components of wall shear stress are derived at the outer diameter of the disks. The maximum radial wall shear stress occurs particularly in the vicinity of the inlet jet. The zone near the outer diameter of the disks holds a significant influence on torque generation due to its greater distance from the rotational axis. As illustrated in Figure 3, the *k*-ω SST simulation anticipates a larger region with maximum circumferential wall shear stress near the outer diameter. In both simulations, it was observed that the primary area contributing to torque generation is confined to the outer 12.5% of the rotating wall surface. As the flow progresses from the outer to the inner diameter, there is a noticeable reduction in the generated wall shear stress. Upon closer examination of the provided plot, it becomes evident that the most substantial decline in generated wall shear stress occurs in this region, accounting for nearly 90% of the energy loss in the operating flow. In the inner sections, changes in this parameter are insignificant. The domain most affected by the inlet jet is shown in detail in the zoomed area of Figure 3. The *k*-ω SST dampened the fluctuations and presented a smoother drop on both components of wall shear stress. The *k*-ω SST model predicts a larger area directly influenced by the jet shown in the circumferential wall shear stress contour. In the vicinity of the jet's outlet, the presence of an underdeveloped boundary layer results in elevated

circumferential wall shear stress. In this region, the boundary layer is still in the process of development, leading to a high-velocity gradient near the wall surface.

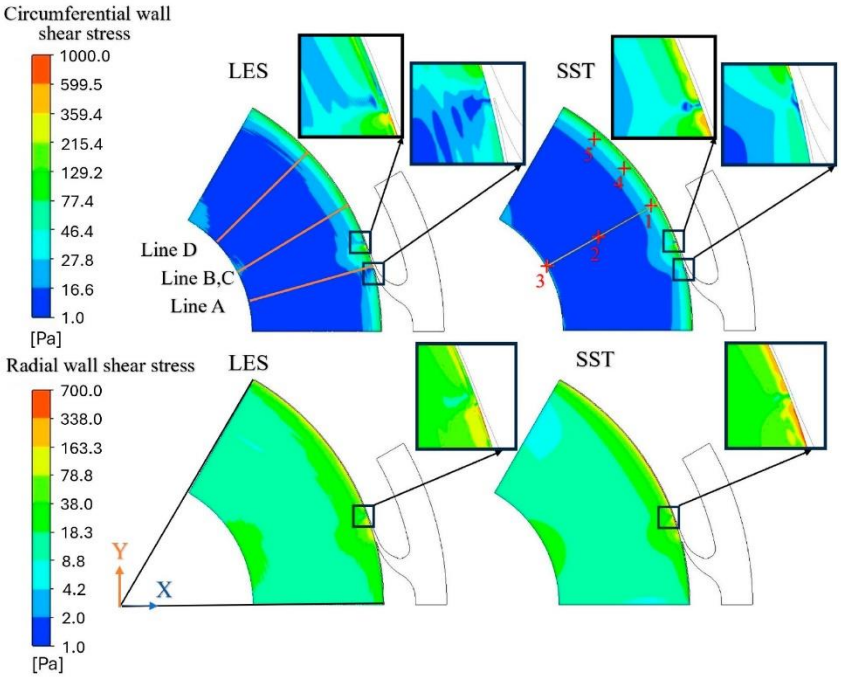

Figure 3. Contours of circumferential and radial wall shear stresses obtained from LES and *k*-ω SST simulations (N6). Lines A, B, C, and D are positioned along the radii, while lines 1–5 represent the distribution along the gap.

To determine the distribution of wall shear stress on the disk's surfaces, components of this parameter are plotted along lines B and C in Figure 4. The area with the higher fluctuations is zoomed in on part of the plot. The *k*-ω SST model displays significant symmetry along lines B and C, in contrast to LES. The *k*-ω SST model predicts higher wall shear stress in radial and circumferential directions, especially in the final 20% near the nozzle jet. Moreover, the fluctuation of wall shear stress in the LES simulation reveals a transient behavior of the flow, which is different from the *k*-ω SST model that shows smoother distributions.

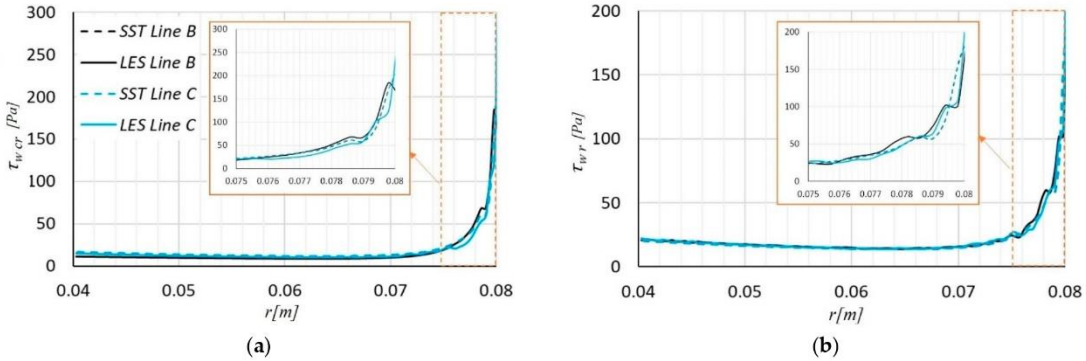

Figure 4. Circumferential (**a**) and radial (**b**) wall shear stress along lines B and C for LES and *k*-ω SST simulation of N6.

Figure 5 represents the pressure and velocity distributions along lines A and D, defined in Figure 3, in the middle of the gap at angles of 15 and 45 degrees relative to the horizontal line. Lines A and B are selected to be just before and after the area with the maximum effect of the nozzle jet, respectively.

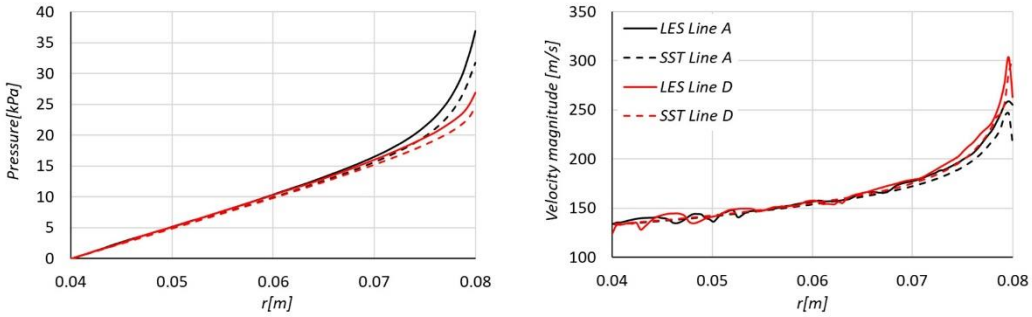

Figure 5. Distribution of pressure and velocity magnitude along the lines A and D.

Upon analyzing Figures 3 and 5, it is evident that there is a noticeable effect of the nozzle, characterized by a drop in static pressure and an increase in velocity when moving from line A to line B. This effect is primarily observed at the outer edge of the corotating disks. However, as one moves from the outer edge to the inner edge, both lines exhibit similar values for pressure and velocity. Additionally, Figure 5 effectively illustrates the velocity fluctuation obtained from the LES throughout the entire studied domain. This fluctuation is particularly pronounced in line D, which is more influenced by the inlet jet.

Figure 6 depicts the dimensional radial velocity profile of the flow within the gap at three specified locations: 1, 2, and 3 illustrated in Figure 3. Moving from the outer to the inner diameter of the disks, the radial velocity increases. This increase in the radial component of the velocity is evident along all studied lines, reaching its maximum in the area close to the wall at line 3.

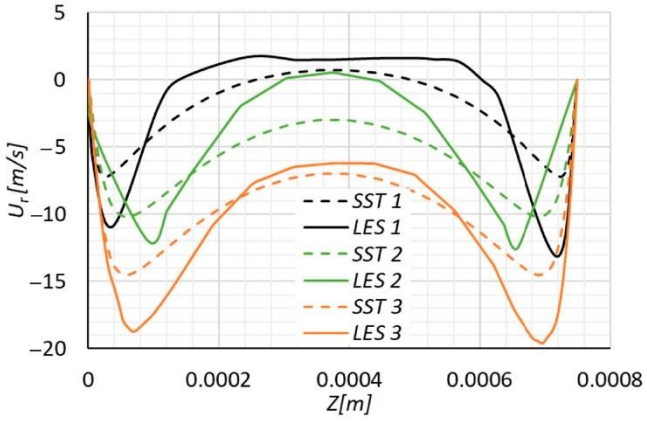

Figure 6. Spanwise profile of radial velocity in locations 1, 2, and 3.

The shape of the velocity profile in the radial direction is influenced by three factors: centripetal force, pressure force, and viscose forces. The magnitude of their effects may vary with the rotational speed. The combined impact of these forces results in a "W" shape of the velocity profile, with the minimum absolute velocity occurring in the mid-gap. Figure 6 illustrates that in the vicinity of the jet, there is a reverse radial flow at mid-gap in the radial direction. This phenomenon can be attributed to the high rotational speed of the system, affecting the force balance on the operating flow. Examining the three locations

presented in Figure 6, it is noteworthy that reverse flow is observed in both *k*-ω SST and LES simulations at location 1. However, at location 2, only the LES simulation predicts reverse flow.

Figure 7 depicts the dimensionless relative velocity profile of the flow inside the gap obtained from parallel corotating disks at three specified locations: 1, 4, and 5 for the y^+ between 1 and 200.

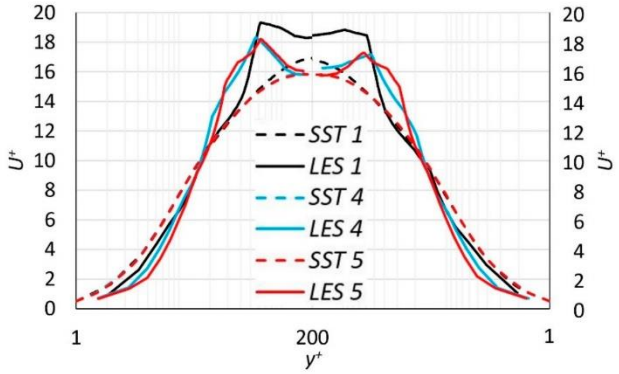

Figure 7. The dimensionless relative velocity profile in locations 1, 4, and 5.

The symbols are $U^+ = \frac{U}{u_\tau}$, $y^+ = \frac{yu_\tau}{\nu}$, and $u_\tau = \sqrt{\frac{\tau}{\rho}}$. In the *k*-ω SST simulation, the velocity profiles taken from both surfaces converge at the center. However, the disparity in the profiles in the case of LES simulation indicates unequal wall shear stress generated on the disks and highlights the transient behavior of flow characteristics. At locations 4 and 5, the dimensionless relative velocity profile is nearly identical, but there is a noticeable difference between location 1, and two others. The higher observable U^+ at dimensionless relative velocity profile at location 1 can be attributed to an undeveloped velocity profile, influenced by the interaction between the inlet flow and the evolving boundary layers on the corotating walls. As one progresses from location 1 to 5, the boundary layers become well-developed.

Examining locations 4 and 5, where boundary layers are well-developed and wall shear stress is consistent, the velocity profiles appear nearly identical, particularly in the LES simulation.

Upon scrutinizing both LES and *k*-ω SST simulations at all specified locations, it becomes apparent that *k*-ω SST predicts higher wall shear stress in both radial and circumferential directions. As a result, the velocity profiles derived from the *k*-ω SST model exhibit a downward shift.

Compared to the circumferential component, the limited portion of the radial component from the total velocity causes the W-shape of this component to not be significantly influential on the overall formation of the velocity profile at the studied locations. The noteworthy phenomenon observed is the interaction of developing boundary layers with the inlet jet.

The fluctuations in parameters during the transient simulation of the flow using the *k*-ω SST turbulence model are neglectable. This consistent behavior was insensitive to the time step size, which varied between 10^{-3} and 10^{-6} s. Throughout the entire domain, the smallest tested time step produced a Courant number lower than one, yet no significant parameter fluctuations were observed. In the converged solution, the parameter fluctuations nearly vanished. In contrast, in the LES simulation, the visible fluctuation was observable. Even post-convergence in the LES simulation, persistent parameter fluctuations highlight the ongoing transient behavior of the system.

Vorticity is another important parameter that is discussed to compare the performance of *k*-ω SST and LES simulation of N6. To evaluate this parameter, two surfaces are defined

at the outer edge of the gap and mid-radii. The surface closer to the outer diameter is positioned in an area where the nozzle jet has the highest influence, resulting in maximum wall shear stress in both radial and circumferential directions, reverse flow, and vorticity. The surface at mid-radii is specified to assess vorticity in the area with a lower impact from the inlet jet. Four distinct lines on the edges of these surfaces are drawn to examine vorticity variation near the wall surface and mid-gap region more precisely. Figure 8 demonstrates the vorticity contours on two surfaces indicated at the outer edge of the disks and mid-radii. The surfaces are generated from the revolution of lines along the gap, between 20° and 30° located at the outer edge of the disks and in mid-radii, and it is presented in Figure 8. On each surface, two lines are defined on the edges at 20° and 30°. The lines are chosen in the described locations to better demonstrate the effect of the jet and the development of boundary layers on fluctuations of parameters. Line 1 is chosen as a location with the maximum influence of the inlet jet, and line 2 is 10° away from line 1 to show how the development of boundary layers will dampen the fluctuations. The two other lines are also chosen in the mid-radii location to determine the vorticity level in a region with fewer transient effects.

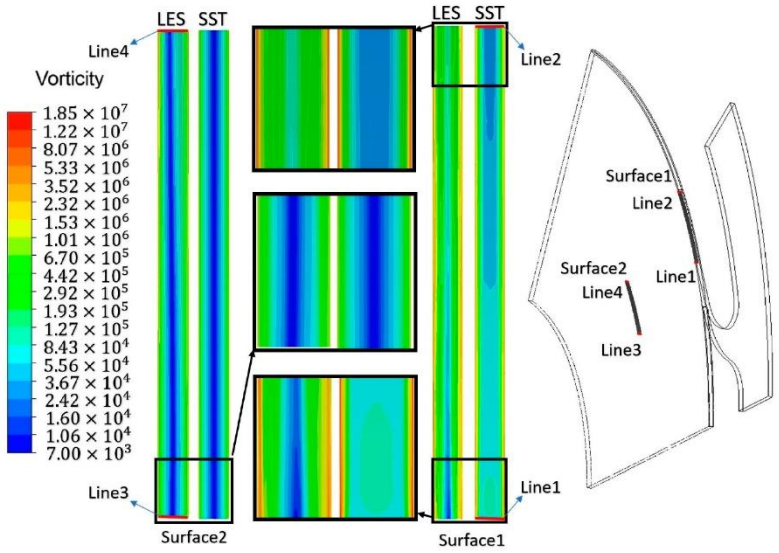

Figure 8. Vorticity contours on two surfaces (Surfaces 1, and 2) at the outer edge close to the nozzle jet and in the middle of the disks from the revolution of lines along the gap, between 20° and 30°, and lines 1–4 are defined at the edge of these surfaces.

The nearly symmetrical vorticity pattern observed in the *k*-ω SST simulation underscores the impact of its time step being 10–1000 times larger compared to the LES simulation.

In a confined region near the nozzle, a notable variation in vorticities by approaching the disk's surfaces is observable. In this specific region, the jet flow, affected by developing boundary layers and the interaction of the inlet jet with the evolving boundary layers, induces fluctuation and additional vorticities in the mid-gap. As the boundary layers progress and the distance from the nozzle increases, the vorticities near the wall escalate. This phenomenon is more pronounced in the LES simulation, which exhibits more fluctuation and represents more transient behavior.

Figure 8 highlights the effect of the inlet jet on the rising level of vorticities observed in both LES and *k*-ω SST simulations. As depicted in the mid-radii contour, the fluctuation of parameters, even in LES simulation, diminishes, and the maximum magnitude of vorticities, which occurs near the walls, is in a lower range in this area. Figure 9 depicts vorticities on the lines defined in Figure 8. With the advantage of a high-resolution mesh and the capability to resolve at least 80% of the eddies in the computational domain, the LES

demonstrates well-resolved vorticity close to the rotating walls. Due to the appropriate time step, an asymmetrical pattern of vorticity distribution is observable in the examined lines. Considering the utilized mesh for *k*-ω SST and LES simulations, the *k*-ω SST can resolve the vorticities closer to the disk's surfaces. As mentioned earlier, to satisfy the mesh requirements of the *k*-ω SST simulation, a fine mesh with the $y^+ < 1$ was utilized. The very small thickness of the first layer enables modeling vorticities close to the disk's surface. However, in adhering to the LES mesh requirements, the mesh consists of cubes. Consequently, although the total number of nodes in the LES simulation is almost 17 times higher than that in the *k*-ω SST simulation, considering the dimensions of cells in the employed mesh in each model, the *k*-ω SST yields a higher magnitude of vorticities in the near-wall area, but in the rest of the domain, the LES simulation shows a higher value of resolved vorticities. In the vicinity of the jet, the *k*-ω SST model shows a higher level of vorticity in the mid-gap area and as mentioned earlier, damps the fluctuations caused by the inlet jet. LES, on the other hand, resolves lower levels of vorticity in this area, leading to higher fluctuations. Additionally, as the distance from the jet increases, LES predicts higher levels of vorticity in the mid-gap, which reduces the velocity.

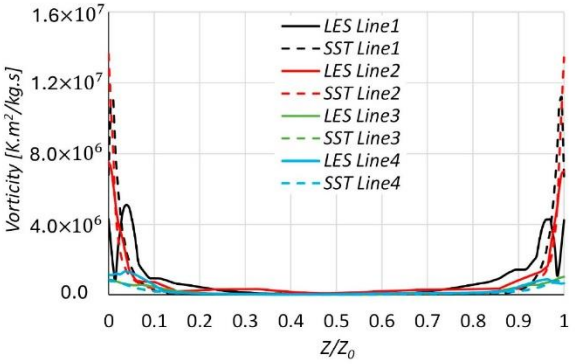

Figure 9. The vorticity magnitude along Line1–Line4 in the gap between corotating disks.

From the *k*-ω SST simulation, it is apparent that vorticity tends to increase in the near-wall area. As we move further away from the jet, a more developed boundary layer exhibits more vorticities in this region. However, owing to the larger parameter fluctuations in the LES simulation, the obtained results do not align with this trend.

The rotating walls produce eddies in the nearby area, leading to an increase in vorticities in this region. As we approach the mid-gap, the range of vorticities decreases. Throughout the entire gap, the transient behavior of the system and parameter fluctuations are observable in the case of LES simulation, underscoring the importance of high-fidelity simulation for such a phenomenon.

To further illustrate the significance of simulating the transient behavior of the system, the Fast Fourier Transform (FFT) of the pressure fluctuation derived from LES simulation at a specific point defined on line 1 is presented. The pressure values are extracted from the corresponding position along Line 1 where Z = 0.

FFT is used to analyze the modes of fluctuations. Using the FFT, the fluctuation signal is converted from the time domain to the frequency domain. In this way, one can get an overview of the entire signal and see how the parameter is distributed across the frequency spectrum. In this respect, the FFT analysis of pressure fluctuations is presented in Figure 10.

From Figure 10, many fluctuations of parameters with microamplitude are observable in higher frequencies, but the main peak of amplitude in both studied time steps is happening in lower values of frequencies. Figure 10b depicts a wider spectrum of frequencies observed from smaller time steps. As previously discussed, the *k*-ω SST simulation dampens all parameter fluctuations, making this model incapable of predicting the transient behavior of the system and any associated effects.

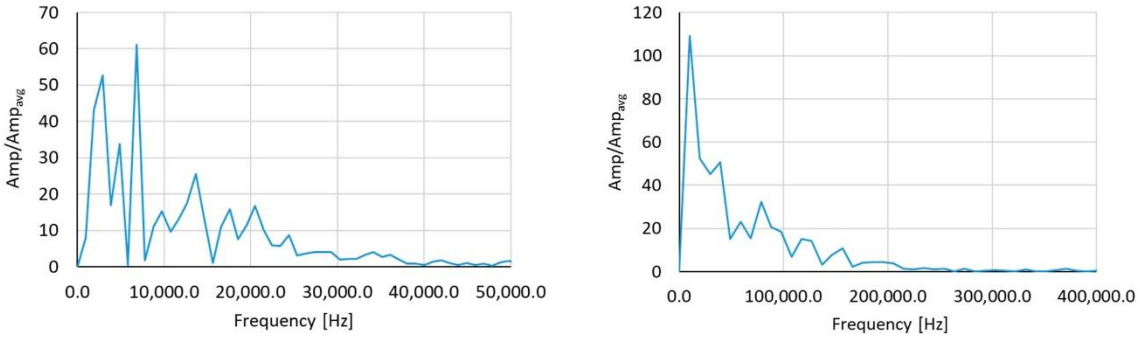

(**a**) (**b**)

Figure 10. Fast Fourier Transform (FFT) analysis of pressure fluctuations obtained from time steps equal to (**a**) 10^{-6} and (**b**) 10^{-7}.

4.2. Comparison between N6 and N40

Analyzing the results obtained from LES and *k*-ω SST simulation of N6 indicated that, although *k*-ω SST is damping all the fluctuations, it still provides a valuable insight into the flow structures and distribution of parameters. Consequently, considering the required computational expenses for LES simulation, *k*-ω SST model is an appropriate alternative numerical solution. In this part, the effect of the number of nozzles on the flow between the disks is discussed. N40 was simulated by the *k*-ω SST model. The parameters derived from the simulation of N6 and N40 are presented in Table 2.

Table 2. Comparison between obtained parameters from the simulation of N6, and N40.

Parameter	N6 (LES)	N6 (*k*-ω SST)	N40 (*k*-ω SST)
The angle of fraction [deg]	60	60	9
Mass flow rate [kg/s]	0.0023	0.0022	0.0147
Mass-averaged radial velocity [m/s]	−33.0	−28.2	−25.0
Mass-averaged circumferential velocity [m/s]	284.8	302.4	273.7
Mass-averaged static temperature [K]	257	250	261
Area-averaged gauge pressure [Pa]	24,775	22,637	71,287
Torque [Nm]	0.0400	0.0416	0.1750
Specific Power [Ws/kg]	31,882.6	34,570.1	21,836.7
Efficiency	39.2	43.0	26.8

A comparison of N40 and N6 shows a 16.18% drop in system efficiency by increasing the number of nozzles. Although the generated power in N40 is higher than in N6, the considerably higher mass flow rate in N40 caused the drop in efficiency.

The circumferential and radial wall shear stress are visually depicted both as contours on a rotating wall and along line A. As the derived results from the *k*-ω SST simulation represented quite symmetrical behavior, the wall shear stress distribution on both corotating disks is the same. A single line is defined on the surface of one of the rotating disks, positioned at a 15-degree angle compared to the horizontal line, as illustrated in Figure 11. To enhance the representation of areas with higher circumferential and radial wall shear stress, the contours and legends in the figures are presented in logarithmic scale.

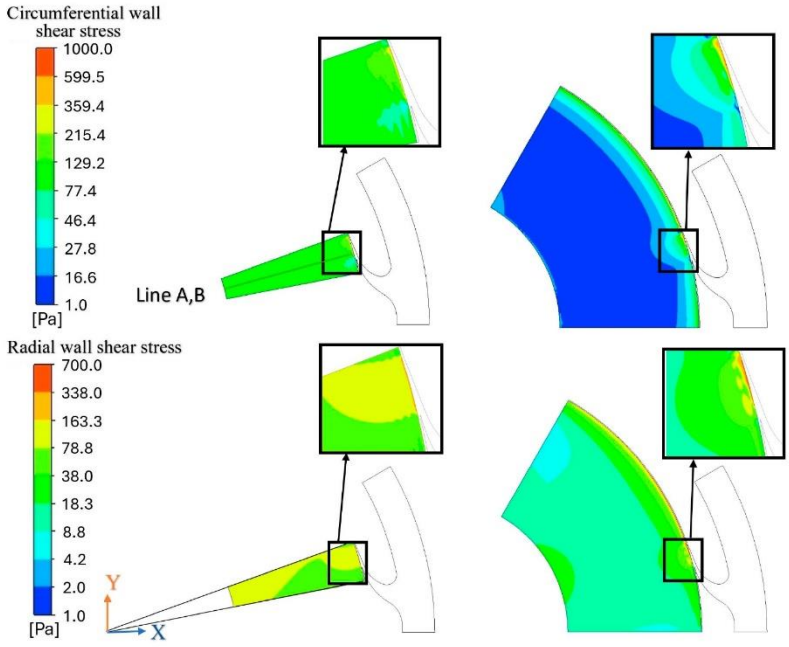

Figure 11. Contours of circumferential and radial wall shear stress obtained from *k*-ω SST simulation of N6 and N40.

Figure 11 illustrates higher values of wall shear stress in both circumferential and radial directions in N40. The increased number of jets in N40 leads to a higher mass flow rate, resulting in a wider range of shear stress in both studied directions.

Upon closer examination of the zoomed area, it is evident that in N6, the lower interaction of the jets results in a wider area with the maximum effect of the jet. However, this phenomenon is primarily observed at the outer edge of the disk.

Line A is positioned just before the area affected by the inlet jet. In Figure 12, circumferential and radial wall shear stress on this line is represented for both N6 and N40. The results derived from N40 show significantly higher values, with most radii exhibiting values nearly four times larger than those observed in N6.

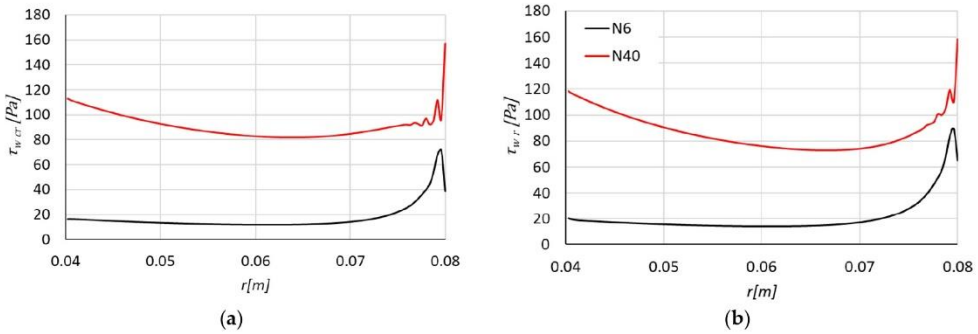

Figure 12. Circumferential (**a**) and radial (**b**) wall shear stress along line A for N6 and N40.

In N40, the effect of jet interactions causes the fluctuation of both components of wall shear stress in the outer edge of the disk, which is evident in Figure 12. In N6, as one moves from the outer to the inner edge of the disks, there is a rapid drop in both components of wall shear stress near the outer edge. However, beyond this drop, the wall shear stress

remains relatively constant throughout the rest of the domain. In contrast, in N40, while there is also a drop in wall shear stress near the outer edge, it increases as one approaches the outlet.

In Figure 11, line B is defined in mid-gap, positioned at a 15-degree angle compared to the horizontal line. Figure 13 represents the velocity and pressure distribution along line B obtained from both N6 and N40. It is shown that the fluctuation of velocity near the outer edge of the disk indicates the impact of jet interaction in N40. In N6, as one moves from the outer to the inner edge of the disks, the kinetic energy of the operating flow decreases, indicating the conversion of flow energy to rotation of the disks. However, in N40, this parameter fluctuates between 240 m/s and 260 m/s, with a noticeable increase in the vicinity of the outlet area.

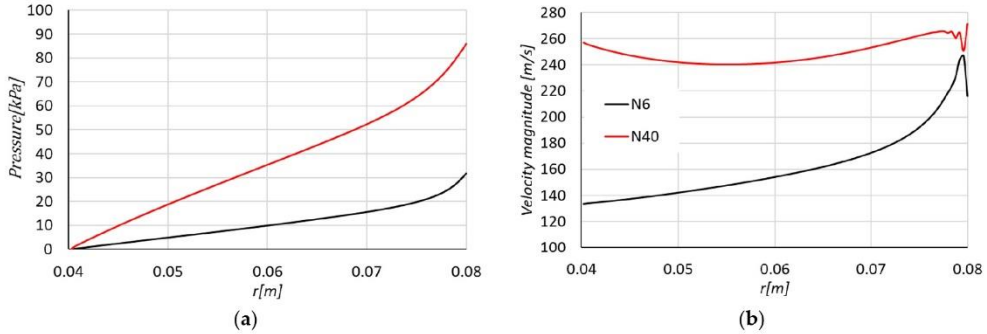

(**a**) (**b**)

Figure 13. (**a**) Pressure and (**b**) velocity distribution along line B for N6 and N40.

In both cases, moving from the outer to the inner edge of the disk, there is a decrease in pressure. However, there is a significant disparity in static pressure between N6 and N40. The nearly threefold higher pressure observed in N40, particularly in the vicinity of the outer edge of the disks, indicates a considerably higher mass flow rate in this case. A comparison of Figures 12 and 13 shows that moving from the outer to the inner edge of the disks, the drop in kinetic energy of the operating flow in N40 is neglectable. The higher number of jets in N40 causes a more than sixfold higher mass flow rate.

5. Conclusions

The *k*-ω SST simulation overestimates the torque of 4.25% and wall shear stress with the representation of the steady-state behavior of the system, though the LES represents a more accurate estimation of all parameters with a demonstration of the transient behavior of the system, revealing the need for high fidelity simulation to observe the fluctuation of such a phenomenon.

Although the *k*-ω SST model dampens parameter fluctuations, it still provides a valuable solution for the flow. Considering the computational costs of LES simulations, this highlights the *k*-ω SST model as a fast approach with appropriate accuracy.

In the LES simulation of N6, the parameters exhibit the maximum range of fluctuation in the vicinity of the outer edge of the disks. In the rest of the domain, the transient behavior appears to be smoother.

Assessment of the results reveals that interactions between the inlet jet and developing boundary layers from parallel corotating disks establish vorticities approaching the disk's surface. Due to the extremely transient behavior of the flow in that region, it does not follow a specific trend.

The outer edge of the corotating disks plays the most important role in power generation, as this area has the maximum distance from the rotational axis. Consequently, in an optimized design of a Tesla turbine, the level of kinetic energy of operating flow should drop in this area.

In N6 and considering both components of wall shear stress, the maximum total wall shear stress occurs in the outer 20% of the disk surface, and in the rest of the domain represents an almost constant value. Considering the high number of nozzles studied in N40, this parameter depicted an increase in the vicinity of the outlet.

Using a high number of nozzle jets results in a noticeable interaction of the nozzle jet, manifesting as fluctuations in parameters near the outer edge of the disks. Moreover, employing a high number of nozzles significantly increases the mass flow rate, resulting in nearly four times more power generation. However, this also causes the efficiency of the system to drop by almost 16%.

Author Contributions: Conceptualization, W.W.; Methodology, K.R.; Software, M.P.; Formal analysis, M.P.; Investigation, M.P. and K.R.; Writing—original draft, M.P.; Writing—review & editing, W.W. and K.R.; Supervision, W.W.; Funding acquisition, W.W. All authors have read and agreed to the published version of the manuscript.

Funding: The presented research was conducted within the UMO-2019/35/B/ST8/01871 research project financed by the Polish National Science Centre and statutory research funds for young scientists financed by the Silesian University of Technology.

Data Availability Statement: The original contributions presented in the study are included in the article, further inquiries can be directed to the corresponding author.

Conflicts of Interest: The authors declare no conflict of interest.

Nomenclature

c_p	specific heat capacity
d_w	wall distance
e	inner energy
f_i	gravitational force
h_{max}	maximum edge length of the cell
h_{wn}	wall-normal grid spacing
k	turbulent kinetic energy
$\dot{m}$	mass flow rate
N	power
p	pressure
q	heat flux
Re	Reynolds number
S	strain rate
T	temperature
t	time step
U	mean velocity
y^+	dimensionless distance from the wall
P_K	shear production of turbulence
σ_ω	specific dissipation rate constant
σ_k	turbulent kinetic energy constant
ρ	density
τ	tangential stress
μ	dynamic viscosity
ω	specific dissipation rate
ω_a	rotational speed
ν	kinematic viscosity

References

1. Rusin, K.; Wróblewski, W.; Rulik, S.; Majkut, M.; Strozik, M. Performance Study of a Bladeless Microturbine. *Energies* **2021**, *14*, 3794. [CrossRef]
2. Pacini, L.; Ciappi, L.; Talluri, L.; Fiaschi, D.; Manfrida, G.; Smolka, J. Computational investigation of partial admission effects on the flow field of a tesla turbine for ORC applications. *Energy* **2020**, *212*, 118687. [CrossRef]
3. Aghagoli, A.; Sorin, M.; Khennich, M. Exergy Efficiency and COP Improvement of a CO_2 Transcritical Heat Pump System by Replacing an Expansion Valve with a Tesla Turbine. *Energies* **2022**, *15*, 4973. [CrossRef]

4. Ciappi, L.; Fiaschi, D.; Niknam, P.; Talluri, L. Computational investigation of the flow inside a Tesla turbine rotor. *Energy* **2019**, *173*, 207–217. [CrossRef]
5. Tesla, N. Turbine. U.S. Patent 1,061,206, 6 May 1913.
6. Pahlavanzadeh, M.; Rusin, K.; Wróblewski, W. Evaluation of dynamic correction of turbulence wall boundary conditions to simulate roughness effect in minichannel with rotating walls. *Int. J. Numer. Methods Heat Fluid Flow* **2023**, *33*, 3915–3939. [CrossRef]
7. Pahlavanzadeh, M.; Rusin, K.; Wróblewski, W. Assessment of Turbulent Parameters Modification to Model Roughness in the Flow Between Rotating Disks of Tesla Turbine. In Proceedings of the 36th International Conference on Efficiency, Cost, Optimization, Simulation and Environmental Impact of Energy Systems (ECOS 2023), Las Palmas de Gran Canaria, Spain, 25–30 June 2023; pp. 524–533. [CrossRef]
8. Farzaneh-Gord, M.; Pahlevan-Zadeh, M.S.; Ebrahimi-Moghadam, A.; Rastgar, S. Measurement of methane emission into environment during natural gas purging process. *Environ. Pollut.* **2018**, *242*, 2014–2026. [CrossRef] [PubMed]
9. Aliakbari, K.; Ebrahimi-Moghadam, A.; Pahlavanzadeh, M.; Moradi, R. Performance characteristics and exhaust emissions of a single-cylinder diesel engine for different fuels: Experimental investigation and artificial intelligence network. *Energy* **2023**, *284*, 128760. [CrossRef]
10. Wieghardt, K.; Tillmann, W. *On the Turbulent Friction Layer for Rising Pressure*; NACA-TM-1314; NASA: Washington, DC, USA, 1951.
11. Nikuradse, J. *Laws of Flow in Rough Pipes*; NACA-TM-1292; National Advisory Committee For Aeronautics: Washington, DC, USA, 1950.
12. Colebrook, C.F. Turbulent Flow in Pipes, with particular reference to the Transition Region between the Smooth and Rough Pipe Laws. *J. Inst. Civ. Eng.* **1939**, *11*, 133–156. [CrossRef]
13. Grigson, C. Drag Losses of New Ships Caused by Hull Finish. *J. Ship Res.* **1992**, *36*, 182–196. [CrossRef]
14. Baviere, R.; Ayela, F.; Le Person, S.; Favre-Marinet, M. An experimental study of water flow in smooth and rough rectangular micro-channels. In Proceedings of the ASME 2004 2nd International Conference on Microchannels and Minichannels, Rochester, NY, USA, 17–19 June 2004; pp. 221–228. [CrossRef]
15. Kandlikar, S.G.; Schmitt, D.; Carrano, A.L.; Taylor, J.B. Characterization of surface roughness effects on pressure drop in single-phase flow in minichannels. *Phys. Fluids* **2005**, *17*, 100606. [CrossRef]
16. Rusin, K.; Wróblewski, W.; Rulik, S.; Pahlavanzadeh, M.; Hasani Malekshah, E. Investigation on the Influence of Surface Roughness of Rotating Microchannel on Flow Conditions. In Proceedings of the ASME Turbo Expo 2023: Turbomachinery Technical Conference and Exposition, Boston, MA, USA, 26–30 June 2023. [CrossRef]
17. Sengupta, S.; Guha, A. Analytical and computational solutions for three-dimensional flow-field and relative pathlines for the rotating flow in a Tesla disc turbine. *Comput. Fluids* **2013**, *88*, 344–353. [CrossRef]
18. Schosser, C.; Pfitzner, M. A numerical study of the three-dimensional incompressible rotor airflow within a Tesla turbine. In Proceedings of the Conference on Modelling Fluid Flow (CMFF'15), The 16th International Conference on Fluid Flow Technologies, Budapest, Hungary, 1–4 September 2015.
19. Lampart, P.; Jędrzejewski, Ł. Investigations of aerodynamics of Tesla bladeless microturbines. *J. Theor. Appl. Mech.* **2011**, *49*, 477–499.
20. Thomazoni, A.L.R.; Ermel, C.; Schneider, P.S.; Vieira, L.W.; Hunt, J.D.; Ferreira, S.B.; Rech, C.; Gouvêa, V.S. Influence of operational parameters on the performance of Tesla turbines: Experimental investigation of a small-scale turbine. *Energy* **2022**, *261*, 125159. [CrossRef]
21. Rusin, K.; Wróblewski, W.; Malekshah, E.H.; Pahlavanzadeh, M.; Rulik, S. Extended analytical model of Tesla turbine with advanced modelling of velocity profile in minichannel between corotating disks with consideration of surface roughness. *Energy* **2024**, *307*, 132775. [CrossRef]
22. Tucker, P. Trends in turbomachinery turbulence treatments. *Prog. Aerosp. Sci.* **2013**, *63*, 1–32. [CrossRef]
23. Pahlavanzadeh, M.; Rulik, S.; Wróblewski, W.; Rusin, K. Application of roughness models to stationary and rotating minichannel flows. *Int. J. Numer. Methods Heat Fluid Flow* **2024**. *ahead of printing*. [CrossRef]
24. Rusin, K.; Wróblewski, W.; Rulik, S. The evaluation of numerical methods for determining the efficiency of Tesla turbine operation. *J. Mech. Sci. Technol.* **2018**, *32*, 5711–5721. [CrossRef]
25. Rusin, K.; Wróblewski, W.; Rulik, S. Efficiency based optimization of a Tesla turbine. *Energy* **2021**, *236*, 121448. [CrossRef]
26. Larkermani, E.; Cao, G.; Georges, L. Characterization of the density-driven counter-flow through a doorway using Large Eddy Simulation. *Build. Environ.* **2022**, *221*, 109319. [CrossRef]
27. LarKermani, E.; Roohi, E.; Porté-Agel, F. Evaluating the modulated gradient model in large eddy simulation of channel flow with OpenFOAM. *J. Turbul.* **2018**, *19*, 600–620. [CrossRef]
28. Wang, R.; Chew, J.W.; Gao, F.; Marxen, O. Large-eddy simulation of axial, radial and mixed centrifugal convection in a closed rotating cavity. *Int. J. Heat Mass Transf.* **2024**, *227*, 125559. [CrossRef]
29. Wilcox, D.C. Formulation of the k-w Turbulence Model Revisited. *AIAA J.* **2008**, *46*, 2823–2838. [CrossRef]
30. Menter, F.R. Two-equation eddy-viscosity turbulence models for engineering applications. *AIAA J.* **1994**, *32*, 1598–1605. [CrossRef]
31. Shur, M.L.; Spalart, P.R.; Strelets, M.K.; Travin, A.K. A hybrid RANS-LES approach with delayed-DES and wall-modelled LES capabilities. *Int. J. Heat Fluid Flow* **2008**, *29*, 1638–1649. [CrossRef]

32. Smagorinsky, J. General Circulation Experiments with the Primitive Equations 1963. Available online: https://eurekamag.com/research/084/250/084250654.php (accessed on 22 December 2023).
33. Piomelli, U.; Moin, P.; Ferziger, J.H. Model consistency in large eddy simulation of turbulent channel flows. *Phys. Fluids* **1988**, *31*, 1884–1891. [CrossRef]
34. Qi, W.; Deng, Q.; Chi, Z.; Hu, L.; Yuan, Q.; Feng, Z. Influence of Disc Tip Geometry on the Aerodynamic Performance and Flow Characteristics of Multichannel Tesla Turbines. *Energies* **2019**, *12*, 572. [CrossRef]

Paper IV

Evaluation of nozzle configuration impact on flow structures and performance in Tesla turbine

International Journal of Heat and Mass Transfer 243 (2025) 126900

Contents lists available at ScienceDirect

International Journal of Heat and Mass Transfer

journal homepage: www.elsevier.com/locate/ijhmt

Evaluation of nozzle configuration impact on flow structures and performance in Tesla turbine

Mohammadsadegh Pahlavanzadeh *, Włodzimierz Wróblewski, Krzysztof Rusin

Silesian University of Technology, Department of Power Engineering and Turbomachinery, Gliwice, Poland

ARTICLE INFO

Keywords:
Large eddy simulation
Co-rotating disks
Tesla turbine
Nozzle configuration

ABSTRACT

Momentum diffusion and kinetic energy transfer play crucial roles in turbomachinery. The Tesla turbine is a radial turbine that operates based on energy transfer between the operating flow and corotating disks. It has applications in various energy systems, such as the Organic Rankine Cycle and combined heat and power systems. Design parameters, particularly the nozzle configuration, significantly impact turbine performance. This study investigates two nozzle supply designs: one-to-many, where the nozzle provides fluid to all gaps, and one-to-one, with the individual nozzle for each gap. To minimize computational costs, only a portion of the entire domain is examined, and flow structures and their effects on Tesla turbine performance are analyzed. Large Eddy Simulation (LES) employing the Smagorinsky subgrid-scale model is used for flow simulation, enabling a comparison of flow structures, fluctuations, parameters, and their impact on system performance. The one-to-many configuration demonstrates lower efficiency with considerably higher fluctuations. The main source of these fluctuations is found to be the interaction of the inlet jet with the disk tips. In the one-to-one configuration, the source of the fluctuations is the rotating disks, with a different trend of distribution along the gap compared to the one-to-many configuration.

1. Introduction

The mini expanders play a crucial role in energy conversion processes, offering efficiency and versatility in various applications. Recently, there has been a growing interest in these expanders, which are becoming more prevalent across various sectors such as combined heat and power, as well as Organic Rankine cycle (ORC) based systems [1–4]. Mini expanders, like the Tesla turbine [5], are often used in situations where space is limited or where traditional blade turbines may not be economically viable. These devices are known for their distinct features, such as reliable performance across diverse conditions and cost-effective production which makes them appropriate for heat recovery systems and sustainable energy purposes [6,7]. The effectiveness of friction turbomachines relies on the exchange of momentum between the flowing medium and rotating disks via momentum diffusion, so the flow analysis is of great importance [8]. The analysis of flow structures in a Tesla turbine is challenging due to the cross-section changes from the outer to the inner diameter of the disks and the submillimeter gap size. Moreover, the rotation of disks raises the complexity of solution [9, 10]. To examine flow structures close to walls, researchers have developed theoretical tools known as wall functions which are widely in use in different turbulence models [11–15]. However, in scenarios involving narrow gaps, it's crucial to consider other significant factors and phenomena, such as the interaction of boundary layers and constriction of dimensions of flow cross sections [16,17]. Accounting for these aspects may lead to results that deviate from the predictions made by theoretical models [18]. Pahlavanzadeh et al. [19] investigated the effect of flow cross-section on flow characteristics between corotating disks with a gap size in the same range as in the Tesla turbine. They discussed the discrepancy between the numerical results and the theoretical velocity profile. They also addressed the deviation between the proposed estimation of the downward shift of the velocity profile due to the rough surface in the literature and the results of the numerical solution. In the context of computational domains at the discussed scale, the flow fluctuations, lead to a transient behavior that is challenging to predict [20–22]. Much of the numerical research addressing this issue diverges from experimental data due to the limited accuracy of the applied models. Considering the computational time and expenses, simulation of

* Corresponding author.
E-mail addresses: mohammadsadegh.pahlavanzadeh@polsl.pl (M. Pahlavanzadeh), wlodzimierz.wroblewski@polsl.pl (W. Wróblewski), krzysztof.rusin@polsl.pl (K. Rusin).

https://doi.org/10.1016/j.ijheatmasstransfer.2025.126900
Received 2 October 2024; Received in revised form 12 February 2025; Accepted 1 March 2025

such a small domain poses challenges. Taking into the account the mesh requirements and accuracy of various turbulence models, the k-ω SST model emerges as the most suitable option for simulating flow in such a small domain [19]. The investigation of flow between co-rotating disks, with a uniform inlet flow at the outer diameter, resembling a simplified version of the co-rotating disks in the Tesla turbine, has revealed the crucial importance of understanding flow behavior in such domains in greater detail.

In aiming for a more realistic depiction of the Tesla turbine's functionality, which involves the delivery of fluid via nozzles at specific points, significant challenges emerge in understanding the flow dynamics, especially in the proximity of the jets. In this critical zone, the interaction between the incoming jet and the developing boundary layers originating from the co-rotating disks leads to complex transient behavior, necessitating a comprehensive analysis. In their study, Rusin et al. [23]. conducted a detailed examination and evaluation of a Tesla turbine model, focusing on the influence of turbulence models on the prediction of operational parameters. They systematically investigated various turbulence models, employing different temporal and spatial discretization techniques. Additionally, they analyzed the distribution of power units across the disks and compared the turbine's power predictions obtained from numerical simulations with initial experimental data. Their analysis revealed a consistent trend of overestimation across all turbulence models when compared to experimental observations. This discrepancy underscores the need for further refinement and validation of turbulence models to accurately predict the operational performance of Tesla turbines. In an earlier study, Rusin et al. [24] conducted a Tesla-style turbine comprising five co-rotating disks. They were focused on efficiency optimization by fine-tuning both geometrical and operational parameters. Central to their investigations was minimizing radial tip clearance, a critical factor in preventing rotor displacement and subsequent rubbing of disks against the casing, particularly under the influence of different rotational speed and manufacturing tolerances. Their approach primarily involved efficiency-driven numerical optimization of the Tesla turbine. This optimization process focused on refining parameters such as inlet nozzle height, inter-disk gap, nozzle angle, pressure, and rotational velocity. By systematically adjusting these key variables, they aimed to enhance turbine performance and mitigate potential operational challenges associated with clearance issues and mechanical constraints.

Two types of nozzle configurations are possible in the Tesla turbine, one-to-one and one-to-many configuration. In the one-to-one case, each rotor gap corresponds to the nozzle width. In the one-to-many configuration, multiple disk gaps are supplied by the flow from a single nozzle, the width of the nozzle extends over the whole rotor width (over all discs and gaps) [25,26].

In the simulation of a Tesla turbine, analyzing the flow structures, and parameters distribution, there is a lack of validation cases. Literature suggests that the turbulence models, e.g. k-ω SST tend to dampen fluctuations, particularly in areas where the flow is turbulent but not fully developed, resulting in smoother flow behavior in the computational domain [27,28]. Therefore, a high-fidelity simulation method like Large Eddy Simulation (LES) proves beneficial in providing a more accurate estimation of the transient behavior of the system and precise calculation of flow structures [29,30].

Exploring flow characteristics in the gap between co-rotating disks using a turbine configuration with six nozzles and optimized parameters, based on recent research [24], is the focus of this investigation.

In the present study, two nozzle configurations, named one-to-one and one-to-many, are investigated (Fig. 1) using a high-fidelity simulation approach, to present a precise analysis of the flow structures, parameters distribution and fluctuations. The source of fluctuations, and the overall performance of Tesla turbine employing each of the nozzle configurations is discussed.

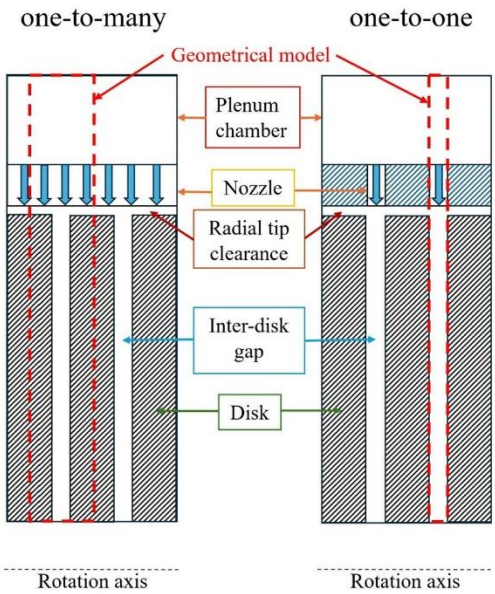

Fig. 1. Schematic of one-to-one and one-to-many nozzle configurations.

2. Mathematical model

The governing equations involve continuity, momentum, and energy conservation as following:

$$\frac{\partial \rho}{\partial t} + \frac{\partial}{\partial x_j}(\rho U_j) = 0 \tag{1}$$

$$\frac{\partial (\rho U_j)}{\partial t} + \frac{\partial}{\partial x_j}(\rho U_i U_j) = -\frac{\partial p}{\partial x_i} + \frac{\partial \tau_{ij}}{\partial x_j} + \rho f_i \tag{2}$$

$$\frac{\partial \left(\rho \left(e + \frac{1}{2}U_i U_i\right)\right)}{\partial t} + \frac{\partial}{\partial x_j}\left(\rho U_j \left(e + \frac{1}{2}U_i U_i\right)\right) = -\frac{\partial}{\partial x_j}(pU_j) + \frac{\partial}{\partial x_j}(\tau_{ij} U_i) - \frac{\partial}{\partial x_j}(q_j) + \rho f_i U_i \tag{3}$$

In LES, the closure of the Navier-Stokes equations is achieved by employing the wall-modeled large eddy simulation (WMLES) model. This model is responsible for computing the subgrid-scale (SGS) eddy viscosity. The fundamental Algebraic WMLES formulation was first introduced in research conducted by Shur et al. [31]. This model integrates a mixing length model with a modified Smagorinsky model [32] and incorporates the wall-damping function proposed by Piomelli et al. [33]:

$$\nu = min\left[(\kappa d_w)^2,\ (C_{Smag}\Delta)^2\right] S\left\{1 - exp\left[-\left(\frac{Y^+}{25}\right)^3\right]\right\} \tag{4}$$

$$\Delta = min(max(C_w d_w; C_w h_{max}, h_{wn}); h_{max}) \tag{5}$$

where $\kappa = 0.4187$, $C_{Smag} = 0.2$, and $C_w = 0.15$ are constants.

3. Model definition

3.1. Calculation domain and boundary conditions

The numerical analysis utilized Ansys Fluent, a commercially available software employing the finite volume method. The study focused on

two Tesla turbine configurations with six nozzles: one featuring a one-to-one nozzle arrangement (referred to as N6O—O) and the other adopting a one-to-many nozzle design (referred to as N6O-M). In N6O—O, the simulation accounted for the plenum chamber's thickness being equivalent to the gap size. In N6O-M, aside from the gap size, half of the disk's size was factored into the thickness of the supply chamber. The one-to-one configuration allowed for direct passage of the nozzle jet through the gap, while the one-to-many setup incurred losses from the interaction between the inlet jet and the disk tips. Each case exhibited symmetrical behavior every 60 ° in the investigated geometry. To enhance computational efficiency, the simulation domain represented only a segment of the entire turbine. Including the entire apparatus would necessitate a significant increase in both simulation time and costs without yielding substantial improvements in data quality.

Fig. 2 illustrates a schematic of the studied cases, showcasing various components of the computational domains and the corresponding

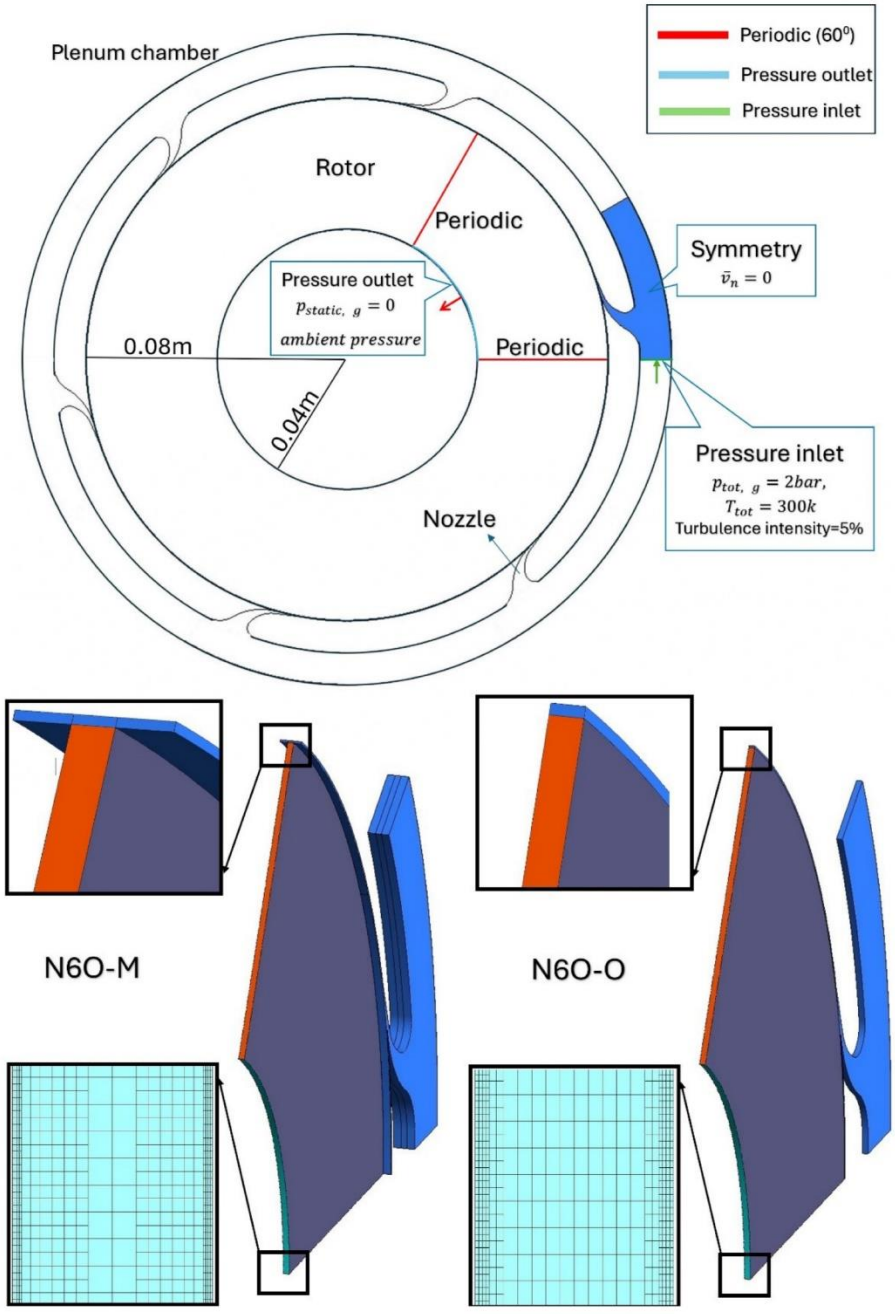

Fig. 2. Schematic of the computational domains, boundary conditions, and generated mesh for (a) N6O—O, and (b) N6O-M.

boundary conditions employed in each case. Additionally, the mesh utilized in each case is depicted. Further details regarding the meshing strategy are elaborated upon in the subsequent section.

In the simulations, air treated as ideal gas was chosen as the working fluid, and an absolute coordinate system was utilized. The computational domain comprised three distinct sections. The first section served as a plenum chamber to stabilize fluid parameters. The second section consisted of a converging nozzle with a nozzle throat width to outer radius of the disk of $d_{th}/R_o = 0.00875$, oriented at an 8-degree angle relative to the tangential direction. The final part represented 1/6 of the rotor disk, which had the outer radius of $R_o = 0.08m$ and the inner to outer radii ratio of $R_i/R_o = 0.5$. The inter-disk gap ratio was $\delta/R_o = 0.0093$, while the ratio of radial tip clearance $\epsilon/R_o = 0.003125$, optimized based on the constraints inherent in real Tesla turbine design and manufacturing limitations. Periodic boundary conditions were imposed on both sides of the disc sector in both Cases, each spanning a central angle of 60 °, as illustrated in Fig. 2. Symmetric boundary conditions were enforced on both sides of the chamber in both instances. Flow within the computational domain was simulated in an absolute frame, and the walls of the disks were set to rotate which means the relative velocity of flow on the disks surface is zero. The rotational speed was set at 17,500 RPM, and the turbine's geometry, along with the selected operating and boundary conditions, were determined based on previous studies of a Tesla turbine, resulting in maximum efficiency. Additionally, the inlet conditions comprised a total pressure of 2 bars, a total temperature of 300 K, and a turbulence intensity of 5%. Ambient pressure was applied at the outlet.

The numerical solution of the conservation equations is following the SIMPLE algorithm which entails a weighted average of second-order upwind and central interpolations of variables. Time discretization is realized through the application of a second-order implicit transient formulation. The spatial discretization of pressure was standard, for density and energy was third order and bounded central differencing was used for spatial discretization of momentum.

In both investigated cases, simulations achieved convergence after almost 72,000 iterations, with the initial time step set at 1e-8 and gradually increased to 1e-6. The Courant number was checked at each time step. The maximum Courant number in the whole computational domain for the time step of 1e-7 was equal to one. After convergence of the solution, the pressure fluctuation at a specific point with the highest converge-diverge nozzle effect was analyzed utilizing Fast Fourier transform (FFT). Then the parameters were time-averaged over 0.0002 s to cover the biggest amplitude of frequency.

3.2. LES mesh setup

The success of an LES simulation requires the resolution of at least 80% of the turbulent kinetic energy. To achieve this, it is necessary to resolve eddies whose sizes are larger than approximately half the size of the integral length scale (l_0). The integral length scale is a local quantity that can be evaluated using k and ω values obtained from the Reynolds-Averaged Navier-Stokes (uRANS) simulation:

$$l_0 = \frac{k^{0.5}}{(C_\mu \omega)} \tag{6}$$

where $C_\mu = 0.09$.

Based on Kolmogorov's energy spectrum to resolve 80% of the eddies we have:

$$\frac{l_0}{\Delta} \geq 4.8 \tag{7}$$

where $\Delta = \sqrt[3]{cell\ volume}$, assuming that the cells are of cubic shape.

To adhere to the mesh requirements for the LES method, the adjustment to the cubic mesh was made. The mesh for LES simulations was specifically generated only in the gap between the co-rotating disks. In the plenum chamber, the hexahedral mesh was created with edge sizes between 0.05 mm – 0. 2 mm and with a total number of nodes equal 600k in the N6O—O case and 1.8 M in the N6O-M case. The LES simulations started on the 5 M grid and 2.56 M cubic cells, with initial conditions from the converged k-ω SST solution obtained after 10,000 and 14,000 iterations for the N6O—O case, and N6O-M case, respectively. The presence of rotating walls induced the generation of small eddies in the adjacent wall area. To meet the LES criteria in at least 90% of the domain, the mesh underwent two rounds of modification in both studied cases, achieving a total number of cells of 50 M in the N6O—O case, and 60 M in the N6O-M case. The dimensionless wall distance to the disk surface ($y^+ = \frac{u_\tau y}{\nu}$) was maintained within the range of 0.7 to 2.2 in both cases, with the maximum value occurring in the region most influenced by the nozzle's effect on the flow structure. The mesh modification process was conducted to ensure that the ratio of the integral length scale to the cell size (l_0/Δ) remained higher than 4.8. In the case N6O—O, this entailed two rounds of modification to the first two layers of the mesh near the walls, and in the N6O-M case, it employed two rounds of cell modification, the first for the first three layers and then for the first two layers close to the wall, accompanied by a switch from the k-ω SST model to LES.

For further assessment of the quality of the present LES, one widely used criterion, index quality [34], is calculated and shown in Fig. 3. The index quality is calculated by Eq. (8), where μ denotes molecular viscosity, μ_{SGS} denotes sub-grid scale viscosity, α_ν and n are constants fixed here at 0.05 and 0.53, respectively, following Ref [34].

$$LES_{IQ_k} = \frac{1}{1 + \alpha_\nu \left(\frac{\mu + \mu_{SGS}}{\mu}\right)^n} \tag{8}$$

Two planes are defined in the mid-gap and along the radii, at 30 ° compared to the horizontal coordinate, and normal to the gap. The instantaneous index quality on these two planes, presented in Fig. 3, shows a minimum value of 0.8 and a maximum value of 0.95 in the studied area. The contour indicates that the dissipation modeled by the sub-grid is less than 20% of the total dissipation.

4. Results and discussion

The findings from simulation of both studied cases indicate that the mass flow rate considering the full disks and the gap between them were 0.0021 kg/s and 0.0079 kg/s, for N6O—O, and N6O-M, respectively.

Isentropic Efficiency of Nozzle can be defined as the ratio of actual enthalpy drop to isentropic enthalpy drop between the same pressures:

$$\eta_N = \frac{h_1 - h_{2a}}{h_1 - h_{2s}} \tag{9}$$

where h_1 is the initial enthalpy before the nozzle in the plenum chamber and h_{2a},and h_{2s} represent the actual and isentropic enthalpies at the nozzle exit, respectively.

From the simulation, at the nozzle's inlet the average gauge pressures were 2 bars, and this value at the nozzle's outlet, were 0.57, and 0.76 bar for N6O—O and N6O-M, respectively. Additionally, the average total temperature at the nozzle's inlet was 300 K in both cases, and the average static temperature at the nozzle's outlet was 250 K and 259 K for N6O—O, and N6O-M, respectively. This difference implies a nozzle isentropic efficiency of 98.6% in N6O—O, and 96.7% in N6O-M.

The primary goal of this investigation is to thoroughly assess the flow characteristics within the gap between co-rotating disks. Consequently, the average parameters at the inlet to the gap are vital. Table 1 represents the derived parameters at the inlet to the gap in the N6O—O case and N6O-M case. Moreover, this table represents the total parameters of power and total-to-static isentropic efficiency for both cases, which are determined from the following relations:

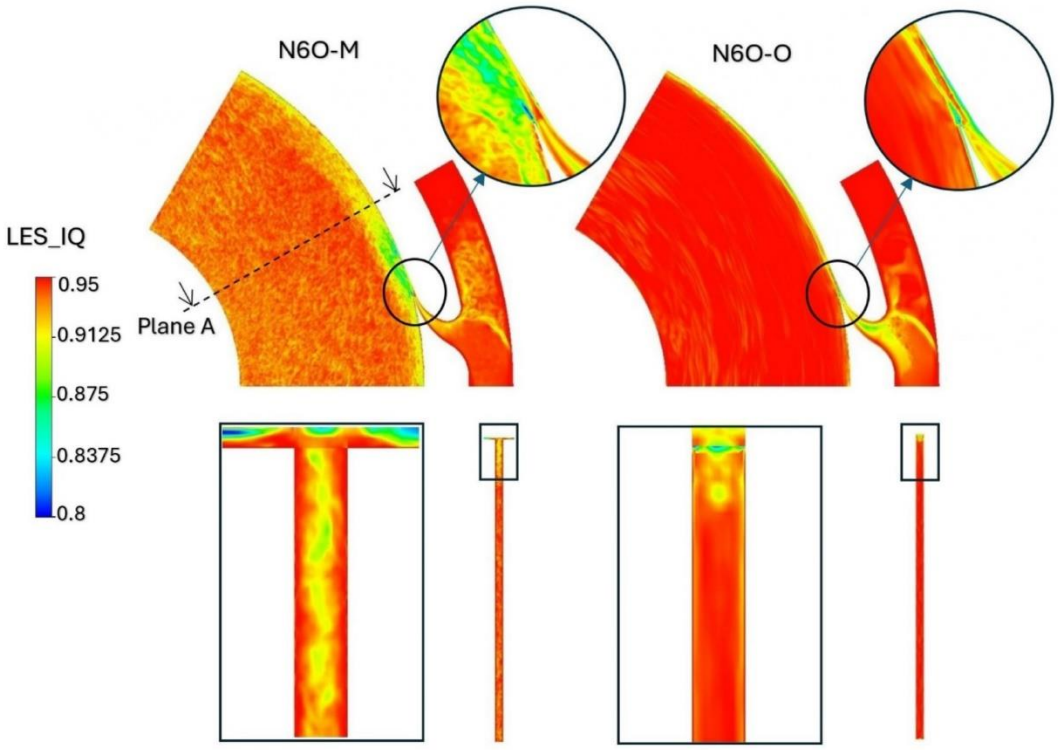

Fig. 3. Instantaneous index quality of LES simulation on two planes at mid-gap and along the radii, at 30 ° compared to the horizontal coordinate.

Table 1
Comparison between obtained parameters from simulation of N6O—O, and N6O-M.

Parameter	N6O—O	N6O-M
Mass flow rate [kg/s]	0.0021	0.0079
Mass-averaged radial velocity [m/s]	33.0	118.5
Mass-averaged circumferential velocity [m/s]	284.8	241.7
Mass-averaged static temperature [K]	257	257
Area-averaged gauge pressure [Pa]	25,298.8	45,478.2
Torque [$N{\cdot}m$]	0.040	0.088
Power [W]	73.30	161.26
Efficiency	42.9	25.1
Power/Mass flow rate [m^2/s^2]	34,904.7	20,412.6

$$N = \omega_a \int \boldsymbol{r} \times \boldsymbol{\tau} dA \tag{10}$$

$$\eta = \frac{N}{\dot{m} c_p T_{in} \left(1 - \left(\frac{p_{out}}{p_{in}}\right)^{\frac{\gamma-1}{\gamma}}\right)} \tag{11}$$

As presented in Table 1, the mass flow rate is considerably higher in the one-to-many configuration of the supply system. In N6O-M, aside from the gap size, half of the disk's size was factored into the thickness of the supply chamber which caused a higher mass flow rate. The Reynolds number based on the hydraulic diameter of the gap $D_h = 2\delta$ and relative velocity $\overline{W}$ takes form $Re = \frac{\rho \overline{W} 2\delta}{\mu}$ and was 6734 and 11,645 at the inlet to the gap for N6O—O, and N6O-M, respectively. Considering the Reynolds number based on radial velocity ($Re = \frac{\rho \overline{V}_r 2\delta}{\mu}$), the values are 1038 and 6702 for N6O—O and N6O-M, respectively. In the N6O-M configuration, the interaction of the inlet jet with the tip of the disks increases and contracts the flow in the tip region of the gap. This phenomenon causes an increase in static pressure at the gap inlet. The comparison between N6O-M, and N6O—O, reveals that although the torque and consequently the power in N6O-M is considerably higher than N6O—O, it is still almost four times bigger mass flow rate in this case causing lower efficiency. The bigger mass flow rate in N6O-M reduced efficiency by 17.8%.

The circumferential wall shear stresses are responsible for the torque generation; therefore, their distribution is of great importance for the turbine performance. The circumferential wall shear stress on the disk surface of each case is depicted in Fig. 4 on a logarithmic scale. Moreover, to better illustrate the drop in this parameter moving from the outer to inner diameter of the disks and fluctuations under the effect of the nozzle jet, the mean circumferential wall shear stress values are plotted along the lines, defined on the radius of the parallel disk surfaces.

Four lines are defined on the parallel surface of the disks. Lines A and B are defined at 20 °, and lines C and D are defined at 40 ° relative to the vertical axis. Lines A and B cross the area with the highest nozzle effect, whereas lines C and D are positioned farther from the nozzle to observe a more developed boundary layer.

As demonstrated in Fig. 4, the N6O-M configuration exhibits higher values of mean circumferential wall shear stress on the disk surface than the N6O—O configuration. This explains the higher generated torque in the N6O-M case.

The converging-diverging nozzle effect in the N6O-M configuration is also stronger. This effect is created due to the interaction between the inlet nozzle and the disk edges, when the fluid must enter the inter-disk gap. It generates there an area with the highest mean circumferential wall shear stress. In the N6O-M configuration, consideration of the disk

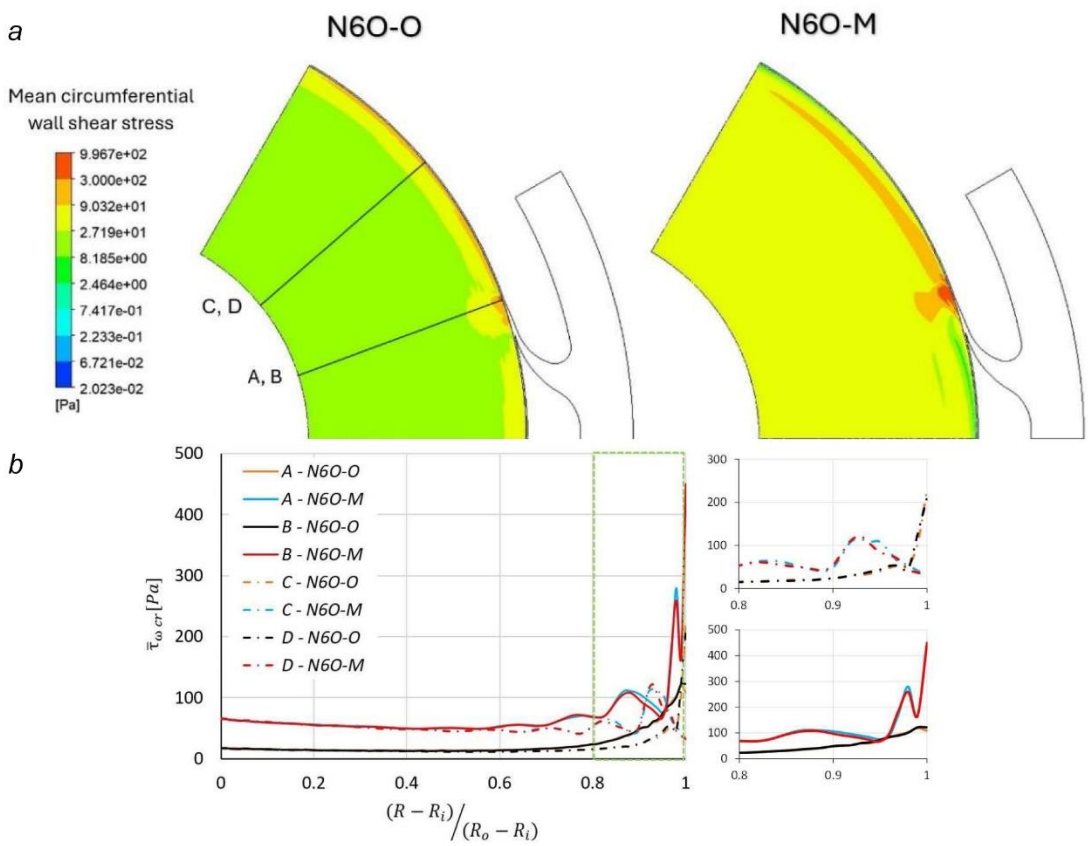

Fig. 4. (a) Contour of circumferential wall shear on the disks surface (b) circumferential wall shear stress along lines A, B, C, and D.

thickness and the interaction of the inlet jet with the disk tips results in a more intensive convergent-divergent nozzle effect, which pushes the area with the highest mean circumferential wall shear stress slightly toward the inner diameter.

The plotted mean circumferential wall shear stress along the defined lines clearly demonstrates this effect. Considering lines, A and B, the N6O-M configuration shows higher values both near the jet at the outer diameter of the disks and throughout the rest of the domain. The observable fluctuations in both cases, after averaging the variables over an appropriate number of time steps, were negligible.

In the zoomed-in area of the plot, which is presented separately for the two groups of lines, it is observable that in the vicinity of the nozzle, the N6O-M configuration produces nearly four times greater mean circumferential wall shear stress. Furthermore, as the distance from the nozzle jet increases, while the N6O—O configuration shows the area with the highest mean circumferential wall shear stress at the outer diameter of the disks, the N6O-M configuration shifts this area toward the inner diameter, located approximately at radii ratio $(\frac{R-R_i}{R_o-R_i})$ of 0.92.

Fig. 5 demonstrates the mean static gauge pressure, mean radial velocity, and mean tangential velocity, on a surface defined at mid-gap. To better discuss the mean static pressure, line E is defined at thirty degrees compared to the vertical axis. Moreover, lines 1, 2, and 3 are defined to present spanwise mean radial velocity profiles. These lines are defined to be at radii ratio of 1, 0.5, and 0, to cover the areas with high nozzle jet effect, farther from the jet with a more developed boundary layer.

As depicted in Fig. 5, in N6O—O there is a smooth change in mean static pressure from inlet to outlet. Considering the N6O-M, there is a visible converge-diverge effect of the nozzle which causes a sharp drop in mean static pressure in the vicinity of the nozzle. Considering the relative scale of the contour, the mean absolute static pressure in this area reaches to $6.7 \times 10^4 Pa$.

The contour shows higher pressure throughout the gap between the co-rotating disks in the N6O-M case, which, as discussed in Table 1, has an almost four times bigger mass flow rate compared to N6O—O.

The mean radial velocity contour presented in Fig. 5 indicates higher absolute values of mean radial velocity on the defined mid-gap plate across the domain in the N6O-M case. The nozzle effect causes a significantly higher mean radial velocity in the N6O-M case. Although there are visible fluctuations in mean radial velocity at mid-gap in both cases, these fluctuations are more intense in the N6O-M case.

The mean tangential velocity contour presented in Fig. 5 clearly demonstrates a higher level of this parameter in the mid-gap area of the N6O-M case compared to the N6O—O case. Additionally, the contour shows that the area with the highest fluctuation of this parameter is near the nozzle region, where the interaction of the inlet jet with the developing boundary layers generates strong turbulence.

In the N6O—O case, the maximum values of the mean tangential velocity are at the outer diameter of the disks. In contrast, in the N6O-M case, the nozzle effect shifts this region slightly toward the inner diameter.

Fig. 6 demonstrates the mean pressure distribution along line E. The linear behavior of the pressure distribution indicates that the maximum difference occurs at the outer diameter of the disks, with a value of

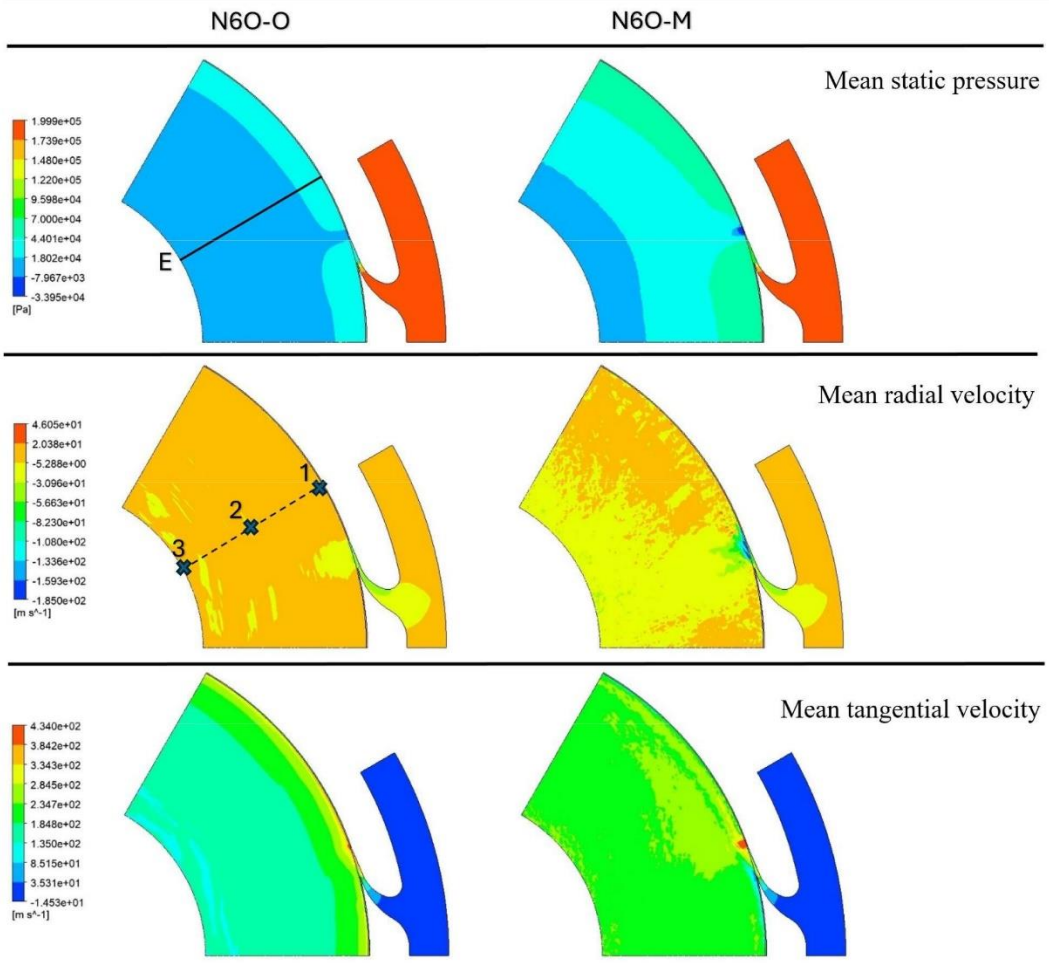

Fig. 5. Contours of mean static pressure, mean radial velocity and mean tangential velocity on a mid-gap plane.

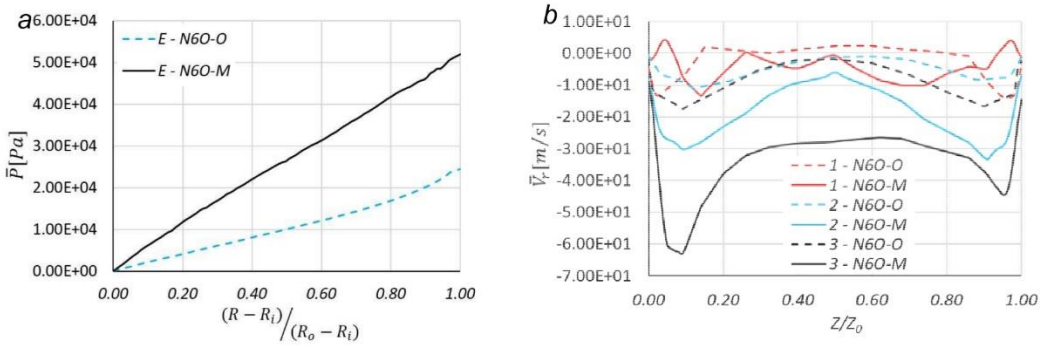

Fig. 6. (a) Pressure distribution along line E, (b) radial velocity profile along lines 1, 2, and 3.

approximately $2.5 \times 10^4 Pa$.

The spanwise radial velocity profiles along lines 1, 2, and 3 are plotted in Fig. 6. The shape of the velocity profile in the radial direction is influenced by three factors: centripetal force, pressure force, and viscous forces. The magnitude of their effects may vary with the rotational speed. The combined impact of these forces results in a "W" shape velocity profile at all studied locations in the N6O—O case. The same trend occurs in the N6O-M case, except along line 1, which is under

maximum nozzle effect.

At the closest location to the outer diameter of the disks, reverse flow is observed in both cases, but the location of this phenomenon within the gap differs. In the N6O—O case, reverse flow occurs at mid-gap, while in the N6O-M case, it occurs near the wall.

Overall, the N6O—O case exhibits smoother behavior with lower fluctuations compared to the N6O-M case.

To better understand the fluctuations in each case and their sources, the Reynolds stresses were analyzed. The magnitudes of Reynolds stresses along lines 1, 2, and 3, as defined in Fig. 5, were calculated. In N6O—O case the maximum Reynolds stresses magnitude obtained from the studied lines were 61.5 *Pa*, 4.77 *Pa*, and 956 *Pa* for lines 1, 2, and 3, respectively. These values in N6O-M case were 1.67×10^4, 1.71×10^4, and 1.68×10^4 along lines 1, 2, and 3.

Reynolds stress results from velocity fluctuations. By comparing the obtained values from the two cases, it is evident that in the one-to-many configuration of the supply nozzles (N6O-M), the interaction of the inlet jet with the disk tips generates significantly higher fluctuations compared to the one-to-one configuration (N6O—O).

To investigate the locations where the maximum and minimum levels of fluctuations occur, the normalized Reynolds stress magnitudes were calculated by dividing these values by their maximum value. Fig. 7 compares the obtained values for each case.

Fig. 7 shows a different distribution of normalized Reynolds stress magnitudes in the N6O—O and N6O-M cases. In the N6O-M case, the minimum values are observable on the disk surfaces, and these values increase as they approach the mid-gap area, reaching a maximum at the gap center. This trend is consistent along all three lines investigated.

In contrast, the N6O—O case exhibits a different distribution pattern. Except for line 3, the distribution follows a "W" shape, with maximum values near the wall area, indicating that the fluctuations are close to the disk surfaces. Along line 3, the minimum values are observed close to the disk surfaces, increasing towards the mid-gap. Line 3, having the maximum distance from the inlet jet among the chosen lines, represents the most developed boundary layer.

In the N6O—O case, since the gap and nozzle width are the same size, there is no interaction between the inlet jet and the disk tips. Therefore, we can conclude that the source of fluctuations, in this case, is the interaction of the inlet jet with the developing boundary layer from the parallel disks, causing the maximum Reynolds stress magnitude to be in the area close to the disk surfaces.

In the N6O-M case, the fluctuation of velocity is the outcome of interaction of inlet jet with disk tips and a developing boundary layer from parallel surfaces of disks.

A three-dimensional demonstration of a vortex core can well represent the source of fluctuations. For this aim, the vortex core of flow, colored by velocity magnitude utilizing the Q-Criterion method, is presented in Fig. 8. To better represent the vortexes in the area close to the nozzle jet, the Q-Criterion was set to be equal to $2.5 \times 10^9 s^{-2}$. Different Q-Criterion values were tested to find the best one representative of small vortex generated on the disks surface of the N6O—O case compared to high level of vorticities in the N6O-M case.

Fig. 8 demonstrates the interaction of the inlet jet flow with the disk tips in the N6O-M case. This interaction causes a convergent-divergent shape of the flow structure at the entrance to the gap. Additionally, there is a visible growing vortex from the disk surfaces. The developing boundary layers produce vorticities in the near-wall area. Therefore, in the N6O-M case, the level of fluctuation is influenced by both phenomena.

Fig. 8 also presents the vortex generation from the disk surfaces in the N6O—O case, which is the only source of fluctuations in this configuration. The interaction of the inlet jet with the developing boundary layers, which is maximal at the outer diameter of the disks, generates vortices and fluctuations that dissipate as they approach the outlet.

In the presented Q-Criterion level, the flow structures in the N6O-M case are strongly affected by vorticities generated by the interaction of the inlet jet with the tips of the disks, while small vorticities are produced by wall shear stress on the disk surfaces, in the N6O—O case. Considering the presented results in Fig. 8, in the N6O—O case, the viscous effect damps and lowers the level of fluctuations, whereas the generated turbulence in the N6O-M case is too strong to be damped by this effect.

5. Conclusion

The comparison of general parameters obtained from the LES simulation of the Tesla turbine with N6O—O and N6O-M nozzle configurations shows that the N6O—O design is 17.8 percent points more efficient, with lower mass flow rate and power generation.

Parametric analysis of the observed results demonstrates that the higher mass flow rate and the formation of a convergent-divergent nozzle structure in the area close to the inlet nozzle cause higher velocity and lower pressure in this region in the N6O-M case. This phenomenon shifts the area with the maximum circumferential wall shear stress slightly toward the inner diameter of the disk.

Analyzing the Reynolds stress magnitude and its distribution along the gap at different locations reveals quite different trends in the studied cases. In the N6O-M case, these values increase as they approach the mid-gap. In contrast, in the N6O—O case, where wall shear stress is the only source of fluctuations, the maximum values are observable near the disk surfaces and decrease as they approach the mid-gap.

The main source of fluctuations in the N6O-M case is the interaction of the inlet jet with the disk tips, which results in significantly higher levels of fluctuations compared to the N6O—O case, where the only source of fluctuation is the interaction between the inlet jet and the developing boundary layers from the parallel disk surfaces.

In the N6O—O case, the viscous effect damps and lowers the level of fluctuations, whereas the generated turbulence in the N6O-M case is too strong to be damped by this effect.

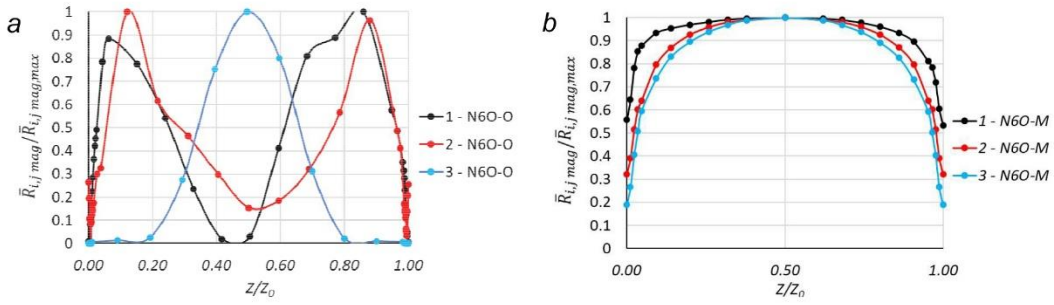

Fig. 7. Normalized Reynolds stresses magnitude along lines 1, 2, and 3 observed from (a) N6O—O, and (b) N6O-M.

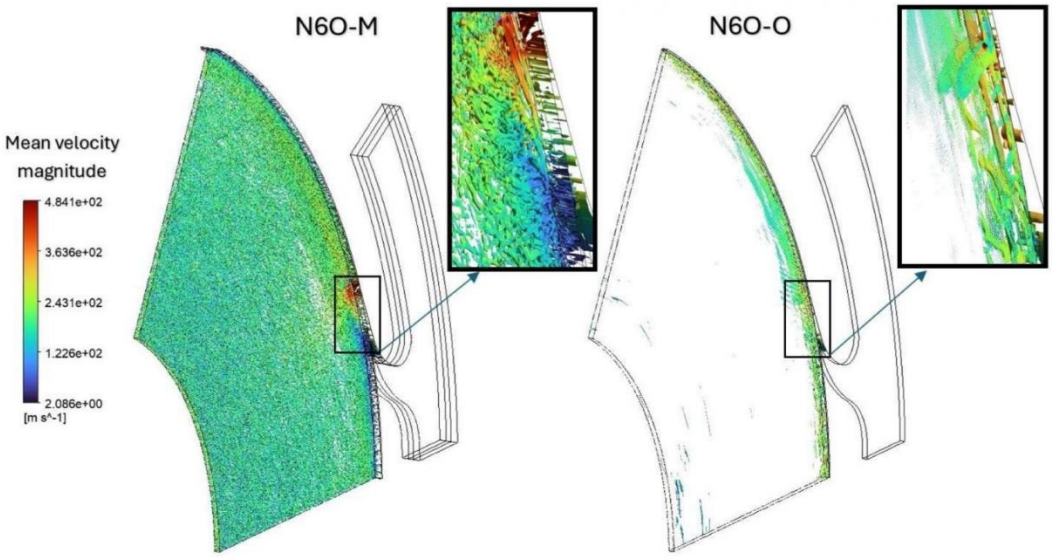

Fig. 8. The vortex core of flow, colored by velocity magnitude utilizing the Q-Criterion method for Q-Criterion equal to $2.5 \times 10^9 \boldsymbol{S}^{-2}$.

Nomenclature

c_p	specific heat capacity	T	temperature
d_w	wall distance	t	time step
d_{th}	Nozzle throat width	$\overline{V}_r$	radial velocity
e	internal energy	$\overline{W}$	relative velocity
f_i	gravitational force	y^+	dimensionless distance from the wall
h_{max}	maximum edge length of the cell	P_K	shear production of turbulence
h_{wn}	wall-normal grid spacing	σ_ω	specific dissipation rate constant
k	turbulent kinetic energy	σ_k	turbulent kinetic energy constant
$\dot{m}$	mass flow rate	ρ	density
N	Power	τ	tangential stress
p	Pressure	μ	dynamic viscosity
q	heat flux	ω	specific dissipation rate
Re	Reynolds number	ω_a	rotational speed
R_{ij}	Reynolds stresses	ν	kinematic viscosity
R_i	inner radius of the disk	δ	gap between co-rotating disks
R_o	outer radius of the disk	ϵ	radial tip clearance between the casing and the disks
S	strain rate		

CRediT authorship contribution statement

Mohammadsadegh Pahlavanzadeh: Writing – original draft, Visualization, Validation, Software, Methodology, Investigation, Formal analysis. **Włodzimierz Wróblewski:** Writing – review & editing, Supervision, Project administration, Methodology, Investigation. **Krzysztof Rusin:** Writing – review & editing, Validation, Supervision, Methodology, Formal analysis.

Declaration of competing interest

The authors declare that they have no known competing financial interests or personal relationships that could have appeared to influence the work reported in this paper.

Acknowledgement

The presented research was conducted within the UMO-2019/35/B/ST8/01871 research project financed by the Polish National Science Centre and statutory research funds for young scientists financed by the Silesian University of Technology.

Data availability

No data was used for the research described in the article.

References

[1] L. Pacini, L. Ciappi, L. Talluri, D. Fiaschi, G. Manfrida, J. Smolka, Computational investigation of partial admission effects on the flow field of a tesla turbine for ORC applications, Energy 212 (2020) 118687, https://doi.org/10.1016/J.ENERGY.2020.118687.

[2] L. Talluri, O. Dumont, G. Manfrida, V. Lemort, D. Fiaschi, Geometry definition and performance assessment of Tesla turbines for ORC, Energy 211 (2020) 118570, https://doi.org/10.1016/J.ENERGY.2020.118570.

[3] G. Ghim, J. Lee, Condensation heat transfer of low GWP ORC working fluids in a horizontal smooth tube, Int. J. Heat. Mass Transf. 104 (2017) 718–728, https://doi.org/10.1016/J.IJHEATMASSTRANSFER.2016.08.090.

[4] G. Xu, J. Fu, Y. Quan, J. Wen, B. Dong, Experimental investigation on heat transfer characteristics of hexamethyldisiloxane (MM) at supercritical pressures for medium/high temperature ORC applications, Int. J. Heat. Mass Transf. 156 (2020) 119852, https://doi.org/10.1016/J.IJHEATMASSTRANSFER.2020.119852.

[5] Tesla N. Nikola Tesla U.S. Patent 1,061,206 - Turbine, 1913.

[6] A. Ganguly, S. Sengupta, S. Pramanik, Waste heat recovery using Tesla turbines in Rankine cycle power plants: thermofluid dynamic characterization, performance assessment and exergy analysis, Appl. Therm. Eng. 207 (2022) 118141, https://doi.org/10.1016/J.APPLTHERMALENG.2022.118141.

[7] K. Aliakbari, A. Ebrahimi-Moghadam, M. Pahlavanzadeh, R. Moradi, Performance characteristics and exhaust emissions of a single-cylinder diesel engine for different fuels: experimental investigation and artificial intelligence network, Energy 284 (2023) 128760, https://doi.org/10.1016/J.ENERGY.2023.128760.

[8] K. Rusin, W. Wróblewski, S. Rulik, M. Pahlavanzadeh, E. Hasani Malekshah, Investigation on the influence of surface roughness of rotating microchannel on flow conditions, in: Turbomachinery — Multidisciplinary Design Approaches, Optimization, and Uncertainty Quantification; Radial Turbomachinery Aerodynamics; Unsteady Flows in Turbomachinery, 13D, 2023, https://doi.org/10.1115/GT2023-101917.

[9] M. Pahlavanzadeh, K. Rusin, W. Wróblewski, Assessment of turbulent parameters modification to model roughness in the flow between rotating disks of Tesla turbine, Simul. Environ. Impact Energy Syst. (2023), https://doi.org/10.52202/069564-0048.

[10] K. Rusin, W. Wróblewski, E. Hasani Malekshah, M. Pahlavanzadeh, S. Rulik, Extended analytical model of Tesla turbine with advanced modelling of velocity profile in minichannel between corotating disks with consideration of surface roughness, Energy 307 (2024) 132775, https://doi.org/10.1016/J.ENERGY.2024.132775.

[11] C.F. Colebrook, Turbulent flow in pipes, with particular reference to the transition region between the smooth and rough pipe laws, J. Instit. Civil Eng. 11 (1939) 133–156, https://doi.org/10.1680/ijoti.1939.13150.

[12] J. Nikuradse, Laws of flow in rough pipes nikuradse, Nation. Advis. Comm. Aeron. (1933).
[13] K. Wieghardt, W. Tillmann, National advisory committee for aeronautics on the turbulent friction layer for rising pressure national advisory commit'17ee for aeronautics on the turbulent friction layer for rising pressure*, NASA (1944).
[14] C. Grigson, Drag losses of new ships caused by hull finish, J. Ship Res. 36 (1992) 182–196, https://doi.org/10.5957/JSR.1992.36.2.182.
[15] G. Indelicato, P.E. Lapenna, A. Remiddi, F. Creta, An efficient modeling framework for wall heat flux prediction in rocket combustion chambers using non adiabatic flamelets and wall functions, Int. J. Heat. Mass Transf. 169 (2021) 120913, https://doi.org/10.1016/J.IJHEATMASSTRANSFER.2021.120913.
[16] S.G. Kandlikar, D. Schmitt, A.L. Carrano, J.B. Taylor, Characterization of surface roughness effects on pressure drop in single phase flow in minichannels, Phys. Fluids 17 (2005) 100606, https://doi.org/10.1063/1.1896985.
[17] M. Pahlavanzadeh, S. Rulik, W. Wróblewski, K. Rusin, Application of roughness models to stationary and rotating minichannel flows, Int. J. Numeric. Methods Heat & Fluid Flow (2024), https://doi.org/10.1108/HFF-05-2024-0379 ahead-of-print.
[18] R. Baviere, F. Ayela, S. Le Person, M. Favre-Marinet, An experimental study of water flow in smooth and rough rectangular micro-channels, in: International Conference on Nanochannels, 2004, 2004, https://doi.org/10.1115/ICMM2004-2338 asmedigitalcollection.
[19] M. Pahlavanzadeh, K. Rusin, W. Wróblewski, Evaluation of dynamic correction of turbulence wall boundary conditions to simulate roughness effect in minichannel with rotating walls, Int. J. Numer. Methods Heat. Fluid. Flow. (2023), https://doi.org/10.1108/HFF-03-2023-0160/FULL/PDF ahead-of-print.
[20] A.L.R. Thomazoni, C. Ermel, P.S. Schneider, L.W. Vieira, J.D. Hunt, S.B. Ferreira, et al., Influence of operational parameters on the performance of Tesla turbines: experimental investigation of a small-scale turbine, Energy 261 (2022) 125159, https://doi.org/10.1016/J.ENERGY.2022.125159.
[21] H. Wang, K. Luo, C. Huang, A. Zou, D. Li, K. Qin, Numerical investigation of partial admission losses in radial inflow turbines, Energy 239 (2022) 121870, https://doi.org/10.1016/J.ENERGY.2021.121870.
[22] P. Lampart, Ł. Jędrzejewski, Investigations of aerodynamics of Tesla bladeless microturbines, J. Theoretic. Appl. Mech. (2011).
[23] K. Rusin, W. Wróblewski, S. Rulik, The evaluation of numerical methods for determining the efficiency of Tesla turbine operation, J. Mech. Sci. Techn. 32 (2018) 5711–5721, https://doi.org/10.1007/S12206-018-1118-4.
[24] K. Rusin, W. Wróblewski, S. Rulik, Efficiency based optimization of a Tesla turbine, Energy 236 (2021) 121448, https://doi.org/10.1016/J.ENERGY.2021.121448.
[25] W. Qi, Q. Deng, Z. Chi, L. Hu, Q. Yuan, Z. Feng, Influence of disc tip geometry on the aerodynamic performance and flow characteristics of multichannel tesla turbines, Energies. 12 (2019) 572, https://doi.org/10.3390/EN12030572, 2019; 12:572.
[26] W. Qi, Q. Deng, Y. Jiang, Q. Yuan, Z. Feng, Disc thickness and spacing distance impacts on flow characteristics of multichannel tesla turbines, Energies. 12 (2019) 44, https://doi.org/10.3390/EN12010044, 2018;12:44.
[27] D.C. Wilcox, Formulation of the k-w turbulence model revisited, AIAA J. 46 (2008) 2823–2838, https://doi.org/10.2514/1.36541.
[28] B.E. Launder, D.B. Spalding, The numerical computation of turbulent flows, Comput. Methods Appl. Mech. Eng. 3 (1974) 269–289, https://doi.org/10.1016/0045-7825(74)90029-2.
[29] E. Larkermani, H. Bihs, G. Winckelmans, M. Duponcheel, T. Martin, B. Müller, et al., Development of an accurate central finite-difference scheme with a compact stencil for the simulation of unsteady incompressible flows on staggered orthogonal grids, Comput. Methods Appl. Mech. Eng. 428 (2024) 117117, https://doi.org/10.1016/J.CMA.2024.117117.
[30] L. Marocco, M. Sala, G. Centurelli, S. Straub, L. Colombo, LES simulations and Nusselt number decomposition of turbulent mixed convection of liquid metals flowing in a vertical pipe, Int. J. Heat. Mass Transf. 182 (2022) 121977, https://doi.org/10.1016/J.IJHEATMASSTRANSFER.2021.121977.
[31] M.L. Shur, P.R. Spalart, M.K. Strelets, A.K. Travin, A hybrid RANS-LES approach with delayed-DES and wall-modelled LES capabilities, Int. J. Heat. Fluid. Flow. 29 (2008) 1638–1649, https://doi.org/10.1016/J.IJHEATFLUIDFLOW.2008.07.001.
[32] J. Smagorinsky, General Circulation Experiments With the Primitive Equations, 1963. https://eurekamag.com/research/084/250/084250654.php. accessed December 22, 2023.
[33] U. Piomelli, P. Moin, J.H. Ferziger, Model consistency in large eddy simulation of turbulent channel flows, Phys. Fluids 31 (1988) 1884–1891, https://doi.org/10.1063/1.866635.
[34] I.B. Celik, Z.N. Cehreli, I. Yavuz, Index of resolution quality for large eddy simulations, J. Fluids. Eng. 127 (2005) 949–958, https://doi.org/10.1115/1.1990201.

Paper V

Roughness effects on flow in Tesla turbine with parametric adjustment of porous layer model

RESEARCH ARTICLE | JANUARY 03 2025

Roughness effects on flow in Tesla turbine with parametric adjustment of porous layer model

Mohammadsadegh Pahlavanzadeh ; Krzysztof Rusin ; Włodzimierz Wróblewski ; Sebastian Rulik

Physics of Fluids 37, 015139 (2025)
https://doi.org/10.1063/5.0247548

Physics of Fluids ARTICLE pubs.aip.org/aip/pof

Roughness effects on flow in Tesla turbine with parametric adjustment of porous layer model

Cite as: Phys. Fluids **37**, 015139 (2025); doi: 10.1063/5.0247548
Submitted: 7 November 2024 · Accepted: 6 December 2024 ·
Published Online: 3 January 2025

Mohammadsadegh Pahlavanzadeh,[a] Krzysztof Rusin, Włodzimierz Wróblewski, and Sebastian Rulik

AFFILIATIONS

Department of Power Engineering and Turbomachinery, Silesian University of Technology, Gliwice, Poland

[a]Author to whom correspondence should be addressed: mohammadsadegh.pahlavanzadeh@polsl.pl

ABSTRACT

Momentum diffusion and kinetic energy transfer are critical factors in turbomachinery, which significantly influence the performance of the Tesla turbine. In this investigation, a systematic study was conducted to model surface roughness in flow through the gap between corotating disks of a Tesla turbine. The aim was to define a porous layer instead of a roughness and modify the parameters of the porous material to model real roughness effects. The advantages of the porous layer model lies in its ability to directly simulate the actual roughness effect on flow and independency from equivalent sand-grain roughness. The investigation began with the results of the validation of the porous medium layer (PML) model against experimental tests on a minichannel. The parameters of the PML model were adjusted to achieve the same pressure drop as observed in the experiments. In the next step, the model was implemented in the Tesla turbine analysis. Turbulence closure was k-ω shear stress transport model, which was verified by the results of the large eddy simulation for the case with smooth rotor walls. Three different heights of the porous layer, each with modified parameters, were tested to investigate the effect of roughness height on turbine efficiency and flow parameters. The study demonstrated that the PML roughness model accurately represents the real roughness effect on flow, effectively simulating Tesla turbine performance in the tested cases. Analysis of the results indicates that as the roughness height increases, greater momentum transfer occurs between the operating fluid and the disks.

I. INTRODUCTION

The investigation of the effect of roughness on flow characteristics has been an active area of research in recent years.[1,2] The study of turbulent flows over rough surfaces finds applications in several fields, including friction in turbomachinery.[3] The effectiveness of friction turbomachines is based on momentum exchange between the flowing medium and rotating disks by diffusion of momentum, and therefore, detailed flow analysis is of great importance.[4,5] The Tesla turbine[6] is a friction turbomachine that works according to this principle and the operating fluid flows through a small gap between the corotating disks of the turbine rotor. Friction plays a crucial role in this process. In recent years, there has been growing interest in mini expanders, which can be implemented in various industries, such as combined heat and power (CHP) systems and organic Rankine cycle (ORC) systems, or for energy recovery applications.[7–9]

In an earlier study, Rusin *et al.*[10] examined a Tesla-type turbine with five corotating disks. Their research focused on optimizing efficiency by fine-tuning both geometrical and operational parameters. In their study, parameters subjected to the optimization process were inlet nozzle height, inter-disk gap, nozzle angle, pressure, and rotational velocity. Their approach primarily involved efficiency-driven numerical optimization of the Tesla turbine. The optimized parameters of their study are considered in the present paper.

Roughness effect on flow characteristic in submillimeter flow cross sections has various applications.[11] Rough walls make the turbulent boundary layer complex and induce an increase in skin friction drag,

$$C_f = \frac{\tau_w}{\frac{1}{2}\rho U_b^2}, \tag{1}$$

where τ_w and U_b are the wall shear stress and the velocity of bulk flow, respectively.

To assess flow behavior in the near wall region, theoretical wall functions have been formulated with a term regarding the implementation of roughness by a downward shift of velocity profile.[12–15] According to the Nikuradse measurements of the pressure drop in the pipe, the mean velocity profile in the log-law region for both smooth and rough cases is expressed as follows:[16]

$$U^+ = \frac{1}{\kappa}\ln(y^+) + C - \Delta U^+, \tag{2}$$

Physics of Fluids ARTICLE pubs.aip.org/aip/pof

where $U^+ = \frac{U}{u_\tau}$ is the dimensionless velocity and $y^+ = \frac{u_\tau y}{\nu}$ is the dimensionless wall distance. U represents the mean velocity, u_τ is the skin friction velocity (defined as $u_\tau = \frac{\tau_w}{\rho}$, where τ_w and ρ are the total wall stress and fluid density, respectively), y is the normal distance to the wall, ν is the kinematic viscosity, C is the smooth-wall intercept, which is assumed to be 5.1, κ is the von Karman constant equal to 0.41, and ΔU^+ represents the roughness function that describes the downward shift of dimensionless profile.

The most popular method of defining and account for the roughness in computational fluid dynamics (CFD) simulations is by applying the representative parameter: equivalent sand grain roughness. It can be determined by estimations based on various roughness parameters, documented in Ref. 17. There is another methodology to implement roughness in CFD simulation developed by Aupoix.[18] This method involves modifying the turbulence parameters on the wall, which leads to artificial changes in the eddy viscosity which is supposed to simulate the increase in wall shear stresses. The degree of change depends on the dimensionless sand-grain roughness.

Recently, Forooghi *et al.*[19] and Thakkar *et al.*[20] conducted direct numerical simulation (DNS) investigations on various irregular rough surfaces to identify key surface parameters affecting flow properties, such as ΔU^+ or k_s. These studies concur that, among these parameters, the skewness *Sk* of the surface height probability distribution function exhibits the greatest sensitivity in determining flow properties, particularly at constant roughness density. The literature[21,22] also discussed the implementation of roughness in simulations of simple computational domains by modifying momentum exchange. Kleinstreuer and Koo[23] related a relative surface roughness to the porous medium layer (PML) model for laminar flow. Their approach allowed the evaluation of microfluidic variables as a function of PML characteristics, i.e., layer thickness and porosity, uncertainties in measuring hydraulic diameters, as well as the inlet Reynolds number.

The investigation of flow characteristics inside the gap between corotating disks of a Tesla turbine, and the effect of surface roughness and nozzle configuration on flow parameters, has long been an interesting topic for researchers.[5,24,25] Pahlavanzadeh *et al.*[26,27] investigated the flow structures in the gap between corotating disks with uniform inlet flow, which can be regarded as a simplified model of the flow in a rotor of a Tesla turbine. They tried to find the best approach to simulate the flow inside such a domain considering different effective parameters. A systematic approach was utilized by studying different cases that focused on the formation of velocity profiles in each case. Roughness was one of the effective parameters taken into account.

This study examines the possibility of parametric modification of the PML model to implement roughness in the simulation of a Tesla turbine. The method was examined in the minichannel flow using a systematic approach and then applied to the Tesla turbine.

II. MATHEMATICAL MODEL

Numerical simulations were performed using Ansys Fluent commercial software, which is based on the finite volume method. The finite volume method is used to resolve discretized Reynolds-averaged Navier–Stokes equations. The investigation detailed in the paper involved conducting numerical simulations using the k-ω shear stress transport (SST) turbulence model.

The $k-\omega$ *SST* model constituted the turbulence closure, in which the transport equations of the turbulence kinetic energy k and specific dissipation rate ω are solved,

$$\frac{\partial(\rho k)}{\partial t} + \frac{\partial}{\partial x_j}(\rho U_j k) = \frac{\partial}{\partial x_j}\left[\left(\mu + \frac{\mu_t}{\sigma_k}\right)\frac{\partial k}{\partial x_j}\right] + P_k - \rho k\omega, \quad (3)$$

$$\frac{\partial(\rho\omega)}{\partial t} + \frac{\partial}{\partial x_j}(\rho U_j \omega) = \frac{\partial}{\partial x_j}\left[\left(\mu + \frac{\mu_t}{\sigma_\omega}\right)\frac{\partial \omega}{\partial x_j}\right] + \alpha^*\frac{\omega}{k}P_k - \beta^*\rho\omega^2. \quad (4)$$

In addition, two roughness methods are employed in different sections of the research.

A. Aupoix method

The Aupoix roughness method[18] modifies the turbulence parameters on the wall: turbulence kinetic energy and specific eddy dissipation rate, based on dimensionless sand-grain roughness k_s^+ as follows:

$$k_w^+ = \max\left(0; k_0^+\right), \quad (5)$$

$$k_0^+ = \frac{1}{\sqrt{\beta}}\tanh\left[\left(ln\frac{k_s^+}{ln10} + 1 - \tanh\frac{k_s^+}{125}\right)\tanh\frac{k_s^+}{125}\right], \quad (6)$$

$$\omega_w^+ = \frac{300}{k_s^+ 2}\left(\tanh\frac{15}{4k_s^+}\right)^{-1} + \frac{191}{k_s^+}\left(1 - \exp\left(-\frac{k_s^+}{250}\right)\right), \quad (7)$$

where k_w^+ and ω_w^+ are the dimensionless modified turbulent kinetic energy and specific dissipation rate, and the constant β is equal to 0.09.

B. PML method

In the PML method, a porous layer modifies the resistance to fluid flow, and the momentum term should be amended on porous parameters.

The governing equations involve continuity, momentum, and energy conservation in the following form:

$$\frac{\partial \alpha\rho}{\partial t} + \frac{\partial}{\partial x_j}(\alpha\rho U_j) = 0, \quad (8)$$

$$\frac{\partial(\alpha\rho U_j)}{\partial t} + \frac{\partial}{\partial x_j}(\alpha\rho U_i U_j) = -\alpha\frac{\partial p}{\partial x_i} + \frac{\partial \alpha\tau_{ij}}{\partial x_j} + \alpha\rho f_i - R, \quad (9)$$

$$\frac{\partial\left(\alpha\rho\left(e + \frac{1}{2}U_i U_i\right)\right)}{\partial t} + \frac{\partial}{\partial x_j}\left(\alpha\rho U_j\left(e + \frac{1}{2}U_i U_i\right)\right) = -\frac{\partial}{\partial x_j}(\alpha p U_j) + \frac{\partial}{\partial x_j}(\alpha\tau_{ij}U_i) - \frac{\partial}{\partial x_j}(q_j) + \rho f_i U_i, \quad (10)$$

where α is porosity, and R is the resistance term to flow in the porous medium.

Inside the porous layer, the porosity may vary, $0 \le \alpha < 1$, and the resistance term can be presented as follows:

$$R = \left(R_C + R_F U_i^\beta\right)U_i, \quad (11)$$

where R_C is a resistance constant, R_F is the resistance speed factor, and β is a resistance speed power (for $\alpha = 1$, $R = 0$).

Assuming steady fully developed 2D flow in an isotropic porous medium, the resistance part of Eq. (9), according to the Brinkman–Forchheimer-extended Darcy equation, can be written as

Physics of Fluids ARTICLE pubs.aip.org/aip/pof

$$R = \frac{\mu}{K}u + \frac{\rho C_f}{K^{1/2}}u^2. \quad (12)$$

in which the C_f is equal to 0.55, K is the permeability, $R_C = \frac{\mu}{K}$, and $R_F = \frac{\rho C_f}{K^{1/2}}$.

In the present approach, the resistance constant (R_C) and the resistance speed factor (R_F) are defined as a function of porosity (α). The porosity changes from 0 at the base of the porous zone to 1 at the interface with fluid. This variable is counted as the representative of roughness obstacles, and then the deviation of this parameter from the basement up to the interface will change. In this investigation, the porosity is assumed to be a second-order function of the thickness of the porous zone with the derivation of zero at the interface between the porous and flow zones. Moreover, R_C is defined to be a function of porosity $\left(R_C = \frac{\mu}{K\left(\frac{\alpha^3}{(1-\alpha)^2}\right)}\right)$ and R_F is a function of R_C $\left(R_F = \frac{\rho C_f}{\left(\frac{\mu}{R_C}\right)^{\frac{1}{2}}}\right)$.

Moreover, the viscosity of the fluid is corrected according to the Einstein equation. An effective viscosity, μ_e, is introduced to account for the effect of the porous medium on the diffusion term in the momentum equation as

$$\mu_e = \mu_r \mu, \quad (13)$$

$$\mu_r = 1 + 2.5(1 - \alpha). \quad (14)$$

III. VALIDATION OF NUMERICAL MODEL ON MINICHANNEL FLOW

The study started with the simulation of flow in a minichannel and validation of the results with an in-house experimental test setup. The roughness was implemented in the simulation considering both the PML method and the Aupoix method. The porous layer in the PML method had a thickness equal to the highest roughness peak. Figure 1 represents a schematic of real roughness, the equivalent sand grain roughness used in the Aupoix method, and the porous layer in the PML method. There are various methods to estimate equivalent sand-grain roughness based on different roughness parameters, but no universal formula exists for this calculation. In the current study, given the uniform distribution of the targeted roughness, the equivalent sand-grain roughness in the Aupoix method was set equal to the roughness height.

A. Numerical approach

In this part of the study, CFD simulation of water flow through the channel is carried out characterized by a width (z) of 50 mm, a length (x) of 150 mm, and a height (y) of 0.75 mm, at varying flow velocities. A developed inlet flow and ambient pressure at the outlet were considered. The side walls were non-slip and smooth and the top and bottom walls were rough.

The simulation incorporated roughness using the Aupoix method and drag correction utilizing a PML model, for a roughness height of 60 μm. The thickness of the porous layer is equal to the highest roughness peak, and permeability is used to modify the drag generation in the minichannel. To generate the same drag in the minichannel as it results from the theoretical lines for the roughness height equal to 60 μm, the permeability was adjusted to be $K = 23\,\text{nm}^2$.

The minichannel was simulated using the Reynolds-averaged Navier–Stokes (RANS) method and k-ω SST turbulence model. The mesh independence study was carried out by varying the number of nodes along the length, width, and height of the minichannel. In all cases, the hexahedral mesh was generated with the thickness of the first layer of 0.5 μm to ensure that $y^+ < 1$. In simulations involving flow over porous media, particularly in cases with small flow cross sections, sharp parameter gradients often arise at the interface between the flow field and the porous layer. To address this issue, the mesh layer thickness on both sides of the interface must be sufficiently fine. Accordingly, various mesh layer thicknesses in this region were tested, and the layer thickness was progressively reduced to minimize parameter gradients. Finally, the mesh layer thickness equal to 1 μm were employed, as an ignorable parameters gradient were observed using this thickness.

Table I represents the mesh size in the minichannel and the friction coefficients obtained in each case. In Table I, n_x, n_y, n_z are representative of node numbers along x, y, and z direction. The difference in the computational domain for simulations utilizing the PML and Aupoix methods lies in the addition of a porous layer to the top and bottom surfaces of the channel. Consequently, the total height of the channel in both cases are the same. The difference is when using the PML method, the flow field is constricted by the combined thickness

TABLE I. Mesh size in minichannel model.

Mesh size			
Porous medium layer $n_x \times n_y \times n_z$	Flow field $n_x \times n_y \times n_z$	Total nodes	Friction factor
500 × 20 × 80	500 × 30 × 80	2 000 000	0.0215
450 × 18 × 72	450 × 27 × 72	1 458 000	0.0214
400 × 16 × 64	400 × 24 × 64	1 024 000	0.0212
300 × 12 × 48	300 × 18 × 48	432 000	0.0205
150 × 6 × 24	150 × 9 × 24	54 000	0.0155

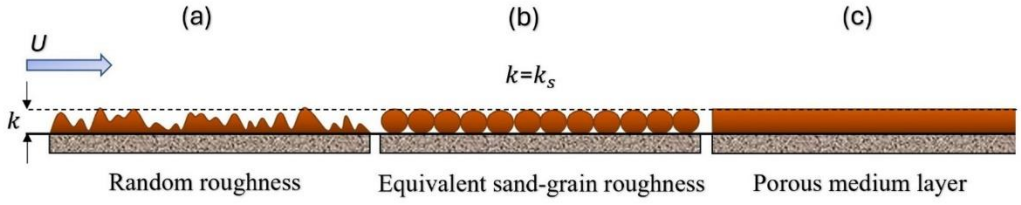

FIG. 1. Schematics of (a) real random roughness, (b) equivalent sand-grain roughness, and (c) porous layer with the same thickness as the highest roughness peak.

Physics of Fluids ARTICLE pubs.aip.org/aip/pof

of the two porous medium layers ($2 \times 60\,\mu$m). The PML model with the same number of nodes along the channel length and width, as well as a specific number of nodes along the thickness of the porous zone, was added. In this way, the blockage effect due to roughness is considered, which is an important upgrade over the Aupoix method.

As shown in Table I, the change in friction factor on the meshes with the node number greater than 1.024M is negligible. Consequently, in this part of the investigation, a mesh with a total number equal to 1.024M is used.

B. Experimental test setup

An in-house stationary test setup was constructed to investigate the effect of roughness on drag increase in the minichannel. The test rig is presented in Fig. 2. The operating fluid was water, and the channel characterized by a width (w) of 50 mm, a length (l) of 150 mm, and a height (h) of 0.75 mm, was examined at varying flow velocities.

The in-house test rig collected the necessary flow parameters to determine the friction factor for different Reynolds numbers (Re). Experiments were performed on minichannels that spanned a range of Re to capture the transition from laminar to fully turbulent flow regimes. This empirical study included channels with rough surfaces where aluminum oxide sheets with rough structures were attached to the top and bottom walls of the channel, having arithmetic mean deviation (R_a) of 11.3 μm, root mean square (R_q) of 13.16 μm, maximum peak to valley height of the profile (R_z) of 49.8 μm, and a total aluminum oxide sheet thickness, considered as the total roughness height (h_r) of 60 μm. The roughness height was added to the channel height to maintain a constant main flow cross section. The pressure was measured at two selected points along the 30 cm long channel, 15 cm apart. The first 15 cm section allowed the flow to fully develop and pressure readings were taken in the middle of the channel and near the outlet. The water volume flow rate and temperature were averaged and recorded every second using a flow meter and a thermocouple, respectively. Data from the channel with the mentioned roughness were used to calculate the friction factor. The pump operation increases the water temperature, and at a constant mass flow rate, the system reaches steady conditions after a while. However, changes in the mass flow rate also cause temperature variations. To minimize the impact of these fluctuations on the test results, the system was allowed to stabilize at each mass flow rate before data collection. Data collection was initiated only after the fluid temperature reached a stable state. After passing through the test section, the water is recirculated into a constant-temperature tank, where the maximum temperature change is limited to 0.6 °C per hour during operation at a constant flow rate. The pressure drop was calculated with a full-scale accuracy of 0.25% using the pressure transducer. Flow rate and temperature measurements were taken with full-scale accuracy and reading error of 0.5% and ±0.1 °C, respectively.

C. Results

The Fanning friction factor (f) was determined across a range of Re for laminar and turbulent regimes. The theoretical estimations for laminar flows are the following:

$$f = \frac{C}{Re}, \tag{15}$$

where the constant C is contingent upon the channel's aspect ratio denoted as $\alpha^* = \frac{h}{w}$, where h and w represent the height and width of a rectangular conduit.

$$C = 24(1 - 1.3553\alpha^* + 1.9467\alpha^{*2} - 1.7012\alpha^{*3} + 0.9564\alpha^{*4} - 0.2537\alpha^{*5}). \tag{16}$$

The Swamee and Jain[28] approximation is applied to resolve the Fanning friction factor within the turbulent regime,

$$f = 0.0625\left[\ln\left(\frac{h_r}{\frac{D_h}{3.7} + \frac{5.74}{Re^{0.9}}}\right)\right]^{-2}. \tag{17}$$

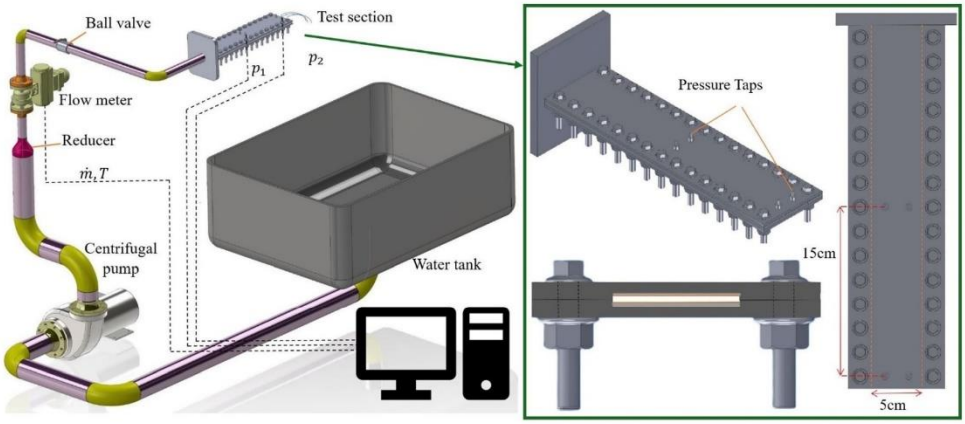

FIG. 2. Schematic of the in-house water test rig.

Physics of Fluids ARTICLE pubs.aip.org/aip/pof

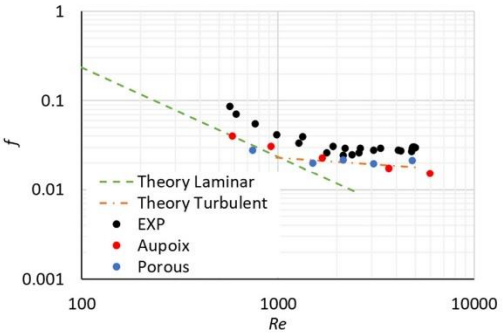

FIG. 3. Comparison of CFD simulations with experimental data and theoretical formulas for laminar and turbulent flows as a function of Re, using the Aupoix roughness and PML drag correction, considering the actual channel dimensions.

The literature[29,30] discusses that there is no fluid flow below a specific height of the roughness elements. As a result, the effective flow cross section can be reduced by the height of the roughness. Consequently, demonstrating the friction factor considering actual dimensions of the channel might represent deviation from theoretical estimations of friction factor in laminar and turbulent regime. Figure 3(a) presents a comparison of the friction factor distributions derived from experimental results, CFD simulations, and theoretical predictions considering actual dimensions of the channel. The reduction of effective flow cross section in experimental tests caused the deviation of obtained friction factor with theoretical lines. The comparison between the CFD simulations and theoretical predictions shows that the drag correction obtained using the PML method in the minichannel is appropriate and aligns well with the theoretical estimations.

IV. TESLA TURBINE SIMULATIONS

The second case, the main objective of the present investigation, was the Tesla turbine. This section starts with the validation of the k-ω SST turbulence model against the large eddy simulation (LES) model applied to the Tesla turbine with smooth walls. In the next part, the analysis was performed with the PML method for the roughness modeling.

A. Computational domain and boundary conditions

Figure 4 shows a schematic of the studied case including different parts of the computational domain and the applied boundary condition. The analysis focuses on a Tesla turbine design featuring six nozzles. Given the turbine's symmetrical geometry, which repeats every 60 °, simulating the entire structure would demand an excessive number of computational cells, significantly increasing the calculation time. The nozzle configuration used in this study is referred to as a "one-to-many" design, where a single nozzle supplies fluid to all the gaps between the corotating disks.

An absolute coordinate system is applied to model the plenum chamber, nozzle, and tip clearance regions, while the rotating frame is used for the gap between the corotating disks, incorporating porous zones to simulate surface roughness. The computational domain is divided into three distinct sections, as illustrated in Fig. 4.

1. Plenum chamber: This section forms part of the turbine's supply system.
2. Nozzle: A converging nozzle with a throat size of 0.7 mm, oriented at an 8° angle relative to the tangential direction.
3. Gap between corotating disks: Representing 1/6th of the entire gap (equivalent to 60°), with outer and inner diameters of 160 and 80 mm, respectively. This part includes the porous zones, simulating the roughness of the turbine's disk surfaces.

Corotating disks have the outer and inner diameters of 160 and 80 mm, respectively, and the gap size between them is 0.75 mm. To be in line with the prepared in-house test setup of the Tesla turbine, in which the roughness is implemented by erosion of material from the disks surface, the main flow field is maintained to be constant and two porous layers are added on both sides of the gap in rough cases. The radial tip clearance between the casing and the disks is set at 0.25 mm, based on the constraints of the real Tesla turbine design and manufacturing limitations. Periodic boundary conditions were applied on both sides of the disk sector with an angle of 60°. The thickness of the plenum chamber is equal to the thickness of the size of the gap plus the disk (2.75 mm). Symmetry boundary conditions were applied on both sides of the chamber. The plenum chamber, nozzle, and tip clearance were set in an absolute reference frame. The gap between disks and the porous zones were defined in the rotating frame.

The operating fluid was air, treated as an ideal gas. The geometry of the turbine and the selected operating and boundary conditions were determined taking into account the operating point with maximum efficiency from our previous study.[10] The inlet conditions were a total pressure of 2 bars, a total temperature of 300 K, and a turbulence intensity of 5%. Ambient pressure is applied at the outlet. The rotational speed was 17 500RPM.

The numerical solution of the conservation equations involves a weighted average of second-order upwind and central interpolations of variables. Time discretization is implemented using a second-order implicit transient formulation.

B. Mesh independence study

The mesh independence study was conducted by varying the number of nodes in the radial, circumferential, and axial directions for both the gap and porous layer as presented in Table II. In all cases, the hexahedral mesh was generated with the thickness of the first layer of 1 μm to ensure that $y^+ < 1$.

In the mesh independence check, the main focus was on the gap between corotating disks. In the gap, the distribution in the radial direction was denser in the rotor tip region, where we expect higher gradients of the flow parameters. The minimum and maximum distances were 10 and 500 μm, respectively. In the circumferential direction, the higher resolution was applied close to the nozzle jet with a minimum and maximum spacing of 0.25 and 0.5 mm, respectively. Along the gap, the minimum and maximum spacing was 1 and 80 μm, respectively, and these values along the thickness of the porous layer were equal to 1 and 10 μm. In the plenum chamber, the hexahedral mesh is generated with edge sizes in the range of 0.05–0.2 mm and the total number of nodes was 980k. Throughout all cases, a constant number of nodes in the plenum chamber was considered to ensure the same conditions at the inlet into the gap.

Physics of Fluids ARTICLE pubs.aip.org/aip/pof

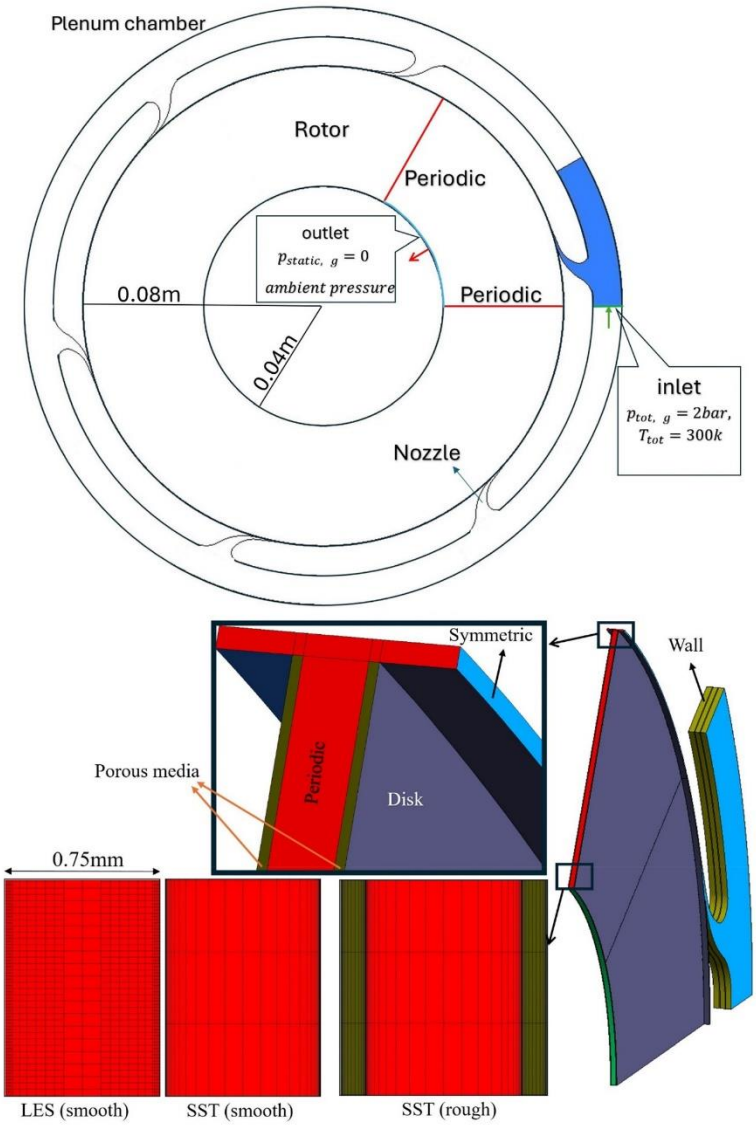

FIG. 4. Schematics of different parts of the computational domain, boundary conditions, and mesh.

In the naming convention used in this research, "N6" stands for six nozzles; "S" or "L" at the next stage indicates SST or LES, and "S" or "R" at the final stage represents the smooth or rough case, respectively. The numbers following "R" denote the roughness height in micrometers.

In each case, the generated torque (T) considering the full gap between two corotating disks equipped with six nozzles was calculated. The mesh independence study was carried out for the N6-S-R60 case, and the results are presented in Table II. In this table, n_r, n_θ, and n_z are the nodes number along the radial, circumferential, and gap, respectively. The mesh data in the table relate only to the gap between corotating disks. In the plenum chamber, the same mesh size of 980k was used in all cases.

Changes in torque on meshes with 1.49M nodes and more in the gap are lower than 0.8%. Additionally, the generated torque remained almost constant for mesh sizes of 2.12M and higher. Then the mesh

Physics of Fluids ARTICLE pubs.aip.org/aip/pof

TABLE II. Node distribution, total number of nodes, and torque generation for the mesh independence study.

Mesh size				
n_r	n_θ	n_z (Porous/gap/porous)	Total	Torque (N m)
122	362	18/30/18	2 914 824	0.123
110	324	16/27/16	2 124 906	0.123
97	289	14/24/14	1 492 389	0.122
61	181	9/15/9	364 353	0.116
48	144	7/12/7	186 548	0.105

chosen for further study had 2.12M nodes in the gap between the corotating disks.

C. Verification of the numerical model for the smooth case

LES simulations resolves large-scale turbulent eddies directly, capturing more accurate flow structures and transient phenomena. It provides detailed insights into turbulent flow behavior, particularly in unsteady flows.[31,32] LES simulation performs sufficient in capturing flow features such as separation, reattachment, and secondary flows in complex geometries or highly three-dimensional turbulent flows.[33,34] Due to the lack of a benchmark case, validation of the Tesla turbine simulation is performed by comparing the general parameters observed from the LES and k-ω SST simulations in smooth cases (N6-L-S and N6-S-S).

The wall-modeled large eddy simulation (WMLES) is implemented with the near-wall modeling by the subgrid-scale (SGS) model. The foundational Algebraic WMLES formulation was initially introduced in the research of Shur *et al.*[35] This model integrates a mixing length model with a modified Smagorinsky model[36] and incorporates the wall-damping function proposed by Piomelli *et al.*[37]

The required mesh for LES simulation is only generated in the gap between the corotating disks. In the plenum chamber, the hexahedral mesh is generated with an edge size in the range of 0.05–0.2 mm and 980k nodes in N6-L-S. The initial phase of the LES simulation started with 2.56M cubic cells, initialized with the converged k-ω SST solution obtained after 14 000 iterations. The success of an LES simulation requires the resolution of at least 80% of the turbulent kinetic energy. To achieve this, it is necessary to resolve eddies whose sizes are greater than approximately half the size of the integral length scale (l_0). The integral length scale is a local quantity that can be evaluated as follows using k and ω values obtained from the RANS simulation:

$$l_0 = \frac{k^{0.5}}{(C_\mu \omega)}, \tag{18}$$

where $C_\mu = 0.09$.

Based on Kolmogorov's energy spectrum to resolve 80% of the eddies, this requirement has to be satisfied:

$$\frac{l_0}{\Delta} \geq 4.8, \tag{19}$$

where $\Delta = \sqrt[3]{\text{cell volume}}$.

The presence of rotating walls induced the generation of small eddies in the adjacent wall area. To meet the LES criteria in at least 90% of the domain, the mesh underwent two rounds of modification, achieving a total number of cells of 60M. The mesh modification process was carried out to ensure that the ratio of the integral length scale to cell size (l_0/Δ) remained higher than 4.8. N6-L-S used two rounds of cell modification, first for the first three layers and then for the first two layers of near-wall cells, accompanied by a switch from the k-ω SST model to LES.

The simulations achieved convergence after almost 72 000 iterations, with the initial time step set at 1×10^{-8} s and gradually increased to 1×10^{-6} s. The Courant number was checked at each step and for the time step equal to 1×10^{-7} s was equal to one. After the solution convergence with the Courant number of one was achieved, the pressure fluctuations at a specific point with the most pronounced converge–diverge nozzle effect were analyzed using the fast Fourier transform (FFT). The period of these fluctuations was identified as 0.0002 s. Therefore, the parameters were time-averaged over this period to provide a smoother representation of their distribution. Figure 4 shows a schematic representation of the computation domain, boundary conditions, and modified mesh.

To validate the performance of the k-ω SST turbulence model in the Tesla turbine, the general parameters obtained from the N6-S-S and N6-L-S simulations are compared in Table III.

The power and efficiency of the system are calculated as follows:

$$N = \Omega \int T dA, \tag{20}$$

$$\eta = \frac{N}{\dot{m} c_p T_{in} \left(1 - \left(\frac{p_{out}}{p_{in}}\right)^{\frac{\gamma-1}{\gamma}}\right)}, \tag{21}$$

where Ω is the rotational speed.

Additionally, the generated power was also estimated as follows using the Euler equation for turbomachinery:

$$N_E = (v_{\theta,in} r_{in} - v_{\theta,out} r_{out}) \dot{m} \Omega. \tag{22}$$

As shown in Table III, the k-ω SST model overestimates all the general parameters compared to LES. The overestimation is 1.2% for mass flow, 17% for torque, and approximately 4% for efficiency.

The acceptable overestimation of the parameters obtained from N6-S-S compared to N6-L-S demonstrates the appropriate performance of the k-ω SST turbulence model in the simulation of a Tesla turbine. The literature discusses that the k-ω SST model tends to

TABLE III. Comparison between the parameters obtained from the simulation of N6-S-S and N6-L-S.

Parameter	N6-S-S	N6-L-S
Mass flow rate (kg/s)	8.0×10^{-3}	7.9×10^{-3}
Torque (N m)	0.103	0.088
Power (W)	188	161
Power-Euler's equation (W)	190	159
Efficiency	29.1	25.1
Power/Mass flow rate (m^2/s^2)	23 592	20 412

Physics of Fluids ARTICLE pubs.aip.org/aip/pof

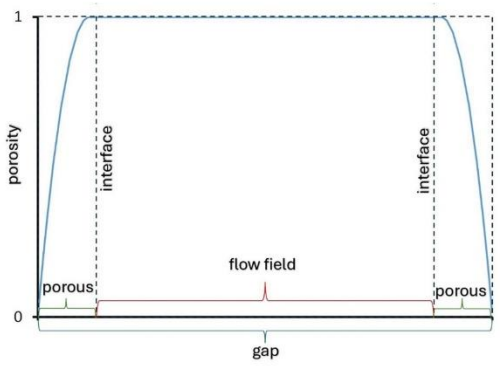

FIG. 5. Schematic of the porosity distribution along the gap between corotating disks.

dampen fluctuations, particularly in regions where the flow is turbulent but not fully developed, and presents a smoother parameters distribution in the computational domain.[38,39] Despite this tendency, the strong agreement between the k-ω SST model and the time-averaged LES simulation supports its use for the Tesla turbine simulations.

D. Tesla turbine simulation with roughness model

The accuracy of the k-ω SST turbulence model in simulating the Tesla turbine, along with the effectiveness of the PML and Aupoix roughness methods, was evaluated in Secs. IV A–IV C. In this section, the performance of the adjusted parameters of the PML roughness method is tested in Tesla turbine simulations. The global parameters obtained from these simulations are then compared with those obtained from Aupoix's method. A porous medium layer with the same modifications as those tested in the minichannel was applied to the disk surfaces of the Tesla turbine. In the case of the Tesla turbine simulation, the mesh layer thickness at the interface between the flow field and the porous layer was also set to 1 μm, similar to the thickness used in the minichannel. With this value, the parameter gradients in this region were negligible. Figure 4 [SST (rough)] presents a schematic of the gap, illustrating the addition of the porous layer on both disk surfaces and the generation of the mesh. Figure 5 shows the porosity distribution along the gap, with values ranging from zero at the wall to one where the flow encounters no resistance. The other porous parameters were defined as functions of porosity.

As described in the PML method, the R_C and R_F are defined as a function of α which is modeled as a second-order function of the porous zone's thickness, with a zero derivative at the interface between the porous and flow zones. To this end, three heights of roughness were considered in this study: 30 μm (N6-S-R30), 60 μm (N6-S-R60), and 120 μm (N6-S-R120). A comparison of the turbine performance parameters for the rough and smooth cases is presented in Table IV.

The comparison of global parameters presented in Table IV shows acceptable agreement between these approaches. The maximum disparity in system efficiency between the two methods is 2.7%pt. in the N6-S-R120 case.

In the model, the porous medium layer is added on both sides of the disk surfaces. With an increase in porous layer thickness, the flow cross section also increases. As demonstrated in Table IV, there is no change in the mass flow rate with the increase in the thickness of the porous layer. The addition of the PML enhances momentum transfer, leading to increased torque generation. This effect becomes more pronounced with greater porous layer thickness. A constant mass flow rate combined with a substantial increase in torque generation, enhances the turbine's efficiency. Additionally, the increase in momentum transfer between the operating fluid and the rotating disks influences the distribution of the velocity components.

The enhancement of momentum transfer due to the addition of the porous layer leads to increased torque generation. This effect increases with the thickness of the porous layer and alters the distribution of the velocity components.

Figure 6 compares the distribution of the radial and tangential components of the velocity in a mid-gap plane by the increase in the porous layer.

The velocity distribution in the radial direction within the Tesla turbine domain is influenced by three key forces: centripetal, pressure, and viscous forces. The relative magnitude of these effects varies with rotational speed. An increase in shear stress, a component of viscous forces, impacts the formation of both velocity components. As surface roughness on the corotating disks increases, greater momentum transfer occurs between the operating fluid and the disks, leading to a faster reduction in the energy level of the flow.

The tangential velocity component, which is critical for torque generation, diminishes more rapidly with increased wall shear stress caused by higher roughness. This enhanced momentum transfer results from rough surfaces reducing boundary layer thickness, thereby

TABLE IV. Comparison of general parameters obtained for the smooth and rough cases.

Parameter	N6-S-S	N6-S-R30 (PML)	N6-S-R30 (Aupoix)	N6-S-R60 (PML)	N6-S-R60 (Aupoix)	N6-S-R120 (PML)	N6-S-R120 (Aupoix)
Mass flow rate (kg/s)	8.00×10^{-3}	8.05×10^{-3}	8.08×10^{-3}	8.05×10^{-3}	8.00×10^{-3}	8.06×10^{-3}	8.04×10^{-3}
$p_{static,g}$ (Pa) gap entrance	47 722	40 353	39 140	37 016	35 902	28 604	32 962
Torque (Nm)	0.103	0.112	0.119	0.123	0.125	0.141	0.132
Power (W)	189	204	217	225	229	258	241
Power-Euler's equation (W)	190	208	218	221	227	257	240
Efficiency (%)	29.2	31.4	33.1	34.7	35.2	39.7	37.0
Power/mass flow rate (m^2/s^2)	23 592	25 851	268 556	28 517	28 625	32 637	29 975

Physics of Fluids ARTICLE pubs.aip.org/aip/pof

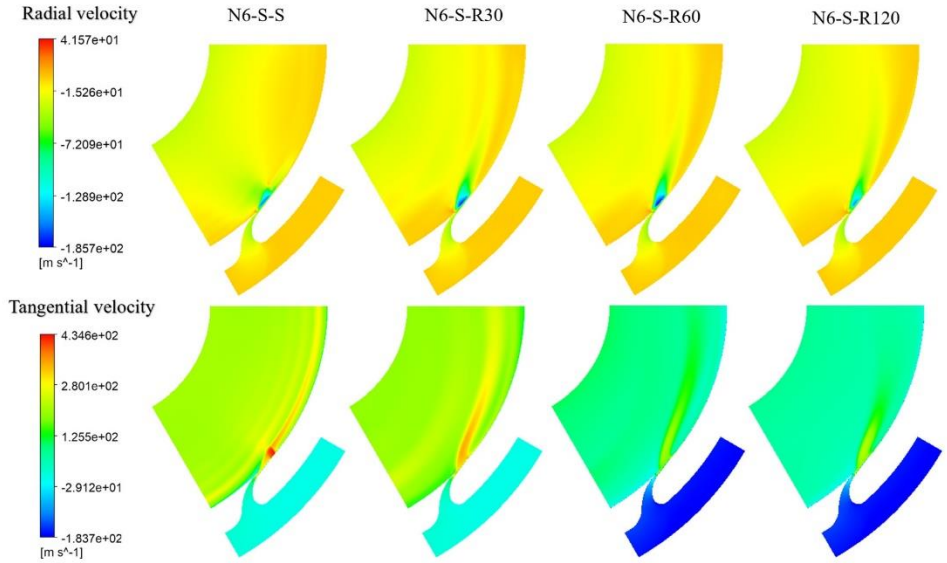

FIG. 6. Radial and tangential velocity profiles of all smooth and rough cases on a plane, defined in mid-gap.

intensifying the interaction between the fluid and the rotating surfaces. This interaction generates more effective drag forces, ultimately increasing torque and power output. Furthermore, the heightened surface roughness amplifies turbulence within the flow. While smoother surfaces tend to support more laminar flow, the introduction of roughness promotes the formation of small-scale eddies and vortices, increasing turbulence. This turbulence enhances fluid mixing but also leads to greater energy dissipation, potentially affecting overall turbine efficiency.

As roughness height increases, the distribution of radial velocity undergoes significant changes. Specifically, the region where the maximum influence of the inlet nozzle jet is observed shifts inward toward the disks' inner diameter. For example, as shown in the contours in Fig. 6, in the N6-S-S case, the effect of the inlet nozzle jet on radial velocity is concentrated near the outer diameter of the gap. With increased roughness height, the resulting changes in flow behavior cause the flow to lose energy earlier along its path, moving the point of maximum velocity impact closer to the inner diameter.

To further discuss flow conditions in the computational domain and the effects of the nozzle and roughness, the Mach number on a mid-gap plane is presented in Fig. 7.

In each case, the maximum Mach number was observed in the area with the maximum inlet jet effect, and among all studied cases, the N6-S-S and N6-S-R120 demonstrate the maximum and minimum values of the Mach number in this area, respectively.

The Mach number contour presented in Fig. 7 demonstrates a critical value, indicating the presence of a shock wave in both the N6-S-S and N6-S-R30 cases. This phenomenon significantly affects flow behavior, leading to flow deflection and increased fluctuations. These effects are revealed by the sharper changes observed in the velocity component contours and the Mach number, which highlight the instability introduced by the shock wave.

Both the maximum Mach number and the minimum gauge pressure appear in the smooth case. The contraction of inlet flow to the gap with the disks edge causes the flow separation and low pressure area in the tip region of the rotor. The flow separation in this region results in a converging-diverging formation, with a high Mach number occurring in the diverging section. This configuration accelerates the flow through the converging part, followed by a rapid expansion and the development of supersonic velocities in the diverging region.

As the roughness height increases, the effect of flow separation diminishes. Additionally, the increased shear stress promotes an earlier transition to a turbulent regime and reduces the boundary layer thickness. As a result of these combined effects, the throat size of the converging-diverging flow formation enlarges with increased roughness height, leading to a reduction in the Mach number at the diverging section of the nozzle.

Additionally, the smooth case exhibits a higher average pressure and Mach number on the mid-gap surface compared to the rough cases. Figure 7 illustrates the lowest values of both Mach number and relative pressure in the N6-S-R120 case.

Analysis of simulation results with different porous layer thicknesses demonstrated the effective performance of the introduced roughness method. Modifying the porous parameters in the PML method to account for the actual shape of roughness can accurately model the flow parameters and distribution within the computational domain. This method also effectively addresses the impact of roughness on the constriction of the flow cross section, which significantly improves alignment with theoretical predictions of friction in both laminar and turbulent regimes. In reality, the flow among the

Physics of Fluids ARTICLE pubs.aip.org/aip/pof

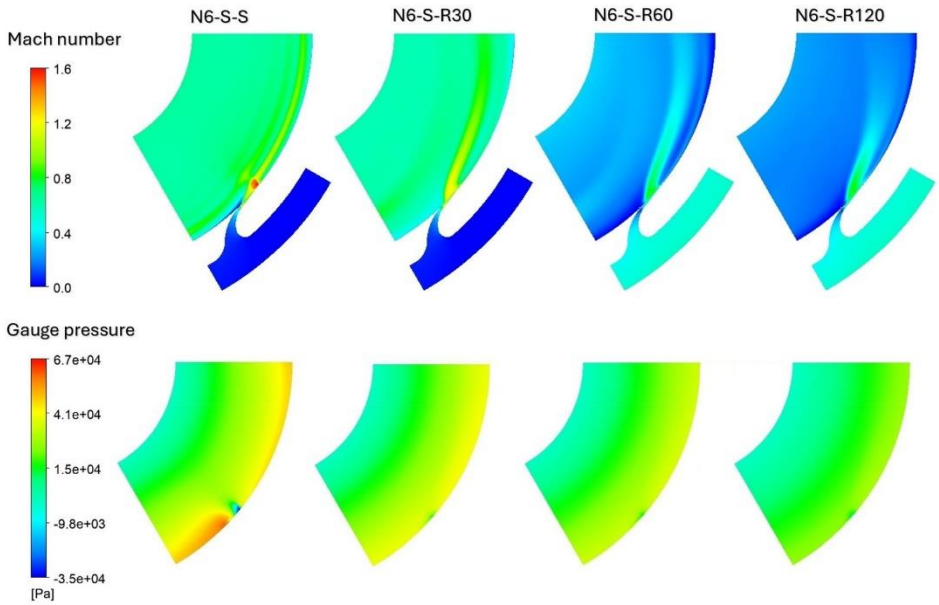

FIG. 7. Distribution of the Mach number and gauge pressure on a mid-gap plane for smooth and rough cases.

roughness elements is limited and the PML method effectively captures this behavior.

In the presented study, the modification of porous parameters was based on a real roughness shape used in experimental investigations in the minichannel section.

Mass flow-averaged parameters along the gap, from the outer to the inner radius, are calculated, and the distributions of the radial and circumferential velocity components, gauge pressure, and Mach number for all cases are shown in Fig. 8.

A comparison of the observed results from the N6-S-S and N6-S-R120 cases reveals a 6.6%, 13.3%, and 13.9% increase in radial velocity, tangential velocity, and Mach number, respectively, along with a 40% decrease in pressure at the entrance to the gap. Additionally, the results show a 16.6%, 28.2%, and 28% reduction in radial velocity, tangential velocity, and Mach number, respectively, at the inner diameter of the gap. The static gauge pressure in this section of the domain is equal to zero across all studied cases. An increase in the thickness of the porous layer amplifies the disparity in radial and tangential velocity in this region. Since the tangential velocity component is dominant, the Mach number distribution follows a similar pattern.

At the entrance to the gap, the implementation of roughness increases the flow cross section, while a noticeable drop in pressure occurs. The combination of these effects, along with changes in radial velocity, results in nearly the same mass flow rate across all studied cases. At the inner diameter of the gap, the static gauge pressure was set to zero. In the rough cases, the higher flow cross section combined with lower radial velocity ensures that the mass flow rate remains consistent. Additionally, the distribution of the velocity components and Mach number indicates a reduction in the kinetic energy of the operating flow with increased thickness of the porous layer.

The pressure distribution along line A shows a smaller pressure gradient between the entrance to the thickness of the gap and the outlet when the porous layer increases.

Changes in rotational speed can influence the impact of roughness on system efficiency. To explore this further, the efficiency of the system is calculated from Eq. (21) and presented in Fig. 9 for cases N6-S-S, N6-S-R30, and N6-S-R60 at different rotational speeds.

Figure 9 illustrates the characteristic comparison of cases N6-S-S, N6-S-R30, and N6-S-R60 at different rotational speeds. As shown in the figure, the system achieves maximum efficiency when the rotational speed is within the range of 17 000–26 000 (rev/min). The maximum efficiency of the system was achieved at 26 000 (rev/min) for the N6-S-S case and at 22 000 [rev/min] for both the N6-S-R30 and N6-S-R60 cases, with efficiencies of 30.57%, 33.62%, and 34.97%, respectively. The largest efficiency improvement was observed between the N6-S-S and N6-S-R60 cases, with a 4.61% increase in efficiency at 22 000 (rev/min). Increasing the thickness of the porous layer enhances the efficiency of the turbine, with the peak efficiency occurring within this specific rotational speed range. The observed efficiency gains are significantly lower at both higher and lower rotational speeds.

The results demonstrated sufficient performance of the methodology in simulating the Tesla turbine, making it appropriate for use in simulations of more complex computational domains.

V. CONCLUSION

Increased surface roughness enhances turbulent mixing in separated shear layers, reducing their thickness and improving momentum

Physics of Fluids ARTICLE pubs.aip.org/aip/pof

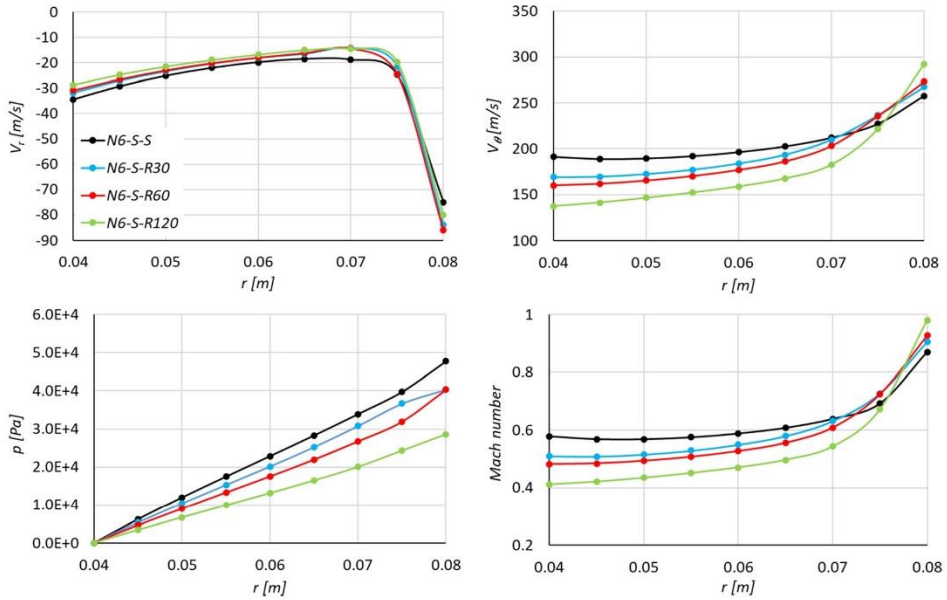

FIG. 8. Distribution of radial (V_r) and tangential (V_θ) velocity, gauge pressure (p), and Mach number along line A.

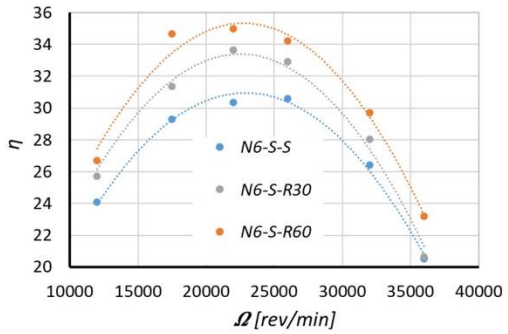

FIG. 9. Efficiency of the system in different rotational speeds.

transfer. To simulate this effect in computational fluid dynamics (CFD), a porous medium layer with parameters adjusted to match the actual roughness shape can be employed. This study systematically tested this approach on a Tesla turbine, using a specific roughness profile and tailoring porous medium parameters accordingly. Validation was conducted using experimental data from a minichannel test with the same height as the gap between the Tesla turbine's corotating disks. The validated methodology was then applied to simulate the Tesla turbine, demonstrating its effectiveness.

At each step, the results were compared with Aupoix roughness method and the results demonstrated sufficient performance of the introduced roughness implementation method in complex computational domains.

The flow separation because of inlet jet to the gap creates a converging–diverging pattern of inlet flow at this area. As the height of the roughness increases, this phenomenon is dampened by viscous forces, leading to a smoother transfer of operating flow from the inlet to the outlet. The roughness method effectively improved the momentum transfer to the corotating disks, improving system efficiency.

The mass flow-averaged parameters indicated a more rapid decrease in the kinetic energy of the operating flow as the porous layer thickness increased.

Analyzing the results from the smooth and two rough cases at different rotational speeds reveals that roughness has the greatest impact on improving turbine efficiency when the rotational speed is in the range of 17 000–26 000. The efficiency improvement observed with the implementation of a 60 μm porous layer compared to the smooth case was 4.61% at 22 000 (rev/min).

In the present study, a specific roughness shape was considered, and the porous medium parameters were adjusted to replicate the real roughness shape and generate the same drag in the flow. For future work, it is recommended to apply this procedure to various roughness shapes to establish a connection between the porous parameters and roughness characteristics, such as the root mean square of roughness height or any other roughness parameter.

ACKNOWLEDGMENTS

The research presented was conducted within the UMO-2019/35/B/ST8/01871 research project financed by the Polish National

Physics of Fluids ARTICLE pubs.aip.org/aip/pof

Science Center and statutory research funds for young scientists financed by the Silesian University of Technology.

AUTHOR DECLARATIONS

Conflict of Interest

The authors have no conflicts to disclose.

Author Contributions

Mohammadsadegh Pahlavanzadeh: Formal analysis (lead); Investigation (lead); Methodology (lead); Software (lead); Validation (lead); Visualization (lead); Writing – original draft (lead). **Krzysztof Rusin:** Conceptualization (equal); Formal analysis (equal); Investigation (supporting); Methodology (equal); Supervision (equal); Writing – review & editing (equal). **Włodzimierz Wróblewski:** Conceptualization (lead); Methodology (equal); Project administration (lead); Supervision (lead); Writing – review & editing (equal). **Sebastian Rulik:** Investigation (equal); Methodology (equal); Validation (supporting); Writing – review & editing (equal).

DATA AVAILABILITY

The data that support the findings of this study are available within the article.

NOMENCLATURE

c_p	Specific heat capacity
d_w	Wall distance
e	Inner energy
f_i	Gravitational force
h_{max}	Maximum edge length of the cell
h_{wn}	Wall-normal grid spacing
k	Turbulent kinetic energy
$\dot{m}$	Mass flow rate
N	Power
N_E	Power-Euler's equation
p	Pressure
$p_{static,g}$	Gauge static pressure
$p_{total,g}$	Gauge total pressure
P_k	Production of turbulence kinetic energy
q	Heat flux
Re	Reynolds number
r_{in}	Radii of gap inlet
r_{out}	radii of gap outlet
S	Strain rate
T	Temperature
t	Time step
U	Mean velocity
y^+	Dimensionless distance from the wall
α^*, β^*	Closure coefficients in specific dissipation rate equation
μ	Dynamic viscosity
μ_t	Turbulent viscosity
$v_{\theta,in}$	Mass flow average tangential velocity at gap entrance
$v_{\theta,out}$	Mass flow average tangential velocity at gap outlet
ρ	Density
σ_k	Turbulent kinetic energy constant
σ_ω	Specific dissipation rate constant
τ	Tangential stress
Ω	Rotational speed
ω	Specific dissipation rate

REFERENCES

[1]V. D. Romanin and V. P. Carey, "An integral perturbation model of flow and momentum transport in rotating microchannels with smooth or microstructured wall surfaces," Phys. Fluids **23**(8), 82003 (2011).

[2]M. Zayernouri, S. W. Park, D. M. Tartakovsky, and G. E. Karniadakis, "Stochastic smoothed profile method for modeling random roughness in flow problems," Comput. Methods Appl. Mech. Eng. **263**, 99–112 (2013).

[3]L. Ciappi, D. Fiaschi, P. H. Niknam, and L. Talluri, "Computational investigation of the flow inside a Tesla turbine rotor," Energy **173**, 207–217 (2019).

[4]P. Lampart and Ł. Jędrzejewski, "Investigations of aerodynamics of Tesla bladeless microturbines," J. Theor. Appl. Mech. **49**(2), 477–499 (2011).

[5]K. Rusin, W. Wróblewski, S. Rulik, M. Pahlavanzadeh, and E. Hasani Malekshah, "Investigation on the influence of surface roughness of rotating microchannel on flow conditions," in Volume 13D: Turbomachinery—Multidisciplinary Design Approaches, Optimization, and Uncertainty Quantification; Radial Turbomachinery Aerodynamics; Unsteady Flows in Turbomachinery (2023).

[6]N. Tesla, U.S. patent US1061206A (5 May 1913).

[7]G. Manfrida, L. Pacini, and L. Talluri, "An upgraded Tesla turbine concept for ORC applications," Energy **158**, 33–40 (2018).

[8]L. Pacini, L. Ciappi, L. Talluri, D. Fiaschi, G. Manfrida, and J. Smolka, "Computational investigation of partial admission effects on the flow field of a tesla turbine for ORC applications," Energy **212**, 118687 (2020).

[9]G. Ghim and J. Lee, "Condensation heat transfer of low GWP ORC working fluids in a horizontal smooth tube," Int. J. Heat Mass Transfer **104**, 718–728 (2017).

[10]K. Rusin, W. Wróblewski, and S. Rulik, "Efficiency based optimization of a Tesla turbine," Energy **236**, 121448 (2021).

[11]B. Dai, M. Li, and Y. Ma, "Effect of surface roughness on liquid friction and transition characteristics in micro- and mini-channels," Appl. Therm. Eng. **67**(1–2), 283–293 (2014).

[12]K. Wieghardt and W. Tillmann, "On the turbulent friction layer for rising pressure," Report No. NACA-TM-1314 (National Advisory Committee for Aeronautics, 1944).

[13]B. E. Launder and D. B. Spalding, "The numerical computation of turbulent flows," Comput. Methods Appl. Mech. Eng. **3**(2), 269–289 (1974).

[14]C. F. Colebrook, "Turbulent flow in pipes, with particular reference to the transition region between the smooth and rough pipe laws," J. Inst. Civil Eng. **11**(4), 133–156 (1939).

[15]C. Grigson, "Drag losses of new ships caused by hull finish," J. Ship Res. **36**(02), 182–196 (1992).

[16]J. Nikuradse, "Laws of flow in rough pipes," Report No. NACA-TM-1292 (National Advisory Committee For Aeronautics, 1933).

[17]M. Kadivar, D. Tormey, and G. McGranaghan, "A review on turbulent flow over rough surfaces: Fundamentals and theories," Int. J. Thermofluids **10**, 100077 (2021).

[18]B. Aupoix, "Roughness corrections for the k-ω shear stress transport model: Status and proposals," J. Fluids Eng., Trans. ASME **137**(2), 021202 (2015).

[19]P. Forooghi, A. Stroh, F. Magagnato, S. Jakirlić, and B. Frohnapfel, "Toward a universal roughness correlation," J. Fluids Eng., Trans. ASME **139**(12), 121201 (2017).

[20]M. Thakkar, A. Busse, and N. Sandham, "Surface correlations of hydrodynamic drag for transitionally rough engineering surfaces," J. Turbul. **18**(2), 138–169 (2017).

[21]T. Ozgumus, M. Mobedi, and U. Ozkol, "Determination of Kozeny constant based on porosity and pore to throat size ratio in porous medium with rectangular rods," Eng. Appl. Comput. Fluid Mech. **8**(2), 308–318 (2014).

[22]P. Forooghi, B. Frohnapfel, F. Magagnato, and A. Busse, "A modified parametric forcing approach for modelling of roughness," Int. J. Heat Fluid Flow **71**, 200–209 (2018).

[23]C. Kleinstreuer and J. Koo, "Computational analysis of wall roughness effects for liquid flow in micro-conduits," J. Fluids Eng. **126**(1), 1–9 (2004).
[24]K. Rusin, W. Wróblewski, S. Rulik, M. Majkut, and M. Strozik, "Performance study of a bladeless microturbine," Energies **14**(13), 3794 (2021).
[25]M. Pahlavanzadeh, W. Wróblewski, and K. Rusin, "On the flow in the gap between corotating disks of tesla turbine with different supply configurations: A numerical study," Energies **17**, 4472 (2024).
[26]M. Pahlavanzadeh, K. Rusin, and W. Wróblewski, "Evaluation of dynamic correction of turbulence wall boundary conditions to simulate roughness effect in minichannel with rotating walls," Int. J. Numer. Methods Heat Fluid Flow **33**, 3915 (2023).
[27]M. Pahlavanzadeh, K. Rusin, and W. Wróblewski, "Assessment of turbulent parameters modification to model roughness in the flow between rotating disks of Tesla turbine," in the 36th International Conference on Efficiency, Cost, Optimization, Simulation and Environmental Impact of Energy Systems (2023).
[28]P. K. Swamee and A. K. Jain, "Explicit equations for pipe-flow problems," J. Hydraul. Eng. **102**, 657–664 (1976).
[29]S. G. Kandlikar, D. Schmitt, A. L. Carrano, and J. B. Taylor, "Characterization of surface roughness effects on pressure drop in single-phase flow in minichannels," Phys. Fluids **17**(10), 100606 (2005).
[30]M. Pahlavanzadeh, S. Rulik, W. Wróblewski, and K. Rusin, "Application of roughness models to stationary and rotating minichannel flows," Int. J. Numer. Methods Heat Fluid Flow **34**, 4085 (2024).
[31]L. Marocco, M. Sala, G. Centurelli, S. Straub, and L. Colombo, "LES simulations and Nusselt number decomposition of turbulent mixed convection of liquid metals flowing in a vertical pipe," Int. J. Heat Mass Transfer **182**, 121977 (2022).
[32]R. Wang, J. W. Chew, F. Gao, and O. Marxen, "Large-eddy simulation of axial, radial and mixed centrifugal convection in a closed rotating cavity," Int. J. Heat Mass Transfer **227**, 125559 (2024).
[33]E. Larkermani, G. Cao, and L. Georges, "Characterization of the density-driven counter-flow through a doorway using large eddy simulation," Build. Environ. **221**, 109319 (2022).
[34]W. P. Jones and M. C. Paul, "Combination of DOM with LES in a gas turbine combustor," Int. J. Eng. Sci. **43**(5–6), 379–397 (2005).
[35]M. L. Shur, P. R. Spalart, M. K. Strelets, and A. K. Travin, "A hybrid RANS-LES approach with delayed-DES and wall-modelled LES capabilities," Int. J. Heat Fluid Flow **29**(6), 1638–1649 (2008).
[36]J. Smagorinsky, "General circulation experiments with the primitive equations," Mon. Weather Rev. **91**, 99–164 (1963).
[37]U. Piomelli, P. Moin, and J. H. Ferziger, "Model consistency in large eddy simulation of turbulent channel flows," Phys. Fluids **31**, 1884–1891 (1988).
[38]D. C. Wilcox, "Formulation of the k-w turbulence model revisited," AIAA J. **46**(11), 2823–2838 (2008).
[39]F. R. Menter, "Two-equation eddy-viscosity turbulence models for engineering applications," AIAA J. **32**(8), 1598–1605 (1994).